DISSERTATION

Titel der Dissertation

„*Apertureless scanning near-field optical microscopy and manipulation of nanostructures at electrified interfaces*“

Verfasser

Mag. rer. nat. Christoph Huber

angestrebter akademischer Grad

Doktor der Naturwissenschaften (Dr.rer.nat)

Wien, Mai 2012

Studienkennzahl lt. Studienblatt:	A 091 419
Dissertationsgebiet lt. Studienblatt:	Chemie
Betreuerin / Betreuer:	Univ.-Prof. Dipl.-Ing. Dr. Wolfgang Kautek

„Und is da Weg a noch so steil, a bissl wos geht olle weil"

Acknowledgement

Abstract

The introduction of lithographic processes based on the use of masks allowed a tremendous step forward in miniaturisation and commercialisation of high-end electronic components. Although the advantages of mask based lithographic processes are overwhelming, they all have to deal with the same restriction, known as the Abbe Limit, which limits the highest possible resolution to the half of the wavelength of the used light.

To overcome this constriction a new method was investigated, which is based on non-propagating waves at the end of a pointed probe to produce surface features with minimal size smaller than 10 nm. The so called apertureless near-field microscope, deals with a laser illuminated tip located at small distance (several nanometres) to a substrate. Therefore classical diffraction (Frauenhofer) doesn't come into account but near-field diffraction (Fresnel) is getting important. The achievable resolution limit is then given by the radius of curvature of the used tip (typ. ~10 nm)

If the geometry and illumination properties are chosen carefully, extremely high field enhancement (up to 10^6) can be realised at the end of the tip, due to the antenna effect, geometrical singularities and surface plasmon resonance.

This work started with theoretical investigations, based on a specially designed Matlab toolbox, using the Boundary Element Method to calculate the influence of various experimental parameters e.g. polarisation, dielectric properties etc. on the field enhancement factor. Moreover thermo-mechanical studies were performed to understand the behaviour of the heated cantilever system due to laser illumination and rule out awkward experimental setups.

The calculated results could be verified experimentally.

The mechanism of surface modification was studied with three different AFM (Atomic Force Microscope) working modes (contact, semi-contact, non-contact) at different laser parameters (repetition rate, polarisation, energy, angle of incidence etc.), and at different substrates (gold, polymer).

The influence of thermal-energy transfer in contact or through radiation, incubation and heat accumulation in the modification area was investigated.

It could be shown that surface modification is mainly driven by thermal energy transfer in contact or non-contact working regime and laser induced ablation is negligible.

Zusammenfassung

Die Einführung lithographischer Prozesse basierend auf der Verwendung von Masken ermöglichte einen wahrhaften Boom in der Miniaturisierung und Kommerzialisierung von elektronischen Hochleistungsbauteilen. So überzeugend die Vorteile lithographischer Maskentechniken auch sein mögen unterliegen sie doch alle derselben Limitierung, dem Abbe Limit. Dieses besagt, dass im Bereich der klassischen Optik die Auflösungsgrenze durch die halbe Wellenlänge des verwendeten Lichts gegeben ist.

Im Rahmen dieser Arbeit wurde eine Methode untersucht, welche es erlaubt das Beugungslimit zu durchbrechen. Dazu werden die Eigenschaften nicht propagierender Wellen genutzt um Oberflächenmodifizierungen im 10 nm Bereich zu realisieren.

Bei der aperturfreien Nahfeld-Mikroskopie wird der Abstand zwischen einer Spitze und einer Oberfläche bis auf wenige Nanometer reduziert. Somit gilt nicht mehr die klassische Frauenhofer Beugung (Fernfeld) sondern die Fresnel Beugung (Nahfeld), deren Auflösungslimit in diesem Fall durch den Krümmungsradius der verwendeten Spitze, welche wie eine Punktlichtquelle zu betrachten ist, gegeben wird. Bei entsprechender externe Beleuchtung kann es zu enormen Feldverstärkungen am Ende der verwendeten Spitze kommen (bis zu 10^6). Diese Verstärkung beruht auf Antenneneffekten, der Singularität am Ende der Spitze und Oberflächenplasmonenresonanzen.

Zuerst wurden theoretische Untersuchungen zur Berechnung der Feldverstärkung bei unterschiedlichen geometrischen und dielektrischen Randbedingungen mittels einer, auf der Boundary Element Method (BEM) basierenden, selbst entwickelten Matlab Toolbox durchgeführt, um optimale experimentelle Bedingungen zu garantieren.

Weiters wurden die mechanischen Auswirkungen, des laser-induzierten Heizens der Spitze mittels der kommerziellen COMSOL Multiphysics Software, berechnet. Die erhaltenen theoretischen Daten konnten auch experimentell bestätigt werden.

Zur Untersuchung des Mechanismus der Oberflächenmodifizierung, welcher in der Literatur immer noch kontrovers diskutiert wird, wurden Experimente mit 3 unterschiedlichen kraftmikroskopischen Arbeitsmodi (contact, semi-contact, non-contact) mit unterschiedlichen Laserparametern (Repetitionsrate, Polarisation, Energie, Einfallswinkel etc.) auf unterschiedlichen Substraten (Gold, Polymer) durchgeführt.

Der Einfluss von thermischem Energietransfer im Kontakt oder über Hitzestrahlung, Inkubationseffekte und Wärmeansammlung in der Modifikationszone wurde untersucht.

Es konnte gezeigt werde, dass der Mechanismus vorwiegend auf thermischer Energieübertragung im Kontakt oder über Wärmestrahlung basiert, und laser-induzierte Abtragung vernachlässigbar ist.

Table of content

1 Introduction

1.1 *Scientific Challenge*

In 1956 the hard disc drive for information storage was introduced by IBM. One year later the RAMAC 305 (capacity ~4.4 Mb) was leased for 3200$ per month, which corresponds to today's purchase price of 160.000$. About 50 years later a 2.5 inch 120 Gb hard disk was available for about 80$ (2010). This means that the price per Mbyte has decreased by 60 million times, whereas the recording density has increased by about 150 million times.[1]

The innovative trend of modern technology lies in smaller, cheaper, faster and better performance. To go this way scientists have developed lithographic techniques to provide mass production of microelectronic and microoptic devices. Most of them deal with far field illumination of the material, which should be modified. So they all face the same limitation, which is well know as the Abbe Limit:[2]

$$d = \frac{\lambda}{2n\sin\alpha}$$ (Eq.1)

The Abbe Limit describes the theoretical spatial resolution boundary due to the diffraction limit of light; where n is the diffraction index, λ the wavelength and α the opening angle of the light cone.

The most widely used technique is the mask far-field optical lithography with wavelengths from the near UV to the near IR domain due to several reasons, like costs and simplicity. The typical resolution limit of UV sources is about 150 nm. New small wavelength EUV (Extreme Ultra-Violet) sources enable a resolution better than 50 nm but this approach also requires expensive developments of new optics, photopolymers etc. A 193 nm exposure tool is approximately 15 million dollar, an EUV exposure tool around 30 million dollars.[3]

Several approaches have been discussed to improve the resolution like the increase of the diffraction index by immersion (solid and liquid) techniques which enhances the resolution by a factor of 2, mainly limited by the diffraction index of the available materials.[4, 5] or electron beam lithography.

A completely different approach is to go beyond the far-field illumination and enter the near-field regime, where the resolution is no longer diffraction limited. The idea of working within

the near-field of a light source is not as new as one might expect. Already in 1928 Edward Hutchinson Synge published his idea of performing optical near-field images by scanning a tiny aperture in very small distances over a surface.[6] But it took until 1982 that Denk and Pohl measured the first optical near-field scan trace at the IBM research laboratory. (See Ch.1.2)

The first attempts were made by shining light through a tiny aperture as suggested by Synge but the best achievable resolution until now is around 50 nm. This limit is based on the hindered throughput of laser light through tiny apertures and on construction limitations. Theoretically the diameter of a metallic aperture is limited through the cut-off effect, which means that propagating light becomes evanescent when the diameter of the aperture is below the critical cut-off diameter ($d_c = 0.6\lambda/n$). This results in a drastic λ–dependent loss and leads to a minimal aperture of about $\lambda/10$.[7, 8] Furthermore the tip immediately reaches high temperatures, which lead to the evaporation of the metal coating and subsequently light leakage. Another drawback is the bluntness of the tips due to of the production process, which makes it difficult to keep the tip in close proximity (< 5 nm) to the surface with shear force techniques.[9]

To overcome these problems the apertureless scanning near-field optical microscope (aSNOM) was developed (See Ch.1.3). Apertureless means that you do not shine through a tiny aperture but illuminate a solid SPM (Scanning Probe Microscopy) tip. The resolution limit in this approach is given by the size of the SPM tip, which is currently smaller than 10nm. In theory different mechanism like surface plasmons, the lightning rod effect and the antenna effect are mentioned to give rise to a significant local field enhancement at the end of the tip.[10-13] The strongly confined field is used to perform optical spectroscopy with high resolution or surface modification in the nanometric regime. The process of surface modification is still under discussion. On one hand people claim that it is due to thermal effects and on the other hand it is explained by the field enhancement at the end of the tip.

Nanostructuring of metal surfaces down to scales of less than 10 nm by nanosecond pulse laser illumination of STM (Scanning Tunnelling Microscope) tips was demonstrated and explained by near-field enhancement.[14] In contradiction to this, the observation of an increasing tunnelling current under laser illumination on the timescale of ms (millisecond) was taken as proof for thermal expansion and direct contact even with a reduction of the pulse length from 10 ns (nanosecond) to 100 fs (femtosecond)[15] in analogy to thermal nanoindentation of polymers.[16]

Also SPM (Scanning Probe Microscope) tips at sufficiently high intensities of ns laser [17] and fs laser irradiation [18] can deliver morphological and structural changes in materials at the nanometric level.

Femtosecond lasers as light source for aSNOM are considered to be reasonable due to several inherent features, such as distinct and sharp laser energy density threshold for ablation that is significantly lower than that for nanosecond or longer pulses, minimization of heat- and shock-affected areas, possibility of controlled machining of high conductivity materials e.g., thin gold films, multiphoton absorption processes enabling modification of transparent targets, and greater processing selectivity.[19]

A crucial part for studying the origin of surface modifications is the control of the tip-sample gap. In STM the tunnelling current between tip and sample is the common tool for predicting the tip to sample gap, whereas in an AFM (Atomic Force Microscope) setup the distance control is a very challenging task. One way to solve this problem is the use of a shear forces feedback mechanism. However, most of the commercial AFMs are working with the light lever principle, where the laser reflection of the backside of a vertical flexible cantilever on a PSD (Position Sensitive Device) is used to generate topographic pictures. Sophisticated approaches such as the employment of the phase shift as feedback signal have been reported to avoid tip contact for commercial SPM setups.[20]

This work is concerned with optical field enhancement and confinement for an asymmetrically illuminated nanoscopic SPM tip suspended over different materials like gold, polyphenylene oxide, polycarbonate or AZ4620 according to an apertureless scanning near-field optical microscope (a-SNOM). In the first chapter the theoretical background is provided. The second part describes the experimental setup of the Department of Physical Chemistry in Vienna and the Weizmann Institute of Science in Rehovot. In the third part the theoretical investigations of the field enhancement parameters, following the Boundary Element Method (BEM)[21] and thermo-mechanical studies with COMSOL are illustrated, underlined with experimental results. Furthermore various experiments at different working parameters e.g. AFM mode, laser illumination and substrate material are conducted and discussed. In the fourth chapter the results are summarised. In the fifth chapter supplementary information on the Matlab Tool box and the Floating Tip working principles is given.

1.2 History of Near-field

It was in 1928, the 22nd of April when Edward Hutchinson Synge, an Irishman living in Dublin described a new type of microscopic method in a letter to his colleague Albert Einstein. Einstein agreed with the proposal of Synge from the theoretical point of view but called it "prinzipiell unbrauchbar" (useless).[22] Nevertheless he suggested that Synge should publish his idea in a scientific journal.[6]

In addition to the theoretical idea of an aperture based near-field optical microscope, Synge was also the first to implement the idea of scanning, which is fundamental in lots of different technologies like television, SPM or electron microscopy. In 1932 he recommended to use piezo-electric quarz crystal for rapid and accurate scanning as well and calculated already the sensitivity of a piezo-electric transducer.[23]

13 years later John A. O´Keefe, without knowing the article of Synge, suggested by himself to scan a tiny aperture to generate a picture of the surface beyond the diffraction limit of light. The first experimental realisation was done only a few months later by Albert V. Baez who used acoustic waves ($\lambda = 14$ cm).[24]

More ten 10 years later Charles W. McCutchen provided the first intuitive picture for the understanding of the image formation in near-field optical microscopy, with a principal analogue to the radio receiver. But like Einstein he was very sceptical about the potential of this setup.[25]

It took until 1972 that the first experimental proof of near-field microscopy with electromagnetic radiation was published. Eric A. Ash and G. Nicholls from the University College of London used microwaves (λ=3cm) and an aperture of 1.5 mm to image an aluminium test pattern.[26] At a tip to sample distance of 0.5 mm they were able to achieve a resolution of λ/60, which is far beyond the diffraction limit. They also predicted the construction of an infrared microscope with comparable resolution.

It took more than 50 years after the first idea of Synge, that Winfried Denk recorded the first optical scan trace at the IBM Research Laboratories in Rüschlikon, Switzerland in 1982. (Fig. 1.1) The first publication with Dieter W. Pohl appeared with some delay in 1984, where they called their setup "optical stethoscope" in analogy to the acoustic stethoscope used in medical diagnostics.[27]
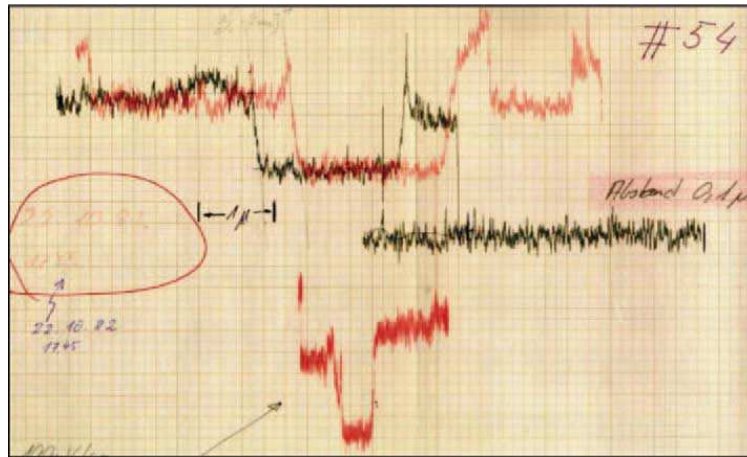
Fig. 1.1: First documented evidence of a scan trace measured by an optical near-field microscope with an aperture probe. The picture is from the laboratory book of Winfried Denk at the IBM Laboratories in Switzerland.[22]

Parallel to the group of Dieter W. Pohl, Fischer and Zingsheim pioneered in the field called nanosphere lithography. They used small particles in suspension and by evaporation of the solvent they create a two dimensional lattice. After deposition of a metal and removal of the particles the remaining metal film forms the well known Fischer pattern.[28] They are used as test samples for microscopy or Raman. One year later, in 1983 Fischer and Kuhn presented their experimental setup for near-field optical microscopy at the second Meeting of Molecular Electronic Devices.[22]

At the same time Aaron Lewis and co workers were trying to realize a "scanning nanometre optical spectral microscope".[29] Their first experimental results were done by a thermally pulled glass capillary in the patch-clamp technique. They studied the near-field excited fluorescence and demonstrated a resolution on the order of the aperture (~100nm).[30] They also introduced the acronym NSOM (Near-field Scanning Optical Microscope), which changed to SNOM in 1988 to emphasize the analogy to other scanning techniques like STM.[22]

In 1985 John Wessel proposed a method very similar to Synge´s original idea, although he didn't know his work. But he was inspired by the invention of STM by Binning in 1982 and the discovery of SERS (Surface Enhanced Raman Scattering)[31, 32]. He was also the first to mention the analogy to classical antenna theory.[33]

In 1991 Eric Betzig introduced aperture probes formed at the end of a metal coated, thermally pulled quartz fibre, which was the first commercially used method for fibre production in near-field optics.[34] Another breakthrough was the introduction of the shear force feedback, which is the most common way of non-contact distance control today.[35]

In 1994 the first single fluorescent molecule image by spatial mapping was published [36] which gave birth to the single molecule spectroscopy.[37]

Many variations of near-field optical microscopes have been reported, like STOM (Scanning Tunnelling Optical Microscope) but in this work we want to look on the aSNOM (apertureless Scanning Near-Field Optical Microscope) approach based on the commercial AFM setup. This development of apertureless approach went parallel to the aperture based near-field microscopy and was driven by the calculations and measurements of the field distribution near a tiny aperture. Fig. 1.2a shows the calculated field distribution of an aperture. Two intensity enhanced lobes at the rim of the aperture according to the incoming polarisation are visible.
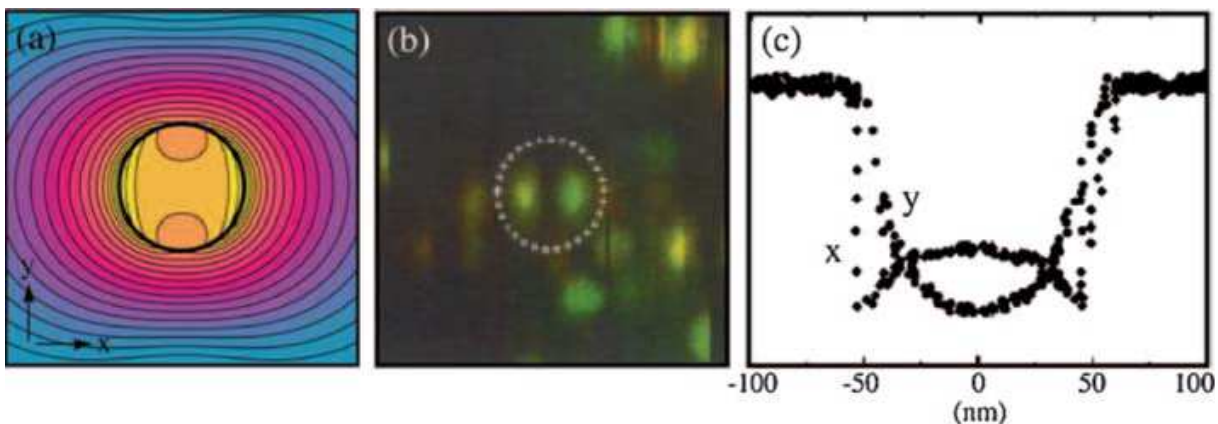
Fig. 1.2: The motivation of working with apertureless near-field microscopes is clearly illustrated in these three pictures. (a) shows the calculated field distribution along an aperture, indicated by the black ring. (b) The experimental evidence of the calculation in (a) is provided by a single molecule fluorescence picture. (c) Scattering intensity along a thin AlAs layer sandwiched between two GaAs half spaces. x and y are the major axis of (a).[38]

To improve the resolution of near-field microscopes, which is limited by the size of the aperture due to the intensity lobes located at the rim, scientists like Pohl suggested to reduce the size of the rim to a single point for maximum resolution.

Prior to the experimental evidence, as already mentioned, it was John Wessel in 1985, who proposed the concept of an apertureless scanning near-field microscope by using an elongated metal particle, irradiated by laser light to establish an enhanced light field at its extremities.[33]

It was again Dieter W. Pohl together with Ulrich C. Fischer who realized the first experimental demonstration of field enhancement effects with an apertureless near-field microscope by illuminating a small protrusion on a flat gold surface.[39]

In the following years, many groups joined this attempt and the introduction of metal tips as scattering centres started. Especially Inouye & Kawata, Boccara, Wickramasinghe and Keilmann pioneered in the development of various illumination and detection techniques.[40-50]

Pompe et al recognized that illuminating the SPM tip with sufficient high laser fluencies led to surface modifications of the investigated sample.[51] This was the start for a still on going discussion about the mechanism of surface nanostructuring in the near-field of a laser illuminated tip.

A lot of work was done to show that the mechanism is based on field enhancement effects [14, 17, 52-57], whereas not less operating expense was undertaken to explain the modifications by thermal effects.[58-62] In the second half of the 90ies especially K. Dickmann from the Advanced Technical College of Münster and P. Leiderer from the University of Konstanz published several papers, where they tried to proof their theory. Although the efforts have decreased there is still no proof of principal until today.

The latest developments and applications will be discussed in Chapter 1.4.

1.3 Principles of Near-field

The well know Abbe Limit, which claims that light can not be confined to dimensions smaller than $\sim\lambda/2$ may also be considered as a special case of Heisenberg's uncertainty principle.

$$\Delta x \, |p_x| \approx h/2\pi \qquad (Eq.2)$$

Δx is the position and p_x is the momentum, which is defined as $p_x=h/\lambda=hk_x/2\pi$. (The whole calculation is valid for y, z as well). In a medium i the wave vector has to satisfy:

$$k_i{}^2 = k_x{}^2 + k_y{}^2 + k_z{}^2 \qquad (Eq.3)$$

with $k_i = 2\pi/\lambda_i = n_i|k_o|$ (k_o is the wave vector in vacuum, λ_i is the wavelength in the medium i and n_i is the refractive index)

So to fulfil the requirements of classical optics, which deal with propagating light only, all k vectors have to be real. So none of them can be larger than k_i according to Eq.3. This leads to the positional uncertainty for a propagating beam of light:

$$\Delta x \geq 1 \, / \, |k_x| = \lambda_i/2\pi \qquad (Eq.4)$$

If you now claim position accuracy much bigger than the wavelength, which leads to a $k_x \gg$ than k_i, this can only be realized by at least one wave vector ($k_y{}^2$, $k_z{}^2$) being negative and therefore k_y or k_z being imaginary (See Eq.3). This means that in the direction of the imaginary wave vector the light field is not propagating but following an exponential decay, also called evanescent wave or near-field.[63]

Although often used as equal in literature there is a difference between the terms *optical near-field* and *evanescent wave*, because the evanescent wave is just a special case of the optical near-field.

As already mentioned, an optical near-field can be explained as non propagating wave with an imaginary wave vector, determining its spatial confinement. This is only possible if light is regarded as a wave and not as a particle.

One example for generating a near-field is to shine light on structures, much smaller than the wavelength of the used light. A very simple case would be a sphere S with a radius of a, where $a \ll \lambda$ is fulfilled. What you can observe in the far field region, which is also called Frauenhofer region (in contrast to the Fresnel region for the near-field), is the scattered light of the sphere. What is not observable in the far-field is the rapidly decaying near-field with an expansion of about a.[64]

A similar case would be the illumination of a small aperture ($d \ll \lambda$). Beside the conventionally scattered light a hemispherical optical near-field with a diameter in the range of the aperture can be observed.

To understand the reason for the extension of the near-field the first example will be investigated a little bit more in detail. In a dielectric material like in the already mentioned sphere S the electrons stay around the nuclei which together form the atoms. By shining light on S a displacement of the equilibrium position due to the Coulomb forces of the electric field of the incident light takes places. This leads to the generation of electric dipole moments.

In Fig. 1.3 the sphere S is composed of smaller spheres S_{1i} with a dipole moment of p_{1i}. This dipole moment is the vectorial sum of the electric dipole moments p_{2k} in S_{1i}, which arrange as a results of the attractive and repulsive Coulomb interaction with the surrounding electric dipoles. (*i* is the *i* th sphere, *k* is the *k* th dipole moment)
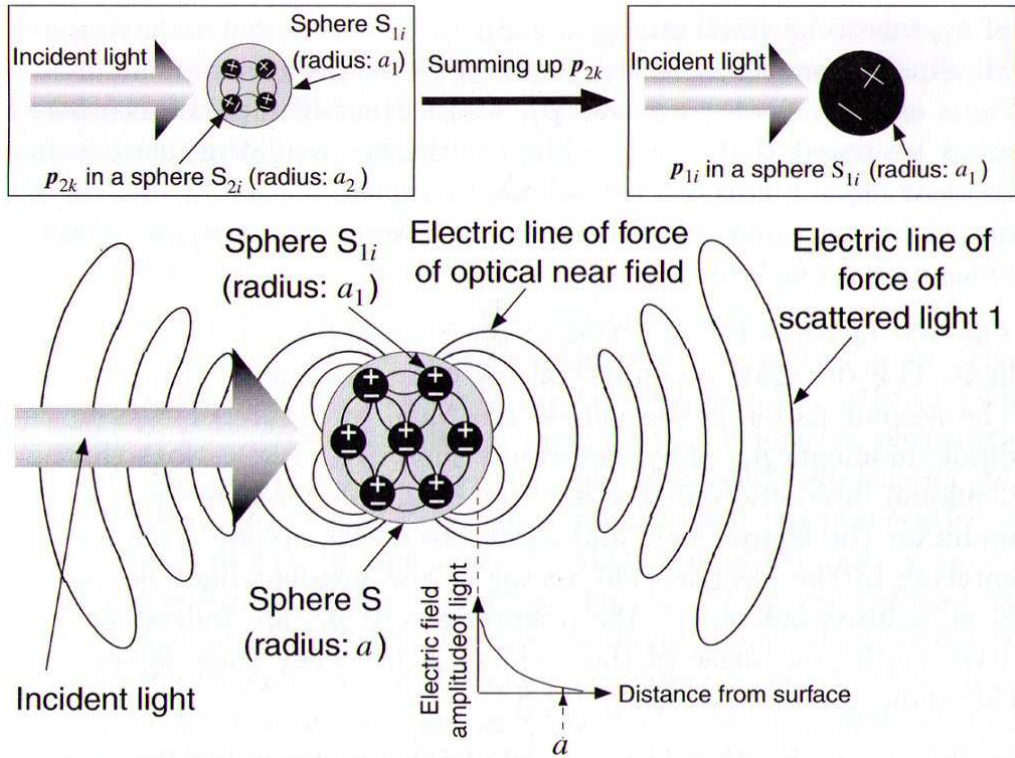
Fig. 1.3: Schematic description of the origin of a near-field around a sphere, S.[64]

It is valid to note that the size of the sphere S_{1i} must be small enough to be considered as having a single dipole moment p_{1i}. This dipole moment oscillates in phase with the electric field of the incident light.

Beside the direction of the electric field vector of the incident light also the shape and size of the structure determines the orientation of the dipole moments. The magnitude and orientation of the Coulomb forces is shown by the electric lines of force.

The electric lines of force tend to take the shortest possible trajectory. However the electric lines of force are not only found in but also on the surface, in very close proximity (Fig. 1.3). This leads to the strong confinement of the optical near-field.

The other type of electrical field generated by an oscillating dipole doesn't start from one dipole moment and ends at another one but forms closed loops of electrical force lines that propagate into the far-field. These lines represent the scattered light.[64]

If an interface between two different materials at an angle above the critical angle is illuminated, a surface wave, called evanescent wave is generated. It doesn't carry energy away from the surface and shows an exponential decay, whose decay length is in the order of the wavelength. (Fig. 1.4) This is in contradiction to the decay length of the near-field around a sphere, which is said to be in the same dimension as the radius of the sphere.
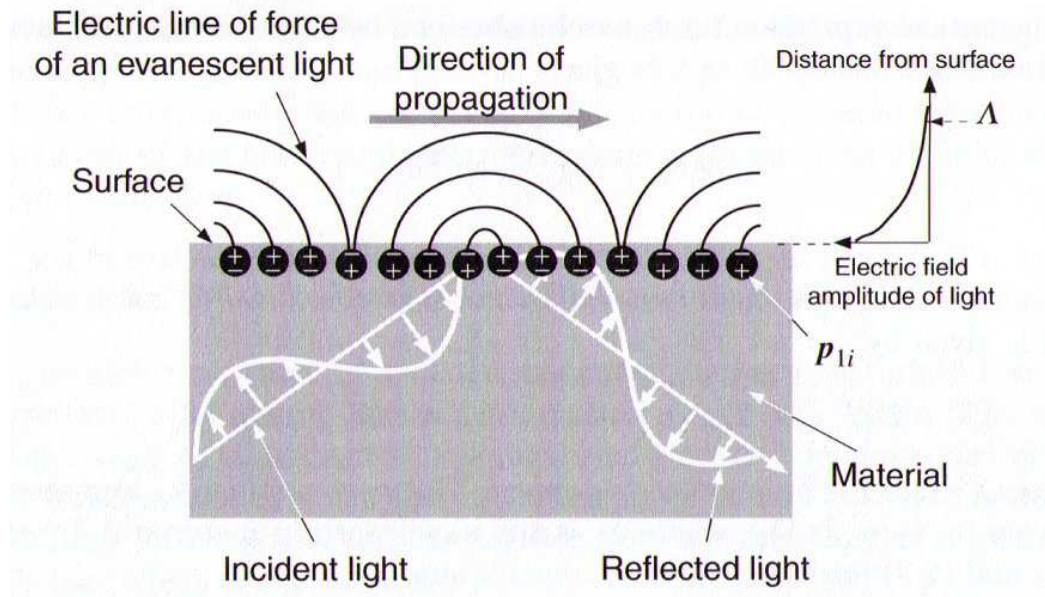
Fig. 1.4: Scheme of an interface where an evanescent wave is created by illuminating the interface at an angle larger than the angle of total internal reflection.[64]

Like in Fig. 1.3 the material is a dielectric and above the surface is vacuum. But in this case the boundary can be regarded as infinitely plane and therefore the orientation of the dipole moments p_{1i} is spatially phase and wavelength dependent. This leads to a periodic arrangement of the dipole moments and no propagating light is generated. (reason for total internal reflection)

Summing up all the electric force lines, which are connecting the electric dipole moments p_{1i} on the boundary, ends up in an optical near-field thickness in the order of the used wavelength. Consequently this is still in the field of classical optics. A widely used application would be the ATR-IR (Attenuated Total Reflection- Infrared) Spectroscopy.

The orientation of the dipole moment in Fig. 1.3 doesn't depend on the phase and the wavelength of the used light and therefore the only spatial quantity is the radius of the sphere, which then determines the extension of the near-field and gives the opportunity to go beyond the diffraction limit of light.[64]

1.4 Near-field Optical Microscopy

1.4.1 Basic concept

There are two main SNOM approaches found in literature. The first one is the aperture Scanning Near-field Optical Microscope, which was first suggested by Synge in 1928 and theoretical described by the Bethe-Bouwkamp theory.[65, 66]

In the aperture approach a tiny aperture is scanning over a surface in a distance much smaller than the wavelength to illuminate and/or collect light from the tip-sample system.

The second approach is called apertureless Scanning Near-Field Optical Microscope. In this approach a small structure, usually a STM or AFM tip serves as dipole, which interacts with the sample surface and radiates homogeneous waves, detectable in the far-field.

Both approaches have the limitation of being only able to probe sample surfaces due to the fast decay of the optical near-field.[67]

In the beginning of the near-field optic most of the research was done with aperture probes whereas in the last decade the interest of the scientific society shifted more and more into the apertureless approach. This is due to several reasons.

- Due to the singularity of an apertureless probe, which determines the resolution it can achieve a much higher resolution than an aperture probe. Image resolution of up to 1 nm has been reported.[47, 68]

- The production of reproducible ultra small apertures is a challenging task, which prohibits the cheap mass production.[67]

- The optical skin depth, which defines the penetration of light into a material limits the optical and the lateral topographical resolution, because the metal coating has to excess the skin depth in size and leads to big radius of curvature for aperture tips.[69] Therefore a single point contact can not always be guaranteed and distinctive differences in the topographical and near-field optical picture can occur.[70]

- Theoretically the diameter of a metallic aperture is limited through the cut-off effect, which means that propagating light becomes evanescent when the diameter of the aperture is below the critical cut-off diameter ($d_c = 0.6\lambda/n$). This results in a drastic λ–dependent loss and leads to a minimal aperture of about $\lambda/10$.[8, 71]

- The spectral response of an aperture probe is limited by the material of the waveguide, whereas a metallic tip can easily be used from ultraviolet to near infrared because of the possibility to use external optics.[72]

The apertureless SNOM can further be divided into two types. The first one is the scattering type SNOM, called (s-SNOM) where the elastic scattered light contains information of the tip-sample interaction and is detected in the far-field.[12, 47, 73-75]

The second one, is the tip-enhanced SNOM, where the locally enhanced field is used to excite photon-matter interaction like Raman scattering [76-78], fluorescence [79-83] and harmonic generation.[3, 84]

_____

As already mentioned above there are several approaches in the SNOM research and so it is not surprising that there exists a proper amount of different probes. In Fig. 1.5 the most common types of tips are illustrated.
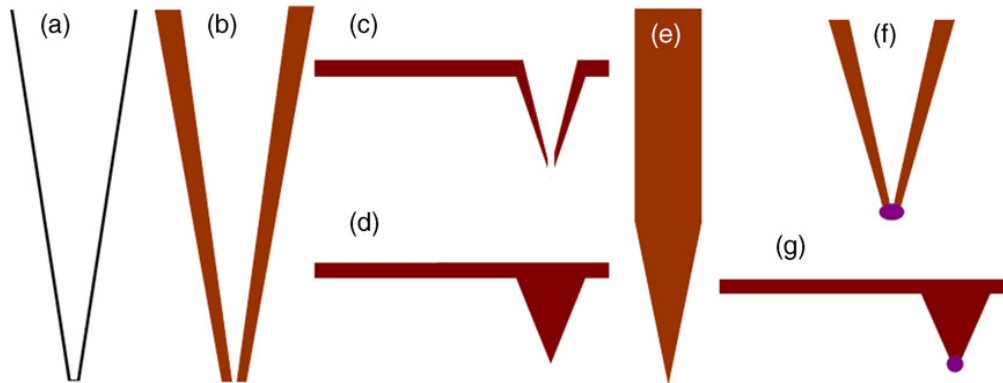

Fig. 1.5: (a) Dielectric aperture probe, (b) dielectric aperture probe coated with a metal film, (c) hollow AFM cantilever for aperture SNOM, (d) AFM cantilever with or w/o metal coating (e) STM tip, normally etched from Au, (f) metal coated aperture probe with active medium on the aperture and (g) AFM tip with active medium at the tip end.[85]

Optical fibre tips are normally produced by chemical etching [86-88] or thermal techniques (heating and pulling).[89] The typical throughput of a thermally generated tip is about 10^{-5} due to the small radius of the tip end. The etched aperture tips nominally reach a throughput of about 10^{-4}, because bigger cone angles can be manufactured.

The exponential decay of the light throughput with decreasing aperture diameter makes it very difficult to reach resolutions below 50 nm. It is not possible to increase the power of the incoming laser because the damage threshold of the metal cladding is reported to be already around 10-20 mW.[90] That's why extensive research has been carried out to modify the geometry of the aperture.[91-98] This leads to the triple-tapered fibre, which can produce improved throughput up to 3 orders of magnitude [93] or to the TOA (Tip on Aperture) approach.[96]

The tips used for apertureless SNOM, especially for AFM based SNOM are typically commercially produced tips with the advantage of high reproducibility and a reasonable variety of different coating materials like Au, Pt, W_2C or DLC (Diamond-like Carbon).

Tips used for STM based SNOM are homemade and require certain knowledge to guarantee good tip quality. Standard materials are Au or W but also Ag tips are used.

Depending on the system to measure different tips are suitable. A metal coated tip is desirable, for low intensity measurements like Raman, where the scattering cross section is about 10^{-14} times smaller than in fluorescence, because strong tip-sample coupling can occur due to SPR (Surface Plasmon Resonance) leading to very high enhanced fields at the end of the tip. This field can be further increased by the help of plasmonic surface structures like in

_____

SERS (Surface Enhanced Raman Scattering) [99] to gain sufficient high intensities for TERS (Tip Enhanced Raman Scattering).

Beside the different tip types the illumination mode plays an important role in the experimental setup. Depending on the transmissivity of the sample different illumination modes have to be chosen. In Fig. 1.6 all possible modes are displayed. For opaque samples only illumination from the top is applicable, whereas for transparent samples the whole bunch of varieties is accessible.
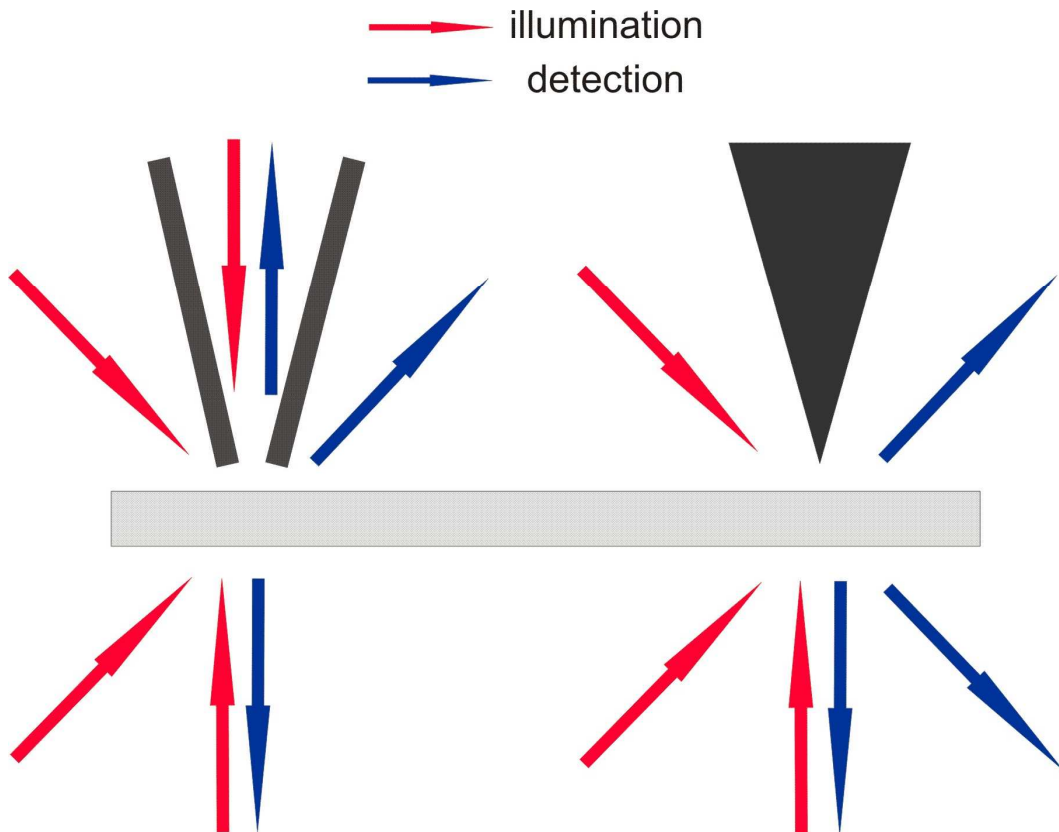
Fig. 1.6: Different illumination modes used in SNOM setups. The left scheme shows the possibilities for the aperture SNOM, whereas the right scheme displays the apertureless SNOM illumination possibilities.

Below we will concentrate on the apertureless approach because this is the main topic of this work.

1.4.2 Tip enhancement

Beside the fact that apertureless probes lead to better light confinement and therefore higher resolution, apertureless tips provide a second advantage which is summarized under the term field enhancement. This term includes three different principles of increasing the light intensity at the very end of tip.

Surface Plasmon Resonance

The simplest approach to understand this phenomenon is to look at a small spherical metal particle, whose size is much smaller than the wavelength of light. The optical properties of such a particle are mainly determined by the response of the electrons upon a resonant electromagnetic excitation and are described by the dielectric function. The dielectric constant is the sum of a contribution of the free electrons and of a contribution of the interband transitions. The behaviour of the free electrons can be described by the well known Drude model, which is similar to the Lorentz harmonic oscillator model. The interband transition is not important when considering alkali metals because there is no effect on the dielectric function in the visible due to the large band gap but cannot be ignored if noble metals are investigated. If the size of the metal becomes smaller than the mean free path of the electrons, a second damping term comes into account due to the collisions of the electrons with the boundaries of the system.[100]

Working with noble metals and light in the visible range can lead to a resonant collective oscillation of unbound electron also known as SPR (Surface Plasmon Resonance).[101] This effect is qualitatively explained by Bohren and Huffmann, who described the polarizability, α_s of small spheres in the quasi-static approximation. Quasi-static means that the field is spatially static (no retardation effects) but oscillates temporally (important $a \ll \lambda$) [100]:

$$\alpha_s = 4\pi a^3 \frac{\varepsilon_1 - \varepsilon_2}{\varepsilon_1 + 2\varepsilon_2} \qquad \text{(Eq.5)}$$

λ is the wavelength of light, a is the radius of the sphere, ε_1 is the dielectric constant of the metal ($\varepsilon = \varepsilon'(\omega) + i\varepsilon''(\omega)$) and ε_2 is the dielectric constant of the embedding medium (usually real).[102] Resonant behavior appears if the nominator vanishes which is valid for $\varepsilon_1' = -2\varepsilon_2$ and $\varepsilon_1'' = 0$. The condition $\varepsilon_2'' = 0$ is not perfectly fulfilled by noble metals but good enough to show a clear resonance. In the case of an uniform external field magnitude E_0 (e.g. plane wave excitation), vacuum as embedding medium is ($\varepsilon_2 = 0$) and if $a \ll \lambda$ is valid the field strength surrounding the particle E_s can be written as:[101, 103]

$$E_s = 2 \frac{\varepsilon_1 - 1}{\varepsilon_1 + 2} E_0 + E_0 = E_0 \frac{3\varepsilon_1}{\varepsilon_1 + 2} \qquad \text{(Eq.6)}$$

Again it can be easily seen that a maximum occurs when $\varepsilon_1 = -2$ and the field strength surrounding the particle is increased by the factor $\Gamma = E_s / E_0 \approx 3\varepsilon_1/\varepsilon_1''$.

This model is only valid for spherical particle. If the particle is of ellipsoidal shape, which is more similar to near-field probes and the incoming field is along one of the principle axis d_j (j = 1,2,3) the polarisability changes to:

$$\alpha_j = 4\pi v \frac{\varepsilon_1 - \varepsilon_2}{3\varepsilon_2 + 3L_j(\varepsilon_1 - \varepsilon_2)} \qquad \text{(Eq.7)}$$

v is the volume and L_j is a geometrical factor.[102] For every principle axis the resonance condition follows:

$$\varepsilon_1 = \varepsilon_2(1 - \frac{1}{L_j}) \qquad \text{(Eq.8)}$$

In general the elongation of a spheroid leads to a red shift of the resonance condition and to an increase in the enhancement factor Γ.[103]

The lightning rod effect

The lightning rod effect is a well known electrostatic phenomenon, where electric charges are confined due to the shape of a conducting material. Arresters are used to protect buildings from the flash of lightning.[104, 105]

Given that the sharp tip of near-field probes can be assumed as a singularity, Maxwell's equations, which are first or second order differential equations can become singular if the first or second derivative is not defined. Of course the tip end is not a singularity but sharp enough to strongly enhance the incoming field.[38]

If a nanometre sized tip is now illuminated by an electromagnetic wave the free electrons of the metal induce surface charges, which enhance the field at the singularity of the tip due to charge confinement. As shown in Fig. 1.7 the polarisation of the electric field component is fundamental for this effect. When the polarisation is along the tip axis (right case in Fig. 1.7) the surface charges oscillate and form a rotationally symmetric field with the highest amplitude at the tip end. When the electric field vector is aligned perpendicular to the main tip axis, no surface charge accumulation at the tip end takes place.[106] Field enhancement factors in the case of a gold tip (r = 5nm) immersed in water illuminated with 810 nm have been calculated to be around 55. The used technique was the MMP (Multiple Multipole).[107]
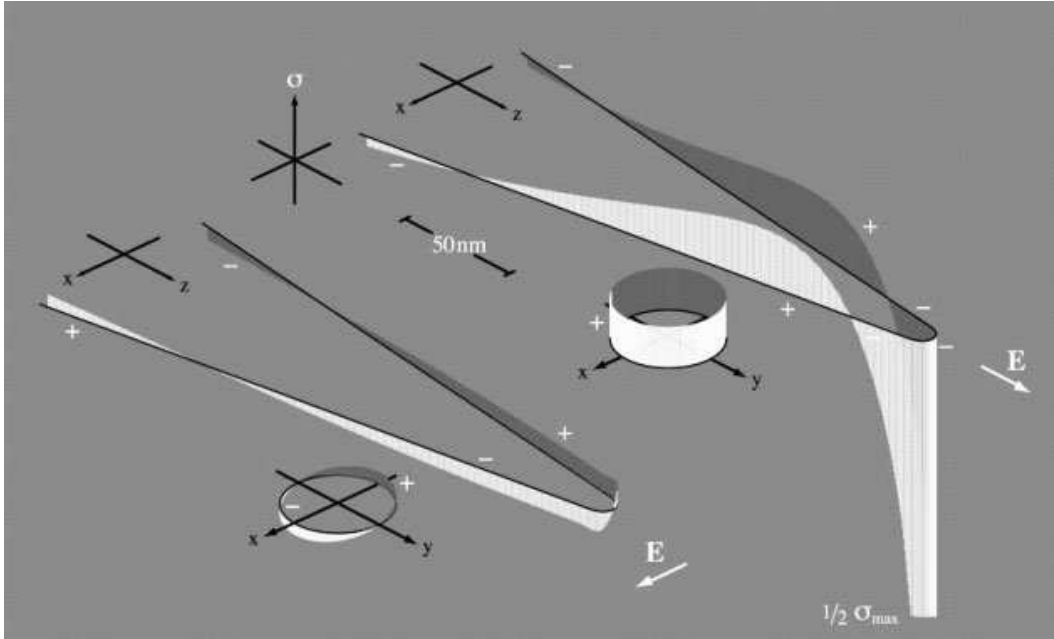
Fig. 1.7: Surface charge distribution along a metallic tip structure. If the polarisation is along the major tip axis a standing wave with its maximum at the tip end confines the surface charges and leads to high field enhancements. At perpendicular oriented electric field vectors no field enhancement at the tip end is observed.[38]

Tip acting as an antenna

An antenna is defined as a structure built for radiating or receiving electromagnetic waves and transferring energy to or from a certain volume.[108] The space between two antenna arms is called feed gap and is the area where energy transfer by converting radiation into local oscillation takes place.

There are lot of different types of antenna but the easiest one is the dipole type,[109] which can be used as model for near-field probes as well. When thinking of an apertureless probe-sample system the corresponding antenna model is called $\lambda/4$ antenna. In this configuration one of the antenna arms is substituted by a surface. In contrast to the $\lambda/2$ antenna which is made of two arms, and whose total length is half of the wavelength.[108]

Whereas in the radio wave regime a metal can be seen as perfect conductor, in the visible range light can be absorbed frequency depended.[102, 110] That's why a lot of work concentrated on the fundamental differences between the radiowave antennas and their optical counter piece [111, 112] and the development of sophisticated light structures to guide light, build optical switches, biosensors etc.[113-118]

In 1997 Girard and Martin demonstrated that also in non plasmonic materials like tungsten pronounced enhancement can be found.[119] They also showed a significant difference between metals and dielectrics, besides the general lower enhancement. Calculation of the field

_____

enhancement vs. the opening angle of a near-field probe pointed out that metals have their highest enhancement at sharp angles, dielectrics peak at about 45° cone angle.

When considering dielectric tips the antenna effect can play an important role when the tip's length is an odd integer multiple of half of the wavelength.[120] This theory was used from Bohn et al. to calculate enhancement factors for dielectric tips, like silicon, where enhancement factors of about 15 were found.[121]

The dipole-dipole model

Regarding the practical aspect of a near-field setup, tip-sample interactions also have to be taken into account. Therefore a simple but useful model, especially for the description of basic spectroscopic observations will be discussed.

In this approach the tip is represented by a single dipole situated at the centre of the tip end, which is regarded as a sphere with a diameter, a much smaller than the wavelength. The external field $E_0(\omega)$ induces the tip dipole p_t according to:[122]

$$p_t = \alpha(\omega)E_0(\omega) \qquad \text{(Eq.9)}$$

where $\alpha(\omega)$ is the polarisability already described in Eq.5. If the tip now approaches a surface the external field changes by the contributions of the Fresnel fields reflected by the surface to E_p which leads to a change in the tip dipole as well.[123]

In the dipole-dipole model the surface is replaced by a second dipole with the same dimensions, a, and at the same distance, d, from the boundary as the tip dipole but denoted as image dipole.

The superposition of the fields of the tip dipole, p_t and the image dipole, p_{image} gives now the field above the surface. The dipole moment of the image dipole with $\varepsilon_3(\omega)$ being the dielectric function of the sample is:

$$p_{image} = \frac{\varepsilon_3(\omega)-1}{\varepsilon_3(\omega)+1}p_t \qquad \text{(Eq.10)}$$

where

$$\beta = \frac{\varepsilon_3(\omega)-1}{\varepsilon_3(\omega)+1} \qquad \text{(Eq.11)}$$

is the quasi-static Fresnel reflection coefficient. So the total induced tip dipole moment follows:

$$p = \alpha[E_p + E_{image}(2a+2d)] = \alpha_{eff}E_p \qquad \text{(Eq.12)}$$

α_{eff} is the effective polarisability of the tip-sample system.[124]

$$\alpha_{eff} = \frac{\alpha(1+\beta)}{1 - \dfrac{\alpha\beta}{16\pi(a+d)^3}}$$
(Eq.13)

The scattering efficiency of the tip consequently depends on the magnitude of the tip dipole which comes out of his polarisability. If the polarisation of the incident light is parallel to the surface, the image dipole is also parallel but points into the opposite direction leading to a partial cancellation of the total dipole moment.[125]

It is obvious that the scattered signal contains information of the tip, the sample and about the distance between them. So if the distance between tip and sample is kept constant and the tip doesn't change during the scanning process variations in the scattered intensity should be due to local changes in the dielectric constant of the sample $\varepsilon_3(\omega)$.[124, 126, 127]

1.5 Application

1.5.1 Optical Nano-Lithography

In 1985 Wessel proposed in his famous article the idea of scanning a small particle nearby the surface. He suggests using the enhanced field below this particle not only for spectroscopy but also for what he called *sub-micrometer optical lithography.* He also recommended to use this new technique to record information at extremely high density.[33]

One of the first experimental realisations of near-field surface modification under laser illumination was done by Pompe et al. in 1994, where the generation of small hills on a gold surface with a diameter of about 30 nm under the tip of an STM was demonstrated.[51]

At the beginning all the research was done by STM configuration (Dickmann, Yates, Leiderer) because of its advantage in keeping the tip-sample gap constant in a very narrow range due to the exponential decay of the tunnelling current. It soon turned out that under laser illumination of the tip-sample system a sharp rise in the tunnel current occurred, which can be interpreted as thermal expansion of the STM tip.[59]

This was the starting point of a still ongoing discussion concerning the origin of surface modifications. Dickmann et al.[14, 52, 56, 57] claimed that the physical origin of the surface modification is due to the field enhancement at the end of the probe, whereas Leiderer et al.[15, 61] tried to proof that the most important factor for nanostructuring is the thermal expansion of the tip, which subsequently leads to indentation of the tip into the surface. This yield to extensive theoretical [52, 128, 129] and experimental [58] work to determine the heat induced tip

expansion. Tip expansion in the range of several nanometres were calculated with and temperature increase of 350-800° C dependent on the used laser fluence.[129-131]

Despite the good distance control STM bears the big disadvantage of operating only with conductive samples, which is even more challenging if the sample tends to oxidise because this demands the use of UHV (Ultra High Vacuum). Due to this drawbacks the use of AFM based near-field optical systems was again introduced by Dickmann et al.[132] but already published several years before under the term *thermo-mechanical writing*.[16]

In the following years a lot of research was done in the field of one/two photon absorption, photo-polymerisation, isomerisation and matter migration, local ablation, or depassivation in organic and inorganic materials. An excellent overview is given by Royer et al.[133]

Good evidence of the origin of near-field modification was published by Wurtz et al., who investigated a locally one photon absorption free radical photon polymerization. The dye Eosin absorbs the light and is then able to react with the amine MDEA (Methyldiethanolamine) to form a radical. This radical starts the polymerization of PETIA (Pentaerithrilol Triacrylate), which leads to a fast development of a 3D network. In this experiment the thermal component due to laser heating could be excluded. Because Eosin absorbs in the green, the author changed the wavelength into the red where eosin doesn't absorb but the tip is still heated and no polymerization was observable. Also the change from p- to s-polarisation leads no longer to a polymerization.[134]

Rivoal et al.[135] demonstrated theoretically that near-field enhancement leads to an enhancement in the far-field as well, which was also confirmed by the experiments of Wurz et al. To increase the resolution during the photo-polymerization a two-photon polymerization process is chosen by Schwartz et al.[136] Using a metal coated Si AFM tip a resolution of 70 nm was already achievable.

An extensive study was done by Bachelot et al. in the field of matter migration, where an azobenzene dye molecule was grafted to a polymer matrix (PMMA, Polymethyl-methacrylate).[11] This dye changes his isomeric configuration due to light absorbance. The change in configuration leads to a change in volume of the polymer matrix grafted to the dye molecule.[137] These effect was already investigated with fibre SNOM.[138]

In the apertureless SNOM the metallised AFM tip, operated in tapping mode was illuminated and the surface modification was investigated with the same tip immediately after the illumination process. In Fig 1.8 the results in dependence on the polarisation direction are illustrated. So when working with s-polarized light (a) with respect to the tip major axis, no surface modification in the near-field is visible, but changing the polarisation direction by 90°

with the electric field vector parallel to the tip axis (b) near field modification is found. In both cases far field fringes due to scattered light are visible. In (c) the dot height, which corresponds to the field enhancement, is evaluated against the polarisation angle, showing reasonable angle dependence.
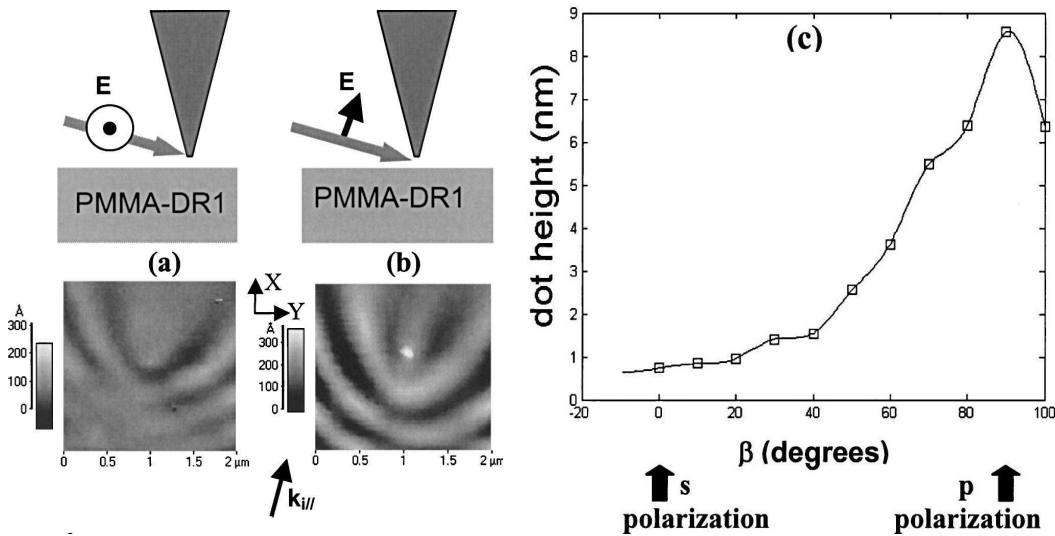

Fig. 1.8: *In (a) s-polarized light illuminates the tip-sample gap but no near-field modification is detectable. (b) By using p-polarized light with the same laser intensity surface structures are visible. Both cases show far field fringes. (c) shows the dot height dependency vs. the polarisation angle.[11]*

To eliminate the far-field fringes a different illumination method was chosen. By using a prism with the polymer on top and illuminating the tip in the evanescent field of the total internal reflected beam the far field fringes can be completely suppressed if working at the right incident angle. The achievable resolution in both illumination modes was about 30 nm.[11] Grigoropoulos et al. worked with Si tips on thin film Au surfaces, illuminating the tip sample system under grazing incidence with an Ti:Sapphire laser. They claimed a resolution of about 10 nm and a field enhancement factor of about 150 (Fig. 1.9).[139]
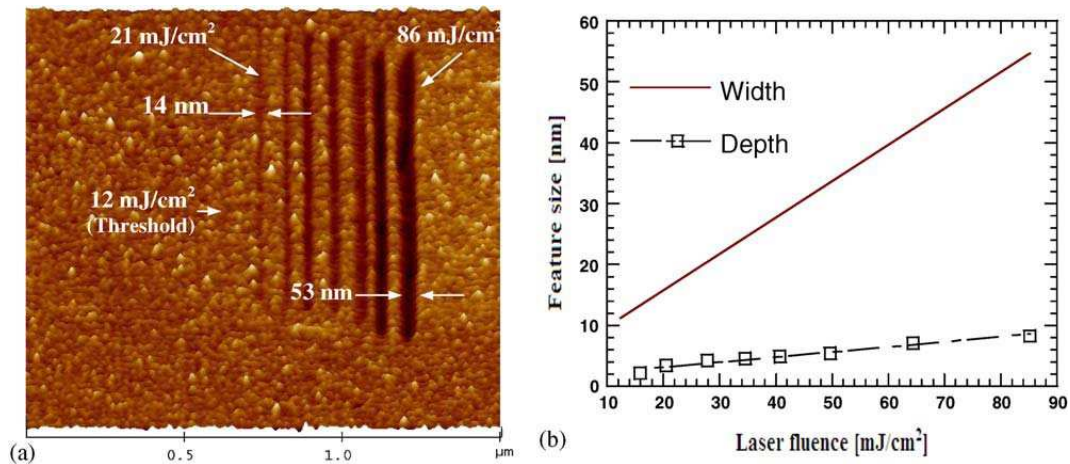
Fig. 1.9: Surface modification of an Au thin film with a Si-AFM tip under fs-laser illumination. In (a) one can see the topography of the modified area, which is evaluated in (b).[139]

Although the very popular work of Grigoropoulos et al. shows consistent results the explanation of the structure formation with near-field enhancement alone is pretty ambitious. Albeit they claimed a small tip sample separation, the way the principle of keeping the tip-sample gap is described, is questionable and so it is more likely that the tip was always in contact with the surface.

Several other works have been published in the field of near-field ablation but the mechanism of surface structuring is still unclear.[55, 140, 141]

A very promising approach was investigates by Prior et al.[142] The so called *"Floating Tip Nanolithography"* uses a new technique of controlling the tip to sample distance, which is one of the crucial parameters in the determination of the mechanism of surface nanostructuring. The idea is to use the phase shift of an oscillation AFM tip, which occurs several nanometres away from the surface as feedback signal for distance control. Fig. 1.10 describes very reasonable the different origin of surface structuring. The sample is a typical photoresist (AZ4620) illuminated by fs laser. Modification was mediated by an AFM tip made of silicon. In Fig. 1.10(a) there is a clear modified line with no displaced polymer on the edges of the structure. This can be explained by material evaporation. Fig. 1.10(b) shows a structure generated by scratching the surface with the AFM tip, where pronounced material displacement at the edges of the trench is visible. The most significant difference is obvious in (d) and (f) which displays a magnification of the intersection of two lines. In (d) the two lines show no disturbance, while in (f) the first line is overwritten by the second one.
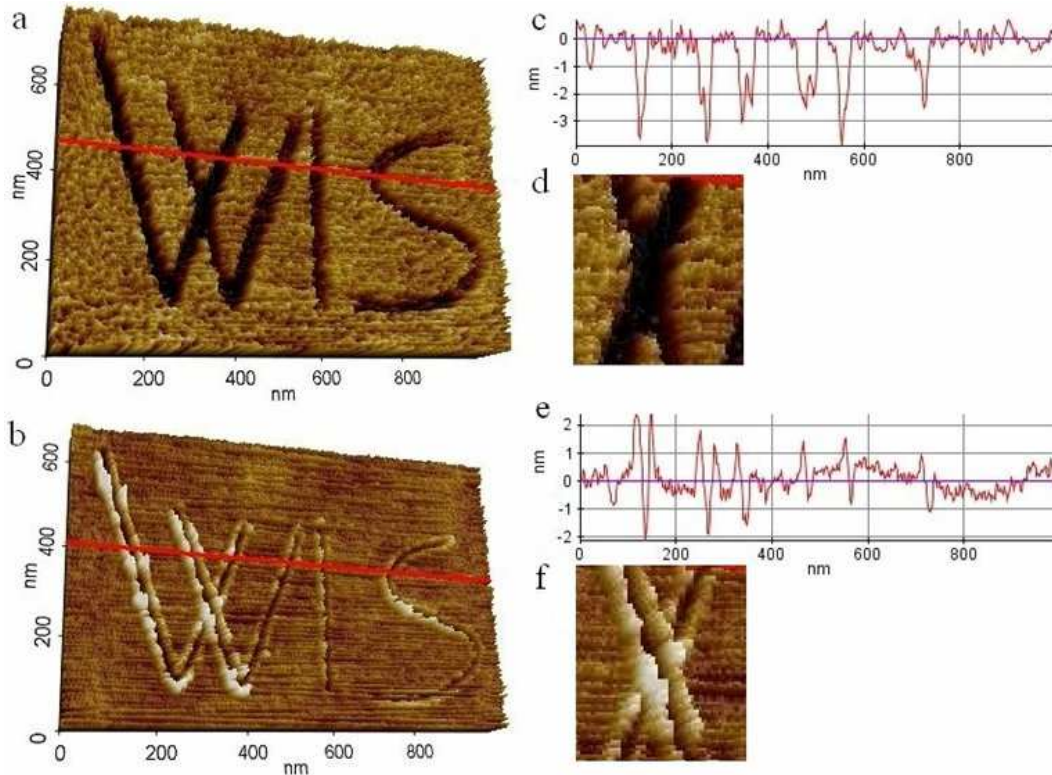
Fig. 1.10: The difference between modification due to ablation (a) and scratching (b) is shown. There is no material displacement in (c) whereas scratching leads to distinctive hills on the edges (e). There is no influence on the intersecting lines in the ablation mode (d) in contrast to the scratching mode(f), where the second line overwrites the first.[142]

Beside the typical tip based near-field modification to create structures beyond the diffraction limit, there are lot of different approaches. A very interesting one was done by Ben-Yakar et al.

In this work the near-field of nanotube bundles deposited on a glass substrate was used to ablate the glass 4-5 times below the typical ablation threshold, which is a promising tool for fast lithographical nanostucturing of large areas.[143]

1.5.2 Scattering Scanning Near-Field Optical Microscopy (s-SNOM)

In the s-SNOM setup light is focused on an AFM tip and the elastically scattered light is detected. Typically used lasers are in the range of visible to infrared light. The resolution is determined by the apex of the tip, which is about 10nm for commercial Si tips. Choosing the experimental parameters carefully even higher resolution is claimed in literature.[47] Despite the high achievable resolution, dielectric tips do not couple the illuminating power to the probing gap very efficient. Therefore conductive tip materials are favoured and their usability has already been analysed up to the mid-infrared region.[144-146]

The contrast in s-SNOM can easily be explained with the already discussed dipole-dipole model. (Ch.1.4.2) This model gives a good qualitative understanding of the near-field optical contrast of various materials.[122, 124, 127, 147-152] Although latest experimental results [153] lead to a slightly modified formulation derived in Eq.13.

$$\alpha_{eff} = (1+r)^2 \frac{\alpha}{1 - \dfrac{\alpha\beta}{16\pi(a+d)^3}} \qquad \text{(Eq.14)}$$

The introduction of the factor *(1+r)*, with *r* being the Fresnel reflection coefficient of the sample surface, is necessary because the previous formulation *(1+β)* is not suitable for the description of the far-field scattered light since it can exceed unity, which would mean that the mirror dipole radiates stronger than the tip dipole. The square is explained by the illumination of the probe via reflection from the surface.[154-156]

It has to be mentioned that ε, β and α are complex values and therefore the scattered light is also complex, $\alpha_{eff} = se^{i\varphi}$ with the relative amplitude *s* and the nonzero phase shift φ.

Due to the elastic light scattering a large background signal with the same frequency as the near-field signal has to be suppressed. One of the first attempts was made by working with an AFM in tapping mode and taking advantage of the nonlinear dependence of α_{eff} with the distance between tip and sample by electronically filtering the detector signal at the oscillating frequency of the tip.[49] It soon turned out that this is not sufficient and full elimination requires demodulation at higher harmonics.

When approach curves were measured while mapping the near-field intensity in parallel, standing wave amplitude features occur in first order demodulation mode. The use of higher harmonics excludes these features, leading to an even steeper rise in the near-field signal. When applying high harmonic demodulation modes it has to be taken into account that through the contact between tip and sample the oscillation can become non-sinusoidal and therefore artefacts could occur. The most successful way of detecting elastic scattered light is the interferometric concept which gives information about the amplitude and the phase of the near-field signal.[80, 126, 157]

According to Eq. 13 one can predict now a large signal for metals, medium for semiconductors and a low signal for dielectrics. This theoretical assumption is confirmed by Keilmann et al. in Fig. 1.11. S-SNOM images were obtained at two laser wavelengths of a sample with three different materials.
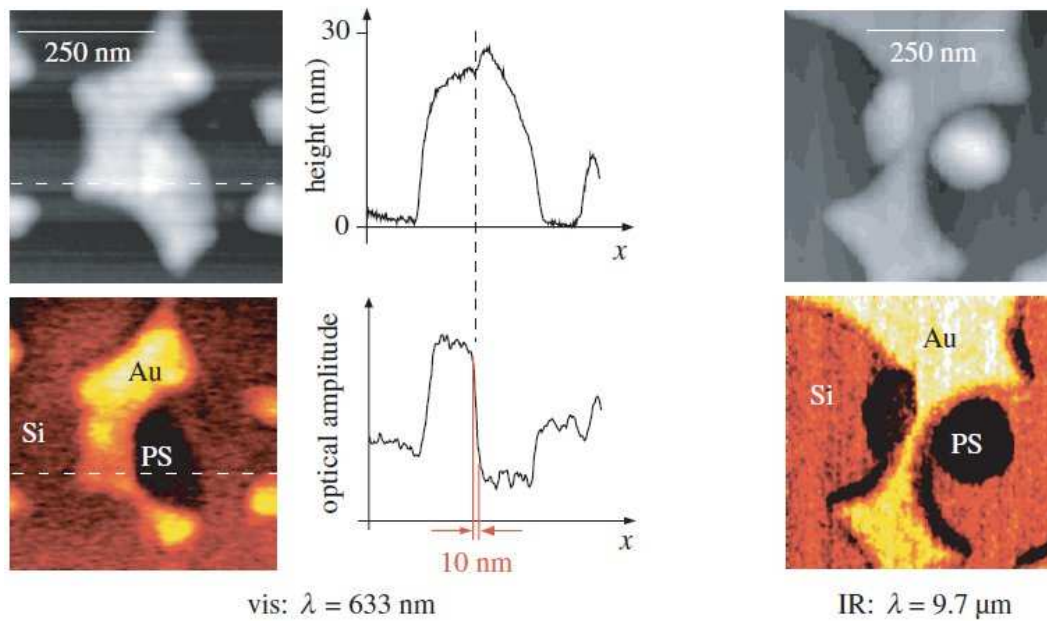
Fig. 1.11: S-SNOM image of three different materials with two different wavelengths. It is shown that the resolution and the relative contrast as predicted with Eq.13 are wavelength independent. The three materials are easily distinguishable. The scan trace shows that there is no corresponding topographical feature which could lead to an artefact in the optical image.[158]

Due to its high resolution s-SNOM has a high potential in analytical chemistry in detecting chemical species on the nanoscale. For this purpose the use of light in mid IR region, especially 3-30µm is favourable. This region is the so called fingerprint region, which is very typical for every molecule. First experiments have shown reasonable contrast.[124, 149, 159]

A tip induced resonance was also extensively studied.[127, 148, 150, 153, 160] The tip was made of gold illuminated off-resonance at 10.6 µm. Whereas the SiC surface shows resonant behaviour at this wavelength caused by phonon-polaritons. The ability of mapping FIB (Focused Ion Beam) implanted zones in these crystals was shown because the induced damage leads to a strong damping that reduces the near-field interaction.[150]

It was also demonstrated that it is possible to map the eigenfield patterns of nanoparticles. Therefore an Au disc with 91 nm in diameter and 20 nm in height was illuminated by 633 nm light, which should fit the resonance condition. To reduce the perturbation through the tip a carbon nanotube tip was used. A dipolar surface plasmon polarition oscillation field pattern could be recorded.[161]

Very useful in the semiconductor industry is the ability of s-SNOM to probe local conductivity.[151, 159, 162]

1.5.3 Tip Enhanced Raman Scattering (TERS)

When illuminating a surface with monochromatic light not only elastic light scattering but also inelastic light scattering takes places. The process is called Raman scattering. This type of vibrational spectroscopy is a powerful tool in the characterisation of material properties. Despite its broad operational capability its major drawback is the low scattering cross section, which is typically 10^{14} times smaller than that for fluorescence spectroscopy.

To overcome this problem field enhancement is essential for the applicability of this technique. One of the first solutions was SERS (Surface Enhanced Raman Scattering), where metal nanoparticles were used to provide enormous enhancement factors of up to 10^{15}. These high fields allow single molecule spectroscopy, as well.[163]

Another approach is the field enhancement at the end of an antenna-like structure, such as an AFM or STM tip. The theory of tip field enhancement has already been discussed in Ch. 1.4.2. In the field of Raman spectroscopy lots of literature is published, claiming tremendous enhancement factors of up to 10^6,[164-166] but comparison of these values is delicate because there are various definitions for calculating the TERS enhancement factor. A very convincing way of defining the enhancement factor in an experiment is described here.[167]

First the contrast has to be defined. It is the ratio between the signal with the tip in contact with the sample and the retracted tip.[164, 168-170]

A more precise definition also takes into account that the far-field signal is also present as background when the tip is in contact with the sample.[171-173]

$$Contrast = \frac{I_{with\_tip} - I_{without\_tip}}{I_{without\_tip}}$$
(Eq.15)

Furthermore it is important to consider the different illumination areas for near and far-field. If working with very thin films it is more reasonable not to look at the areas but at the volume.[164, 169, 172, 174, 175]

$$EF = Contrast \times \frac{V_{focus}}{V_{near\_field}} = Contrast \times \frac{d^2_{focus}}{d^2_{tip}} \times \frac{h_{focus}}{h_{near-field}}$$
(Eq.16)

This definition still leads to some uncertainty because the estimation of the near-field source size is problematic. In most cases, the size of the curvature radius of the tip is taken, although experiments and calculations have shown that the near-field under the tip can be smaller than the area of the tip.[176, 177] For the height of the near-field it can be shown that a value in the range of the curvature radius is reasonable.[174, 178] When comparing the different methods of calculating the field enhancement in literature on one particular example, a difference in the order of two magnitudes occur.[167]

Generally the comparison between experimental results is more useful and of higher practical relevance, when only the contrast is taken into account because this value is free of assumptions like height or diameter of the regarded fields. The idea of including the different volumes in the calculation is based on the better comparability with theoretical results of TERS enhancement.

One of the first reported TERS experiments in literature was done on dye molecules like cresyl blue or rhodamine dyes. They bear the advantage that if choosing the right wavelength of light resonance, enhancement can occur when the electronic transition fits the frequency of the photon. Fig. 1.12 shows a typical TERS spectrum of brilliant cresyl blue (BCB)
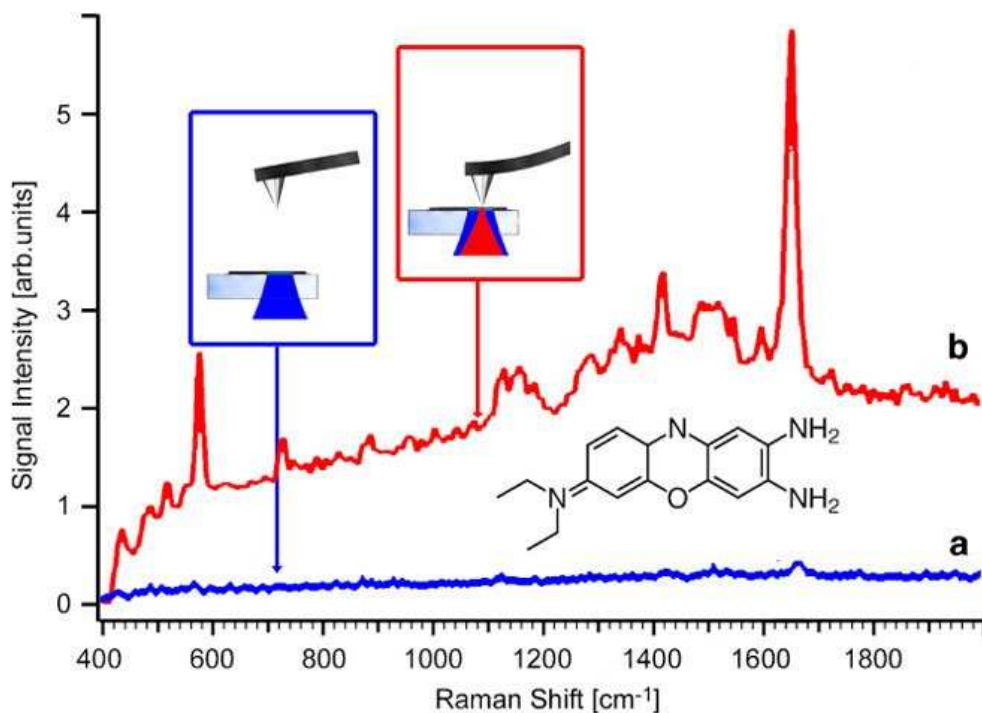

Fig. 1.12: A typical TERS spectrum of BCB with the tip on the surface (red) and without tip (blue). On can clearly see that there is no proper spectrum available if the tip induced field enhancement is not taken into account.[179]

A very prominent field in the tip enhanced Raman scattering research is the study of nanotubes. Since their discovery in 1991 by Iijima, especially carbon nanotubes have gained a lot of attention, due to their unique physical properties, which derive from their 1-dimenional structure.

Carbon nanotubes show very significant Raman bands, which can be used to characterize different samples. Although the way of producing carbon nanotubes is quite easy the production of defined samples (e.g. only metallic) is impossible until now. So the investigation of nanotube samples in the far-field always has to deal with an integrated signal

over all the different types of tubes. Only very time consuming purification techniques can lead to higher quality samples.

To overcome these problems the high spatial resolution of TERS makes it to the ideal tool to study carbon nanotubes. Enhancement factors of up to 10^{12} have been reported for nanotubes in contact with colloidal silver clusters.[99]

Fig. 1.13 shows a topographical study of a single walled carbon nanotube (SWNT) on glass with simultaneously recorded near-field Raman image. The excitation was done at 633nm and the prominent G-band ($\sim$1600cm^{-1}) was recorded.
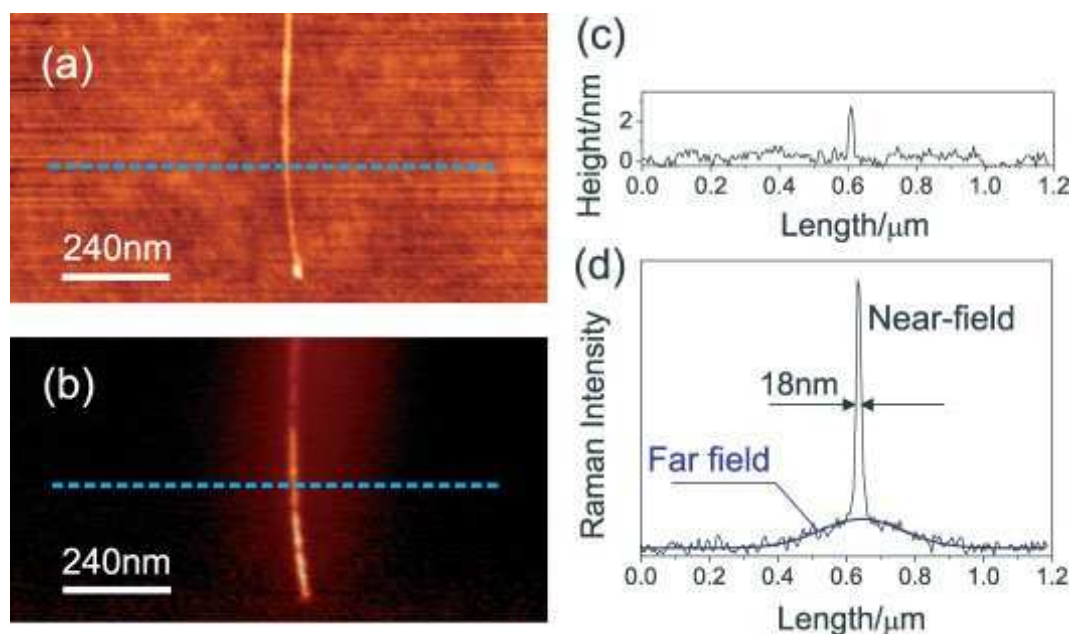

Fig. 1.13: (a) shows the topography image of a SWNT on glass. In (b) the corresponding TERS image is displayed. (c) and (d) compare a line scan (indicated in blue in the pictures) of the topography and the Raman signal.[180]

The highest resolution obtained until now is about 10 nm, limited by the radius of curvature of the tip.[181]

The resolution of the optical image is higher (about 1.3 times) than the resolution in the topography.[181, 182] This can be easily explained by the fourth order dependence of Raman signal on the field enhancement, which leads to steeper traces.

TERS can be used to image defects on isolated SWNTs [181] or to study the polarisation dependence of the RBM and G-band.[183]

In biological samples the focus of TERS was on the investigation of DNA and the corresponding nucleobases.[184] In this field also the tip enhanced CARS (Coherent anti-Stokes Raman Scattering) was implemented to study the nucleobase adenine and the DNA, as well.[185, 186]

Another field of interest can be found in surface catalyst chemistry. Catalysts are finely dispersed metal particles on dielectric surfaces like alumina. This system could also provide a significant SERS effect. There are not many publications in this field up to now but TERS will become more and more important.[187]

Many more applications of TERS, displaying the high spatial resolution and sensitivity of this method with different systems can be found in literature.

1.5.4 Tip-enhanced Fluorescence Microscopy

Several tools in analytical chemistry can provide detailed structural information like electron microscopy, X-ray crystallography or NMR (Nuclear Magnetic Resonance) spectroscopy, but they all have to deal with limitations in living systems due to sample preparation, the inability to identify an individual molecule out of a heterogeneous sample or the low resolution.

The classical fluorescence spectroscopy can overcome all these drawbacks except the resolution. Although there are already new approaches like the STED (Stimulated Emission Depletion) microscope which was developed by Stefan Hell, there is enormous interest in the development of further techniques, which lead to even higher resolution than STED. A very detailed overview about the developments in far-field fluorescence measurements, breaking the diffraction barrier is given by Stefan Hell.[188]

One of the first near-field fluorescence measurements were done by Lewis and Lieberman et al in 1991.[189] Besides the higher resolution, the field enhancement at the end of the near-field probe also causes a local increase of the fluorescence, which increases the sensitivity of this near-field approach to single fluorophore sensitivity.

Fluorescence measurements in the near-field regime always have to deal with a competition between field enhancement induced fluorescence increase and signal reduction due to quenching processes.[190-192]

In general the field enhancement is proportional to the real part of the dielectric function of the tip while the imaginary part defines the quenching probability. Taking this into account metal tips which provide larger enhancement factors are often not favoured. Due to the higher quenching probability they lead to a net decrease in fluorescence at short ranges.[192, 193] As quenching and near-field enhancement are short range effects the use of non metallic tips leads to higher contrast and resolution in dense molecular studies.

The extent of quenching can be calculated to:[194-196]

$$b_{ET} = \left(\frac{q}{k_f^3 d^3} \right) \left(\frac{3\varepsilon_2 n_1 \kappa_1}{2|\varepsilon_1 + \varepsilon_2|^2} \right) \qquad \text{Eq.17}$$

with k_f being the wave number of the fluorescence, q the quantum yield of the emitting state in vacuum, d the distance, ε the dielectric constants, κ the extinction coefficient of the tip and n the refractive index.

The fluorescence emission is a first order process, so the increase due to the enhanced field is lost by quenching at small distances which limits the resolution for metallic tips as already mentioned above. The resolution can be improved by using Si tips.[197]

A resolution of less than 10 nm is reported in literature by measuring CdSe-ZnS nanorods with a silicon AFM tip (Fig. 1.13)[198]
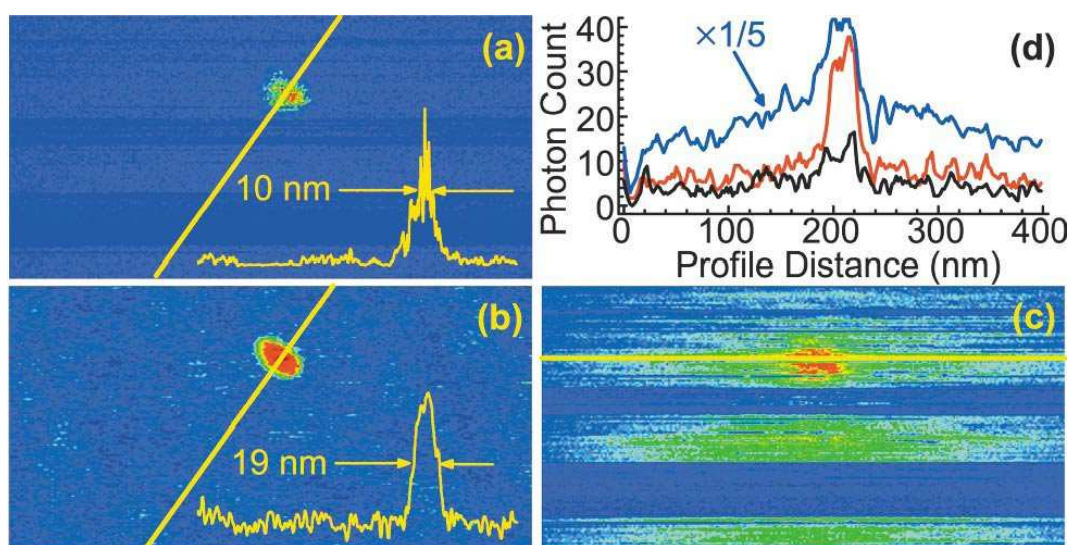

Fig. 1.14: In (a) the scan trace across a CdSe-ZnS nanorod is shown and a resolution of ~10nm is measured. (b) gives the corresponding topography picture. (c) shows the total photon count, where the completely blue areas are due to the blinking of the nanorod. In (d) the scan trace of (c) is shown. The blue line is the overall photon count, whereas the red line corresponds to the photons emitted at a tip-sample gap of 0-0.4 nm and the blue line to a gap of 2.5-4.5 nm. It can be seen that most of the photons are emitted at a small tip-sample gap.[198]

The experiments indicate that one-photon fluorescence spectroscopy is a powerful tool, which provides much higher contrast than claimed in literature, where one-photon fluorescence is depicted to be not appropriate due to the high background signal.[197, 199]

To modify the fluorescence signal and to increase the contrast high resolution fluorescence pictures take advantage of the AFM working principle in tapping mode, where the oscillating tip modulates the far-field signal, which is detected by an avalanche photodiode and processed by a lock-in amplifier.

Another advantage of an AFM in tapping mode is the possibility to investigate biological samples because the mechanical energy contribution into the sample is reduced in comparison to the contact mode.

To further increase the resolution in fluorescence spectroscopy higher-order processes, like multiphoton absorption are under investigation.[169, 200-203] Two-photon excitation for example is a nonlinear process, which shows a square law dependence on the excitation intensity. Therefore the fluorescence signal becomes proportional to the square of the enhancement factor.[204]

To study biological systems under realistic conditions the use of physiological environments is essential, therefore the development of fluorescence measurements under water with high resolution is of growing interest. Some results can already be found in literature.[205]

1.5.5 Second Harmonic Generation Scanning Near-Field Optical Microscopy (SHG-SNOM)

One of the major drawbacks of classical near-field techniques is the poor signal-to noise ratio since the global scattering of the illuminated area is many orders of magnitude larger than the contribution of the local tip induced scattering. Different approaches to solve this challenge are known in literature. A trivial approach is to shift the wavelength of the detected signal, so that the huge background signal of the exciting far-field can easily be filtered like it is done in the tip-enhanced fluorescence microscopy. Nevertheless fluorescence microscopy has to deal with limitations like photo-bleaching or blinking. To overcome these problems a nonlinear approach was suggested by taking advantage of the second harmonic generation in the vicinity of the tip.[206, 207]

The field of nonlinear optics was born with the discovery of second harmonic generation (SHG) by Franken et. al. [208] in 1961 and theoretically described by Amstrong et al. one year later.[209]

As already discussed before, the response of a material on an incident electric field is characterised by the induced polarisation $P(\omega)$

$$P(\omega) = \varepsilon_0 \chi^{(1)} E(\omega) \qquad \text{(Eq.18)}$$

with the linear susceptibility $\chi^{(1)}$. If nonlinear effects are taken into account the total induced polarisation $P(\omega)$ in the frequency domain can be developed in a power series of E:

$$P(\omega) = \varepsilon_0 [\chi^{(1)} E(\omega_{m1}) + \chi^{(2)} E(\omega_{m2}) E(\omega_{m3}) + ...] \qquad \text{(Eq.19)}$$

The electric fields at different frequencies are denoted as $E(\omega_{mx})$ and $\chi^{(2)}$ is the second order non-linear susceptibility, which describes the second order response like the second harmonic generation ($2\omega = \omega + \omega$), optical rectification, sum-frequency generation or difference-frequency generation.

Looking at the second harmonic generation the linear induced polarisation (Eq.18) changes to a nonlinear one:

$$P_i^{(2)}(2\omega) = \varepsilon_0 \chi_{ijk}^{(2)} E^j(\omega) E^k(\omega) \qquad (Eq.20)$$

The second order non-linear susceptibility $\chi_{ijk}^{(2)}$ is a third rank tensor, whose complexity can be largely reduced by symmetry considerations of the medium. This fact bears the great advantage of the nonlinear approach because it gives the opportunity to distinguish properties, which are difficult to study with linear optics.[210]

So if a medium has inversion symmetry the induced dipoles in the dipole approximation will have opposite charge and therefore will cancel out. But there is a symmetry break at the interface leading to a nonlinear polarisation in the interfacial sheet:

$$P(r,t) = P_s \delta(z) e^{i(k_\parallel (2\omega)r - 2\omega t)} \qquad (Eq.21)$$

This enables the solely investigation of the surface SHG in a medium with bulk inversion symmetry.[211] When reducing the size of matter down under the length scale of optical wavelengths the overall geometry starts to play a major role beside the crystallographic symmetry.[212-216]

So considering a near-field probe the mirror symmetry is broken along the tip axis. This gives the unique opportunity by changing the incoming polarisation of light, or the direction of illumination to study directional and polarisation selection rules because the origin of the SHG signal is a superposition of local surface and longitudinal bulk polarisations, where the later one can be cancelled by proper illumination selection. A very educative work was done by Raschke et al.[217]

Besides the advantage of shifting the wavelength of the detected light away from the large background, which is due to far field illumination the generation of a the second harmonic light source bears a further advantage. The intensity of SHG at the apex of a near-field probe depends on the fourth power of the fundamental field and therefore leads to higher confinement of the SHG field, which increases the resolution as well.[218] Nevertheless the radiation pattern can still be described by a single oscillating dipole.[182]

SHG measurements are also favoured for near-field measurements, which need high polarisation sensitivity of the light source like the characterization of magnetic of ferroelectric materials.[219] In Fig. 1.15 the near-field SHG picture of ferroelectric domains of $YMnO_3$ is shown

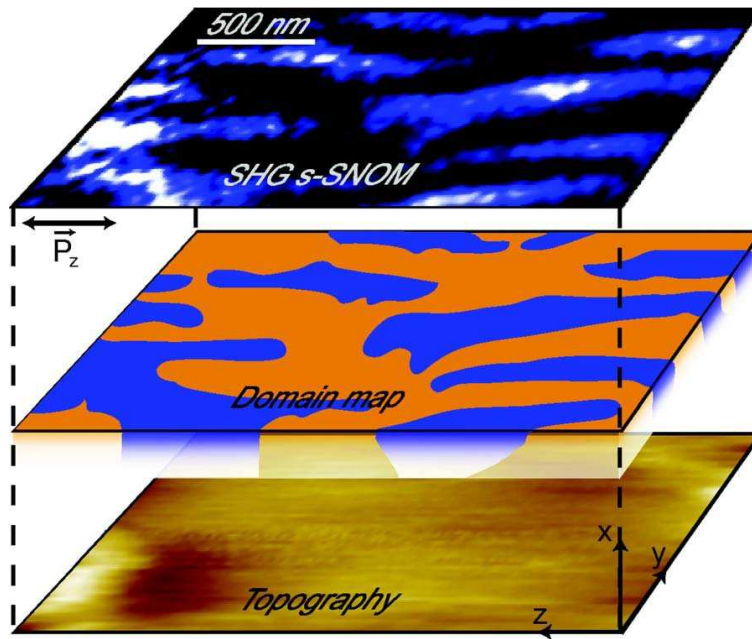*Fig. 1.15: The upper picture shows the SHG SNOM picture of YMnO₃, which is in good correlation with the modelled domain map, calculated by following the discrete dipole model. The lower picture represents the topography.[220]*

Depending on the second order susceptibility of the tip ($\chi^{(2)}_t$) and the surface ($\chi^{(2)}_s$) the main source of SHG light is situated either on the surface or on the extremity of the tip, giving the nonlinear analogue of the scattering type SNOM (s-SNOM) and the near-field fluorescence microscopy.

1.6 Laser

Described in 1917 by Albert Einstein and realized for the first time in 1960 by Theodore H. Maiman at the Hughes Research Laboratories in California,[221] the new technology called LASER (Light Amplification by Stimulated Emission of Radiation) has opened a nearly endless variety of applications from spectroscopy or ablation with electromagnetic waves to off-wall things like nuclear fusion.

Beside the continuous wave laser the pulsed laser gains more and more attention. The trend goes to shorter pulses to increase the peak power and to enable real-time measurements on the ultra short time scale like the movement of electrons in hydrogen molecules.[222]

This work will concentrate on non amplified femtosecond (fs) lasers i.e. pure oscillators because both experimental setups are based on this type of laser. Amplified laser systems produce much higher pulse energies, in the mJ range but only at very low repetition rates (~kHz) due to the amplification process.

_____

On the other side oscillators generate high repetition rate (several MHz) but only low pulse energies, in the nanojoule (nJ) regime. To overcome this gap high numerical aperture focusing optics are necessary to reach sufficient fluencies (energy per area) for surface structuring of various materials and taking advantage of the high repetition rate for machining at the same time.

In addition, the ablation of dielectrics in the sub 100fs regime showed a dramatic increase in the quality of the modified area, further pushing the operative range of oscillating fs-lasers.[223-225] Although using high numerical apertures increases the fluence of an oscillator significantly the typical output power of an oscillator is below 10nJ and therefore still too small for many structuring processes.[226, 227] Two very promising approaches to increase the power of an oscillator by more than one order of magnitude are the increase of the resonator length,[228, 229] or the increase of the pump energies (up to 20W) for the Ti:sapphire crystal from a frequency doubled Nd:YVO$_4$ solid state laser. To avoid the creation of instabilities due to high pulse energies the introduction of a net positive cavity group dispersion delay (GDD) has shown satisfying results.[230] This so called chirped-pulse mode locking approach generates pulses with several picoseconds duration, which have to be compressed beyond the cavity. Pulse energies of more than 650 nJ can be handled at a repetition rate of about 4 MHz. (Femtolasers XL)[231]

For understanding the advantageous use of fs-laser pulses in the field of surface modification a deeper look inside the occurring processes is necessary.

In principle, laser-matter interaction starts with the excitation of the electronic system. So if the energy of the incoming photon surpasses the binding energy of the electrons situated in the valance band ionisation is considered to be possible. In the case of large band gap materials, like dielectrics the typical photon energy is not sufficient for direct ionisation. The use of high intensities, present in fs-laser pulses enables the ionisation of atoms based on multiphoton absorption, which is a highly intensity dependent process.[232]

If higher electric field strengths are applied the Coulomb potential, which describes the binding condition between atomic core and electrons can be disturbed and the generation of free electrons can occur due to tunnelling or over-the-barrier ionization.[233, 234] Further ionization arises from electron-electron collisions (avalanche ionization) and changes the optical behaviour of the dielectric material to a metal-like behaviour.[231]

Emission of free electrons from the surface leads to a charge accumulation in the upper surface layer, which can not be compensated like in real metals and due to the repulsive forces between the positive charged atomic cores Coulomb explosion takes place.[235, 236]

In contrast to dielectrics, metals already posses a proper amount of electrons in the conduction band, which determine the optical absorption. Electronic thermalisation also takes place in the femtosecond regime. The shape and amount of modified material is determined by the electronic thermal diffusion length.[237]

After fs-excitation within several picoseconds the electron-phonon relaxation leads to a thermal equilibrium between lattice and electrons. Subsequently, thermal processes are dominant, which are similar for dielectrics and metals.

In literature there are four thermal processes mentioned.[238] The first two are vaporisation, which happens at every pulse length and boiling, when heterogeneous nucleation occurs at sufficiently long laser excitation. Then subsurface heating due to heat loss at the surface caused by the vaporization and finally, at high intensities phase explosion or explosive boiling based on a rapid phase transition from a superheated liquid takes place.

So fs-lasers are operating in the non thermal ablation regime where the lattice is still cold because energy input ends (fs) before the electron-phonon relaxation (ps) takes place and thermal effects are therefore diminished.[231]

1.7 Atomic Force Microscopy

Invented in 1986 by G. Binning, C.F. Quate and Ch. Gerber the atomic force microscopy (AFM) immediately became an important tool in the field of surface analysis on the nanoscale.[239] Already one year later Binning was able to show the lattice image of a graphite surface demonstrating the possibility of achieving atomic resolution even at ambient conditions.[239]

In principle the method is a pretty simple one. A sharp probe is scanned over a surface and the change in topography is detected via a position sensitive device (PSD) also called four segment diode. The interaction of the tip with the sample surface leads to a bending of the cantilever, which can be regarded as a spring. This changes the position of the diode laser, reflected from the backside of the cantilever on the PSD.

The interactive force between the tip and the surface can be described qualitatively by the Van der Waals force, which describes the potential energy of two atoms at a certain distance. The resulting function is the well known Lennard Jones potential:

$$U(r) = U_0 \left[-2\left(\frac{r_0}{r}\right)^6 + \left(\frac{r_0}{r}\right)^{12} \right]$$ (Eq.22)

r_0 is the equilibrium distance between two atoms, and U_o is the corresponding minimum potential. The equation includes the long distance attraction due to dipole-dipole interaction (first term) and the short distance repulsive interaction based on the Pauli exclusion principle (second term).[240]
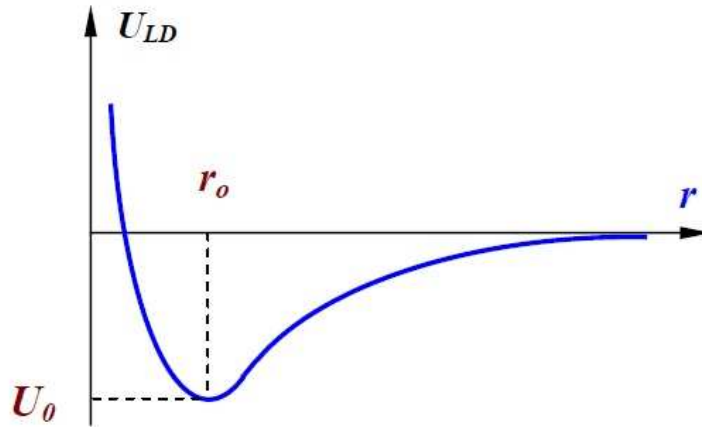

Fig. 1.16: The potential characteristics of the Lennard Jones potential. The equilibrium distance between two non binding atoms is denoted as r_0 with a potential energy of U_0. The distance r defines the mode of operation. The possibilities are contact ($r<r_0$), semicontact ($r_0\pm r$) and the non-contact mode ($r>r_0$)[240]

There are three modes of operation in the atomic force microscopy which can be distinguished by the region, *r* along the Lennard-Jones potential, where the AFM is operated. (See Fig. 1.16)

Contact Mode

In the contact mode the relation $r<r_0$ is valid in most cases (Fig. 1.16). This means that the repulsive forces are dominating the interaction and the tip is in permanent contact to the surface. A more general description would be that the force between the tip and the sample, attractive or repulsive is counterbalanced by the elastic force of the cantilever. Due to the low spring constant of a contact mode cantilever "sticking" occurs when retracting the tip from the surface. In this case r could be larger than r_0. Nevertheless this range of operation is not very stable.

As already mentioned the spring constant of contact mode cantilevers has to follow several restrictions. First of all it is desirable to use a very small spring constant because this increases the force sensitivity of the measurement and decreases the probability of sample or

tip degradation. To prohibit degradation the force applied on the surface should be below the interatomic force constants, which are about 10-100 N/m in solids but go down to 1 N/m in biological samples. Therefore typical spring constants for contact mode cantilevers are in the range of 0.01-5 N/m.[241]

The biggest advantages of the contact mode are, that it is very easy to realize and fast scanning is possible. A major drawback is that even though cantilevers with low spring constants are used the force applied on the surface is rather high and can easily lead to tip or sample degradation.

A very critical point for tip degradation is the approach step. Because of the large gradient of the attractive forces a so called "jump into contact" occurs which produces a hard crash of the tip into the surface. This effect cannot be overcome because it is due to the low spring constant of the contact mode cantilevers, which is necessary for wearless scanning of the surface.

The noise level of contact mode measurements is given by the spring constant times the noise level of the deflection measurement, due to e.g. thermal drift. Taking into account the typical spectral noise density vs. frequency plot (Fig. 1.17) and the fact that constant mode measurements are conducted in the frequency range of 0.01 to several hundred Hz it is obvious that there is a huge influence on the image quality due to 1/f noise occurring in the force detectors. To overcome this problem low temperature measurements and AFMs built with low thermal expansion coefficient materials are desirable.[241]
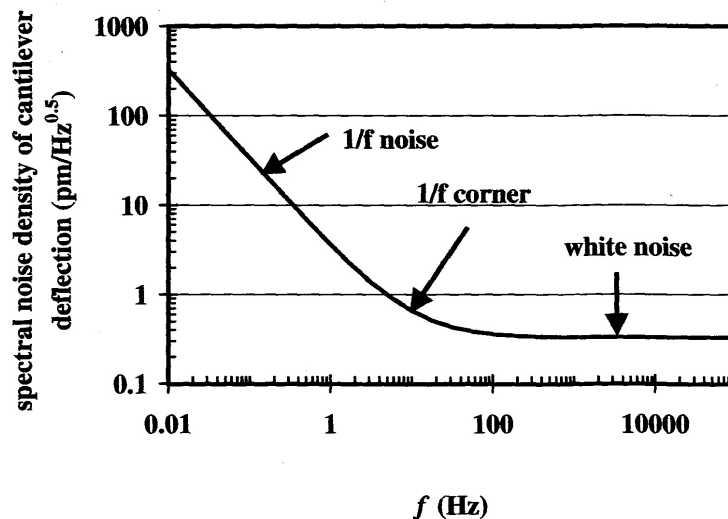

Fig. 1.17: The noise density of a cantilever vs. the frequency is shown. Contact mode measurements are processed in the 1/f region and are therefore very susceptible to noise. On the contrary semicontact measurements work in the hundreds of kHz regime and have to deal with white noise only.[241]

Two types of operating modes within the contact mode are available. One is the constant height mode. In this mode the voltage applied on the z-piezo is kept constant and the change in deflection of the tip during the scanning process is recorded. This mode is useful for very fast scanning on flat surfaces. If the topography is too rough the cantilever will break because there is no feedback system active.

The second option is the constant force mode, which is more commonly used. The force between tip and surface is controlled by a feedback mechanism, which is based on a certain deflection value, defined as setpoint. The value of the setpoint, which corresponds to a certain force or pressure on the surface, is kept constant by a feedback mechanism, which retracts the tip from the surface if the setpoint value is exceeded or moves towards the surface if the value is too low. This reduces the probability of tip degradation but also the speed of scanning.

A possibility to further decrease the probability of tip or surface degradation is the semicontact mode, sometimes also called tapping mode or intermitting contact mode.

Semicontact Mode

In the semicontact mode r is oscillating around r_0. In other words the tip is oscillating and hits the surface shortly within each period of oscillation. The oscillation amplitude is in the range of several tens of nanometres and its dynamics can be described as:

$$m\frac{d^2r}{dt^2} = -kr - \left(\frac{m\omega_0}{Q}\right)\frac{dr}{dt} + F_{ts} + F_d \cos\omega t \qquad (\text{Eq.23})$$

where m is the mass, r is the position, k is the spring constant, w_0 is the resonance frequency (defined as $\sqrt{k/m}$, Q is the cantilever quality factor, which determines the number of oscillations until the amplitude goes down to 1/e, F_{ts} is the force between tip and sample and F_d is the driving force of the piezoelement.[242]

The first term of this relation describes the restoring force of the cantilever, the second term is the energy dissipation term (mostly friction of the cantilever in air), the third is the interaction between tip and sample and therefore also defines the phase contrast. The fourth term is the driving force of the piezo as already mentioned.

The advantage of the semicontact mode is a low force on the sample, important when investigating biological samples, higher lateral resolution and no lateral forces. The scanning speed is much lower than in the contact mode.

Although most textbooks claim that the force applied on the surface is lower than in the contact mode this has to be considered more critically. First of all the force is determined by the ratio of free oscillation amplitude, A_0 and predefined working amplitude, A. Due to the

high spring constant the interaction force can exceed typical values in contact mode if not carefully chosen. Secondly the attractive forces in air due to the capillary effect can reach up to 100 nN and therefore tip or sample deterioration like in contact mode is probably.[242]

In the semicontact mode the force among tip and surface switches periodically between the attractive and the repulsive regime. The absolute value depends on the free oscillation amplitude A_0 and the chosen setpoint A, which corresponds to the working amplitude. The setpoint value has to be defined carefully to guarantee stable working conditions. Fig. 1.18 shows the change in topography caused by different working amplitudes (setpoint).
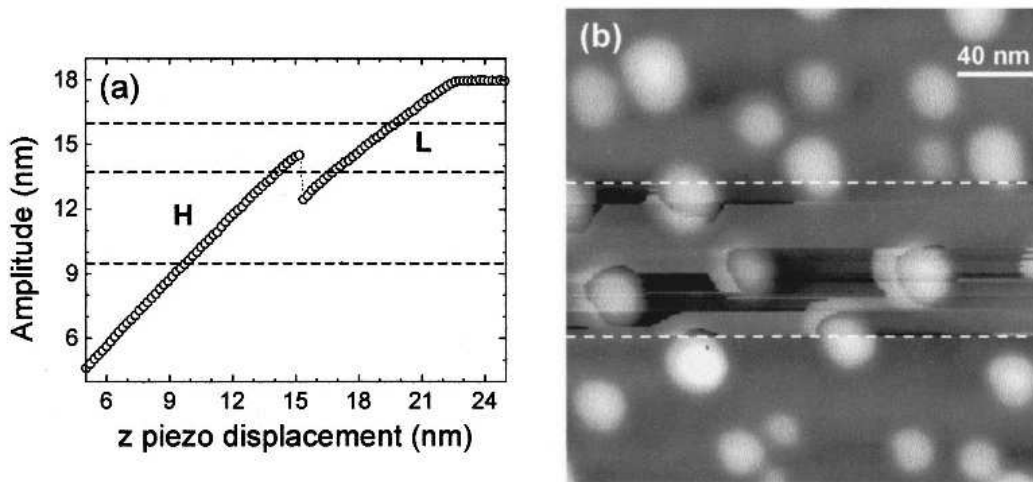
Fig. 1.18: In image (a) in the amplitude spectroscopy the three different parameters for operation are shown by dotted lines. In (b) the three different topographies due to the changed scanning amplitudes indicate a stable (Amp ~ 16nm), unstable (Amp ~ 13,8nm) and again a stable (Amp ~ 9,5nm) region starting from the top.[243]

The reason for the different appearance of surface topography is the variation of the interaction force regimes. When working with small amplitudes image formation due to attractive forces only is possible while high amplitudes guarantee a repulsive force dominated tip sample interaction. The working regime can easily be determined by amplitude and phase spectroscopy. Fig. 1.19 shows a typical Mag/Height (left) and Phase/Height (right) diagram. The red lines denominate the attractive interaction regime and the blue lines the repulsive one.
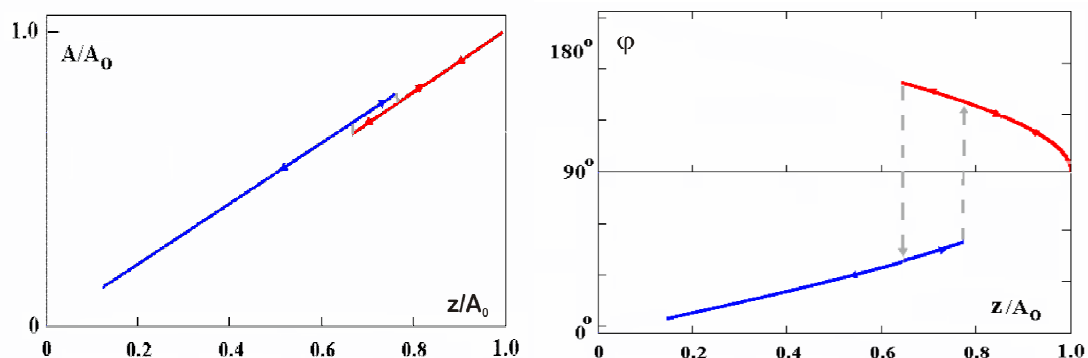
Fig. 1.19: In the left picture an amplitude spectroscopy and in the right picture a phase spectros-copy of a full measurement cycle is shown. The red colour indicates the attractive interaction regime and the blue colour the repulsive one. The switch is most obvious in the phase spectroscopy due to its phase jump of about 90°. Choosing a setpoint in the overlap of the forward and backward scan would lead to unstable working conditions.[242]

It is well know that the phase of cantilever oscillation is completely determined by the setpoint ratio $r = A/A_o$ if only elastic interaction is taken into account. In this case $\varphi = arcsin(r)$ in the repulsive regime and $\varphi = \pi\text{-}arcsin(r)$ in the attractive regime are leading to a phase shift of 90° for both assumptions if r = 1, which corresponds to free oscillation and perfectly fits the theory.[244] The phase spectroscopy in Fig. 1.19 shows the change in the interaction regimes, which manifests in a phase jump of about 90°. In praxis there is always and overlap between the approach and the retraction curve. This area has to be excluded during measurements because the interplay can easily skip between the two interaction regimes and artefacts may occur. Thus it is recommended to conduct amplitude and phase spectroscopy prior to a surface scan to exclude unstable working parameters.

The only wearless way for sample investigation is the non-contact mode, which is the most difficult mode to establish.

Non-contact mode

If thinking of AFM as tool for atomic resolution the non-contact mode is the preferred mode in literature. But despite its high potential real non-contact mode measurements are very sophisticated to realize and demand a deep understanding of the fundamental processes in the picture formation of atomically resolved images.

The working idea in the non-contact mode is to oscillate the tip only in the attractive interaction regime between tip and sample. Therefore small oscillation amplitudes (< 1nm) are necessary to discriminate the different interaction regimes and to increase the sensitivity to short range forces and reduce the contribution of long range forces.[241]

In principal there are two approaches to realize non-contact mode measurements, the amplitude modulation (AM) and the frequency modulation (FM) method. In the first one the cantilever is driven near its resonance frequency, f_0 at fixed amplitude. Due to tip sample interactions during the approach process the amplitude and the phase change. This shift is used as feedback signal to stabilize the tip sample distance. The AM modulation working principal is also used in the semicontact mode.[245] It soon turned out that the time response ($\tau_{AM} \approx 2Q/f_0$) on changes in amplitude and phase is slow because of high Q factors which are preferentially used to reduce the noise during the measurements. So Albrecht et al. introduced the frequency modulation mode, where the changes in the eigenfrequency taking place on a timescale of $\tau_{FM} \approx 1/f_0$.[246]

If the cantilever feels a constant force gradient ($k_{ts}=-\partial F_{ts}/\partial z$) during the oscillation cycle, which is the case for free oscillation or in approximation for small amplitudes, the description of the frequency shift is simple:

$$\Delta f = \frac{f_0}{2k}k_{ts} \qquad \text{(Eq.24)}$$

f_0 is the resonance frequency and k is the spring constant.[241] Since in the experiment the force gradient changes by several orders of magnitude with large amplitudes, a perturbation approach is necessary to describe the frequency shift. The perturbation approach can be transformed to an easier expression by integration by parts to:

$$\Delta f(z) = \frac{f_0}{2k}\frac{2}{\pi A^2} \int_{-A}^{A} k_{ts}(z-q')\sqrt{A^2-q'^2}dq' \qquad \text{(Eq.25)}$$

where A is the half amplitude, z is the position, q' describes the deflection of the cantilever, and k_{ts} is now a weighted average.[247] Eq.25 gives an important connection between the frequency shift and the amplitude. If the amplitude is small the sensitivity to short range forces is high so amplitudes below 1 nm are desirable in the non-contact mode.[248]

The problems are manifold like (i) thermal drift, (ii) forces in the range of nN, (iii) low stiffness of the cantilever for increased force resolution that can generate instabilities (jump into contact), (iv) F_{ts} is not only from the last atom at the tip end (important for atomic resolution) but from many atoms, producing a background force (v) the non monotonic behaviour of the frequency shift also poses a problem for stable feedback because it can lead to devastating tip crashes. Nevertheless the achievable resolution compensate for the necessary efforts to generate real non-contact pictures.[241]

Beside the discussed approaches to measure in non-contact mode in 2007 Prior et al proposed a feedback mechanism, similar to the AM mode but relying only on the phase shift.[249] By

_____

measuring the decay of the evanescent field on the surface of a glass prism they were able to confirm a constant tip to sample gap in the nm regime for arbitrary long time. Although this method is not eligible for atomic resolution and suffers of very low scanning speed (max 100 nm/s) it provides a further method for SNOM to guarantee measurements with a constant tip to sample gap of a few nanometres.[142]

A different geometric setup, but also based on the FM method is the shear force head. A tuning fork with a homemade tip glued on one end is used to measure the frequency shift relative to a reference arm when approaching a surface. It will not be used in this work and therefore not further discussed.

2 Experimental

2.1 Setup at the Department of Physical Chemistry, Vienna

2.1.1 Laser System

At the University of Vienna, at the Department of Physical Chemistry all experiments were performed on a 60 fs high power Chirped Pulse Oscillator [Femtosource XL: Femtolasers Produktions GmbH, Vienna] with a repetition rate of 11 MHz and a pulse energy of up to 210 nJ. (Fig. 2.1) Modelocking is realized by a saturable Bragg reflector. The high pulse energies are reached by stretching the cavity which leads to higher pulse energies at lower repetition rate. The Ti:Sapphire crystal is pumped by a Verdi V-18 [Coherent, Santa Clara, California]. A Pockels cell allows the reduction of the repetition rate from single pulse picking up to 5 kHz. The pulse duration is controlled by the use of a home built autocorrelation before every experiment.
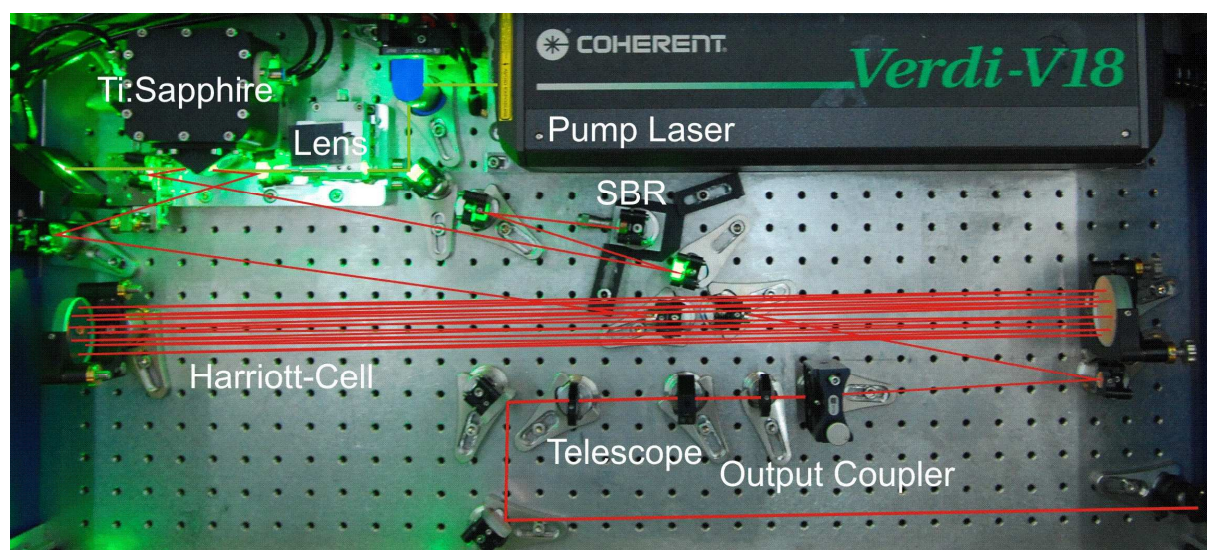
Fig. 2.1: The laser beam path of the Femtosource XL [Femtolasers Produktions GmbH, Vienna] is shown. The 532nm light of the pump laser is drawn in green colour. The fluorescence and laser light are drawn in red colours. Each mirror of the Harriott Cell reflects the laser beam 8 times for stretching the cavity.

2.1.2 AFM

For surface investigation and aSNOM (apertureless Scanning Near-field Optical Microscope) applications a standard multimode SPM (Scanning Probe Microscope) [Ntegra Aura, NT-MDT, Zelenograd, Russia] was used. The detection principle is based on the light lever setup.

_____

The device provides the opportunity to scan by sample or by probe. For experiments the head scanning system due to better optical access to the SPM tip was chosen. The maximum scanning area in x and y direction was 100x100 µm and 10 µm in z direction. It is also possible to decrease the scanning area and the noise by working with smaller driving voltage of the piezotube, which is recommended when reaching the resolution limit in the z direction. To suppress the nonlinearity and the thermal drift of the piezotube the scanner is equipped with capacitive sensors.

2.1.3 Optical System

The laser beam path outside the cavity is shown in Fig. 2.2. The laser passes a $\lambda/2$ plate, for rotating the polarisation, enters a polarizer-Pockels cell-analyzer system, which enables single pulse picking. The linear electro-optical effect, which means a change of the refraction index due to an externally applied electric field, gives a Pockels cell its ability to turn the polarisation of the incoming light proportional to the applied voltage. To work with the Pockels cell the polarizer and the analyzer have to have crossed polarisation. When voltage is applied pulses can pass.

Then the beam travels through a prism compressor to compensate the inherent chirp of the laser pulse and the chromatic dispersion due to different optical components (lens, polarizer, etc.).

To guarantee a position stable laser beam at the SPM tip a beam stabilisation system was installed, which works with two PSDs (Position Sensitive Devices) [MRC Systems GmbH, Heidelberg, Germany] and two piezoactuators [Piezosystem Jena GmbH, Jena, Germany].

The autocorrelation measurement can be performed at any time of the experiment just by turning a flip mirror. In this setup the laser beam is divided in to two equal parts by a 50:50 beamsplitter. The two beams travel different lines, where one is variable and are reunited by a spherical mirror, which focus them on a nonlinear optical crystal. (β-BaB_2O_4) Due to the second order nonlinear susceptibility, which originates in the lack of inversion symmetry, the incoming 800 nm laser light is frequency doubled and generates three 400 nm beams. The collinear beam is the sum of the two k vectors of the incoming beams and is detected by a photodiode. This signal reaches its maximum value when the delay lines have exactly the same length. By changing the delay line one obtains a complete autocorrelation trace, where the pulse length can be calculated from the FWHM of the fitted Gaussian pulse profile.
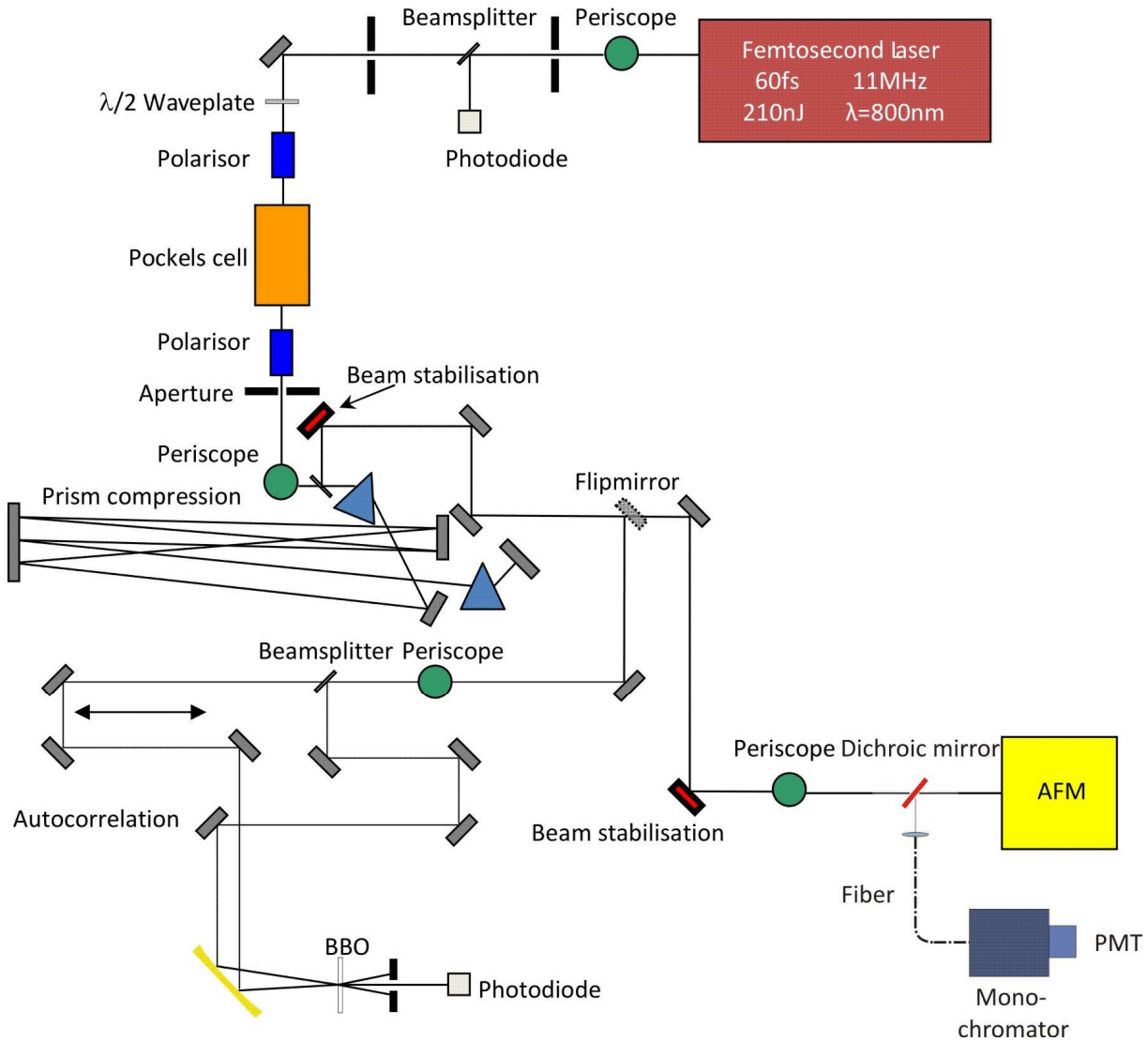
Fig. 2.2: Experimental setup for the aSNOM measurements. A Pockels cell for pulse picking up to 5 kHz, a prism compressor for compensation the inherent and the chromatic dispersion, an autocorrelation for measuring the pulse length, a beam stabilisation system based on two piezoactuators and two PSDs and the aSNOM setup (Fig. 2.3)

After measuring the pulse length the laser is ready to enter the backscattering aSNOM setup, where the same lens is used for focusing the laser and collecting the signal. Hence we used a dichroic mirror [FLWP-650, Melles Griot, Albuquerque, New Mexico] with a cut-off frequency of 650 nm which shifts to approximately 600 nm due to the different angle of incident (0° => 45°), for coupling out SHG (Second Harmonic Generation) light from the tip or fluorescence and to reduce the background (SPM diode laser at 650 nm, fs laser at 800 nm) simultaneously. The harvested light is coupled in a multimode fibre [QP600-1-SR/BX, Ocean Optics, Dunedin, Florida], spectrally processed in a monochromator [SpectraPro 2150i, Princeton Instruments, Trenton, New Jersey] and detected by a Peltier cooled PMT (Photomultiplier Tube) [R6060-02, Hamamatsu, Shizuoka, Japan].

_____

The focusing lens is a double pair achromatic system [FAC1040-A1, Thorlabs, Newton New Jersey] for high quality laser focusing with a numerical aperture (NA) of 0.26 and a focal length of 42 mm. The high focal length has to be chosen because of geometric limitations of the commercial SPM head and the idea of performing measurements in aqueous environment under electrochemical control as well. The diameter in the focal point was measured by cutting edge method to be approximately 7.5 µm. (Ch. 3.2.1)
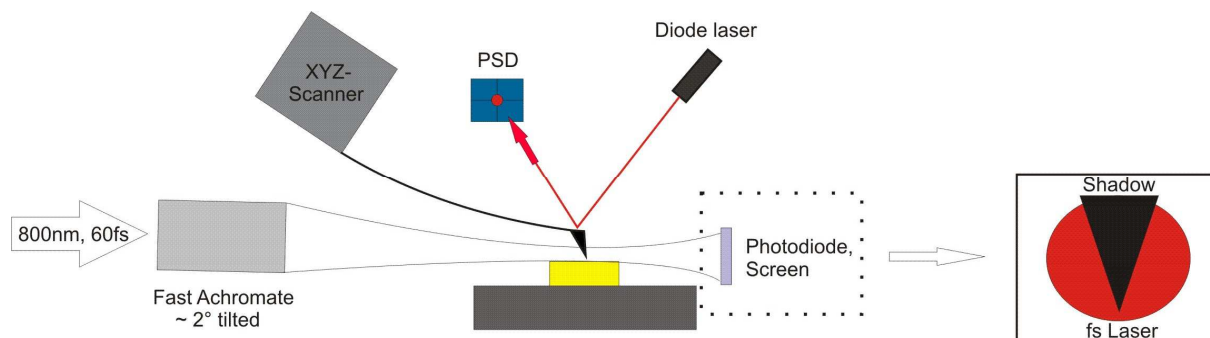

Fig. 2.3: The focused laser beam hits the SPM tip at an angle of incidence of ~1-2° to avoid shading of the tip end because of surface unevenness. The reflected beam is projected at a photodiode or screen to gain an observable for the alignment. (Ch. 3.2.1.1) The picture at the right site of the scheme shows schematically the image on the screen.

In the setup at the Department of Physical Chemistry (Fig. 2.3) the laser beam illuminates the SPM tip from the backside. The focus diameter around 7.5 µm should guarantee, after good alignment, that only the tip and not the cantilever is illuminated by the incoming laser beam, which is in contrast to most other aSNOM setups.[14, 139] This approach should decrease the influence of thermal effects discussed in Ch. 3.1, which constrain the systematic investigation of near-field modification.

The light which is not scattered by the tip itself but reflected from the sample illuminates an installed photodiode or a simple screen for improving the reproducibility of the laser alignment on the tip, which is a crucial part in most of the aSNOM setups.

2.1.4 Contact Measurement

To measure the contact behaviour between a SPM tip and a gold-coated surface the measurement of voltage breakdown was chosen. The simplified setup is shown in Fig. 2.4. The tips were coated with gold or platinum and the samples (glass or mica) were coated with at least a 30 nm thick sputtered or evaporated gold layer.

The tip was connected directly to the holder in order to decrease the noise during measurement. Screened cables with minimum length were chosen. All devices were connected to the same ground to avoid ground loop currents from different ground potentials.

The applied voltage between tip and surface was provided by a commercial lab power supply. To avoid artefacts based on the working principle of the switch-mode power supply a battery with a potentiometer for voltage control was used instead. To avoid too high currents through the tip a serial resistor with either 1 or 0.5 MΩ was introduced into the circuit. Measurements were done with a high-end oscilloscope [Waverunner 64Xi, LeCroy, Chestnut Ridge, New York] for optimum data pre-processing in combination with a precision, high-speed transimpedance amplifier [OPA2380, Texas Instruments, Texas, Dallas]
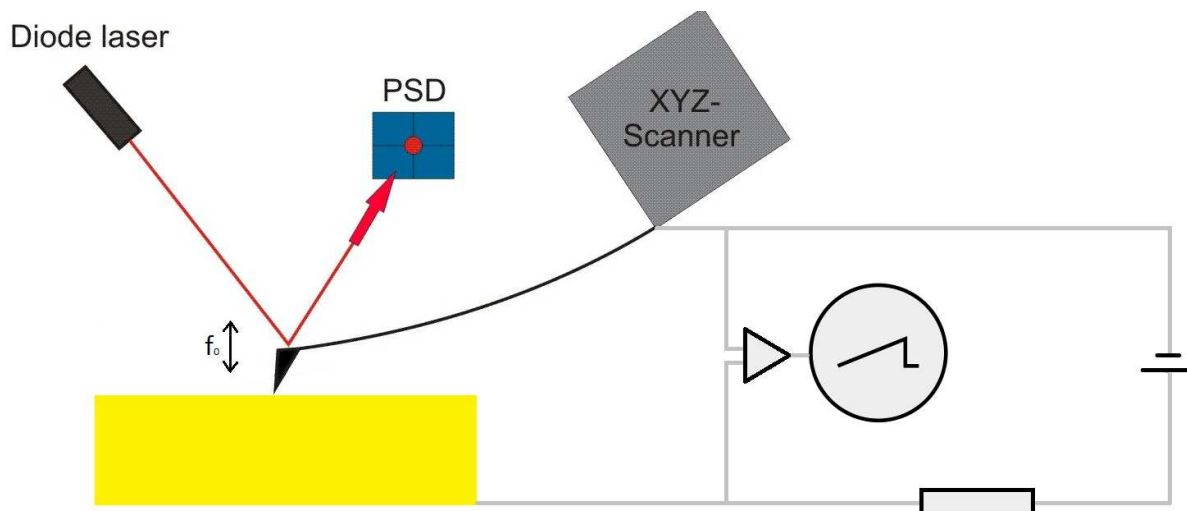
Fig. 2.4: A circuit built to measure the voltage breakdown due to a shortcut which is produced when the tip hits the surface. The voltage between tip and surface has to be small to avoid too high current densities, which could easily destroy the thin conductive coating of a SPM tip.

2.2 Setup at the Weizmann Institute of Science, Rehovot

2.2.1 Laser System

The laser for near-field modifications at the Weizmann Institute of Science is a Micra-5 [Coherent, California, Santa Clara]. This oscillator provides tuneable bandwidth from 30-100 nm by adjusting the in-built prism compression. We tuned the laser to approximately 50 nm bandwidth which results in a pulse length of ~60 fs. The repetition rate is 82 MHz and the resulting pulse energy is 6 nJ. The laser is purged with N_2 to keep a constant overpressure in the housing and to avoid water and dirt adsorption at the optical components.

The laser provides an auto mode-locking and power tracking system which works with two in-built photodiodes for maximum working stability.

2.2.2 AFM

The commercial SPM, XE 120 [Park System, Suwon, Korea] at the Weizmann setup is mounted on an inverted microscope. The XY scanner is spatially separated from the z scanner for crosstalk elimination. Scanning area in the high voltage mode is 100x100 µm in XY and 12 µm in Z direction which can be decreased in the low voltage mode to one-tenth in size for higher resolution. A drawback is that the sensor feedback only works in the high voltage mode which leads to pronounced artefacts if working in low voltage mode is necessary (hysteresis, thermal drift). Software based compensation is necessary.

An advantage is the inverted Olympus microscope [Eclipse TE2000-U, Olympus, Tokio, Japan] which supports the alignment of the fs-laser at the tip when working with transparent samples or can be used for in-situ Raman measurements.

Surface modification was performed by two types of SPM tips. The AC160-TS silicon tip [Olympus, Tokio, Japan] for non-contact measurements with no coating and the ATEC-NC-Au [NanoWorld AG, Neuchâtel, Switzerland] also for non-contact measurements but with Au coating. (Cr/Au ~70nm thickness)

2.2.3 Optical System

The setup at the Weizmann Institute of Science appears much simpler (Fig. 2.5) because the prism compression is built in the laser housing and there is no autocorrelation setup installed. Due to the lack of a Pockels cell all experiments have to be performed with 82 MHz repetition rate.

A homemade shutter was used to control the illumination of the tip. For power adjustment a $\lambda/2$ plate-polarizer system was built. The different polarisation angles were realized by a second $\lambda/2$ plate installed directly in front of the lens to control power and polarisation independently and to minimize spatially variations of the laser at the tip caused by the change of the polarisation angle.

The divergence of the laser beam of the Micra-5 has to be compensated by the installation of a telescope.
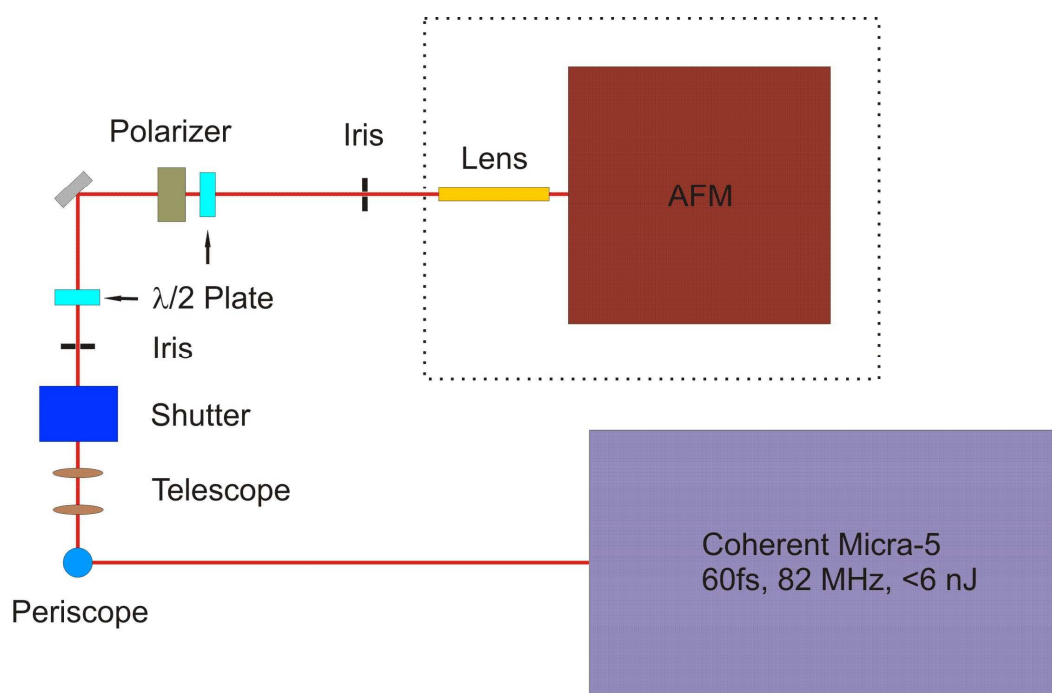
Fig. 2.5: Scheme of the setup at the Weizmann Institute of Science. The laser path is much shorter than at the Department of Physical Chemistry, therefore no beam stabilisation system is required.

The tip is illuminated from the side under an angle of approximately 14 degrees. (Fig. 2.6) Alignment was performed by two CCD cameras. One camera is situated on top and the other one at the bottom built in an inverted microscope (only with transparent samples).

The design of the used SPM tips enables the observation of the tip in the top view, which eases the alignment process. The focusing lens with a numerical aperture (NA) of ~ 0.2 and a focal distance of 15 mm provides a spot diameter of about 15 µm.
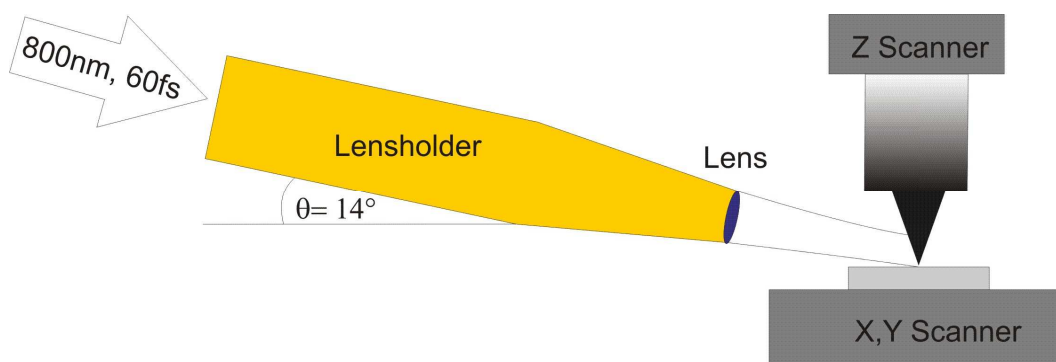
Fig. 2.6: The SPM tip is illuminated from the side at an angle of incidence of about 14°. The incident laser works at 82 MHz repetition rate with 60 fs pulse length. The spot diameter of 5 µm enables the illumination of the tip with minimal illumination of the cantilever.

3 Results and Discussion

The following chapter is divided into two major parts. The first part is dedicated to theoretical investigations, for a better understanding of the possibilities and limitations of near-field microscopy. The geometry of the studied structures is defined by the real dimensions provided by SPM tip manufacturers. The theoretical results are underlined by experimental data. The parameters influencing the field enhancement are studied with a Boundary Element Method (BEM) toolbox for Matlab, developed in cooperation with the Physical Department of the Karl-Franzens University in Graz. The thermo-mechanical properties are investigated with COMSOL Multiphysics software, based on the Finite Element Method (FEM).

The second part illustrates the conducted experiments at the Department of Vienna and the Weizmann Institute of Science.

3.1 Theoretical Investigation

3.1.1 Field Enhancement Study

3.1.1.1 Introduction

In Ch. 1.4.2. the simple dipole-dipole model for estimating field enhancement factors was already discussed. In this model the SPM tip is regarded as a sub-wavelength sized polarisable sphere with a radius corresponding to the radius of curvature of the tip apex and the substrate is idealised as perfectly flat. An incoming light field excites a dipole in the sphere, which interacts with the image dipole excited in the substrate.

This is a simple method to estimate tip-sample interaction. However for a full description of the tip-sample system this approach is not sufficient. The dipole-dipole model does not incorporate retardation effects which have to be taken into account when the size of the investigated structures is comparable to the used wavelength. Furthermore the reflection from the substrate described by the Fresnel coefficients and multipoles are not included.[250]

To describe more complex structures theoretical investigations have to go beyond the analytical solution provided by the Mie theory and a full simulation of Maxwell equations is necessary.

In literature a considerable collection of different methods to solve tip-substrate interactions can be found. Examples include the finite difference in time domain method (FDTD),[128, 130, 251, 252] the method of moments,[253] the generalized field propagator technique,[119, 254] multiple

multipole method (MMP),[14, 106, 255] the Green´s function method,[256] the finite element method (FEM)[257] and also the boundary element method.[258, 259]

In this work the boundary element method was chosen due to its low computational demand and thus its ability to be conducted on a normal desktop workstation.

3.1.1.2 Theory of the Boundary Element Method (BEM)

The principle idea of the boundary element method is the reduction from volume differential equations to boundary integral equations. A convenient way to describe this problem is the quasistatic approximation, which is fulfilled when the particle size is much smaller than the wavelength of the light. The electrostatic Green function (Eq.26) provides a suitable solution scheme for solving the Poisson or the Laplace equation if there are no external charges available (instead of the Helmholtz equation, when solving the full Maxwell equations) to receive the electrostatic potential.[260]

$$\nabla^2 G(r,r') = -4\pi\delta(r-r'), \qquad G(r,r') = \frac{1}{|r-r'|} \qquad \text{Eq.26}$$

If a plane wave excites a nanoparticle, V_i the sources are bound to its interface, ∂V_i. So inside a certain region, $r \in V_i$ the scalar potential $\phi(r)$ follows:

$$\phi(r) = \phi_{ext}(r) + \oint_{V_i} G(r,s)\sigma(s)da \qquad \text{Eq.27}$$

ϕ_{ext} is the potential due to external excitation and $\sigma(s)$ is the surface charge distribution at the interfaces. This equation is valid everywhere except at the boundaries. To fulfil the Laplace or Poisson equation at the boundaries certain boundary conditions have to be chosen, like the continuity of the parallel electric field. This requires σ to be the same inside and outside the particle. Moreover the normal component of the dielectric displacement has to be continuous too. If taken into account we get the boundary integral equation:

$$\Lambda\sigma(s) + \oint \frac{\partial G(s,s')}{\partial n}\sigma(s)da' = -\frac{\partial \phi_{ext}(s)}{\partial n}, \qquad \Lambda = 2\pi\frac{\varepsilon_2 + \varepsilon_1}{\varepsilon_2 - \varepsilon_1} \qquad \text{Eq.28}$$

where ε_1 und ε_2 are the dielectric functions in- and outside the particle. By summing over the surface elements one ends up in the main equation of the quasistatic boundary element method.

$$\Lambda\sigma_i + \sum_j \left(\frac{\partial G}{\partial n}\right)_{ij}\sigma_j = -\left(\frac{\partial \phi_{ext}}{\partial n}\right)_i \qquad \text{Eq.29}$$

The surface charge, σ_i is now defined at a discrete surface element, i or more accurate, at a discrete point situated at the centroid of small surface element (collocation method) (Fig. 3.1)

and can easily be obtained through matrix inversion, which is the limiting step in the simulation because it affords a proper amount of working memory.[260, 261]

The surface derivatives $(\partial G/\partial n)_{ij}$ of the Green function connect the elements i and j of the surface.
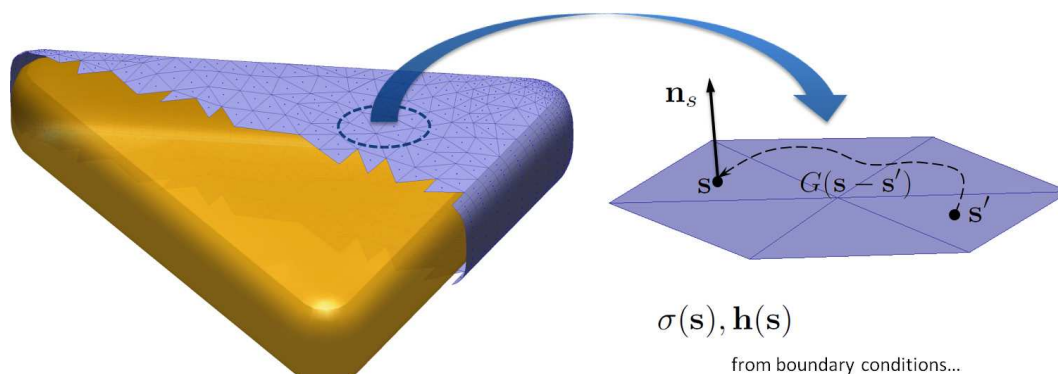

Fig. 3.1: Discretisation of the surface with the collocation method. A continuous surface is approximated by a discrete number of points located at the centroids of small surface elements. The Green function, G(s-s′) connects the different points (s,s′) with each other.[261]

To include retardation effects the full Maxwell equations have to be solved and scalar and vector potentials have to be taken into account, which is fulfilled by the Helmholtz equation.

If the calculation is based on the electromagnetic fields instead of potentials more complex numerical implementations are required. In the potential-based BEM approach inverted matrices are of the order of $N \times N$, whereas in the field-based BEM approach the matrices are of the order $3N \times 3N$.

A more detailed description can be found elsewhere.[261]

3.1.1.3 Model

The BEM approach used in this work is based on the ideas of Garcia de Abajo and Howie[262, 263], which is potential based and therefore the size of the matrices is given by the number, *N* of surface elements, instead of *3N* in the field based approach and it is less general because it assumes bodies with isotropic dielectric functions separated from a dielectric environment by abrupt interfaces. Furthermore the potential based BEM approach has a weaker spatial dependence, which is advantageous for the used collocation method.

The geometric model for the simulation is based on a tapered tip with a hemispherical endcap situated over a substrate. The laser illuminates the tip from the side, like in all performed experiment in Ch.4. The excitation mode is plane wave excitation. The dielectric properties of the tip, the substrate and the background can be chosen independently.

The discretisation is chosen in such a way that areas of high gradients, like the end of the tip or the surface underneath the tip provides an element size below 0.1 nm² and the mean element size is about 30-35 nm². For the plate a free tetrahedral mesh was chosen whereas the tip itself is meshed with a mapped mesh. The model is shown in Fig. 3.2. It is obvious that the highest gradients are expected directly underneath the tip; therefore the highest element density is situated there.
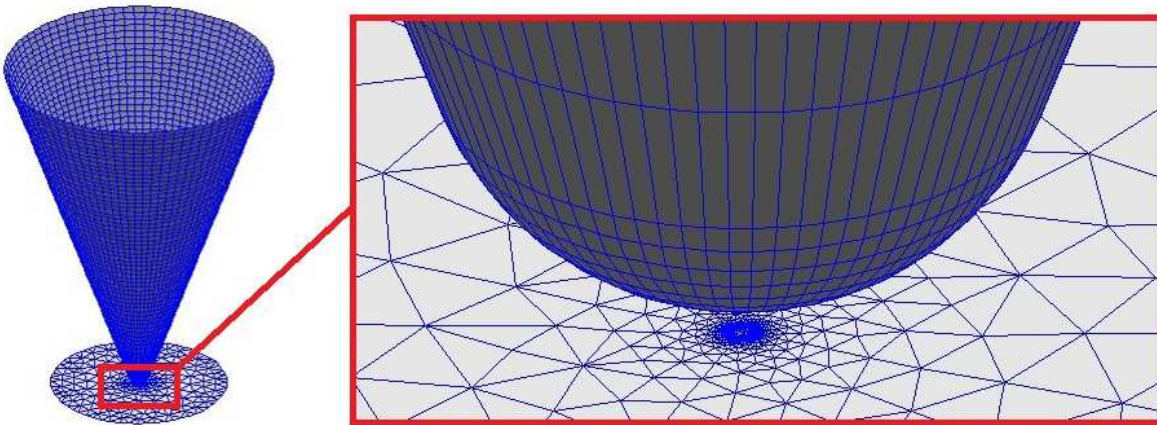

Fig. 3.2: Geometrical structure and mesh of the used model for the calculation of the field enhancement behaviour. The radius of curvature is 10 nm and the average element size is 29 nm².

In all calculations the "bemret" solver is chosen, which solves the full Maxwell equations and therefore also includes retardation effects. The effect of reflected waves is also incorporated by the Fresnel reflection equations.

3.1.1.4 Results

The first step in the field enhancement study is the determination of the tip length used for all investigations because it was already shown in literature that the tip length has a huge influence on the absolute value of the field enhancement factor.

Earlier investigations indicated that the simulation of short tips (< 1000nm) has to be done very carefully because resonance effects may occur which can easily overestimate the enhancement effects.

To avoid this resonance effect the intensity profile over various tip lengths at constant excitation wavelength (800 nm) was calculated. In Fig. 3.3 and 3.4 the difference between silicon and gold tips is shown. The tip length is chosen between 80 nm and 300 nm, where 300 nm in length is close to the maximum size possible to be calculated with the used workstation. (18 GB memory). The angle of incidence relative to the surface was 1.5 °. The

discretisation of the tip was always adapted to the new tip length to guarantee the same element size for every tip size.

The radii of the Si and the Au tips were chosen according to the specifications, provided by the manufacturer and set to be 10 nm for Si and 65 nm for the Au tips. The pure Silicon tip shows moderate dependency on the tip length, although a resonance peak at a tip length of approximately 240 nm is observable. Similar behaviour has already been reported in literature[75] and was explained by the antenna effect.
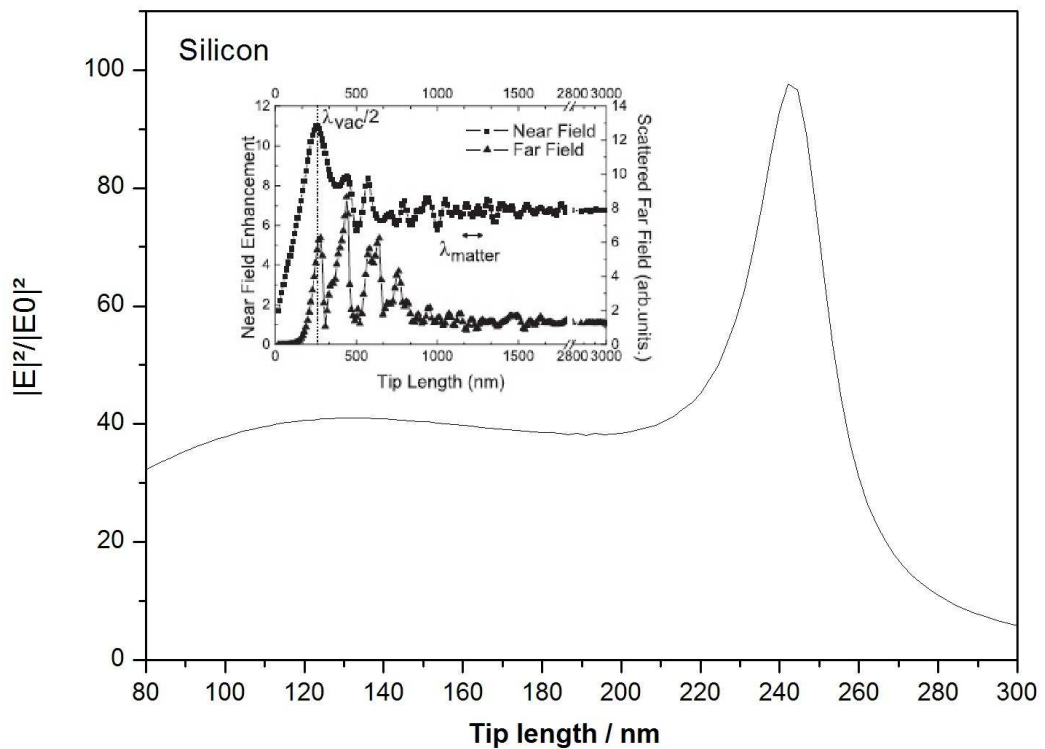
Fig. 3.3: Field enhancement versus tip length for a silicon tip with a radius of 10 nm. A resonance peak appears at approximately 240 nm tip length. Similar behaviour was described in literature by K. Kern et al. and is shown in the insert.[75]

For a gold tip the resonance behaviour is much more pronounced because surface plasmon resonance comes into account (Fig. 3.4). A similar behaviour was observed by J.F. Martin et al. He calculated even longer tips and showed that the field enhancement increases slowly with increasing tip length. The strong resonance peaks, appearing for short tips due to standing waves from reflected surface plasmon polaritons,[264] decrease for increasing tip length.

Because in practice it is difficult to find the exact geometry, which fits the resonance conditions for the available laser wavelength, this work will concentrate on the off-resonance behaviour.
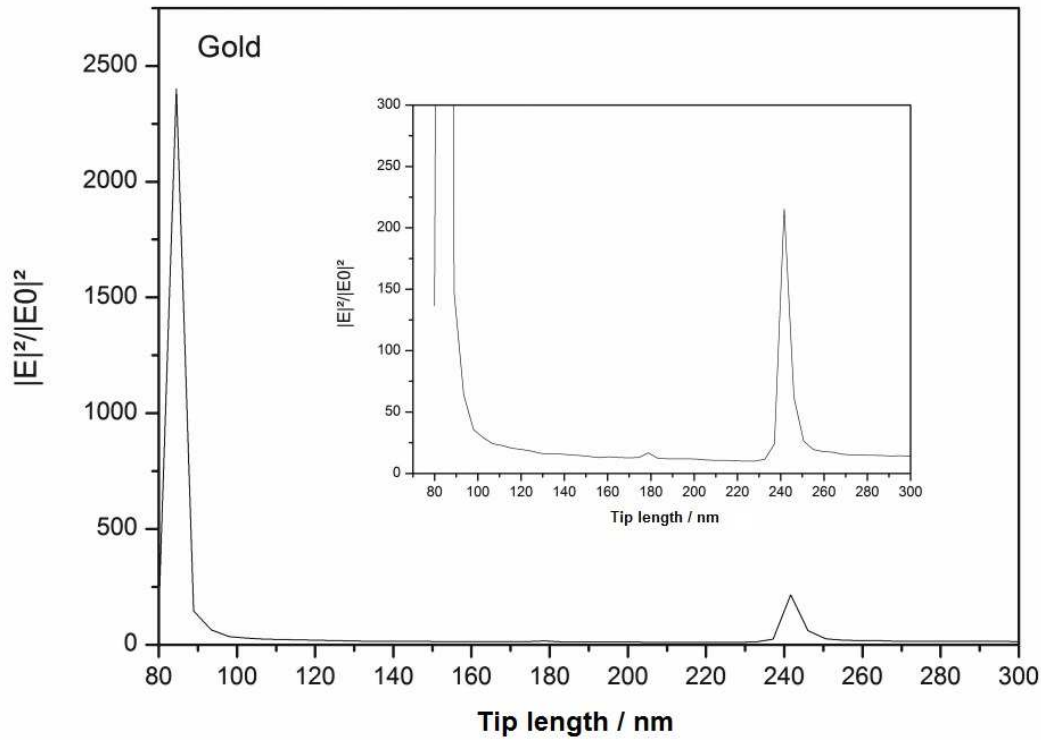
Fig. 3.4: Field enhancement versus tip length for a gold tip with a radius of 65 nm. In the insert the y-axis is zoomed to visualise the off-resonance behaviour.

The distribution of the field intensity for a silicon tip situated at a distance of 2 nm over a gold surface is shown in Fig. 3.5. The laser illuminates the tip at an angle of 1.5 °. The tip length is 300 nm. The field enhancement was calculated for this geometry to be at a factor of 8, which is quite moderate. The major reason for this moderate enhancement is the small angle of incidence because based on the calculation of Fresnel reflection coefficients the field enhancement is prohibited by the reflected wave from the surface underneath for small angles of incidence (Fig. 3.7)

The diameter of the silicon tip is 20 nm and is consistent with the guaranteed diameter of the tip manufacturer. The field under the silicon tip is even more confined, enabling a possible structure size even smaller than 10 nm.

Field intensity |E|^2
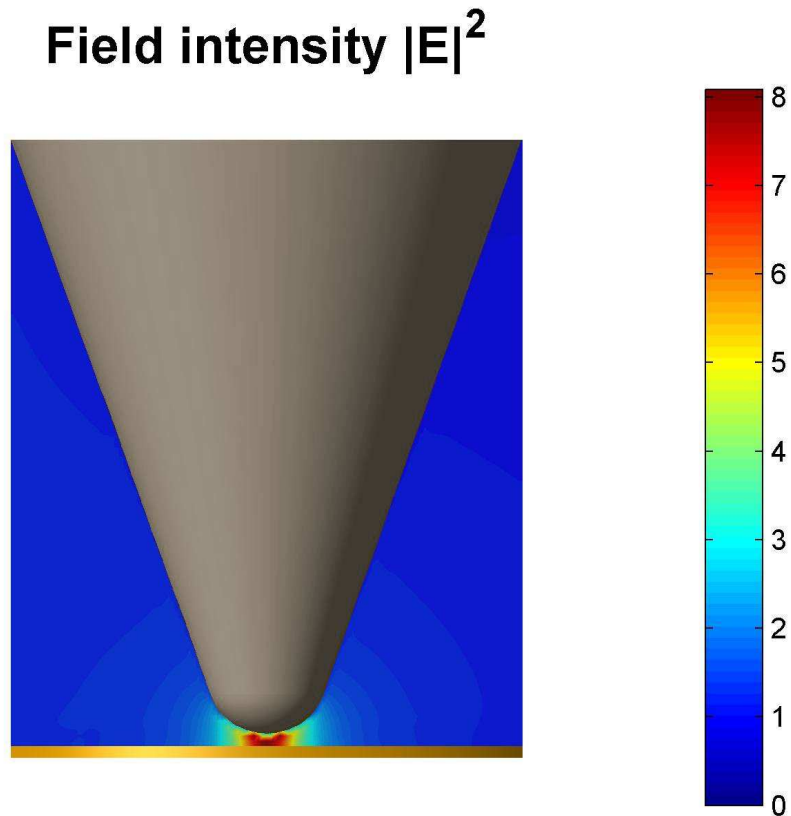
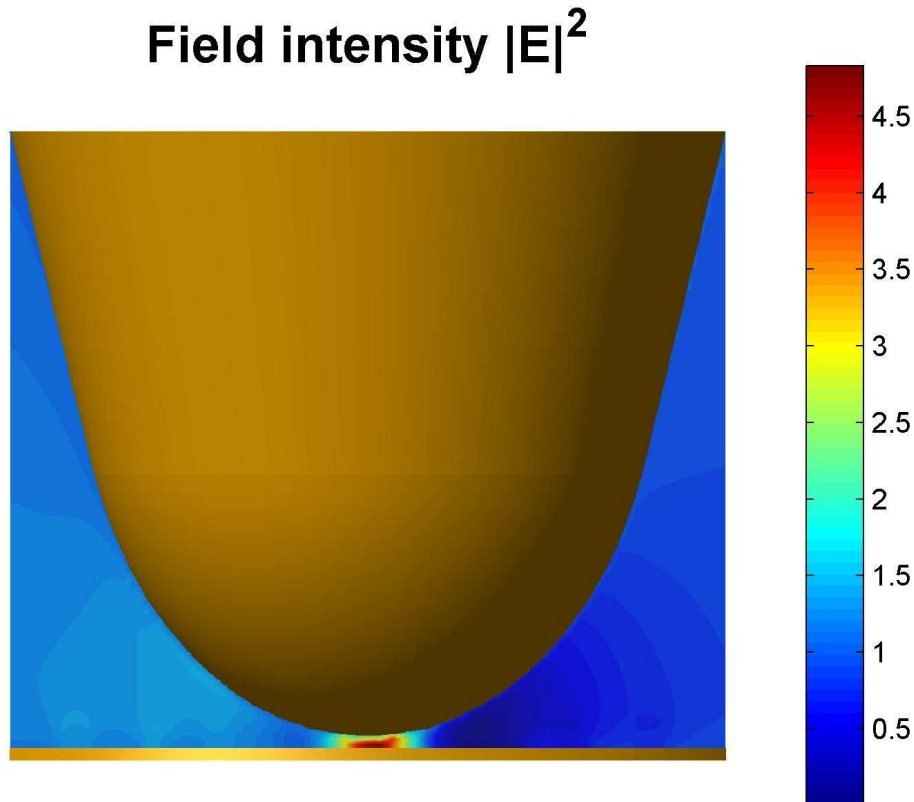*Fig. 3.5: Field enhancement in the tip sample gap of a silicon tip with a radius of 10 nm at a distance of 2 nm to a gold surface. The incident laser is coming from the left side under an angle of 1.5°. The polarisation is parallel to the major axis of the tip.*

In Fig. 3.6 the field intensity distribution for a gold tip at a distance of 2 nm away from a gold surface is shown. The diameter of the tip is 130 nm. All other parameters are the same as in Fig. 3.5. The field enhancement calculated for this geometry is even smaller than for the silicon tip. This is not astonishing because the calculations were done at off-resonance conditions and the diameter of the tip is approximately 6 times bigger than for the silicon tip. It is already accepted in literature that the field enhancement decreases with increasing radius, because the field confinement also decreases.

In Fig. 3.6 the minimal structure size is more than 15 nm, which is small compared to the tip diameter but already 50% bigger than for the silicon tip.

Field intensity $|E|^2$

Fig. 3.6: Field enhancement of a solid gold tip with a radius of 65 nm at a distance of 2 nm to a gold surface. The incident laser is coming from the left side at an angle of 1.5°. The polarisation is parallel to the major axis of the tip.

It was already noted that the angle of incidence plays an important role concerning the maximum field enhancement. This can be explained by the fact that the incoming wave will be reflected at the surface underneath the tip, a phase shift of 90° will be introduced and no enhancement takes place.

One of the most prominent theoretical works from Novotny et al.[106] claims that it is important to have the electric field vector aligned along the major tip axis but this is only true if the calculation is done without a surface underneath the tip.

In Fig. 3.7 the field enhancement is plotted versus the angle of incidence for a silicon tip with a radius of 10 nm. The angle was increased up to 70°, which corresponds to tip illumination parallel to its outer border. The half cone angle of the calculated tip was 20°. Higher angles are not reasonable, because the tip end will no longer be illuminated.

For the geometry chosen it turns out the highest intensity is reached at an angle of incidence of about 20°, which is slightly above the 14° realized at the setup at the Weizmann Institute of Science. As already pointed out in Fig. 3.5 the field enhancement is negligible for the grazing incidence.
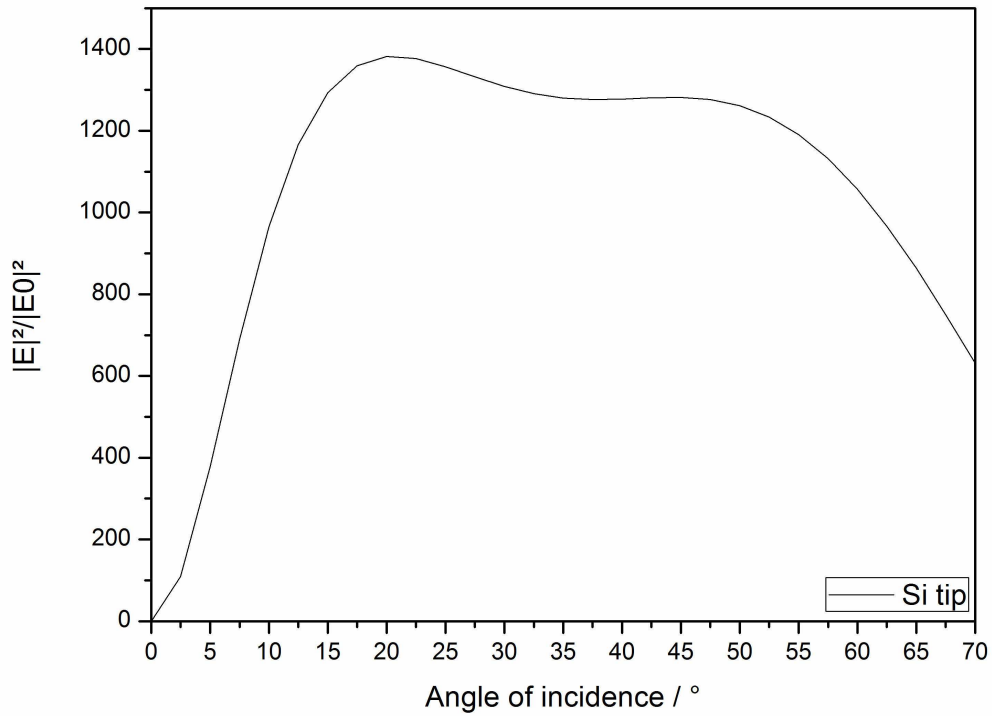
Fig. 3.7: Angle of incidence vs. field enhancement for a silicon tip with a radius of 10 nm. No enhancement is visible for 0°, which could be explained by the phase shift of the reflected wave. The maximum enhancement is situated at 20°.

The behaviour of a solid gold tip with a radius of 65 nm is slightly different. The enhancement is even worse for small angles and reaches its maximum at 50°. It has to be noted that even though the radius of the gold tip is more than 6 times bigger than of the silicon tip the maximum field enhancement at the optimum angle of incidence is nearly four times higher.

Besides the interference of the incoming and reflected wave, multipole excitation is also assumed to influences the characteristic of the field enhancement dependency on the angle of incidence.[265]
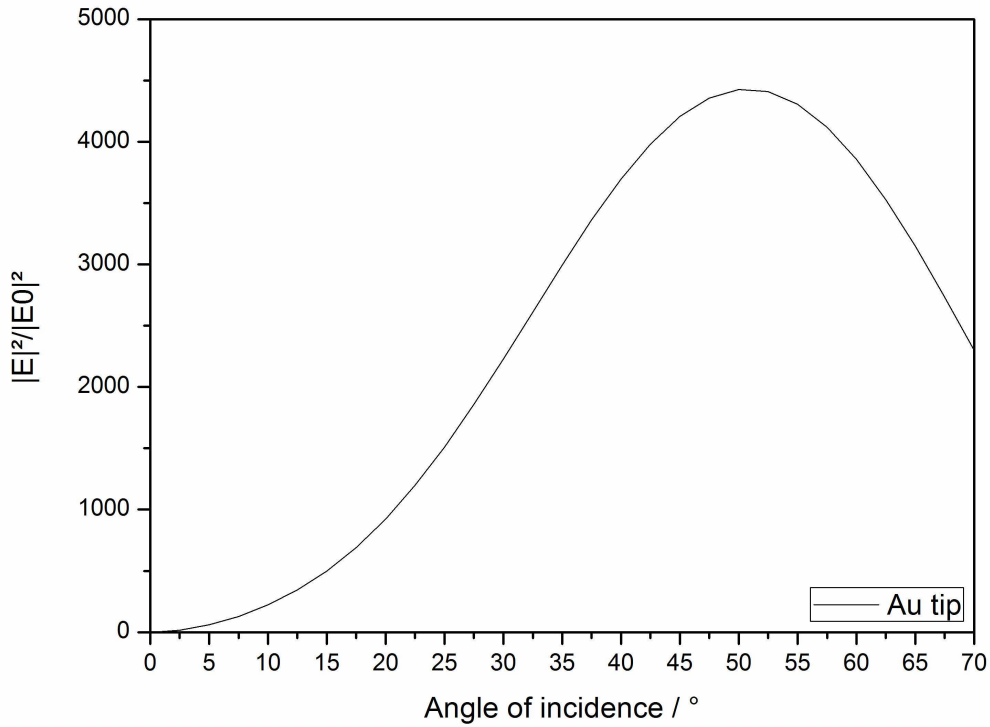
Fig. 3.8: Angle of incidence vs. field enhancement for a gold tip (r=65 nm). The enhancement at small angles is worse than for the silicon tip but the maximum field enhancement is nearly 4 times higher than for the silicon tip with the smaller radius.

A strong component of the electric field vector parallel to the major tip axis is important to guarantee high field enhancement, although it was shown that the angle of incidence and the vicinity of a surface influence this characteristic decisively.

The dependency of the field enhancement on the polarisation direction of the incoming laser light is typically shown as cosine function in literature.[135],[266] In Fig.3.9 this typical behaviour was simulated. Therefore a silicon tip with a radius of 10 nm was calculated. The tip was situated 2 nm away from a gold surface and was illuminated by laser pulses at varying polarisation angles. In this calculation 0° is equivalent to p-polarised light in respect to the major tip axis and 90° corresponds to s-polarisation. As expected the highest enhancement can be observed for a strong electric field component parallel to the major tip axis.
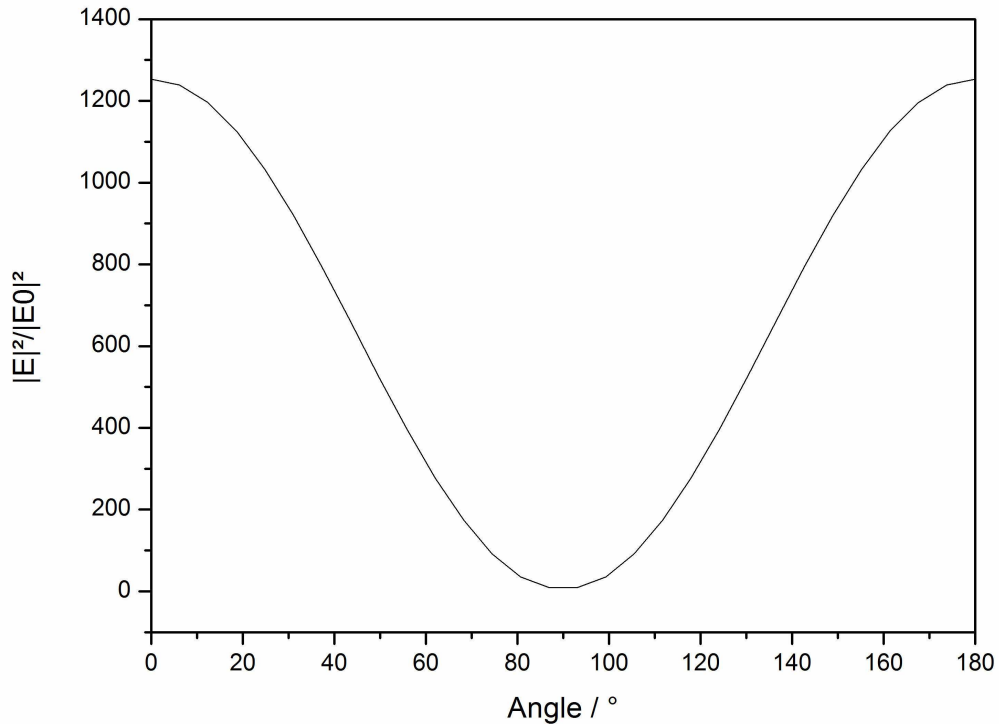
Fig. 3.9: Simulated polarisation dependency of Si tip with r = 10nm at an incidence angle of 14°. The spacing between the silicon tip and the gold surface is 2 nm. The characteristic of this curve is already known in literature.[135]

It is well known that the illumination of the tip causes heating of the whole system and therefore changes the mechanical properties of the cantilever, which is necessary for the light lever principle of SPM based near-field devices.

These changes can be utilised to determine the temperature of the tip. For oscillating cantilevers the shift in the resonance frequency was chosen as reasonable tool for easily estimating the temperature of the tip.[129]

As the resonance frequency shift is caused by the overall heating of the tip-cantilever system, a complementary tool is necessary to calibrate the resonance frequency shift with the temperature of the tip. For this Raman spectroscopy was favoured because silicon tips provide a Raman mode which is highly temperature dependent.[267]

The combination of these two techniques was done by an SPM mounted on an inverted microscope. The conducted experiments indicate a resonance frequency shift of approx. 1Hz for 1 K tip temperature rise for the investigated system.[129]

Wang et al. calculated the tip temperature as a function of the polarisation angle and the temperature showed a similar characteristic as the field enhancement calculated in Fig. 3.9.

In this work Wang's simulation was investigated experimentally on the Weizmann setup, where the resonance frequency based approach was developed. Therefore the resonance frequency shift for different polarisation angles was determined.

In Fig. 3.10 the measured values are depicted. It has to be noted that the determination of the resonance frequency is only possible without a surface nearby because this would prohibit accurate measurements.

The characteristic of the curve fits perfectly the theoretical prediction, except for the extreme values, where buckle occur.
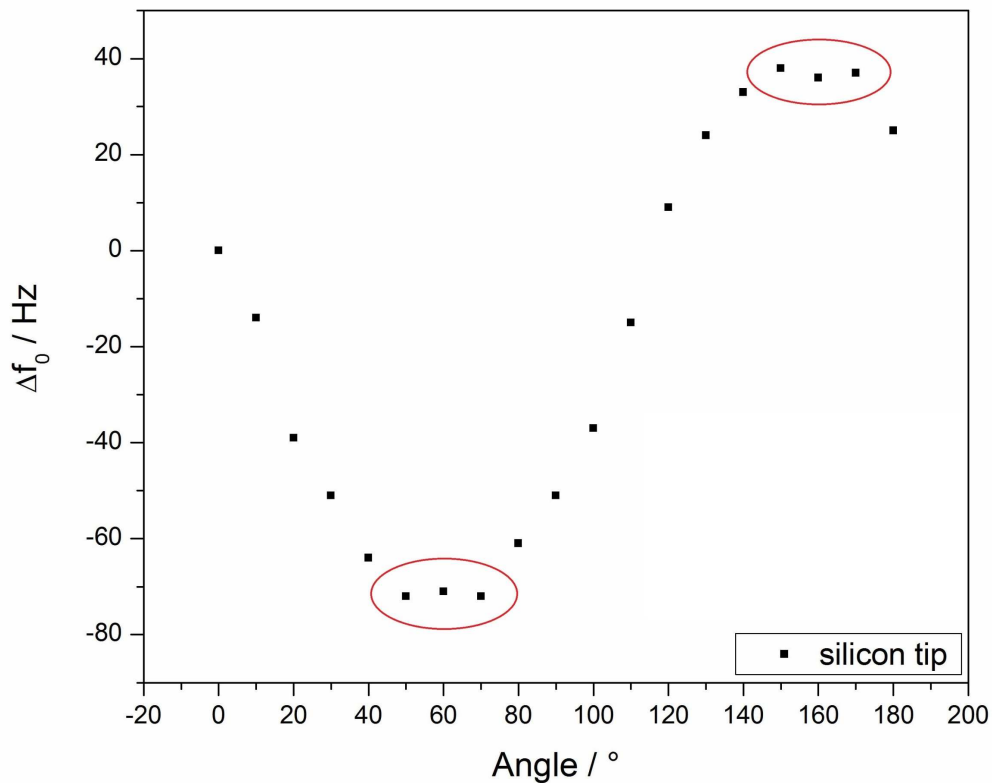
Fig. 3.10: Measured frequency change due to the heating of the cantilever for a silicon tip. The lack of the reflected wave influences the charge distribution at the tip and therefore leads to the buckle indicated by the red marks. 0° means vertical aligned electric field vector. The y-axis is inverted for better comparison.

To understand this behaviour further simulations were performed, where the model was adopted to the changed boundary conditions and it turned out that due to the lack of a surface underneath the tip, no reflected wave emerges and therefore the distribution of the surface charges is slightly shifted leading to a buckle of the field enhancement factor at the extreme values of the curve.

The simulated curve without a surface nearby is shown in Fig. 3.11. The buckle is not that much pronounced than in the experimental work but the tendency is the same.
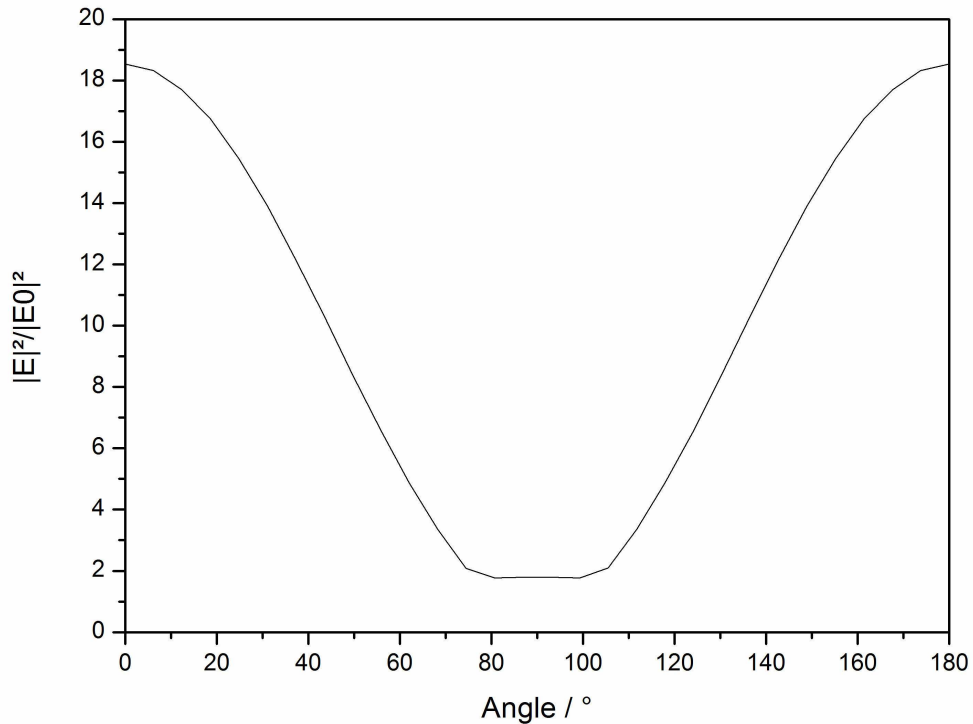
Fig. 3.11: Simulated polarisation dependency for a silicon tip, illuminated at 14° angle of incidence and no surface underneath. The same behaviour can be observed for a blunt Si tip close to the surface.

A reason for the different appearance of the buckles in theory and experiment could be the differences in shape of the ideal structure (simulated) and the real structure (measured), because a change in the geometry also influences the characteristic of the curve, demonstrated in Fig. 3.12 and 3.13, as well.

The illumination parameters are the same, but the cantilever is gold coated now. Therefore the radius is much bigger. The influence of radius is only visible for the s-polarisation. The p-polarisation is unaltered.

In the simulation the dipole character of the tip vanishes for big radii and multipole excitation takes place, especially for s-polarisation. This leads to the occurrence of the local maximum for s-polarisation.

It has to be noted that the absolute frequency shift of the gold coated cantilever is nearly four times smaller than for the silicon cantilever. This may be explained by the higher reflectivity of gold for 800 nm laser light compared to silicon or by the homogeneous gold coating which minimises the bimetallic influence, in contradiction to the silicon cantilever, where only the upper part of the cantilever is coated. Measurements with uncoated silicon cantilever will explain the origin of this effect.

It has to be considered that the influence of the geometry of the simulated tip on the absolute field enhancement values is enormous. Therefore it is important to carefully choose the geometries for simulation.
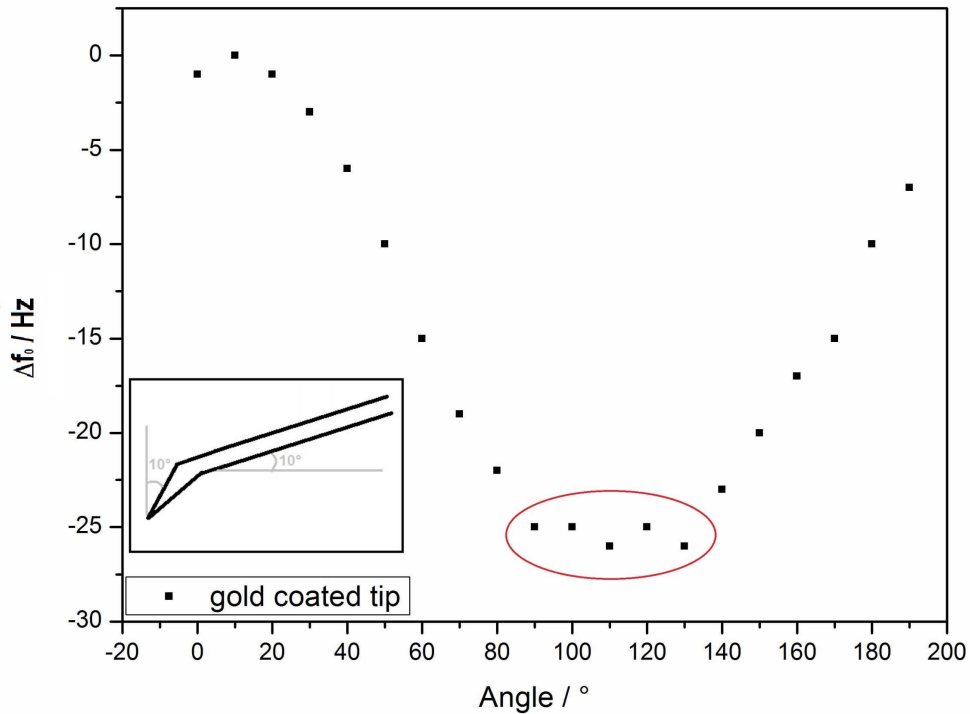

Fig. 3.12: Measured frequency shift of a gold coated silicon cantilever. The drift in the absolute frequency values is the overall heating effect of the whole system. The y-axis is inverted for better comparison.

Especially simulations with tips shorter than 1000 nm are very sensitive to changes in the geometry.

The simulation in Fig. 3.13 was conducted under the same boundary conditions as the experiment was performed. The only difference is the size of length of the tip, which was limited by the performance of the workstation used for simulations. Although this restriction is obstructively the simulated results nicely fit the experimental observations.
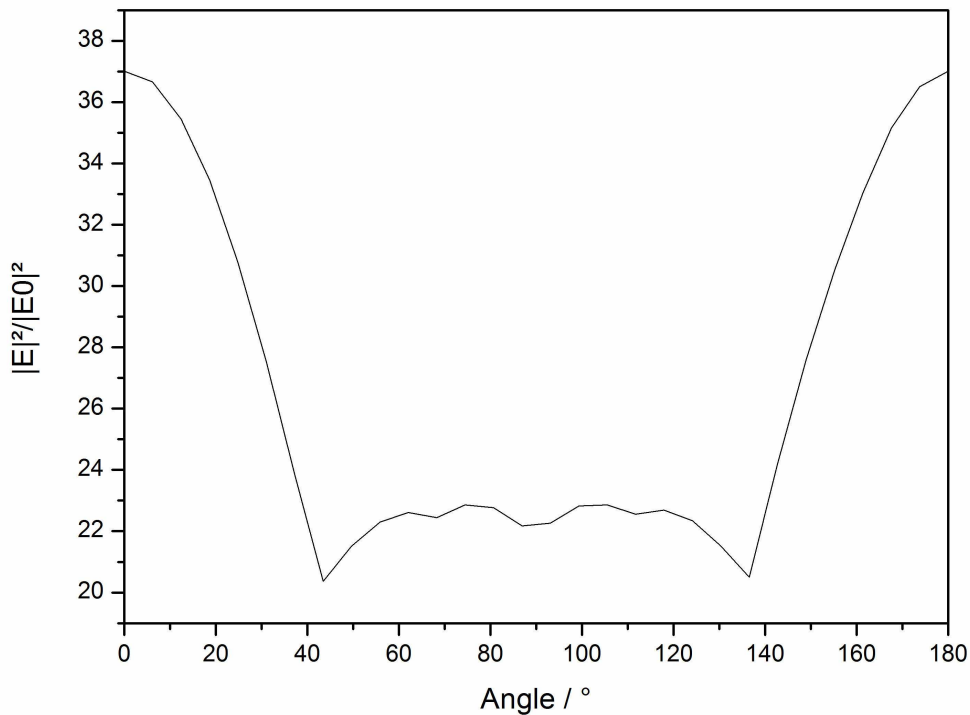
Fig. 3.13: Simulated polarisation dependency for a gold tip (r=65 nm), illuminated under 14° angle of incidence and no surface underneath. Parameters are chosen to fit the experimental conditions in Fig. 31.

The deviation of the extreme value position from the polarisation angle orthogonal to the surface (0°) is due to the experimental setup (Fig. 3.10+3.12). The illumination at the Weizmann setup was done from the side. Therefore a tilt of the tip, due to the mounting of the cantilever on the scanner, has to be taken into account. In addition the orientation of the tip relative to the cantilever was also different for the used silicon and gold tip.

In the previous simulations and in all simulations in literature gold tips are always regarded as solid tips. This may be true for STM or shear force measurements but for SPM measurements there are no solid gold tips available, thus silicon tips with various gold coating thicknesses are used. The range extends from 5 to 65 nm gold coating thickness, depending on the manufacturer.

To investigate the influence of the different coating thicknesses a slightly changed model was established where the overall radius, defined by the outer shell, which corresponds to the gold coating, was kept constant and the thickness of the coating was changed by reducing the size of the silicon core to avoid the influence of geometric changes. (Fig. 3.14)
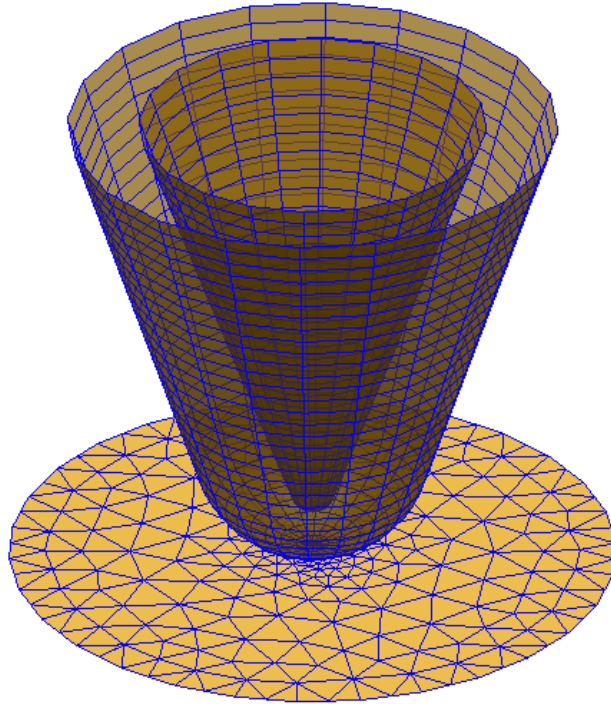
Fig. 3.14: Model to simulate the influence of the different gold coating thicknesses. The overall radius is kept constant and the size of the inner silicon core is reduced to change the thickness of the gold coating which is determined by the outer shell. In this case the thickness of the gold coating is 25 nm.

For evaluation a spectra from 300-900 nm the excitation wavelength for each coating thickness was measured. The radius of the outer shell was 75 nm and kept constant. The thickness of the coating was varied within the range known as typical commercial coating thickness, which is 5-65 nm. The length of the tip was 300 nm. Illumination was done with p-polarised light at an angle of 1.5°.

The illustrated calculations were performed at the Vienna Scientific Cluster (VSC-1) because the double tip structure increased the element number tremendously.

It turned out, that differences in the coating thickness influence the spectra excessively until a thickness of 40 nm is reached. This value nicely fits the calculated skin depth for wavelengths between 300-900 nm, which peaks at ~500 nm and 40 nm skin depth. For thicknesses above 40 nm the coated tip behaves like a solid Au tip, only the absolute values change.

In Fig. 3.15 three exemplary gold coating thicknesses are illustrated. The intensity is normalised for better visualisation. The highest field enhancement for the simulated system is achieved for an excitation wavelength of 650 nm and a coating thickness of 50 nm.

Illumination of the same system with the 800 nm laser light used in this work, would result in the highest enhancement at a coating thickness of 20 nm. Nevertheless the absolute value would be five times smaller than for the resonance condition.
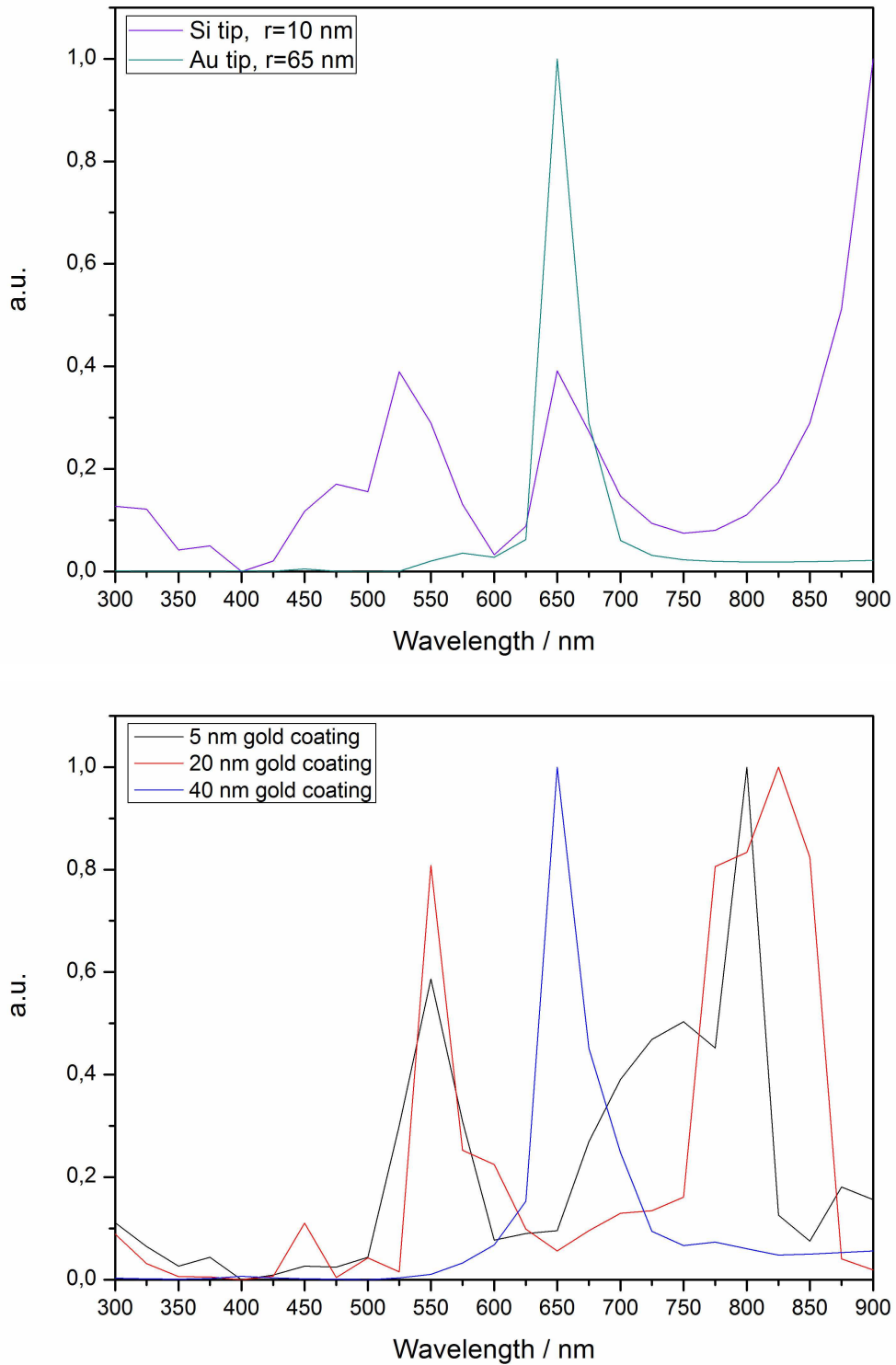
Fig. 3.15: Field enhancement study at different wavelengths for different gold coatings. The upper spectra demonstrate the wavelength dependency for solid silicon and solid gold tips. The lower spectra show three different coating thicknesses. No change for gold coatings thicker than 40 nm can be observed, following the calculated skin depth for light in the range from 300-900nm, where the maximum skin depth at approx. 500 nm can be found to be 40 nm.

In principal theoretical investigations can give useful hints for planning and improving an experimental setup. Furthermore, they can help in understanding observed phenomena. However, especially in the studied system it would not be reasonable to rely solely on the simulated predictions, as the influence of the geometry is very pronounced and small deviations can alter the surface charge distributions significantly, thus leading to completely shifted resonance conditions.

To exploit the full potential of field enhancement in apertureless Scanning Near-field Microscopy the use of an optical parametric amplifier (OPA) to scan over a broad range of wavelengths and measure the tip response simultaneously seems to be a promising way.

3.1.2 Thermo-mechanical Study

3.1.2.1 Introduction

In the last 15 years lots of work was done on the estimation of the generated temperature and the resulting spatial expansion of SPM tips due to external laser illumination during near-field experiments.

These investigations all concentrate on the behaviour of the tip itself, which is reasonable for STM or shear force tips but not sufficient for commercial AFM tips mounted on a cantilever. The behaviour of the cantilever is strongly dependent on its temperature, which influences the bending in contact mode or the resonance frequency in the non-contact or semicontact mode. Especially the reflective coating on the backside of a cantilever, which is common on most of the commercial cantilevers to increase the scattering efficiency of the diode laser from the optical lever system, leads to a huge bending of the cantilever due to different thermal expansion coefficients of different materials.

Although already mentioned in literature[20] of near-field microscopy as possible influence on the reproducibility, no closer examination of this effect can be found. There are only some investigations, which deal with the bimetallic bending as tool for thermal detectors[268] or femtojoule calorimeters.[269, 270]

When looking in literature tip temperatures of 350-800°C for typical laser energies of several tens of mJ/cm² are calculated[52, 128-131, 197, 266, 271-274] and proofed by different experimental approaches like cantilever deflection,[58] Raman band shift,[129] enhanced Raman scattering[275] and atom probe tomography,[274] leading to tip expansion of a few nanometres. But this is already sufficient to generate a hard contact between tip and surface, because it is the typical

_____

tip-sample gap during near-field investigations and thus can lead to a modification of the tip and/or the sample.

The focus in this chapter will be on the thermo-mechanical changes of a typical commercially available AFM cantilever. The temperature of the tip will not be calculated, following the two temperature model, which is necessary when dealing with fs laser heating because there is already a considerable amount of literature on this topic.

3.1.2.2 Model

All experiments were done with the commercially available COMSOL Multiphysics simulation software 4.2a., which is based on the Finite Element Method (FEM). This software allows the connection of different physical problems in a convenient way.

The software also provides a reasonable variety of different extensions, called modules, where major equations to explicit problems (Acoustic Module, Chemical Engineering Module etc.) are already arranged.

The calculated model is based on the geometry data taken from a commercial tip, TAP300Al [BudgetSensors] with a simplification of the asymmetric tip profile, which was changed to be C_4 symmetric along the major tip axes. Since the major interest lies in the temperature influence along the whole tip holder and not in the precise temperature distribution at the tip end, no deviation from this geometric change is expected.

For the calculation the whole chip structure was taken into account to verify that there is no influence of the cantilever holder by inhibited heat flux from the cantilever to the holder, when performing long term laser illumination experiments.

The material of the tip holder is silicon because it is the most common material in commercial SPM tip production. The reflective coating on the backside of the cantilever is aluminium in this case. (Gold would also be a common material). The thickness of the reflective coating ranges from 25-70 nm, and is 30 nm in the calculated model

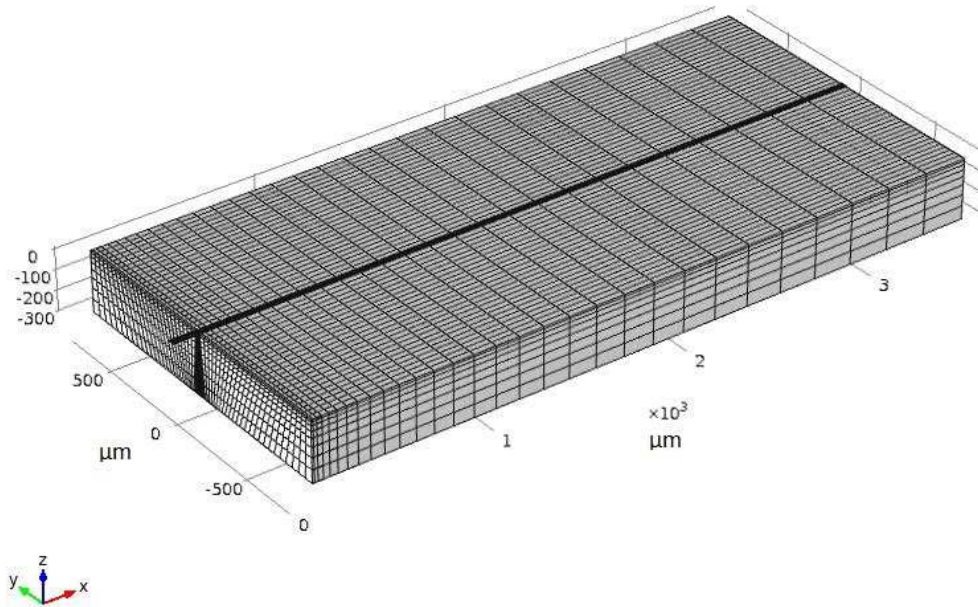After the model was built, the surface has to be discretised with care. (Fig. 3.16)

Fig. 3.16: Overview of the complete model including the mesh. SPM holder TAP300Al-G [Budget-Sensors].

To guarantee a good match of the surface elements with the built geometry different types of meshes have to be combined. Fig. 3.17 shows the cantilever and the tip from below, where three types of meshes have been built. The tip (Fig. 3.19) is discretised by a free tetrahedral mesh, the area around the tip has to be meshed by a free quad to give a continuous transition between tip and cantilever and the remaining part of the cantilever is discretised with a mapped mesh.
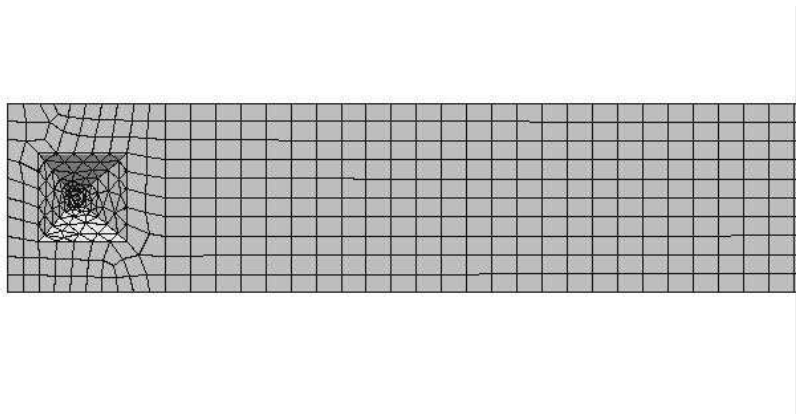
Fig. 3.17: The different types of meshes along the bottom of the cantilever are shown. The free quad mesh has to be chosen to continuously connect the tetrahedral mesh of the tip with the mapped mesh of the cantilever.

Especially the thin reflective Aluminium coating, which plays a major role in the simulation, has to be discretised very carefully by choosing a swept mesh to connect the reflective coating with the cantilever and to reach a sufficient discretisation in the direction of its thickness (30 nm). (Fig. 3.18)
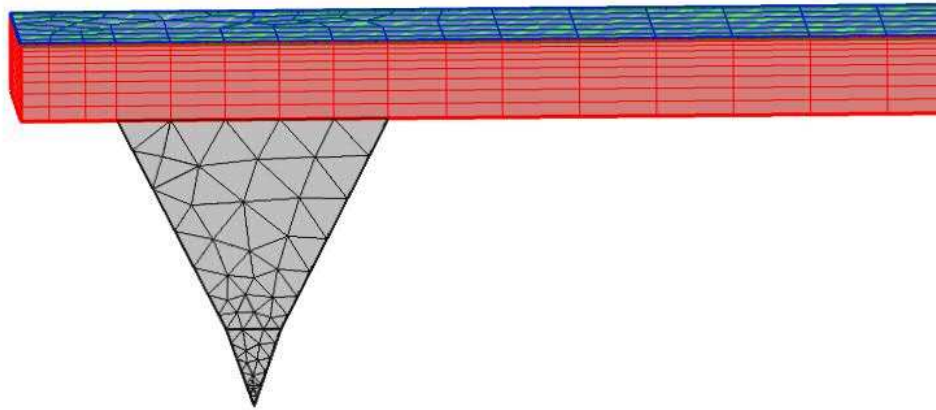
Fig. 3.18: The cantilever is shown in red and the reflective Al coating is coloured blue. The mesh of the coating is not resolved because it is too thin compared to the cantilever thickness (ratio 4000:30)

The tip is described by a free tetrahedral mesh with decreasing element size at decreasing structure size. The different opening angles of the tip, given by the manufacturer are also taken into account.
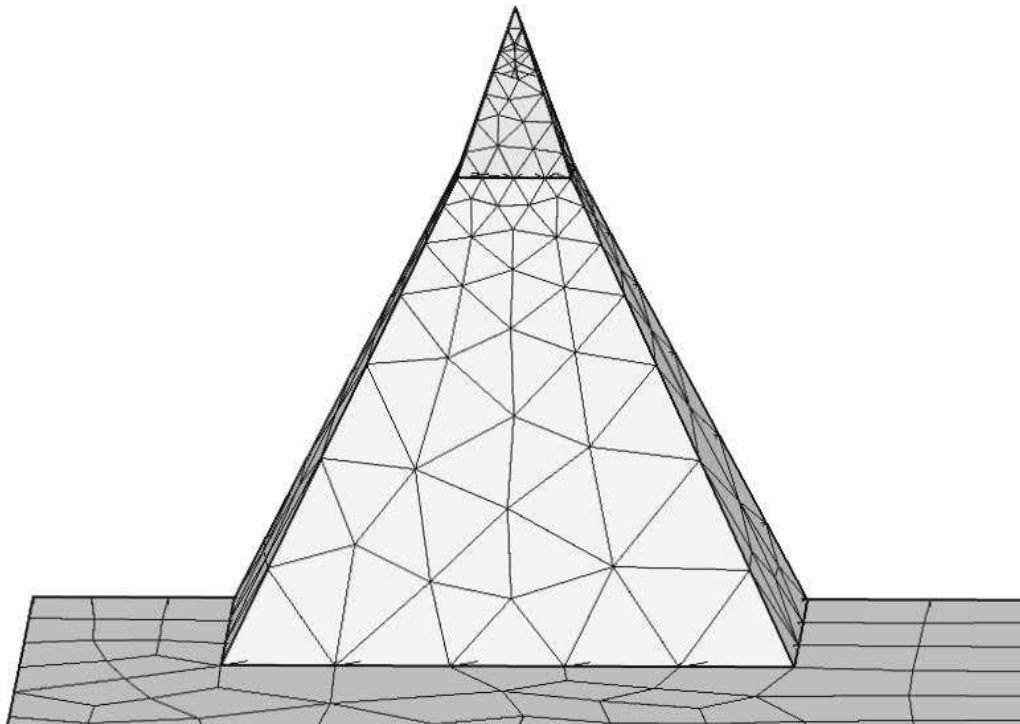

Fig. 3.19: A free tetrahedral mesh is chosen to discretise the tip geometry. The surface elements are adapted to the size of the structure. The depicted element size is coarser than in the simulation for clarity reasons.

The laser heating is approached by a boundary heat source, where the input power in W/m² can be defined. The size of the boundary heat source is equivalent to half the laser spot size of

the SNOM system used at the Department of Physical Chemistry, Vienna, which is approx. 4 µm, if the system is aligned with the highest energy at the apex of the tip. The Gaussian beam profile is not taken into account because its influence is negligible on the investigated parameters here. The size of the spot is more important because it was shown by Zhang that it strongly influences the maximum temperature of the cantilever.[271]

The first parameter is the heat transfer, which is defined as the movement of energy due to a temperature difference. Generally three ways of heat transfer have to be taken into account. The most important in our case is conduction. Heat conduction in solids takes place by either electrons, carrying the heat in metals or by molecular motions, so called phonons in crystals.

The second way of heat transfer is the free convection, which is described as heat transport from a solid surface in air /liquid by the air /liquid's own velocity. In contradiction to forced convection, which is based on air or liquid stream the free convection is very small. About 5-25 W//m²K in air and only 20-100 W/m²K in liquids.[276]

The last heat transfer is due to radiation, i.e. the heat is transferred by radiation. In the described model the focus is laid on heat transfer due to conduction because the contribution of the free convection and the radiation at temperatures below 1000°C are negligible.[277]

To calculate the heat flow along the SPM chip, ignoring viscous heating and pressure work, the following equation was used:

$$\rho C_p \frac{\partial T}{\partial t} + \rho C_p u \cdot \nabla T = \nabla \cdot (k \nabla T) + Q \qquad \text{Eq.30}$$

ρ is the density [kg/m³], C_p is the specific heat capacity at constant pressure [J/kg K], T is the absolute temperature [K], u is the velocity vector [m/s], k is the thermal conductivity [W/m K] and Q is the heat source [W/m²].

In the Solid Mechanics interface COMSOL Multiphysics uses different coordinate systems to describe the motion and deformation of solid objects. For the physical space, called spatial frame, it uses spatial coordinates (x,y,z) and for the continuum mechanics the material (or reference) coordinates (X,Y,Z) are introduced, which label material particles. In the initial configuration material and spatial coordinates of every particle coincide. If deformation of a solid object occurs (due to external or internal forces) each material particle keeps its material coordinates but changes its spatial coordinate.

$$x = x(X,t) = X + u(X,t) \qquad \text{Eq.31}$$

Hence the actual spatial position is defined by the displacement vector *u*. Together with *v* and *w*, they are the primary dependent variables in the Solid Mechanics interface and bear the major information of object deformation.

For structural analysis COMSOL uses a total Lagrangian formulation, which means that the computed stress and the resulting deformation are referred to material configurations and not to the current position in space, which gives the opportunity to evaluate spatially varying material properties only once for the initial material configuration, because they do not change if the solid deforms or rotate.

For structural effects due to the heating of the SPM chip the thermal expansion of the model has to be calculated. It is defined as an internal strain due to a change in temperature. In the direct tensor form the total strain tensor, $\boldsymbol{\varepsilon}$ is written in terms of the displacement gradient, $\nabla \boldsymbol{u}$

$$\boldsymbol{\varepsilon} = \frac{1}{2}(\nabla \mathbf{u} + \nabla \mathbf{u}^T)$$ Eq.32

which is related to the stress tensor, *s* and the temperature by Duhamel-Hooke's law:

$$\mathbf{s} - \mathbf{s}_0 = \mathbf{C} : (\boldsymbol{\varepsilon} - \boldsymbol{\varepsilon}_0 - \boldsymbol{\alpha}\theta)$$ Eq.33

C is the 4th order elastic tensor, ":" is the double dot tensor product, s_o and ε_o are the initial stresses and strains and α is the thermal expansion tensor and $\theta = T - T_{ref}$. T_{ref} is the strain free reference temperature.

The time dependent solution is given by the equation of motion, based on Newton´s second law

$$\rho \frac{\partial^2 \mathbf{u}}{\partial t^2} - \nabla \cdot \mathbf{s} = \mathbf{F}$$ Eq.34

where ρ is the mass density, *u* is the displacement vector, $\nabla \cdot s$ is the divergence operator on the stress tensor and *F* is the body force per unit volume.

All calculations are based on the linear elastic material model, with isotropic properties, where the elastic properties are defined by the Young's modulus and the Poisson's rate. (C= C(E,ν))

The used material constants are summarized in Tab. 1. The origin of these values is the Comsol database. C_p is the heat capacity, ρ is the density, *k* is the thermal conductivity, α is the thermal expansion coefficient *E* is the Young's modulus and ν is the Poisson ratio.

	C_p / J kg^{-1}K^{-1}	ρ / kg m^{-3}	k / W m^{-1}K^{-1}	α / K^{-1}	E / Pa	ν
Silicon	703	2330	163	4.2E-6	1.3E11	0.27
Aluminium	900	2700	160	2.3E-5	7.0E10	0.33

Tab. 1: Material constants used for the thermo-mechanical investigation. Values are taken from the Comsol database. C_p is the heat capacity, ρ is the density, k is the thermal conductivity, α is the thermal expansion coefficient E is the Young's modulus and ν is the Poisson ratio

The equations for the thermo-mechanical effects are solved sequentially by COMSOL with the help of the segregated solver, which solves for temperature first and then performs a stress strain analysis with the computed temperature fields out of the heat transfer equation.

3.1.2.3 Results

Due to the high computation time needed to calculate the whole structure a size reduction based on the symmetry of the structure was performed. Therefore a symmetry surface in the xz-plane was introduced which decreases the number of elements by half and thus reduces the calculation time significantly. At the end of the calculation the results are mirrored along the symmetry surface to rebuild the whole structure again. Test calculations didn't show any difference between the full and the divided structure.

Single-pulse experiments will not be investigated because the influence on the whole cantilever system is negligible due to the small amount of energy of a single pulse. The major impact of a single pulse experiment is obvious in the calculations dealing with the tip expansion only. The following calculation will describe multi-pulse experiments and their influence on the whole cantilever system.

As the typical reaction time of the feedback loop in SPM system is $\geq$0.1 ms the simulation does not exceed this time scale, because the interest is focused on changes which happens on a shorter time scale than the feedback loop.

Several temperatures were calculated and the displacement behaviour in z-direction, which influences the tip-sample gap and the displacement in x-direction, which defines the expansion along the cantilever and therefore decreases the position accuracy are evaluated. The investigated temperature range was chosen within the most common values in literature. A typical temperature development with time of the lowest 4 µm of the tip, which is the area, where the laser energy is absorbed, is shown in Fig. 3.20. The small deviation at the steep heating gradient of the theoretical expected temperature profile is due to the smoothing of the

rectangular heating function, which was necessary to prohibit temperature oscillations due to a discontinuity at the edges.
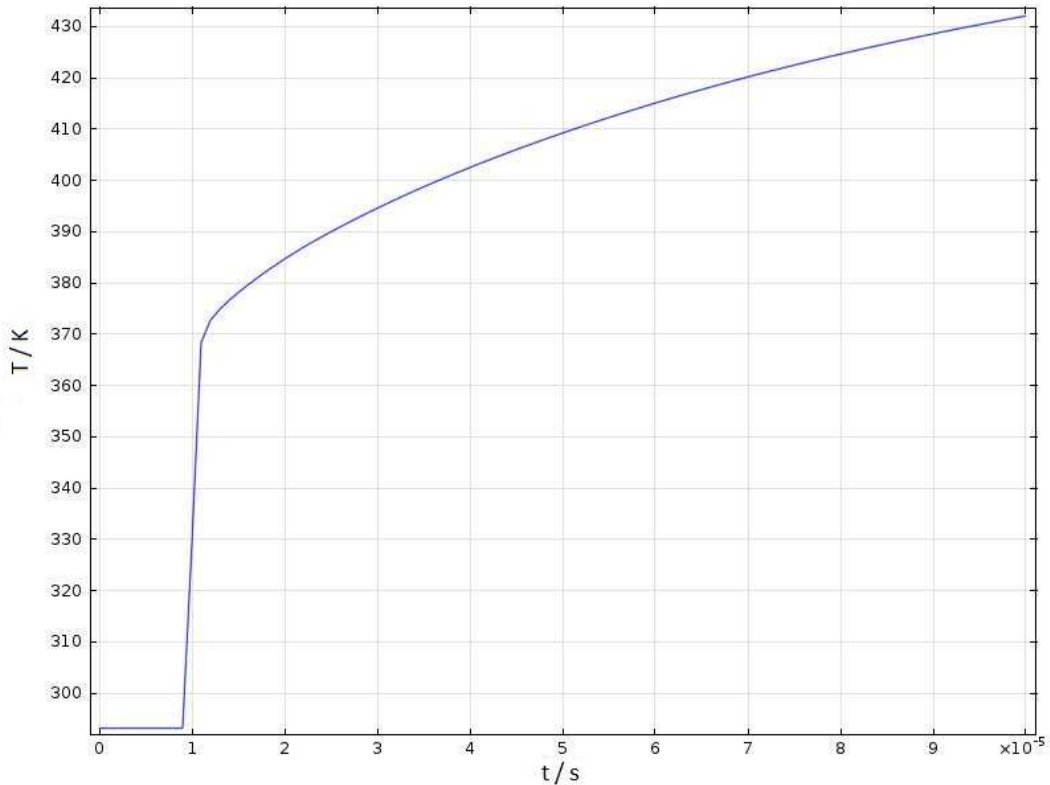

Fig. 3.20: Typical temperature profile extracted from the heated end of the SPM tip. The time scale is 0.1 ms which is the reaction time of common feedback loop systems. The small deviation at the steep heating gradient of the theoretical expected temperature profile is due to the smoothing of the rectangular heating function.

Based on this temperature profile the temperature distribution along the whole system and the displacement values in x, y and z directions were calculated. The simulation time is 1e-4 s with a time stepping of 1e-6 s. The heating is conducted from 1e-5 s until 1e-4, which is the typical reaction time of common feedback loop systems.

In Fig. 3.21 (left) the 3D view of the temperature distribution and the displacement along the cantilever is shown. On the time scale of 1e-4 s the heating of the cantilever is dominant and no pronounced heating of the cantilever holder is visible, although a detailed evaluation of the time dependent heat transfer shows that after 1e-5 s the heat flux already reaches the holder.

In most calculations the holder is regarded as perfect sink, which is true in a first approximation but calculations of the whole system compared to the cantilever with an open boundary, instead of the holder, showed that there is a deviation of several degrees in the absolute temperature (Fig. 3.21, right), which is based on the finite heat conduction from the

cantilever to the holder. To illustrate this effect the temperature colour range was decreased to emphasise the temperature gradient at the contact point between cantilever and holder.
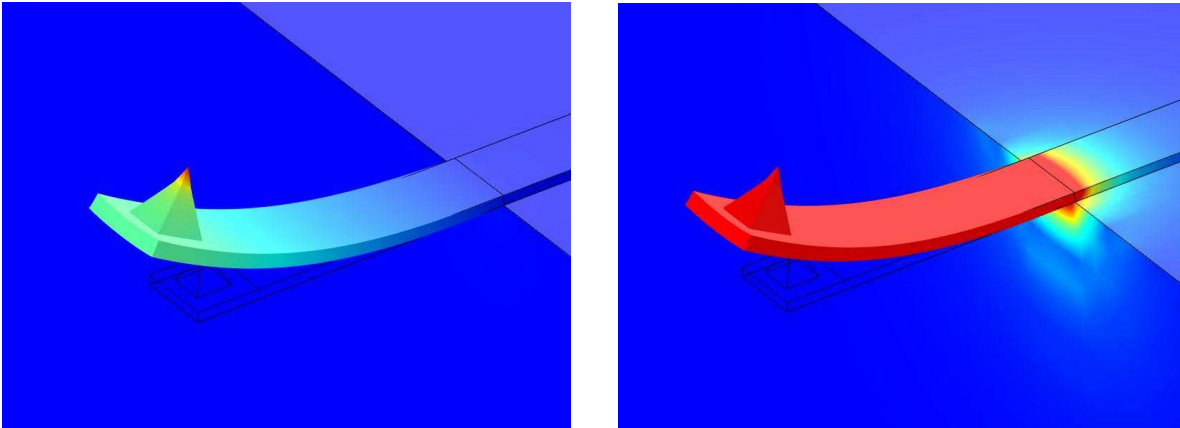

Fig. 3.21: Temperature profile and displacement of the heated cantilever. The displacement field is magnified 1000 times for better illustration. The maximum temperature is 432 K. The black contours of the cantilever indicate the original position. On the right figure the temperature colour range is decreased to show the temperature gradient at the transition between the cantilever and the holder.

The displacement in x and z direction is clearly visible in Fig. 3.22, where the model is aligned along the xz-plane. Especially the bending of the cantilever due to the different thermal expansion coefficients of the two materials is obvious. On a timescale faster than the feedback loop the cantilever bending in z-direction at moderate temperatures (~430 K) is 33 nm, which overshoots typical tip sample gaps by an order of magnitude.
The thermal expansion in x-direction is hard to evaluate exactly due to the bending but clearly exceeds 10 nm, which is in the range of the spatial resolution claimed for an apertureless scanning near-field microscope.

As there are also cantilevers available, which do not use reflective coatings on the backside their bending behaviour was also studied. In Fig. 3.23 the thermal expansion of a non coated cantilever is demonstrated. There is no bending visible due to the homogeneous thermal expansion. Nevertheless the thermal expansion is still around 6 nm for 430 K, which is higher than the tip to sample gap and therefore enough to generate contact between tip and sample.
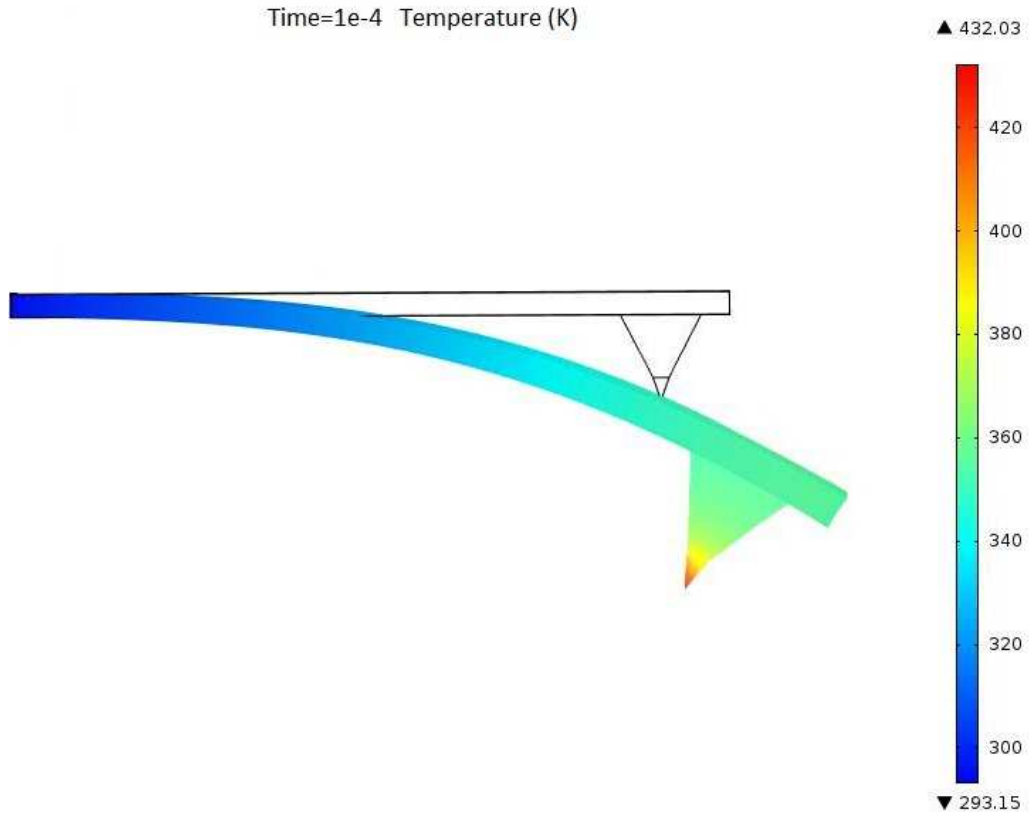The expansion of nearly 15 nm in x-direction is similar to the value calculated for the coated cantilever.

Fig. 3.22: A bimetallic cantilever after laser heating for 9e-5 s. The bending in z-direction is 33nm and therefore more than one order of magnitude higher than the desired tip to sample gap in aSNOM experiments. The black contour lines indicate the original position of the tip before the heating. (Displacement x 1000)

Several calculations were conducted at different temperatures and the results are plotted in Fig. 3.24 for the z-displacement and in Fig. 3.25 for the x-displacement. The values for the displacement were taken at their maximum, which corresponds to a heating time of 9e-5s and is therefore still below the feedback loop reaction time. So every change in the tip position at this timescale will not be compensated by the feedback loop.
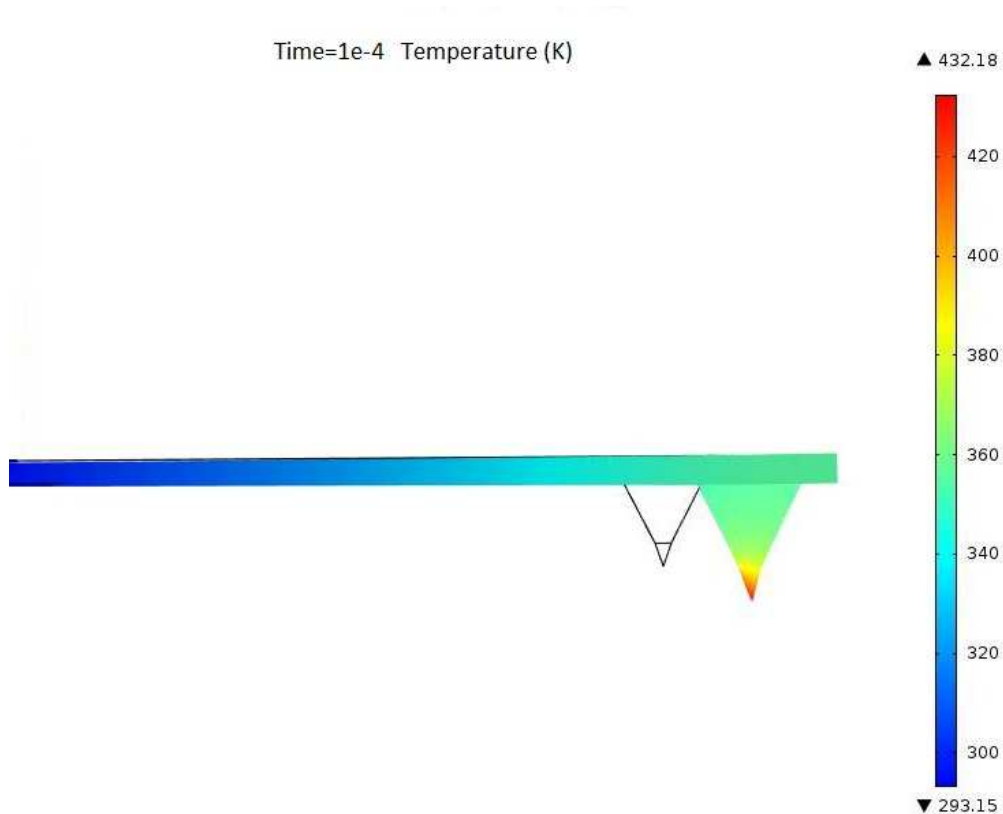
Fig. 3.23: Thermo-mechanical behaviour of a laser heated cantilever without reflective coating. There is no bending visible in z-direction due to the absence of a second material. Nevertheless the thermal expansion is big enough to reach ~6 nm and therefore higher than an aSNOM tip to sample surface distance. (Displacement x 1000)

The scattered line in Fig. 3.24 is situated at 2 nm and is defined as the maximum expansion possible without contact between tip and sample. It is obvious that at very low temperatures this critical value is reached.

The simulated data was fitted by a linear fit, which is reasonable because of the solid mechanics model chosen for this calculation and the intersection points for the coated and uncoated cantilever z-displacement with the critical line were calculated. As the slope of the coated cantilever is steeper it is clear that it will reach the critical line at lower temperatures. Based on the fitted line the intersection temperature for the coated cantilever is 301 K and for the uncoated cantilever it is 337 K. Although the value of the uncoated cantilever is a little bit higher the absolute temperature is still very small.

For the coated cantilever the displacement in z-direction is ~ 2.5 nm per 10 K and for the uncoated one it is only one-fifth, which is 0.5 nm per 10 K.

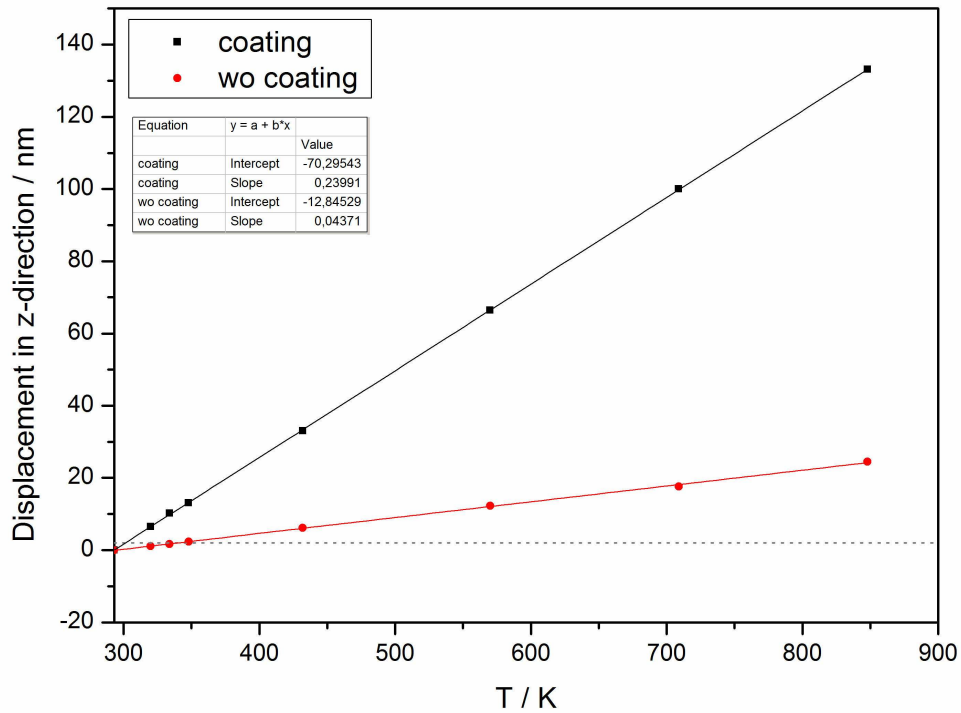| Equation	y = a + b*x	
		Value
coating	Intercept	-70,29543
coating	Slope	0,23991
wo coating	Intercept	-12,84529
wo coating	Slope	0,04371

Fig. 3.24: The z displacement of a coated and uncoated cantilever against the temperature is shown. The scattered line describes the critical value which defines the maximum displacement possible (2 nm) without a contact between the tip and the sample. Based on the intersection points moderate temperature is sufficient to generate contact.

The displacement in x-direction is evaluated in Fig. 3.25. The differences between the coated and uncoated cantilever rely mainly on the bending of the second one. Due to the curvature of the cantilever the shift in x-direction is underestimated. The thermal expansion of the uncoated cantilever is approximately 1 nm per 10 K.

The displacement in x-direction can become a crucial point where high position accuracy is needed. The value of 1 nm/10K can lead to a shift of several tens of nanometres from the desired position at typical surface modification working conditions, which can decrease the applicability in e.g. high density data storage.

Equation	y = a + b*x	
		Value
coating	Intercept	-8,42886
coating	Slope	0,02881
wo coating	Intercept	-30,45212
wo coating	Slope	0,10397
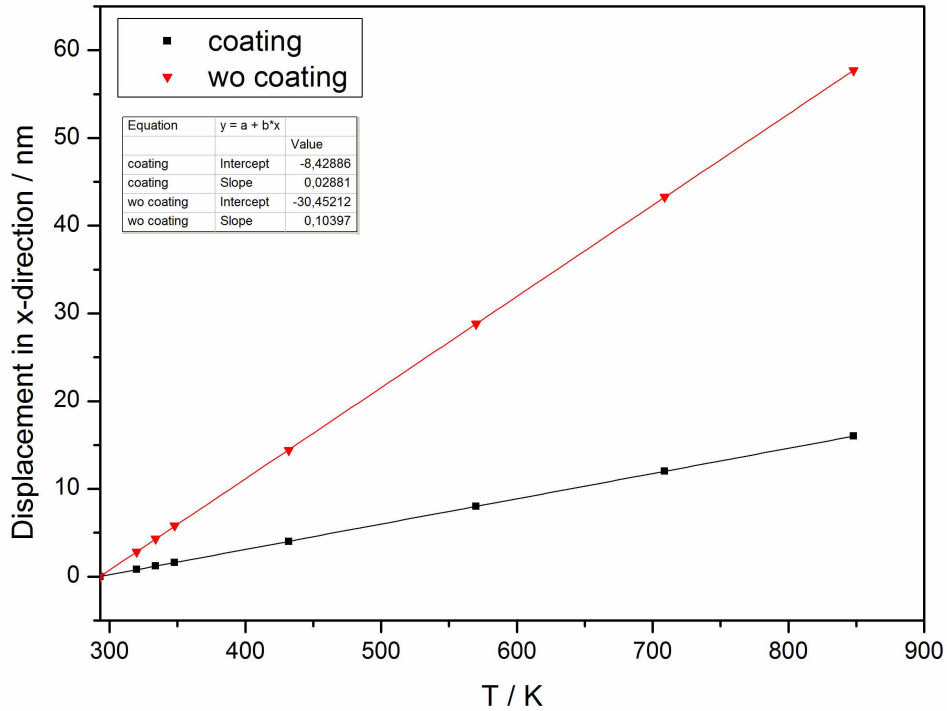
Fig. 3.25: Displacement in x-direction of a coated and an uncoated cantilever. The difference between these two is due to the bending of the cantilever. This additional curvature diminishes the absolute x-displacement value although the expansion is the same.

To proof this effect experimentally a SPM tip was scanned over a soft surface in constant height mode. The sample chosen was a standard photoresist (AZ4620) spin coated on a glass plate.

The position of the tip is constant and the sample is scanned in parallel lines. The distance between tip and sample is set that there is no contact without laser illumination. The laser beam hits the tip in side illumination geometry. When the laser is turned on modifications due to the heated tip are visible. (Fig.3.26, upper line) When the laser energy is increased within a line scan the whole system expands and the resulting surface structure nicely represents the temperature increase of the cantilever. (Fig.3.26, curved line)
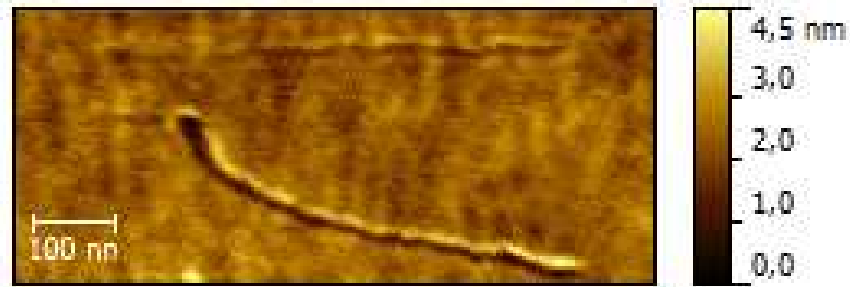
Fig. 3.26: Surface modification in constant height mode. No modification is visible without laser illumination. When the laser is turned on a shallow cavity appears (upper line). When the laser energy is increased during a line scan the cavity becomes more pronounced and the displacement in x direction due to thermal expansion is visible.

The heating of the cantilever due to laser illumination can influence the performance of experiments drastically. Due to the fact that it can not be avoided experiments have to the planned with care. It has already been shown that single shot experiments are difficult to realize because the local heat at the tip itself is high enough for tip expansion in the nanometre regime, which can lead to a tip crash. Beside that the conducted investigations in this work show that also low energy laser experiments with high repetition rates, which generate low tip temperatures, can produce enough heat within the cantilever to displace it in the tens of nanometre regime. Especially cantilevers with reflective coatings on the backside, which are very common in SPMs can be bended at very low temperatures due to the bimetallic effect, which is based on the different thermal expansion coefficients.

The only way to minimize the thermo-mechanical influence on the experiments is the thermal equilibrium. Thus the tip must be illuminated prior to the experiments and solely after the thermal equilibrium is reached experiments can be performed reliably.

It was also discussed that convective cooling in water can overcome the heating problem but calculations show that the influence of free convective cooling, which is the only way possible for SPM measurements, is negligible because the convective heat transfer coefficient is only 4 times higher in water than in air and therefore still very small. (5-25 W/m²K in air, 20-100 W/m²K in water)[276]

It is also very important to keep in mind that the calculations in this work have been performed for only one cantilever geometry. Especially cantilevers used for contact measurements, which are also used in literature for aSNOM, are several times longer and thinner than the calculated cantilever and therefore the thermo-mechanical influence in such a system is even higher.

3.2 Experimental results

3.2.1 Alignment

Most of the work in literature relies on the alignment quality reached by a CCD camera situated on top of the SPM system, but unfortunately this method is pretty coarse and not sufficient to determine the exact fluence at the position of the tip.

Especially for high numerical apertures the focal depth can be only few tens of micrometre and therefore the minimal focus area is hard to align without auxiliary tools. Three possibilities will be discussed in the following.

Cutting edge

The first step in determining the fluence is to measure the focal spot size. Therefore a cutting edge setup can be used, where a sharp razor blade is mounted on a high precision translation stage in front of a photodiode. (Fig. 3.27)
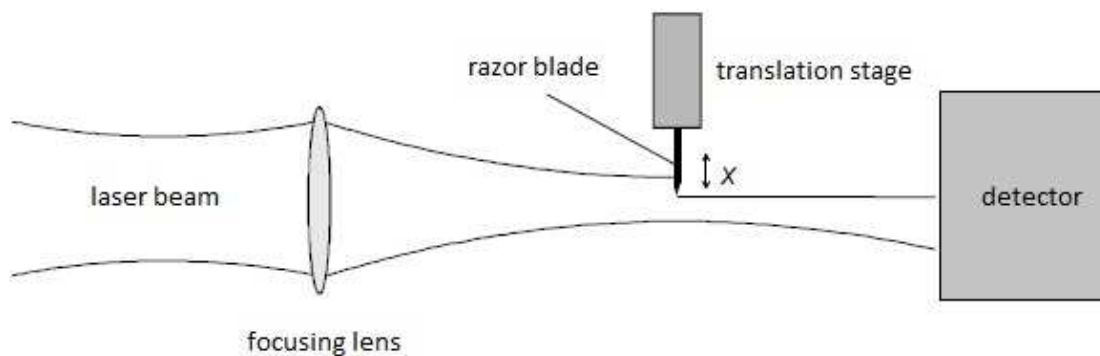
Fig. 3.27: Schematic picture of a cutting edge setup used to determine the spot size of the laser beam at its focal position.

The razor blade is scanned through the laser beam and the intensities and positions are recorded. The resulting sigmoid curve (Fig. 3.28)
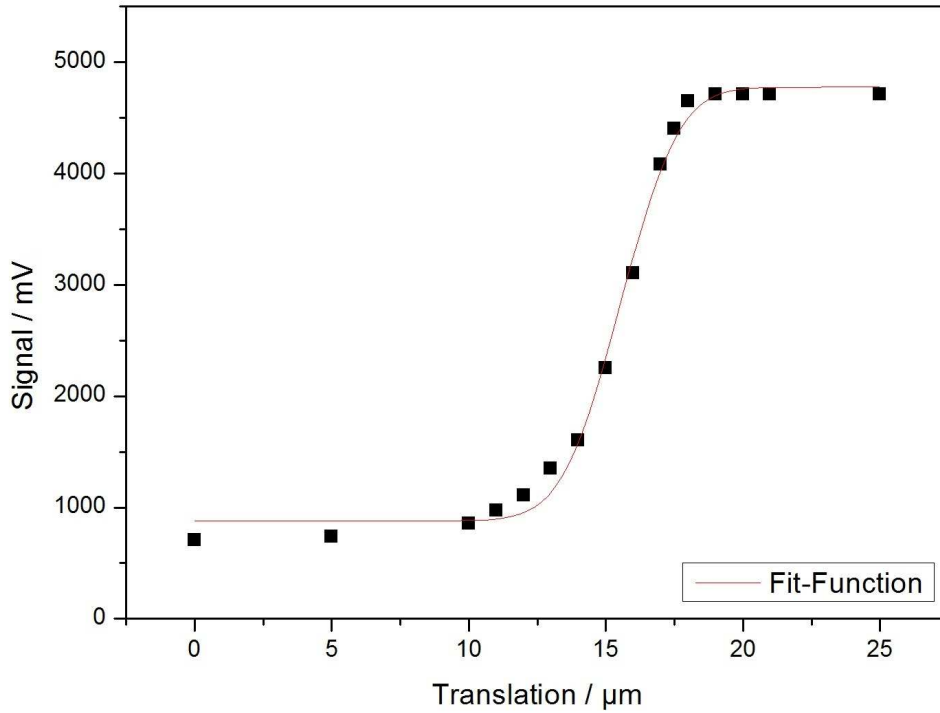
Fig. 3.28: Typical intensity profile of the transmission energy during a cutting edge measurement. The calculated beam diameter of this fit function is slightly below 7.5 µm.

is fitted with the integral form of the following equation

$$E_T(x) = E_0 \sqrt{\frac{\pi}{2}} w_0 \int_x^{\infty} \exp\left[-2\left(\frac{x}{w_0}\right)^2\right] dx \qquad \text{(Eq. 35)}$$

where E is the transmission energy, x is the position value and w_0 is the Gaussian beam radius. The maximum fluence, F_{max} and average fluence, F_{avg} can be calculated according to:

$$F_{max} = \frac{2E_0}{w_0^2 \pi} \qquad\qquad F_{avg} = \frac{E_0}{w_0^2 \pi} \qquad \text{(Eq. 36)}$$

The resulting diameter measured with the cutting edge method was 7.5 µm with an uncertainty of approx. 10%, which is the accuracy limit of this method.[231] Thus the laser spot is small enough to guarantee the illumination of the tip without hitting the cantilever, which is not the case for most other setups described in literature.[53, 139]

To place the maximum fluence on the end of the SPM tip three approaches have been developed and evaluated.

3.2.1.1 The shade of the tip

The general idea of this alignment method is schematically illustrated in Fig. 3.29. The focused laser beam hits the SPM tip and depending on the position of the focal point the

amount of laser light shaded by the tip differs and should reach its maximum when the tip is within the focal depth of the used lens system.

If a screen is placed in prolongation of the incoming laser light the coarse alignment can be done, because based on the relative position of the focal point to the illuminated tip the position of the shadow on the screen is turned by 180°.

Fig. 3.29: Image of the tip shadow on the screen due to the different focal position relative to the tip. On the left picture the focal point is in front of the tip whereas on the right side it is behind the tip.

The accuracy of this method is limited by the aberrations due to the focusing process. So the higher the quality of the beam shape is the higher is the achievable resolution in the direction of the focal depth.

Typical alignment accuracy with this method at the Viennese setup was in the range of several tens of micrometers, which is within the calculated Rayleigh length (~60µm) for the used lens setup.

For more accurate results the screen was exchanged with a photodiode, where the local minimum should be found by an iterative approach. Due to the aberrations near the focal point this method could not be successfully applied.

Nevertheless the method of laser shading is a fast, simple, and very effective possibility to align a laser on a SPM tip.

3.2.1.2 Magnitude vs. Height curves

The basic concept for this approach has already been discussed in Chapter 1, where the temperature dependency of the cantilever force constant, k was mentioned. This temperature dependency leads to a shift in the resonance frequency and therefore to a reduction of the oscillation amplitude of the cantilever if the operating SPM system is based on the amplitude modulation feedback loop.

To probe this effect a point spectroscopic approach was chosen. Therefore an array of spatially distributed points covers the area of interest and a magnitude vs. height curve (Fig. 3.30) was measured at each point. The magnitude is defined as the DC signal of the oscillating cantilever, measured in nA, which is proportional to the oscillation amplitude but

incorporates the lock-in gain as well. The height value describes the relative position of the tip related to a random point of origin.

To generate a Mag/Height curve the oscillating tip has to approach a surface while its amplitude is recorded. At the contact point the tip feels repulsive forces for the first time and thus the free amplitude is reduced. This assumption is only valid if the free oscillation amplitude is high enough otherwise the influence of electrostatic forces, attractive Van der Waals interactions, has to be taken into account too.

In Fig. 3.30 (left) a typical Mag/Height curve is shown. The approach starts on the right side of the figure where the amplitude has its maximum value, which is the free oscillation amplitude. When the distance between tip and sample decreases the amplitude also decrease mainly due to repulsive forces beyond the contact point. On the right side of Fig. 3.30 a line scan of numerous Mag/Heigth curves through the laser beam is depicted. It can be demonstrated that the contact point shifts due to the increasing laser energy towards its Gaussian maximum. The higher energy leads to stronger tip heating and therefore causes two effects which are counter active. The first is the thermal expansion and the second is the reduced oscillation amplitude due to the resonance frequency shift. Based on the measured results the second effect is the dominant one in these experiments.
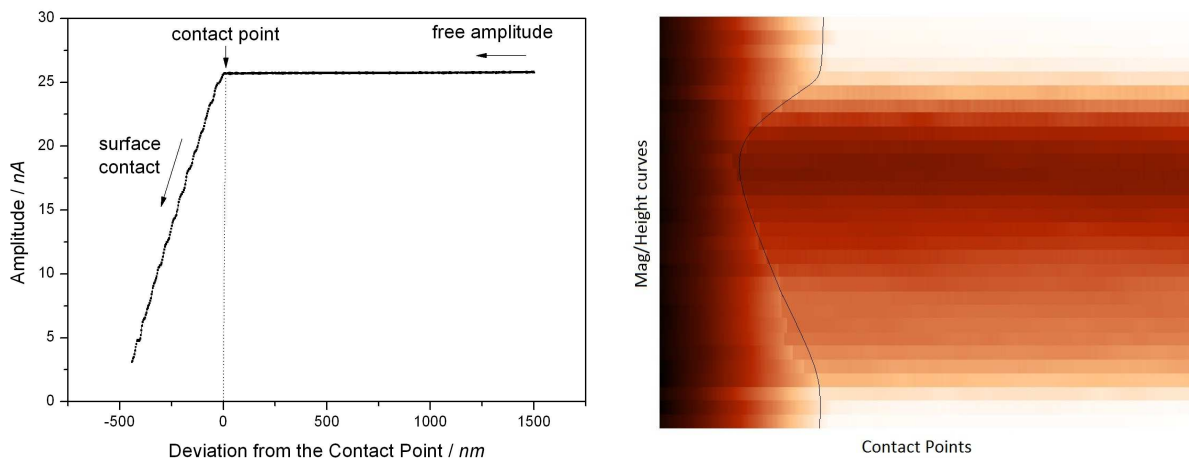
Fig. 3.30: (left) Exemplary Mag/Height curve for determining the focal plane. The amplitude is given in nA, because it is based on the DC signal from the lock-in detected photodiode current. The height is recalculated as deviation from the contact point for illustrative reasons. (right) Line array of Mag/Height curves through the laser beam. The guide for the eye (black line) indicates the position of the different contact points.

To find the focal plane an array of line scans has to be distributed over the surface. In Fig. 3.31 a (10x4) array was built. The spacing in x-direction is 3 µm and 10 µm in y-direction.
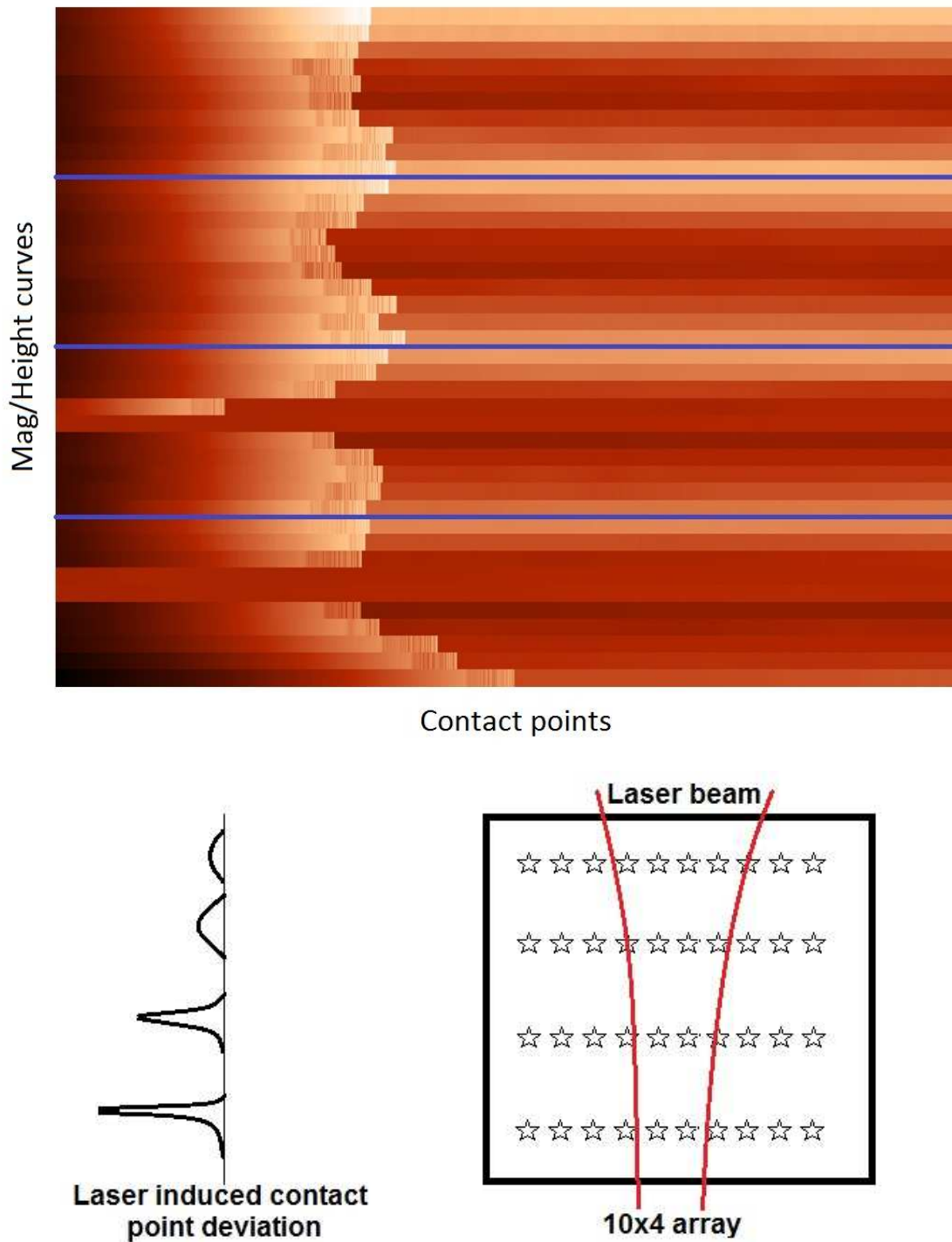
Fig. 3.31: In the upper picture the experimental results of a 2D 10x4 (x,y)-array of Mag/Height curves distributed over the area of laser illumination at 100 mW is shown. Looking from the bottom of the picture upwards the decrease in fluence can be seen. The blue lines indicate the intersection between the different positions along the y-direction (along the focal depth). The lower scheme explains the experimental setup in a schematic way. Each star represents one Mag/Height curve. The deviation of the contact point due to the increase in laser fluence is denoted on the lower left picture.

The y-direction is arranged along the focal depth. In the first two line arrays the laser intensity is too high to receive an evaluable Mag/Height curve. As the fluence decreases when going up in Fig. 3.31 the shift of the contact points also decreases.

In combination with the already measured minimum focal spot size by the cutting edge experiment, this method provides a convenient possibility to locate the focal plane of a laser beam on a surface with a precision of several micrometers.

In Fig. 3.32 two different energies are illustrated. The green line demonstrates the relative contact points at laser energy of 70 mW and is already close to the minimum signal to noise ratio necessary for qualitative evaluation.
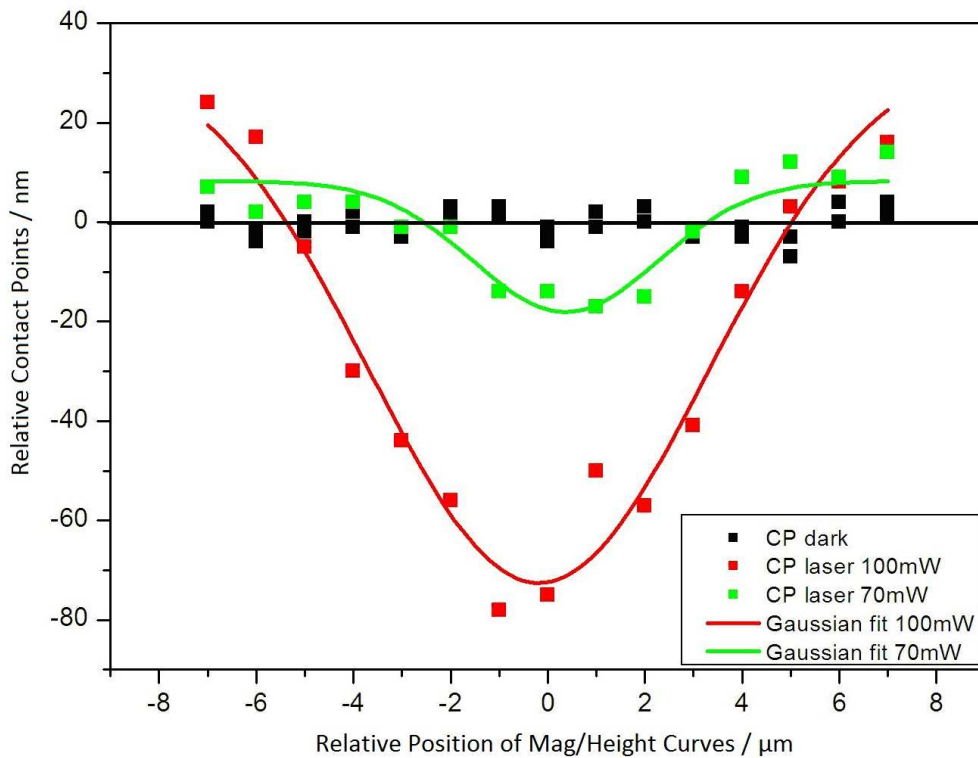
Fig. 3.32: Comparison of different laser energies. The red line was measured with 100 mW and shows a nicely pronounced Gaussian behaviour, whereas the green line (70 mW) is already close to the minimum signal to noise ratio. The black line illustrates the background noise without laser illumination. CP =Contact Point

The major drawback of this method is the high power necessary to see a change in the Mag/Height curves as illustrated in Fig. 3.32. The required values are already close to the damage threshold of the tip. In Fig. 3.33 (left) a typically used tip is shown where no wear is visible. On the right side a tip is depicted, which was illuminated with 120 mW. The destruction of the tip is obvious.
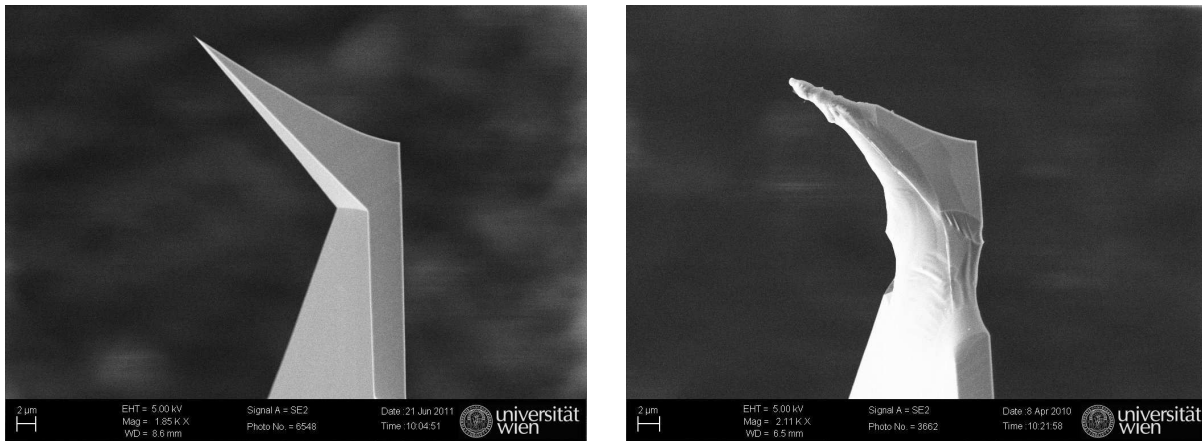
Fig. 3.33: Left side shows an ATEC tip in perfect condition. On the right side the destruction is obvious after illumination with 120 mW laser power.

Although this method is easy to realise the lack of sensitivity constrains its applicability. Besides it is also based on a decrease in the oscillation amplitude due to tip surface contact and therefore a wear of the tip is likely, even for small power values.

3.2.1.3 Backscattered signal

The third approach to determine the fluence at the position of the SPM tip is based on the backscattering setup illustrated in Fig. 2.2. The 800 nm centered, fs laser passes a dichroic mirror (long pass) with a cut-off wavelength of 600 nm to eliminate the fundamental wavelength and the diode laser of the SPM device and focuses on the tip. The backscattered signal is collected with the same lens used for focusing. Light with wavelengths above 600 nm transmits the dichroic mirror. Shorter wavelengths are reflected and guided to the detector.

To align the focal plane the high intensity dependency of the second harmonic light generation is exploited. As the highest energy density is situated in the focal plane the second harmonic light should peak there, as well.

The advantage and disadvantage of the backscattering system is that the same lens is used for excitation and light harvesting. So if the optical beam path is once aligned no readjustment should be necessary if a repositioning of the focal spot is required. The disadvantage of the backscattering system is that the collection efficiency is limited by the numerical aperture of the chosen focusing system which for side illumination setups is often given by geometrical restrictions.

To prealign the backscattering system the second harmonic light is not the best choice because it is very weak. Therefore plasma, formed due to material ablation in the focal plane, was used to perform the coarse alignment of the backscattering system.

The detection of the second harmonic light was based on a lock-in detection to decrease the background signal. Hence a chopper wheel was embedded into the experimental setup and connected with an external lock-in amplifier [eLockIn 204, Anfatec, Oelsnitz, Germany]. Further background reduction was realized by wavelength selection with a monochromator. The incoming light is measured with a Peltier cooled photomultiplier tube (PMT), amplified by the lock-in amplifier and then fed into the SPM to generate a 2D map of the second harmonic light intensity. (Fig. 3.34) To generate this picture the head scanning SPM system was used to move the tip with high spatial precision through the prealigned illuminating fs laser beam.
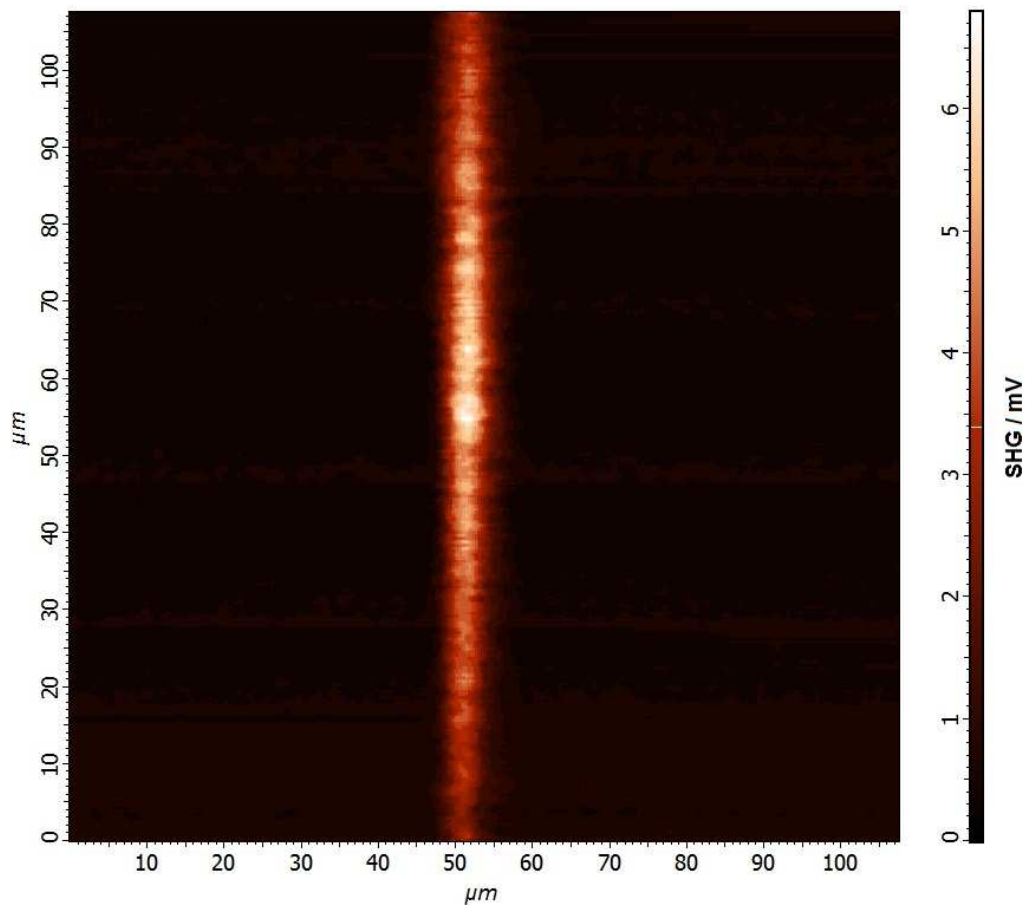
Fig. 3.34: 2D picture of the second harmonic light intensity distribution over the scanned area. The SHG intensity is given in mV It can be seen that in the lower and in the upper part of the picture only the top profile of the Gaussian beam has enough intensity to generate sufficient second harmonic light for detection. In the middle of the picture the measured intensity profile fits well with the measured beam diameter.

The resolution is 256x256 points where each point corresponds to an integrated PMT signal. The intensity profile along the y-direction perfectly fits the expected results. In the middle of the scanned area the intensity profile reflects the beam diameter measured with the cutting edge method perfectly. In the lower and the upper part of the figure only the top of the

Gaussian beam profile exhibits enough energy to generate sufficient SHG signal for detection. In Fig. 3.35 a 3D image was turned in the way that the intensity distribution along the y-direction (focal depth) is obvious. The noise level is < 1 mV, which is small enough for an accurate evaluation.
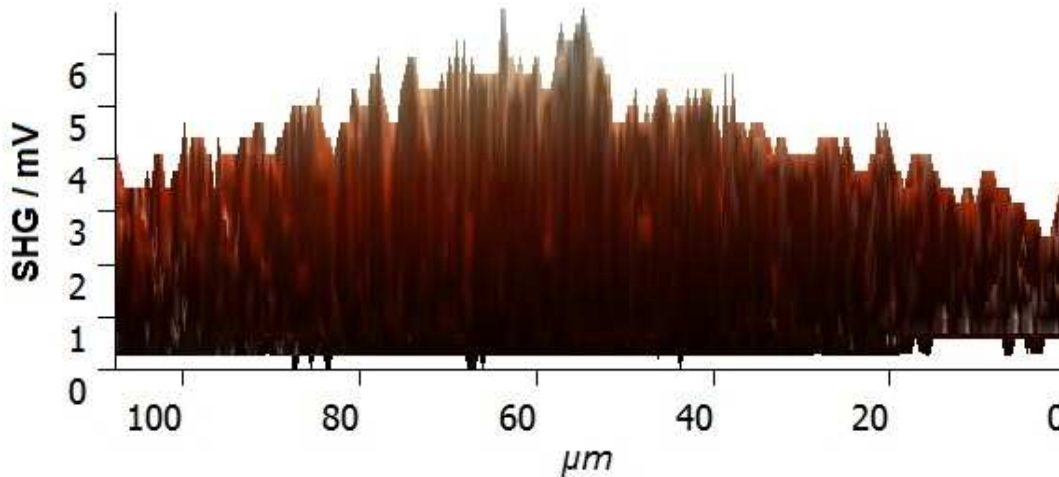

Fig. 3.35: 3D image of the scanned surface aligned along the xz-plane for better visualisation of the second harmonic light distribution along the z-direction (focal depth). The calculated Rayleigh length for the used setup is about 60 μm and can be seen in the figure as well.

The measured signal intensity profile also allows determination of the Rayleigh length which is calculated to be around 60 µm and nicely fits the measured data in Fig. 3.35.

The backscattering approach allows the accurate determination of the distributed laser beam intensity over a monitored surface. Nevertheless the complex alignment of the optical beam path makes it time consuming.

The Mag/Height curve method is easy to realize but needs an iterative energy modulation approach to avoid too high energies which lead to non-evaluable Mag/Height curves. At too low energies the differences in the contact points are no longer distinguishable in a reliable way.

The shade of the tip is the fastest and easiest way of alignment but needs experience in the evaluation of the correct shadow appearance because its behaviour is very dependent on the quality of the focal spot. In the following experiments the shade of the tip was the most common approach to align the laser beam on the tip.

3.2.2 Contact measurement

As already mentioned in this work, (Chap. 3.1.2 and 3.2.1.2) tip heating due to the illuminating laser beam influences the behaviour of the cantilever significantly. Thermal expansion, bimetallic bending or resonance frequency shift can prohibit accurate tip-sample distance control. Therefore the origin of nanometre sized surface modifications generated with laser illuminated sharp tips, like STM or SPM tips is still under discussion in literature.[128, 129, 271]

To investigate the contact behaviour between tip and sample the voltage breakdown was observed. The assembled setup is shown in Fig. 2.4.

To evaluate the home built circuit the semicontact mode, where the tip hits the surface periodically at the cantilever's resonance frequency, was selected. Typical resonance frequencies of the used cantilevers are in the range of 200-350 kHz, which corresponds to a period of 3-5 µs. The theoretical predicted contact time, which is the time within the Van der Waals repulsive forces (3-5 Å), is 1-5 % of the whole period, mainly depending on the oscillation amplitude. So the measured values should switch periodically between the applied voltage (3.95 µs @ 250 kHz) and a value around zero (0.05 µs @ 250 kHz) depending on the resistance of the contact point and the open circuit (which can be regarded as infinitely high in air for our measurements).

To proof this theory the driving voltage of the z-piezo, responsible for the oscillation of the tip, was extracted and a simultaneous measurement of the contact voltage and the driving voltage was performed. In Fig. 3.36 the results are illustrated. The resonance frequency of the tip was around 200 kHz, which can easily be calculated from the period of the driving voltage. The coating of the tip was a 30 nm gold layer and the sample was a mica plate evaporated with ~100 nm of gold. Both metals have been chosen of the same type to avoid contact potential differences due to different work functions.

It can be seen that at one point of each period the contact measurement shows a glitch, which corresponds to the contact happening between tip and surface. Although there was no voltage applied during the experiment in Fig. 3.36 a shift in the absolute potential after some contact events is obvious. This is due to changes in the contact area between tip and sample and therefore differences in the resistivity appear, which determine the charge and discharge behaviour of the investigated system It should be noted that the shift in the absolute zero potential is smaller than 1 mV.
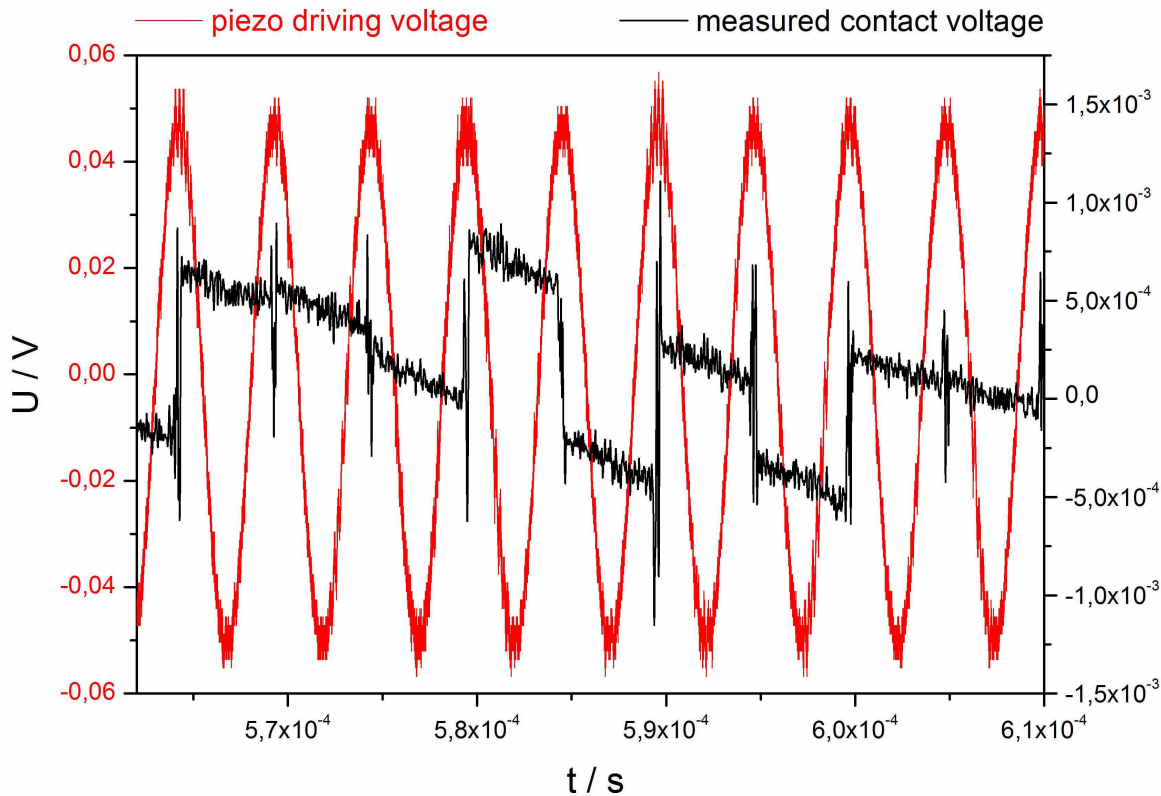
Fig. 3.36: Simultaneous measurement of the driving voltage of the tip and the contact voltage of the tip sample system. The resonance frequency of the tip is approximately 200 kHz. Tip (30 nm) and surface (>100 nm) are covered with a thin gold layer. The connection between the oscillation frequency and the contact happening is obvious. When the driving voltage is at maximum a contact event appears.

The contact point resistance was measured to be approximately 15-20 Ω for gold coated tips on sputtered gold surfaces with a non oscillating tip. This value corresponds to former measurements in literature.[278] The resistance of the cantilever was calculated to be 1 Ω for a 30 nm gold coated system and is already subtracted from the contact resistance.

To use the setup for the determination of a contact event between tip and surface, voltage was applied to increase the differences between contact and non contact situation. It was recommended by the tip manufacturer (NT-MDT) not to exceed a current of 100 nA through the coated tip. The small contact area (~100 nm²) leads to very high current densities, which can easily burn the tip coating because of the Joule effect. Based on the resistivity of our serial resistor the applied voltage must not exceed 50 mV.

In Fig. 3.37 different voltages were applied between tip and surface. Although the slope of the voltage in the non-contact area increases, the maximum value is still far away from the applied one.
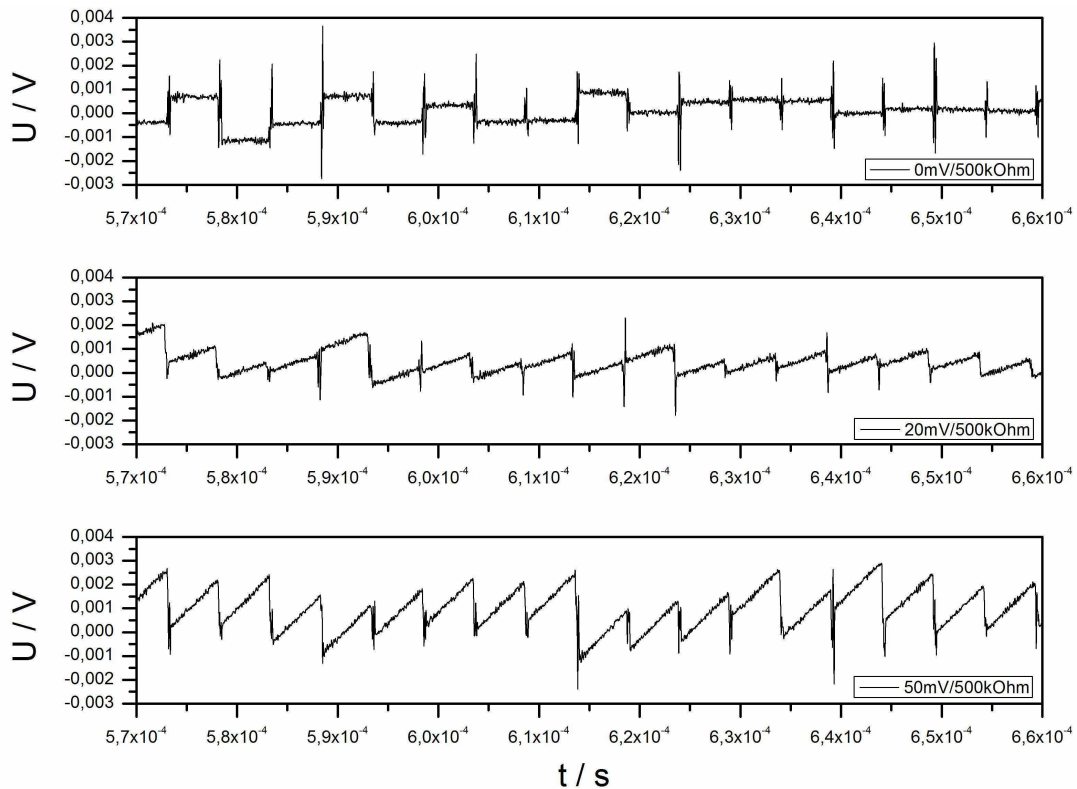
Fig. 3.37: Different voltages between tip and surface. Although the slope of the voltage increases, the maximum value is still more than an order of magnitude smaller than the applied voltage. The time scale was 90 μs.

Due to the high resistivity of the serial resistor the time constant of the system is too high to load the capacitor (the tip/cantilever-sample system in first approximation), within the short period of one oscillation.

To proof this theory a different serial resistor (100 kΩ) was built in the circuit and the slope of the charging curve was evaluated. (Fig. 3.38)

During the investigation of different voltages, it was found that the signal shown in Fig. 3.37 is not always present, indicating the loss of contact in the semicontact mode, which was not expected to be the case with the set of parameters chosen for the experiment.

To verify the idea of contact loss, longer measurement time scales were chosen. In Fig. 3.38 the measuring time was increased from 90 μs up to 3 ms.

The dependency on the changed serial resistor is obvious. The slope of the upper charging curve is approximately 50% higher than from the lower curve with 1 MΩ serial resistance. But more surprising was the observation of the contact behaviour of the tip. In contradiction to the theory of semicontact mode the tip seems to loose contact to the surface for quite a long period.
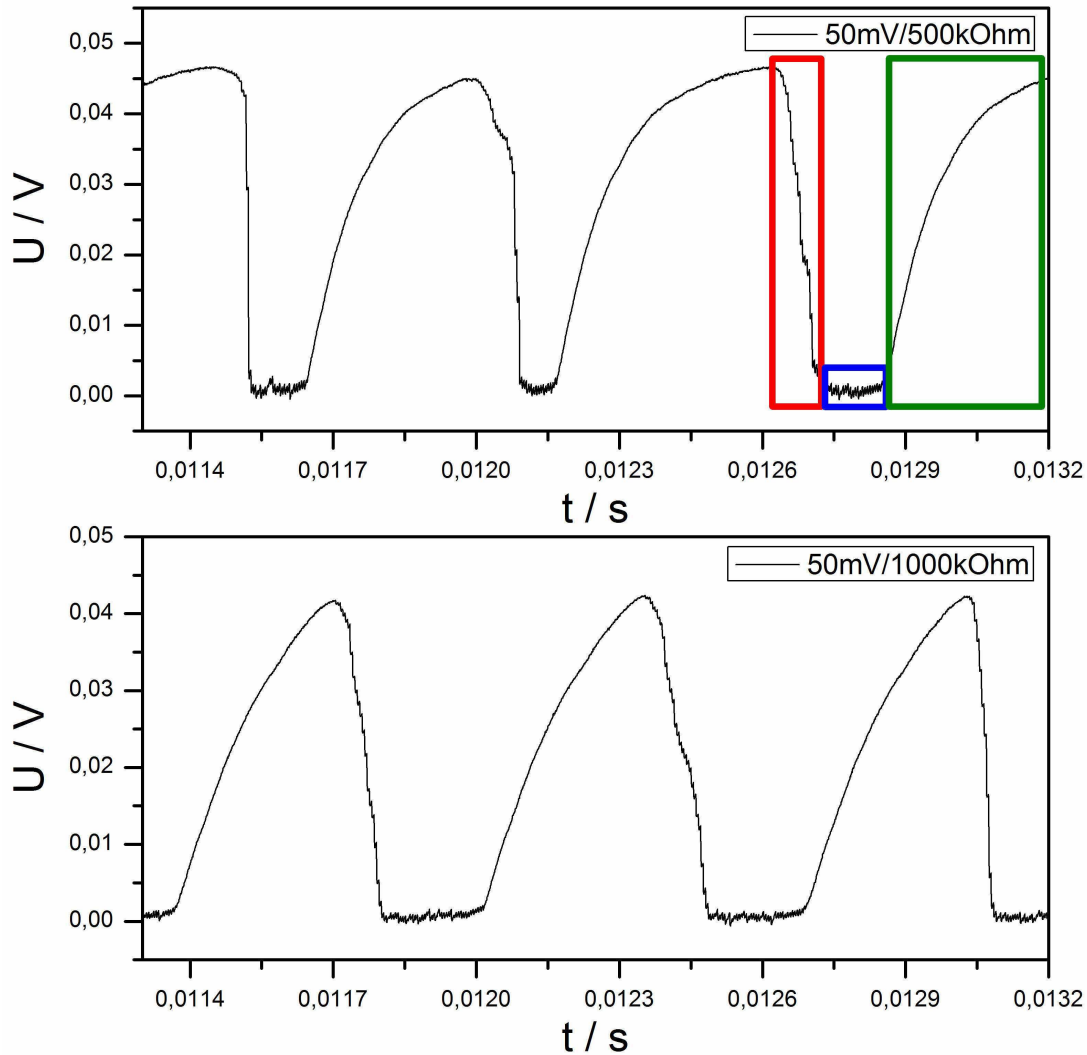
Fig. 3.38: Long time measurement of the contact behaviour between tip and sample. The time scale is 3 ms. Two different serial resistors were chosen to proof the dependency of the charging characteristic. The lower resistance leads to 50 % faster charging. The contact behaviour of the system is in contradiction to the working principle of semicontact mode. The coloured rectangles indicate the areas, which are magnified in Fig. 3.39.

A closer look at the voltage behaviour is done in Fig. 3.39. The red area, describes the moment of contact between tip and sample and the discharging of the capacitor by short cut events. This is obvious because a stepwise modulation of the voltage signal with a constant frequency, corresponding to the resonance frequency, starts.

When the minimum value is reached (blue area) the voltage signal perfectly fits the already measured oscillating signal, whose slope is defined by the voltage and the serial resistor.

The green area describes the simple charging of the capacitor. No electrical contact can be observed.
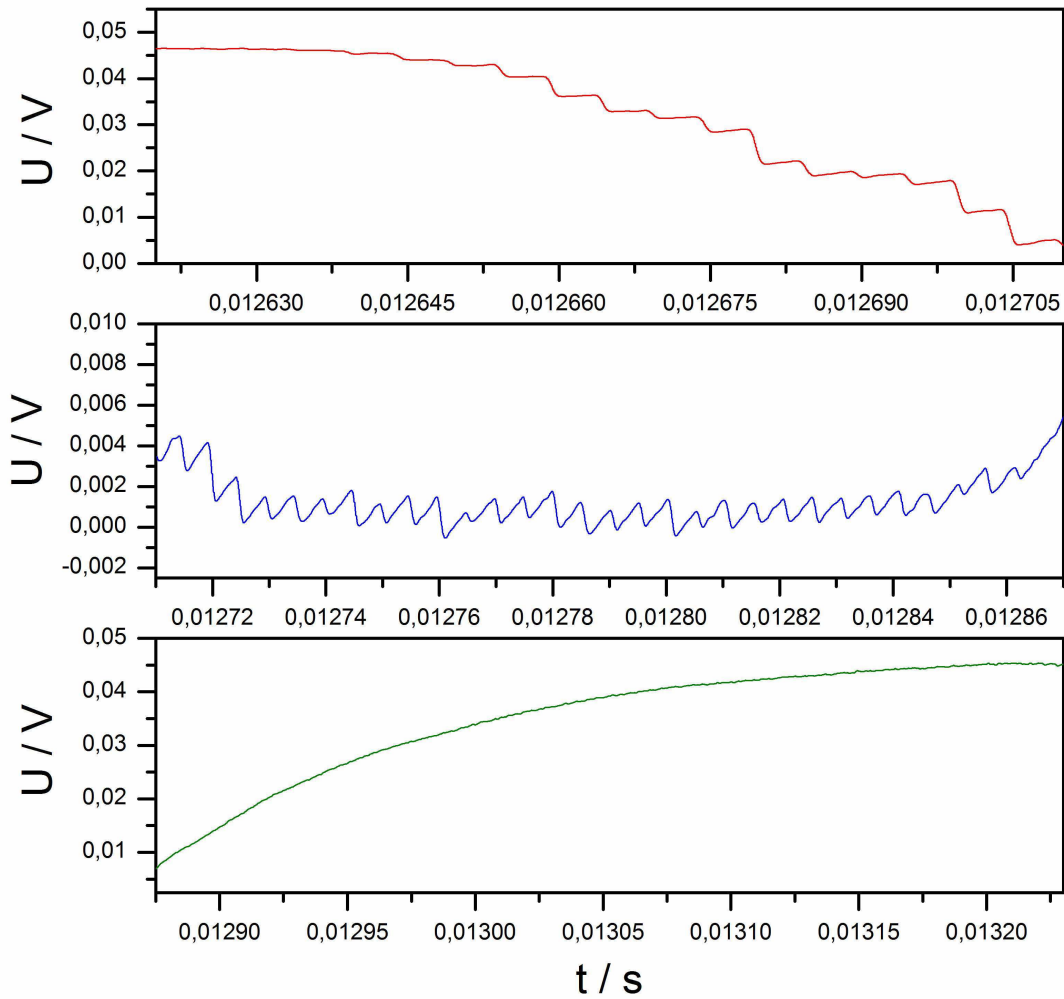
Fig. 3.39: Magnified part of Fig. 3.38. The red line shows the point of contact between tip and sample. This point is indicated by the stepwise modulation of the voltage curve. The blue line corresponds to the already measured oscillating signal after complete discharging of the capacitor. The green line defines the point were no electrical contact exists anymore. This is obvious because the stepwise modulation is lost and the curve shows a realistic charging characteristic.

These experiments were performed at one single point, directly after the landing process. To exclude the effect of tip damage the used SPM tips were examined in the SEM afterwards. The two tips in Fig. 3.40 are both used for contact measurement in ambient atmosphere. The magnification of the undamaged one (left) is nearly 3 times higher (~120.000x) but there is still no modification of the coating visible. Nevertheless the voltage response of this tip is similar to the depicted voltage curves.

The right tip is of the same type but after too high voltage exposition. The gold coating at the very end of the tip was melted and therefore no electrical contact was possible.
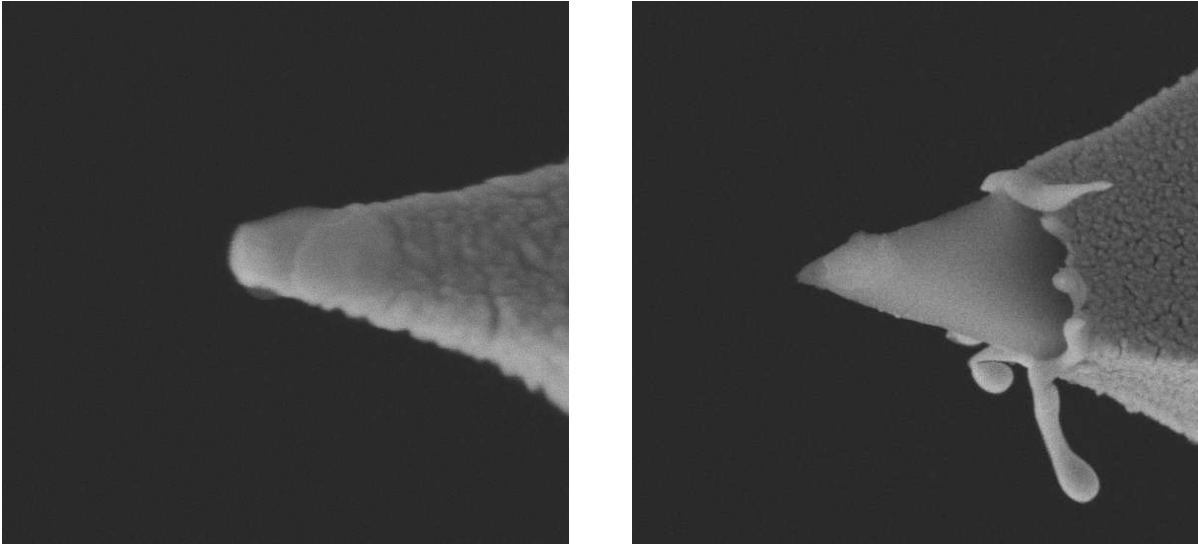
Fig. 3.40: Two different tips after their usage during contact experiments. The SEM picture of the left one is magnified 120.000 x but no modification is visible. The voltage applied at the right tip was 150 mV, already enough to melt the sensitive gold coating. (Mag. 50.000x)

To dispel all doubts further investigations of already used tips in SEM where performed. Therefore the tips were mounted in the way that the electron beam is aligned along the major axis of the tip. So even very small surface damages at the very end of the tips should be visible. As shown in Fig. 3.41 the difference between damaged (right) and undamaged (left) tip is clearly visible. The right tip didn't show a voltage breakdown anymore, whereas the behaviour of the left tip followed the characteristic of Fig. 3.39.
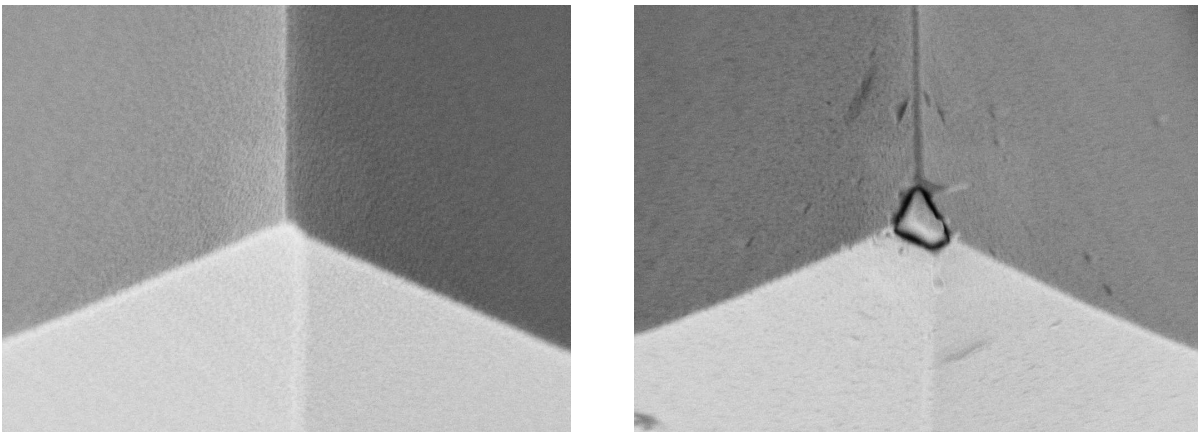
Fig. 3.41: SEM pictures of two tips after a contact experiment. The major axis of the tip is along the electron beam so even minor changes in the quality of the coating should be visible. The differences between damaged and undamaged tips are clearly visible.

Based on the evaluation of the SEM pictures, a degradation of the conductive coating as explanation for the loss of electrical contact can be excluded.

To avoid the influence of surface contaminants, the sample and the tip were prepared directly before the experiment started.

The same experiments were performed under distilled water (18 MΩ) to compensate for effects caused by surface water (capillary forces), present on every surface due to atmospheric humidity.

A similar approach was arranged with an electrolyte instead of distilled water to overcome electrostatic charging, which may accumulate and repel the tip from the surface. But the only difference in the observed contact voltage characteristic to the in air and distilled water experiments was that the resistance of the open circuit could no longer be regarded as infinite and therefore the voltage ratio between open and closed circuit was smaller.

It is well known that potential control of surfaces, especially in liquids is essential, e.g. the wetting character of gold surfaces can easily be tuned by changes in the surface potential. (Lippmann curve)

Depending on the actual potential, a gold surface can show completely different surface properties. At high negative or positive potentials specific ion adsorption may inhibit the electrical contact between tip and gold surface. At even higher positive potentials a reconstruction of the surface in an anodic solid state surface film growth mechanism takes place, where oxygen diffuses into the gold structure through place exchange processes. This effect may also influence the electrical behaviour of the investigated tip sample system.[279-281]

The most promising potential range for reproducible electrical contact measurements is the electrochemical double layer region, where ions are only absorbed unspecifically and can be exchanged easily.

To overcome these uncertainties an electrochemical cell for in-situ SPM measurements was constructed. (Fig. 3.42)

The measuring principle was the three electrode technique. As working electrode an evaporated gold film (>100 nm thickness) on a mica surface was chosen. The reference electrode was a gold wire, bended around the working electrode. The counter electrode was an Ag/AgCl electrode mounted used as Haber Luggin capillary for easier handling.

The electrolyte, 0.05 M H_2SO_4 or 0.1 M Na_2SO_4, was continuously purged with Ar in an external reservoir to expel the oxygen of the solution. The pre-purged electrolyte was pumped into the electrochemical cell. During the measurement the electrolyte was covered by a slight

Ar gas flow. The cell was closed by an elastic plastic cover made of natural rubber, which was mounted around the SPM scanning head to inhibit the diffusion of oxygen.
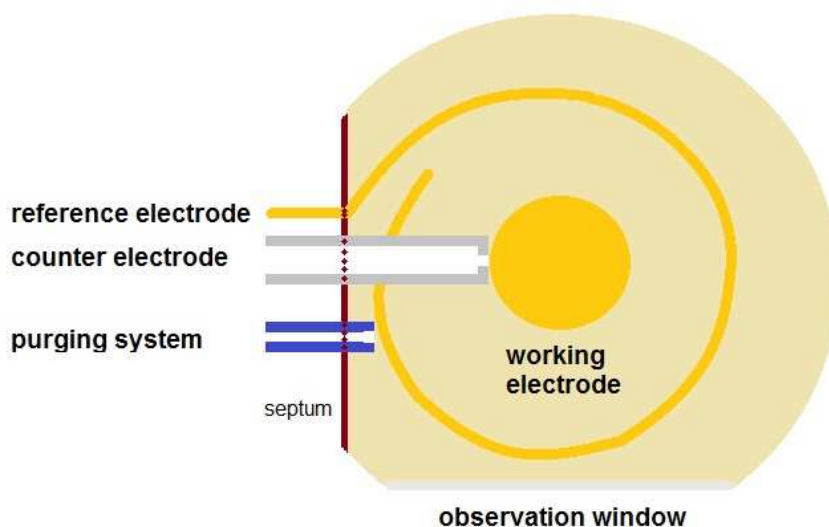

Fig. 3.42: Top view of the constructed electrochemical cell for in-situ SPM measurements. The cell was built of PEEK, because of its chemical stability. The working electrode and the counter electrode were made of gold. The reference electrode was Ag/AgCl mounted in a Haber Luggin capillary. The system was purged with electrolyte and purging gas through the same inlet. The electrolyte was 0.05 M H_2SO_4 and 0.1 M Na_2SO_4, respectively.

The electrolyte was purged at least 20 minutes in the external reservoir before it was pumped through the purge system by the purging gas itself.

The freshly prepared working electrode was cleaned electrochemically by repeatedly changing the applied voltage periodically within the potential range, where oxygen and hydrogen production starts.

To determine the double layer region the potential range was decrease to increase the resolution and so the optimum potential for the electrical contact measurement could be defined.

The voltage behaviour of the subsequently preformed contact measurements was identically to former measurements performed without electrochemical control in an electrolyte.

To investigate the contact behaviour between tip and surface an electrical contact measurement approach was chosen. While short term measurements in the semicontact mode indicated the limitation of the setup because of the high time constant, necessary to avoid tip burning long term measurements showed an unexpected contact loss in the semicontact mode.

Although a broad range of influencing factors could be excluded due to sophisticated experimental setups, like the electrochemical surface potential control the reason for the contact loss is still under discussion.

Further experiments like more accurate potential supply to reduce the applied voltage down to 1-2 mV, to decrease the time constant by decreasing the serial resistor or current measurements instead of voltage measurements may give further useful hints for a full understanding of the contact behaviour between tip and surface.

3.2.3 Surface Modification

A possible application of apertureless near-field microscopy is the use of the localised field to modify different surfaces far beyond the diffraction limit of light to further increase the storage capacity of commercial data storage devices. To proof this idea, different surfaces were chosen [gold, polyphenylene oxide (PPO), polycarbonate (PC), phototresist AZ4620] and modifications were conducted at various experimental parameters.

Viennese setup

At the Department of Physical Chemistry, Vienna two different scanning modes were available, the semicontact mode and the contact mode. In addition a Pockels cell provides the possibility to reduce the inherent repetition rate of the used fs laser from 11 MHz down to single pulse experiments.

As already discussed in Ch. 3.1., the angle of incidence is an important parameter concerning the field enhancement at the end of the tip. Unfortunately geometrical limitations of the scanning head limit the maximum angle of incidence reachable to 1.5°, thus moderate enhancement is expected. Furthermore the simulations predicted higher field enhancement for sharp silicon tips at low angles of incidence than for the relatively dull gold tips, due to the thickness of the gold coating. Therefore sharp silicon tips turned out to be the reasonable choice for experiments based on the setup at the Department of Physical Chemistry, Vienna.

Gold coated tips were tested as well but no modifications could be achieved. This may be due to the strong geometrical restrictions for high enhancement when dealing with surface plasmons (Fig. 3.4). Additionally the stability of the gold coating is moderate and even soft contact can modify the appearance and therefore the resonance conditions.

Prior to the experiments the surface area, planned for modification was scanned to guarantee a flat surface and to exclude areas with already existing surface features. Then the tip was positioned, illuminated and afterwards the surface was investigated with the same tip, used for modification.

The observed surface structures were measured and schematically illustrated in Fig. 3.43, 3.44 and 3.45 for better visualisation.

In Fig. 3.43 the tip was kept in semicontact mode to the surface and laser illumination was done with a repetition rate of 11 MHz for 1 second controlled by a manual shutter. The contact time at a resonance frequency of 350 kHz was estimated to be ca. 100 ns. On average this corresponds to one pulse for each contact event and therefore to an illumination with N = 3.5 x 10^5 pulses.

The resulting structures at two different surfaces, a thin gold film (25 nm) and a spin coated polymer (PPO), whose thickness exceeded 1 µm and can therefore be regarded as infinite in terms of near-field dimensions, are shown. The produced surface cavities showed a shallow shape with diameters in the range of the used tip diameter and depths below 2 nm. The calculated depth to width ratio was between 0.02-0.06.
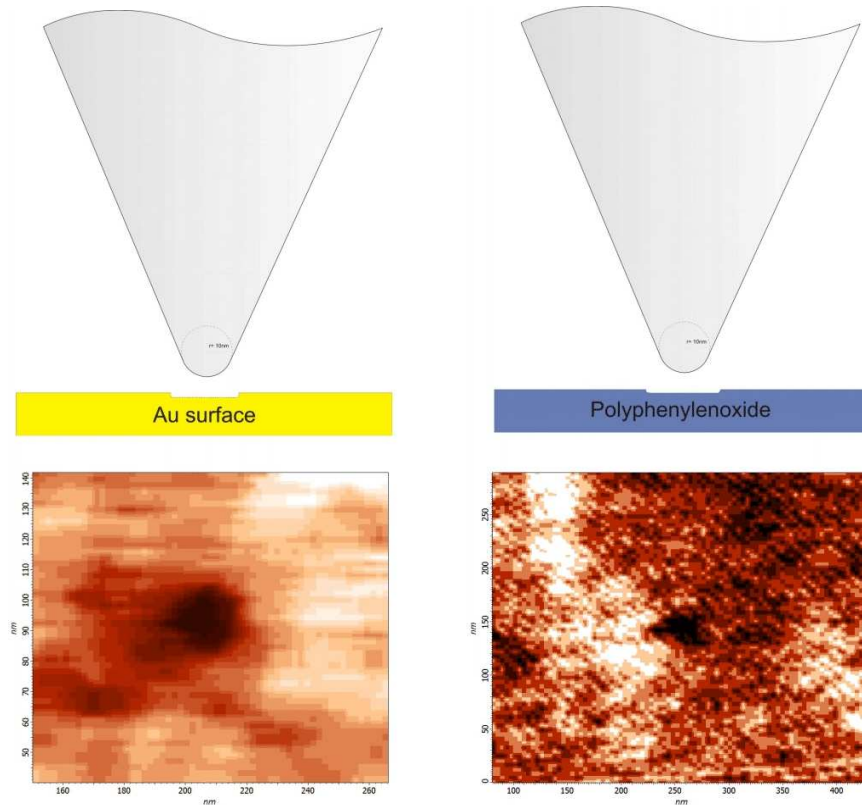

Fig. 3.43: Surface modifications in the tapping mode with a laser repetition rate of 11 MHz. Depth to width ratio is 0.02-0.06 for gold and polyphenylene oxide samples.

When changing from semicontact mode to the contact mode, which means that instead of short contact times the tip stayed in contact with the surface during the whole illumination period, which was again 1 second, the observed surface structures became more pronounced (Fig. 3.44). Especially for the polymer the calculated depth to width ratio increased for more than one order of magnitude to 0.46.

In addition the shape of the polymer holes changed significantly because the sharp edges of the structures vanished and displacement of material takes place, which indicate thermal induced modification mechanism based on melting.

The gold surface didn't show comparable surface structures although minor asymmetric material displacement can be observed, as well. The difference can be explained by the inequality in surface tension of gold and polyphenylene oxide. The depth to width ratio for the

gold surface was 0.16 and therefore still three times higher than for the semicontact modifications.
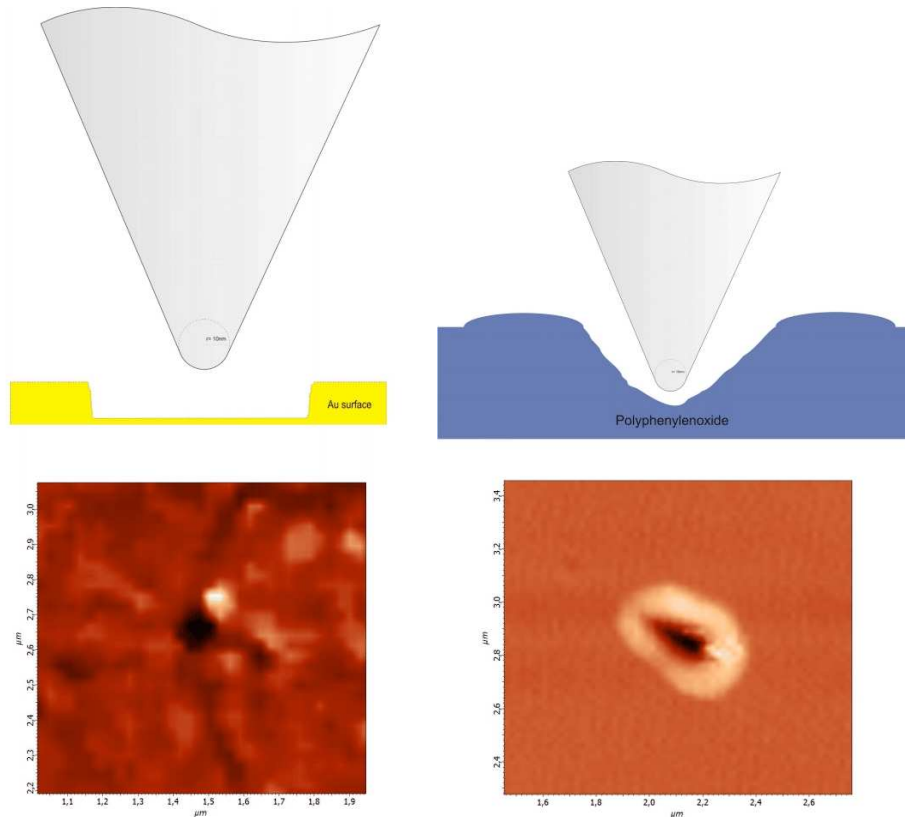

Fig. 3.44: Contact mode modification of gold and polyphenylene oxide surfaces with a laser repetition rate of 11MHz. The observed surface structures show more pronounced features; especially the polymer surface indicates a thermal modification mechanism because of material displacement on the rim of the hole.

Due to the high repetition rate of the used oscillator, laser illumination with the full repetition rate can be regarded as cw (continuous wave) illumination in terms of surface heating and therefore heat accumulation can be observed.

To overcome this influence the repetition rate was reduced to 1 kHz which is small enough to exclude heat accumulation effects because the time between each pulse is sufficiently long to allow the introduced heat to distribute over the system. (Ch.3.1.2)

In Fig. 3.45 the tip was again in permanent contact with the surface but the repetition rate was reduced to 1 kHz. The reduced thermal effect is obvious in the produced structures. No displaced material at the rims of the cavities could be found. The calculated depth to width ratio is similar to the semicontact mode, 11 MHz experiments, where the heat effect is also reduced due to the short contact time.
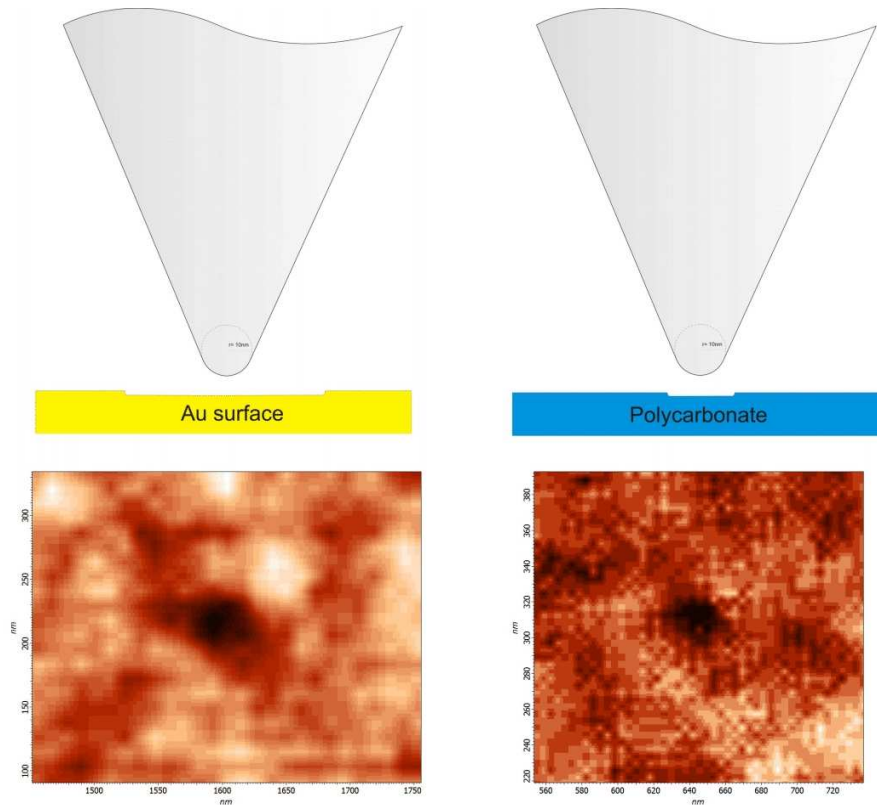
Fig. 3.45: Contact mode modification of gold a polycarbonate surfaces at a repetition rate of 1 kHz, realised by a Pockels cell. The produced holes show decreased thermal influences (depth to width ratio is 0.03) due to the reduced repetition rate.

In Tab. 2 the measured values of the depicted figures are shown. It is obvious that the thermal influence is strongest, when the tip is in permanent contact and laser illumination is done at high repetition rates. Under these conditions the depth to width ratio reaches its highest values.

Material	Technique	Frequency	Pulse No.	Width / nm	Depth / nm	Aspect Ratio
Au	Tapping	11 MHz	3,5E+05	25	1,5	0,06
PPO	Tapping	11 MHz	3,5E+05	32	0,5	0,02
Au	Contact	11 MHz	1,1E+07	85	14	0,16
PPO	Contact	11 MHz	1,1E+07	120	55	0,46
PC	Contact	1 kHz	5,0E+03	24	0,6	0,03
Au	Contact	1 kHz	5,0E+03	68	2	0,03

Tab. 2: Measured values of the surface modifications at different working parameters

Beside the fact that a Pockels cell gives the opportunity to reduce the repetition rate, it further allows the control of the exact amount of pulses too. In Fig. 3.46 a run of 4 different pulse numbers is conducted. The measured line profile nicely demonstrated the correlation of the depth of the cavities with the number of pulses.
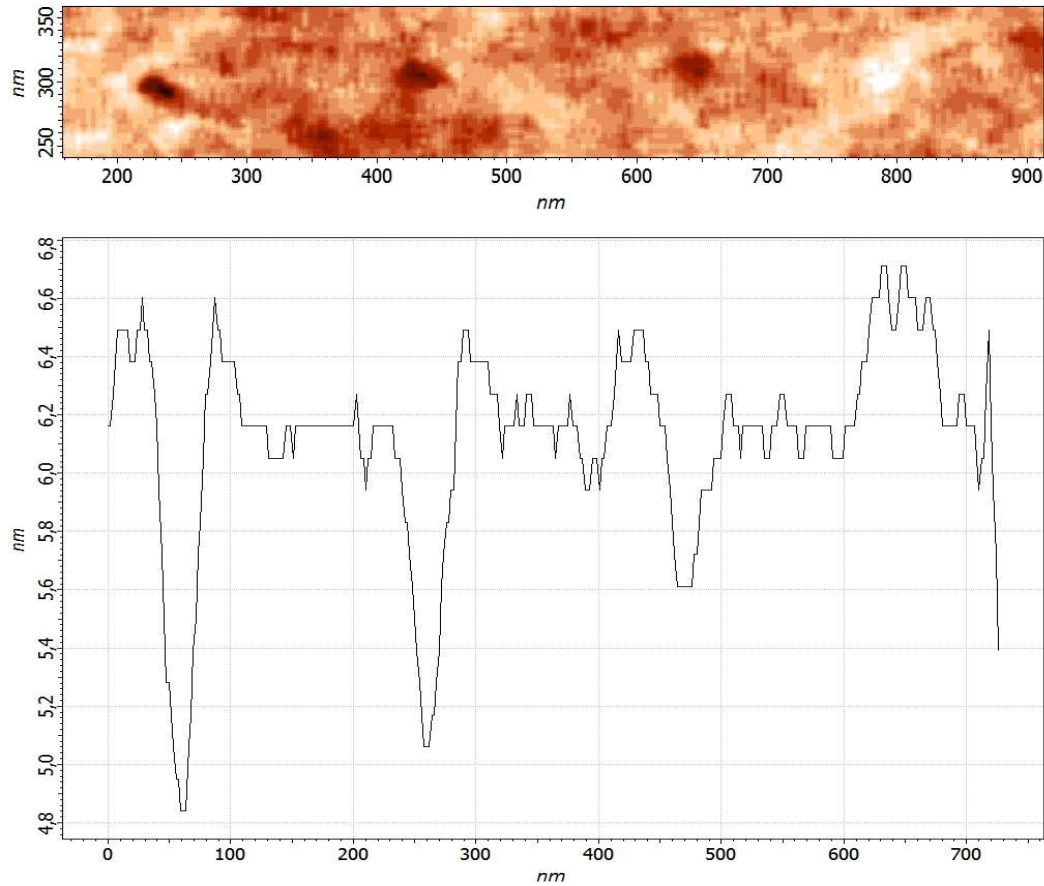
Fig. 3.46: AFM picture of a modified polycarbonate surface with 4 different pulse numbers. No modification is visible for 3000 pulses. The corresponding line profile indicates the correlation between pulse number and depth at constant aspect ratio.

Pulse number	20×10^3	10×10^3	5×10^3	3×10^3
Width / nm	30	26	19	/
Depth / nm	1,2	1	0,5	/
Aspect ratio	0,04	0,04	0,03	/

Tab. 3: Measured values for 4 different pulse numbers with a repetition rate of 1 kHz in the contact mode. The correlation between depth and pulse number is visible.

There is no melting zone visible around the crater, indicating evaporation or densification of the polymer. In Fig. 3.47 the development of the depth and the width with increasing pulse numbers of the surface structures is shown. A guide for the eye (dotted line) indicates the expected ablation rate. A linear characteristic would be expected because the tip is in contact with the surface at every time and heat accumulation due to the low repetition rate can be excluded.

Nevertheless the ablation rate decreases with increasing pulse numbers from rates of 0.1 pm per pulse down to values smaller than 0.06 pm per pulse.
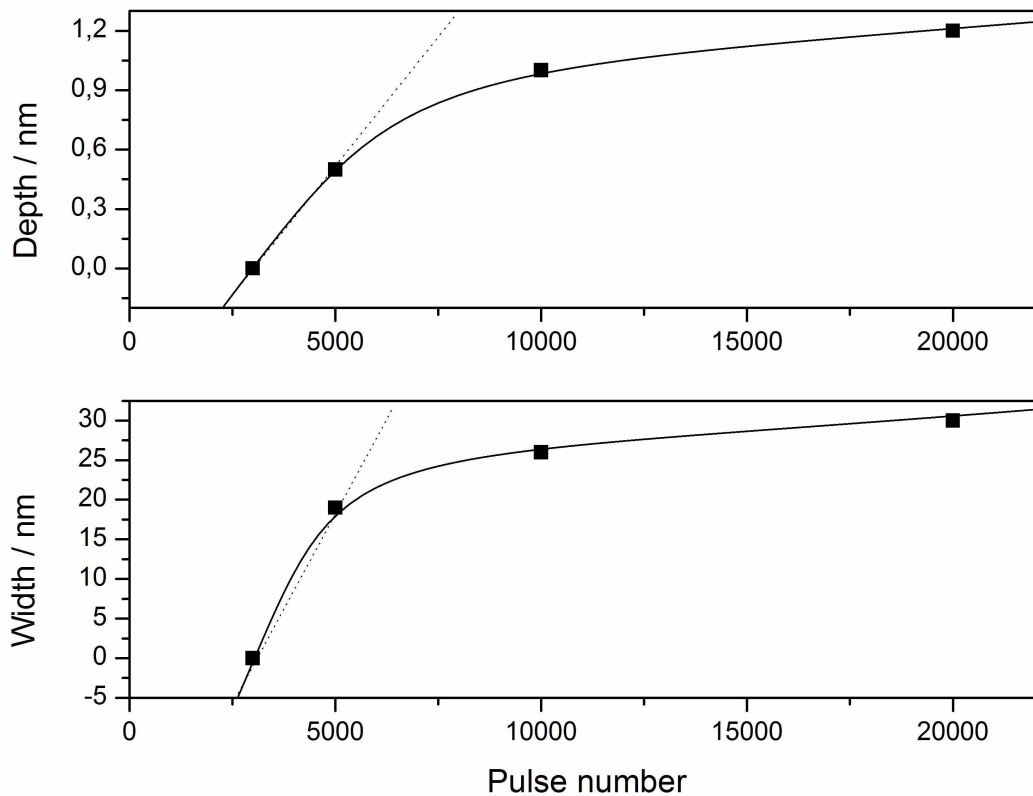
Fig. 3.47: Evaluation of the surface structures produced on polycarbonate with 1 kHz repetition rate. The depth and the width of the surface features are drawn against the pulse number. A linear behaviour for the ablation rate would be expected (guide for the eye-dotted line) but a decrease of the ablation rate for increasing pulse numbers is observed.

Substantial incubation for the modification process is observed. More than 3000 pulses are necessary to produce observable modifications. The appearance of the surface features in semicontact mode (1MHz) with $N \sim 3.5 \times 10^5$ and in contact mode (1kHz) with $N \sim 5 \times 10^3$ is equivalent. To understand this surprising behaviour further experiments are planned.

Bubble formation and water jet

It was proposed that the use of water as cooling medium may reduce the thermal effects during the laser treatment of the surface. Although the convective heat transfer coefficient is small for free convective cooling as already discussed in Ch. 3.1.2 experiments under water were performed. Therefore a special cell, similar to the electrochemical cell (Fig. 3.42) was constructed. The major difference to the electrochemical cell was the use of a second window on the collinear end, relative to the laser path, for alignment purpose and the lack of electrodes.

In Fig. 3.48 (left) the top view of a silicon cantilever over a gold surface is shown. The surrounding medium is water and the spacing between tip and surface is several micrometers.

During the alignment process it was found that if the laser was well aligned, bubble formation took place. This effect was only present when the focus was situated directly on the apex of the tip, where highest field enhancement could be expected. As these bubbles were stable over hours, vapour formation can be excluded. Reduced gas solubility due to the heating of water can be ruled out as well because the dynamics of bubble formation didn't not change over time.

The used cantilever is manufactured from highly n-doped, single crystal silicon. Therefore a possible explanation could be the oxidation of water due to photo-induced exciton generation. Due to the high electric fields induced by the field enhancement effect at the end of the tip band bending can occur and consequently water oxidation is favoured over the recombination of the electron hole pairs. To proof this idea the analysis of the gas would be necessary, which will be a sophisticated task because the amount of produced gas is very small.

Fig. 3.48: (left) Top view of silicon cantilever in water several micrometers away from a thin film gold surface. (right) Bubble formation due to water oxidation in the high electric field at the end of the SPM tip.

If the energy is further increased (>100 mW) water breakdown arises[276] and the resulting shock wave blasts the cantilever of the holder. The time resolution of the CCD camera was not good enough to visualise the complete process. The left picture in Fig. 3.49 is the last one before the cantilever is removed from the holder. Scattered light from the laser is visible on one side of the cantilever, indicating a disturbance in the laser light path. The right one shows the floating rest of the blown cantilever.

Fig. 3.49: (left) Top view of the cantilever directly before it is blown up by the shock wave produced by the water breakdown. The scattered light already indicates changes in the laser beam path. (right) Floating cantilever after detachment from the holder.

_____

The use of water as cooling medium involves some major drawbacks, which limit its applicability at high energies. Especially bubble formation, which already takes place at low energies >20 mW, prohibits the possibility of surface modification under water.

Although it could be shown that surface modification is possible the reproducibility of the results is moderate. The permanent or at least periodical contact between the tip and the surface can lead to a wear out off the tip and therefore changes its response to the incoming laser light.

Laser heating also changes the resonance frequency of the tip. This effect decreases the amplitude of the oscillating cantilever and therefore leads to tip retraction by the feedback mechanism ≥0.1 ms after the amplitude change depending on the SPM parameters.

The thermal effects also influence the size of the structures because the thermal expansion causes a certain position uncertainty, which increases the produced structures.

In Ch. 3.1 it could be shown that grazing incidence, necessary in the illustrated experiments due to geometrical limitations, leads to small enhancement factor and tip shading as a result of surface roughness can occur.

In the near future a modification of the scanning head will give the opportunity to increase the angle of incidence to 8°, which will lead to higher field enhancement for silicon tips of at least one order of magnitude.

Furthermore the realisation of non-contact measurements at the Viennese setup, based on the phase shift is already under construction.

Weizmann setup

At the department of Chemical Physics at the Weizmann Institute of Science the available SPM (XE-120, Park Systems) allows for illumination at higher angles of incidence from the side. Unfortunately no Pockels cell was available. Therefore all experiments were performed at a repetition rate of 82 MHz.

Beside that a home-built feedback mechanism based on the phase shift of the oscillation amplitude near the surface enables the hovering of the tip over the surface without contact. (See Appendix B)

This scanning mode allows guiding the tip in close distance (2-5 nm) over the surface in a wearless way. In Fig. 3.50 the operational capability of the so called "Floating Tip" scanning mode is shown. The left picture shows the topography of a gold surface, scanned in the customary mode and on the right picture the Floating Tip mode was used. It is obvious that the resolution at the edges is not of the same sharpness than in the customary mode but the overall topography could be mapped in a proper way.
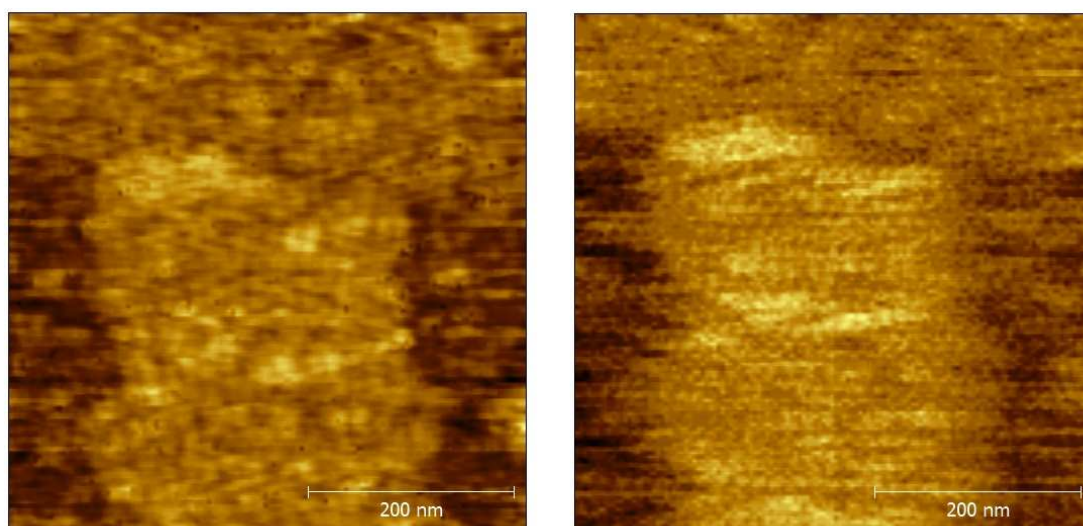
Fig. 3.50: Comparison of the customary scanning mode of the XE-120 SPM with the home-built feedback mechanism based on the phase shift of the oscillating amplitude. A decrease in the resolution is visible but the overall structure could be mapped perfectly.

A drawback of the Floating Tip scanning mode is the low scanning speed reachable, where non-contact conditions could be realized. The maximum scanning speed recommended, is around 100 nm/s. This value is mainly limited by the used external electronic systems (PID, Lock-in).

_____

In the previous experiments surface modifications were realised at single points under a static tip, at least in x and y direction, which was the scanning direction. Simulations showed a huge influence of laser heating on the thermo-mechanical properties of the cantilever, so the idea was to exclude these effects by thermal equilibration of the heated system before each experiment. Therefore a more continuing modification type was chosen, where the tip was already illuminated before the experiment and instead of point modifications the tip was scanned in serpentines over the surface to produce lines.

The influence of the scanning speed, which can be compared to the energy input into the substrate, on the performance of the surface structuring process was investigated in Fig. 3.51. Therefore a polymer surface (photoresist AZ4620: Naphthoquinone Diazide derivative, Nobolakresin Derivative and Propylene Glycol Monomethyl Ether Acetate) was spin coated on a glass substrate. The tip is scanned in serpentines over the surface at a constant distance (~3-5 nm). The scanning speed was increased for each line.
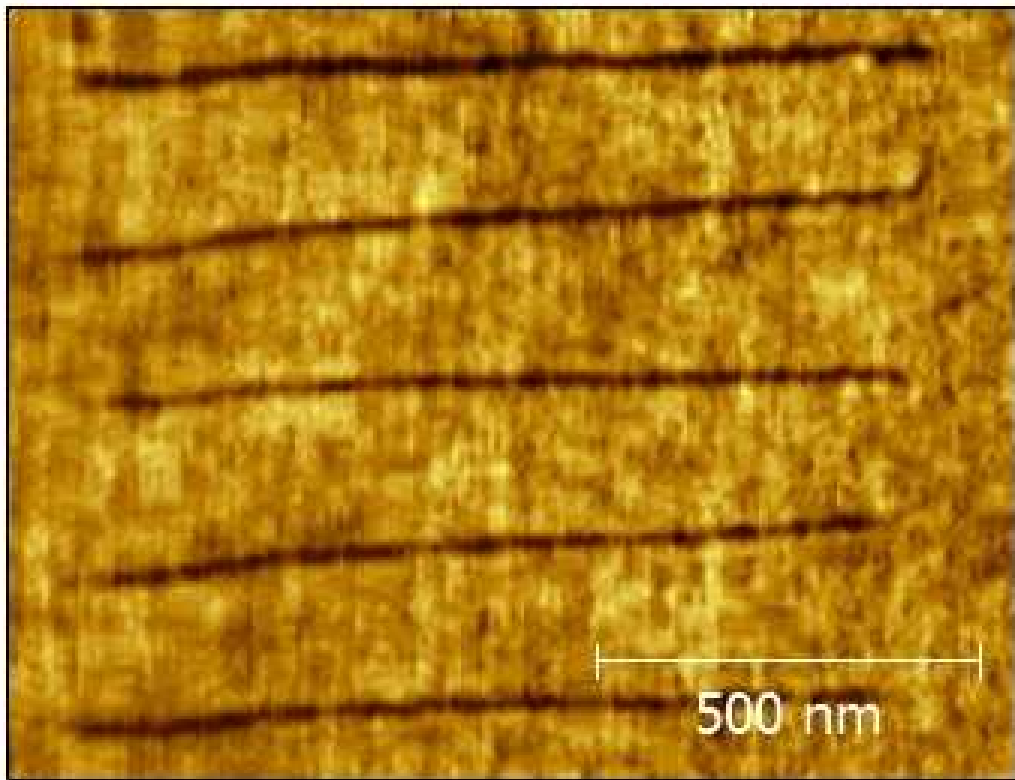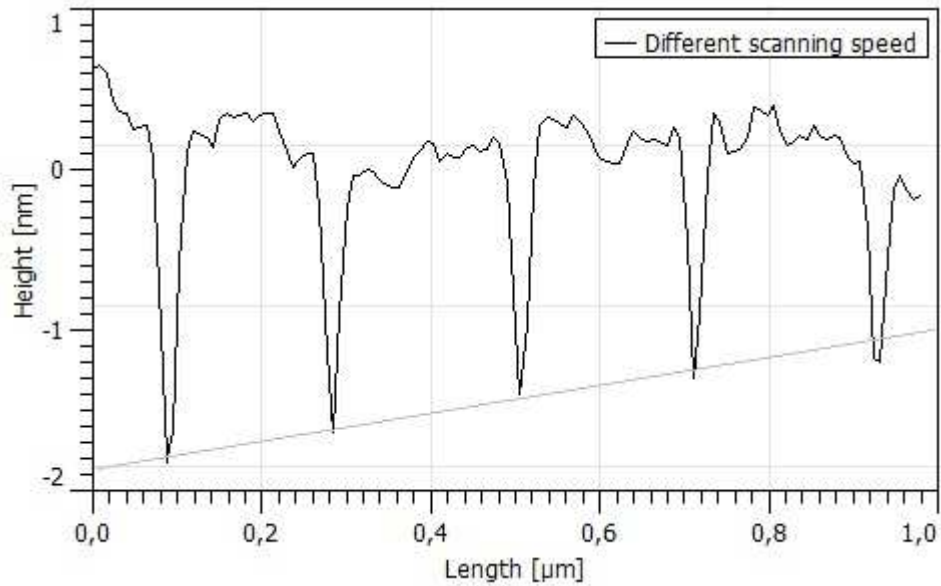
Fig. 3.51: Surface modification at different scanning speed. Increasing scanning speed leads to less pronounced structures because the pulse number per area reduces. The corresponding line profile shows the linear correlation between speed and depth of the structure. The gray line is a guide for the eye. The scanning speed was 100-70-50-30-10 nm/s from the top in the upper picture and from the right in the line profile.

The changes in the structures, due to different scanning speeds confirm the presumption that the mechanism of modification is not mechanical because in this case the dependency on the speed should be negligible. For mechanical structuring the main parameter is the force applied on the surface.

In the Floating Tip scanning mode the distance between tip and surface is controlled by the phase shift value chosen for the measurement. The higher the phase shift the smaller is the tip to sample gap. If the tip to sample gap is too small and the tip gets into contact the appearance of the produced surface structures changes completely.

On the left picture in Fig. 3.52 the phase value was increased from 20 to 120°, which is similar to a tip to sample gap from 1 to 5 nm. Compared to the right picture, where the tip scratches the surface, no displacement of material on the rim of the trench is visible.
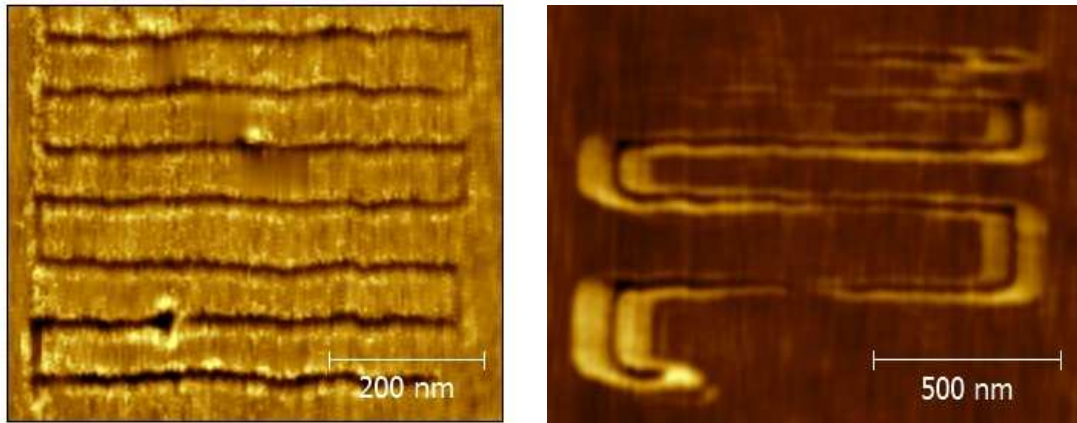
Fig. 3.52: Comparison of the different mechanisms of surface modification. On the left side the mechanism is thermal and lithographical respectively, whereas on the right side the modification is mechanical (no laser). The phase values for the left picture were 20-30-40-50-60-100-120° from the top

The evaluation of the different phase values is shown in Fig. 3.53. A line profile was recorded to measure the exact structure dimensions at every phase value. The depth development follows a non-linear increase. The same behaviour was already measured for the phase to distance dependency, which shows sigmoid characteristic, by scattered evanescent light during the evaluation of the Floating Tip scanning mode.[20]

It has to be noted that based on the surface structures a position accuracy of the tip to sample gap higher than 0.5 nm can be expected.
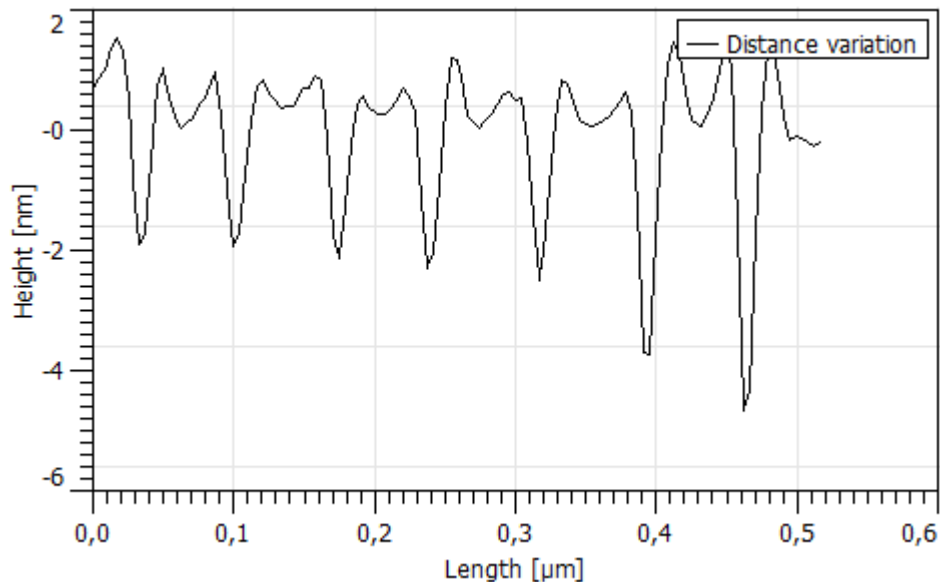
Phase / °	Depth / nm	Width / nm
20	2,4	14
30	2,5	15
40	2,6	14
50	2,8	13
60	3,0	13
100	4,2	14
120	5,1	14

Fig. 3.53: Line profile of tip to sample distance variation by changed phase shift. With increasing phase shift the spacing is decreased. The increase in the depth of the trenches illustrates the decrease in the tip to sample distance. The FWHM remains constant.

As already shown in the theoretical part in this work there is a strong field enhancement dependency on the polarisation direction of the incoming light. It is accepted that an electric field vector parallel aligned along the major axis of the tip gives higher enhancement than the perpendicular alignment.

The experimental proof is shown in Fig. 3.54. All parameters where kept constant except the polarisation direction, which was turned by 90° with the help of a $\lambda/2$ plate. The tip to sample gap was determined by four different phase values for each polarisation direction (20-30-60-120°). The left four lines correspond to s-polarisation, which means that the electric field vector is perpendicular to the major tip axis, whereas the right four lines were done at p-polarisation.
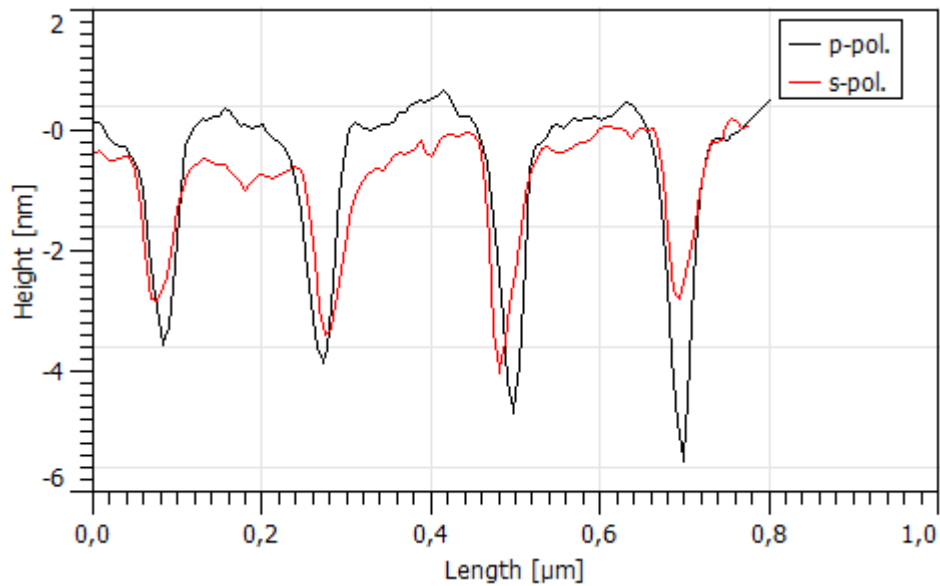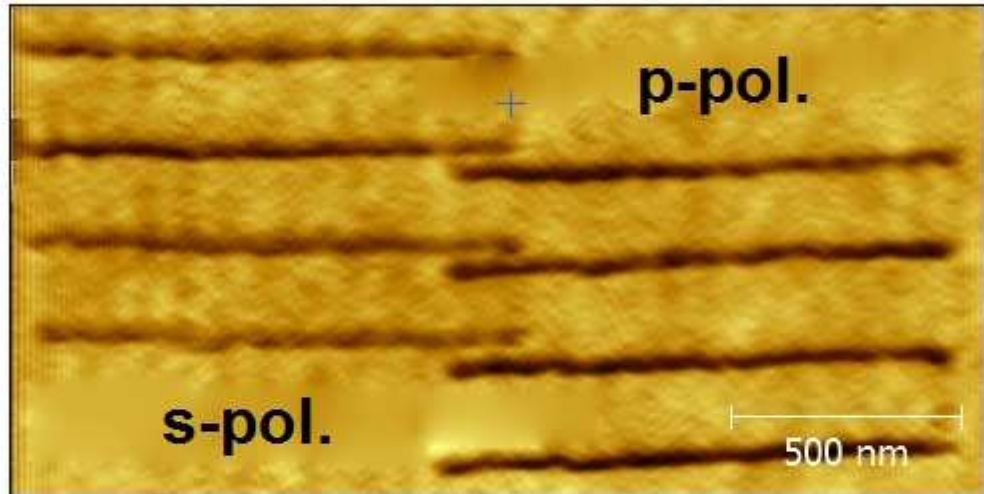
Fig. 3.54: Polarisation dependent structuring of a photoresist (AZ4620). The tip to sample gap was determined by four different phase values (s-pol.: 20-40-60-80°, p-pol.: 80-60-40-20° from the bottom). The structures for p-polarised light are more pronounced than for s-polarised light confirming the theoretical prediction of the field enhancement dependency on the polarisation of incident light.

In Tab. 3 the same evaluation but for different energies at one defined tip to sample gap (20°) is depicted. It is obvious that the polarisation dependency for the depth of the structures (deeper for p than for s-pol.) is the same for different energies.

AZ4620	p-pol.		s-pol.	
Power / mW	Depth / nm	Width / nm	Depth / nm	Width / nm
92	2,7	25	2,4	30
95	3,6	32	3,2	44
97	8,1	37	6,4	48
105	10,5	41	9,2	56

Tab. 3: Comparison of s- and p-polarisation dependent surface modifications at different energies. The depth is more pronounced at p-polarisation, while the width is bigger for s-polarisation. This can be explained by the different orientation of the radiating dipole.

An important observation is the characteristic of the width, which is always bigger for s-polarisation than for p-polarisation. This could be explained by the minor confinement of the enhanced field on the substrate for s-polarised illumination. In Fig. 3.55 two different polarisation directions (s+p) were calculated and the field intensity on the plate is shown, to underline the experimental results theoretically.
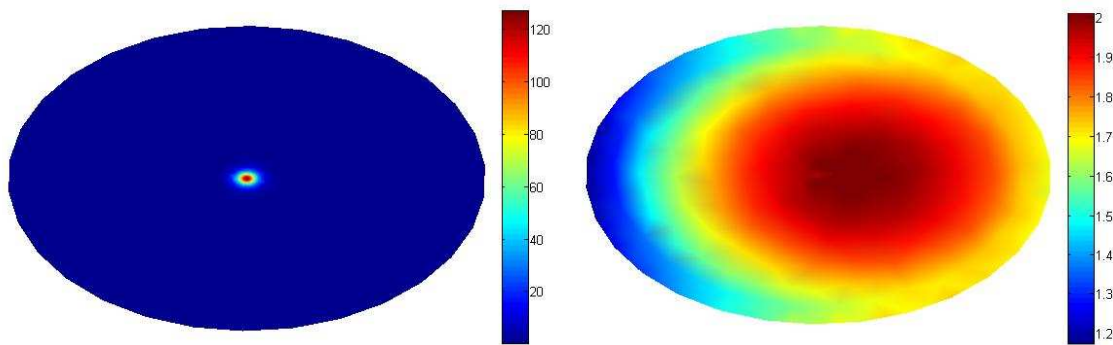
Fig. 3.55: Field intensity distribution on the substrate for two different polarisation directions. The left distribution was calculated for p-pol. light and high confinement of the intensity on the plate is visible. The right one was simulated with s-polarised light. Beside the weak confinement, the enhancement s also reduced by nearly two orders of magnitude

Although the experiments show promising results the laser alignment is still a demanding task. In Fig. 3.56 the experimental parameters were identical for both pictures. The only difference was the position of the laser on the tip. Even though this is an extreme example it highlights the importance of careful alignment procedure.
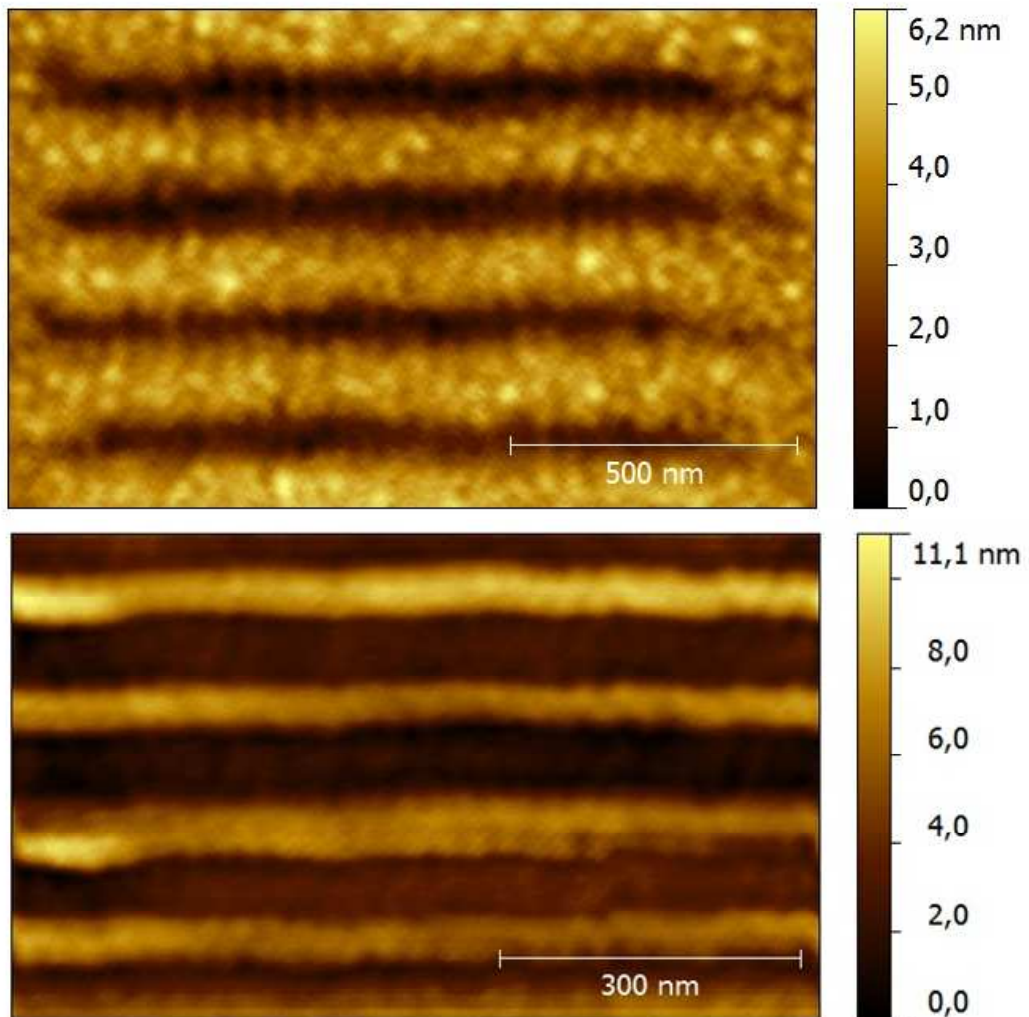
Fig. 3.56: Different position of the laser beam at the tip. All other parameters stayed the same. In the upper picture the expected trenches were visible, whereas in the lower picture a swelling of the photoresist occurred.

The quality of the tip is also essential for producing confined surface structures. In Fig. 3.57 the same experimental parameters as in Fig. 3.52 were used, but the tip was dull due to hard tip crash. Therefore the distance control seems to work no longer properly and the resulting structures are similar to a mechanically modified surface.
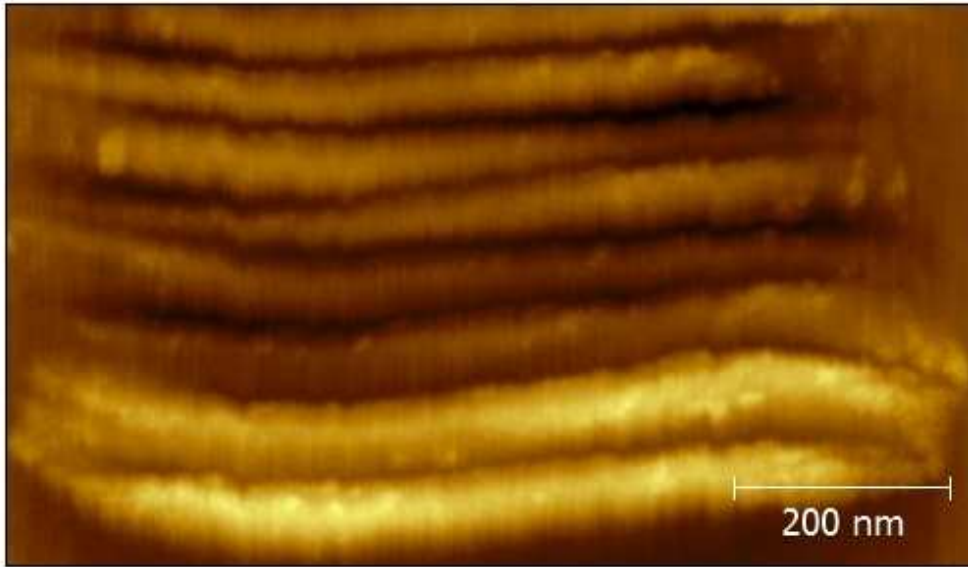
Fig. 3.57: Surface modification with a dull tip. Thus distance control was not working properly and the polymer was scratched by the dull tip.

The already discussed experiments have been performed on a spin coated photoresist surface (AZ4620). After changing the polymer to polyphenylene oxide the observed modification threshold is 3.5 times smaller than for the photoresist although the glass transition temperature is roughly the same (PPO-483 K, AZ4620-453 K)

The change of the polymer to polyphenylene oxide also led to an unexpected change in the surface structure appearance after the modification. The experiments on the photoresist had shown a very symmetric profile of the produced trenches. However polyphenylene oxide showed a completely asymmetric trench shape. (Fig. 3.59)

The experimental setup is indicated in Fig. 3.58. The cantilever alignment and the direction of the incoming laser are shown (not to scale).
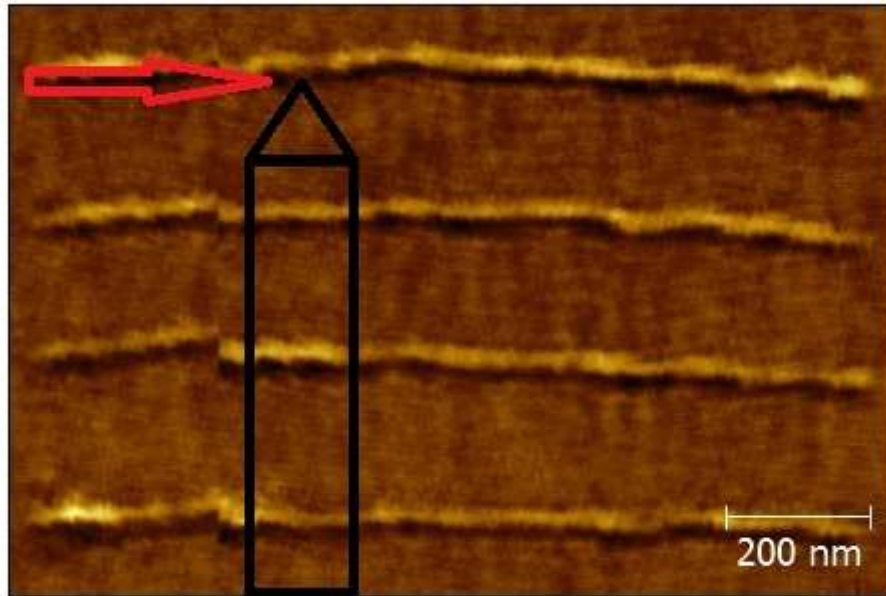
Fig. 3.58: Surface modification of polyphenylene oxide. The geometrical assembly is schematically illustrated (not to scale). The shape of the nano-trenches shows asymmetrical behaviour. The tip to sample gap is decreased from the top to the bottom to be 120-60-30-20°.

The shape of the produced trenches shows no swelling underneath the cantilever but massive one at the opposite side. Although the shape of the trenches is comparable to mechanically modified surfaces, scratching can be excluded because no modification was possible without laser illumination.
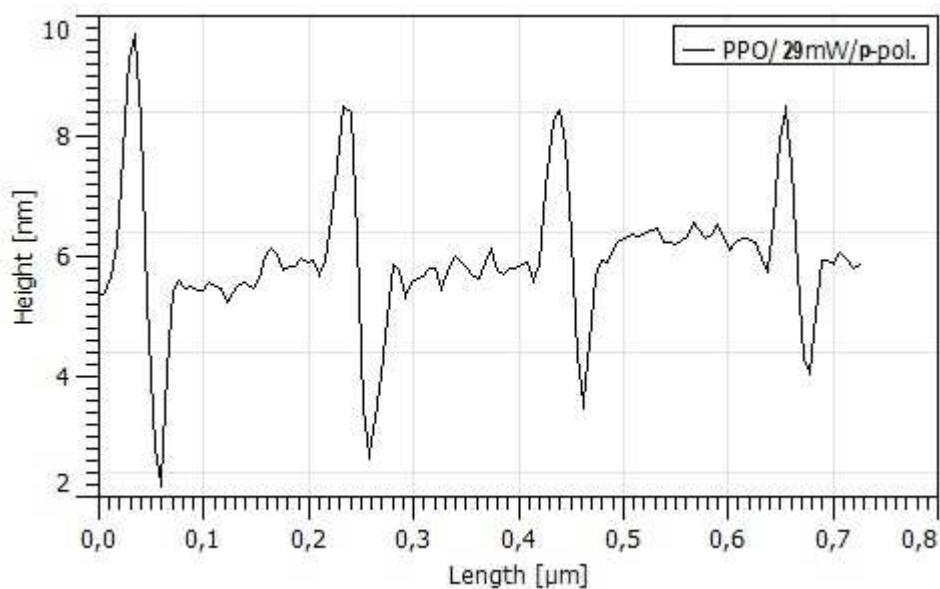
Fig. 3.59: Line profile of PPO nano-trenches. A strong asymmetric behaviour is visible. For the evaluation the depth and height were measured between the crest and the trough of the respective trench. The tip to sample gap is decreased from the left to be 120-60-30-20°.

The size of the structures at 3.5 times smaller laser energies are comparable to the size of the structures produced in the photoresist. The development over increasing energy in depth is the same as for the photoresist. As the glass transition temperature for the photoresist and PPO are nearly the same non-contact heat transfer mediated surface structuring can not be the only modification mechanism

PPO Power / mW	p-pol. Depth / nm	s-pol. Depth / nm
21	2,0	< 0,5
29	3,8	4,7
40	7,9	5,8
50	10,3	8,9

Tab. 4: Measured geometrical dimensions for different laser energies at one defined tip to sample distance (20°). The depth of the created structures with p-polarized light is always bigger than for s-polarised light indicating the effect of field enhancement. For 21 mW and s-pol. light the structure was not evaluable.

For 21 mW and s-polarised light the energy is not high enough to produce evaluable surface structures. Only for p-polarised light where the field enhancement effect is more pronounced, surface modification occurs.

The origin of the asymmetric structure geometry is not understood until now but further investigations are planned.

The experimental results suggest mainly thermally driven (heat transfer from the tip to the sample) modification mechanism. Although the influence of field enhancement can not be excluded completely its impact seems to be of minor importance. Based on the theoretical calculations the field enhancement is negligible for s-polarised laser illumination but the differences in the modification behaviour (depth) are not that pronounced and therefore also indicating that field enhancement is not the major ablation mechanism in these experiments. The modification based on laser ablation is only boosted by the field enhancement effect, as could be demonstrated by the polarisation dependency of surface modifications.

As demonstrated experimentally in Ch. 3.1 a change in polarisation also leads to a change in the tip temperature of several tens of degrees and therefore enough to explain the differences in the depth.

The smaller modification threshold for PPO at similar glass transition temperature could be explained by an infrared active optical phonon resonance, which would lead to increased heat flux between tip and substrate.[282, 283]

The polarisation dependent differences in the width of the surfaces structures may give an indication of optical near-field based surface structuring.

4 Summary

Apertureless scanning near-field microscopy was investigated for the application of fs-pulses on SPM tips both theoretically and experimentally.

Theoretical investigations concentrated on the influence of geometrical and illumination parameters on the field enhancement between and a pointed probe and a substrate. A Boundary Element Method (BEM) toolbox for Matlab, developed in cooperation with the Physical Department of the Karl Franzens University in Graz was employed.

The principle idea of the boundary element method is the reduction from volume differential equations to boundary integral equations. In contrast to the conventional quasistatic approximation, which is fulfilled when the particle size is much smaller than the wavelength of the light, the full Maxwell equations have been solved in this work, including retardation effects.

The geometric model for the simulation is based on a tapered tip with a hemispherical endcap located over a substrate. The laser illuminates the tip from the side, like in all experiments discussed below. The dielectric properties of tips, such as Si, Au, and Si coated with various Au thicknesses, the substrate and the background were chosen independently during the simulations.

The field enhancement was calculated for different tip lengths. For a gold tip illuminated at an angle of 1.5°, the resonance behaviour is much more pronounced than at Si tips because stronger surface plasmon resonances occur. In practice it is difficult to find the exact geometry which fits the resonance conditions for an available laser wavelength, that's why the off-resonance behaviour was investigated.

The field enhancement calculated for a silicon tip at a distance of 2 nm over a gold surface was only 8. The major reason for this moderate enhancement is the small angle of incidence, where the field enhancement is counteracted by the reflected wave from the substrate.

The field enhancement calculated for a gold tip with a diameter of 130 nm is even smaller than for the silicon tip. This is caused by the field enhancement decrease with increasing radius, which is the dominating effect in the off-resonance regime.

It was already noted that the angle of incidence plays an important role concerning the maximum field enhancement. This can be explained by the fact that the incoming wave will be reflected at the surface underneath the tip, a phase shift of 90° will be introduced and no enhancement takes place at 0°.

Summary

_____

A Si tip exhibits the highest enhancement at an angle of incidence of 20°, which is slightly above the 14° realized at the Weizmann setup. A gold tip with a radius of 65 nm shows the maximum enhancement at 50° which could be a substantial challenge for the design of a setup.

Previous simulations in literature only considered solid gold tips. Commercial Au coating thicknesses range from 5-65 nm. The influence of the coating thickness was simulated with a constant overall geometry. The thickness below ca. 40 nm shows a drastic influence both on the resonance wavelength and the absolute enhancement. That indicates that in this very common coating range precise control of the thickness is mandatory.

To exploit the full potential of field enhancement in apertureless Scanning Near-field Microscopy the use of an optical parametric amplifier (OPA) to scan over a broad range of wavelengths and measure the tip response simultaneously appear to be very promising.

Thermo-mechanical properties were studied with the COMSOL Multiphysics software package, which bases on the Finite Element Method (FEM).

The studied geometry was based on a commercial tip (TAP300Al, BudgetSensors). Several temperatures were calculated and the displacement behaviour in z-direction, which influences the tip-sample gap and the displacement in x-direction, which defines the expansion along the cantilever and therefore decreases the position accuracy, is evaluated. The investigated temperature range was chosen within the most common values in literature to be between 300-1000 K.

Thermal expansion causes an uncoated cantilever to touch the substrate at 337 K. An Al-coated cantilever would touch the substrate already at 301 K due to additional bimetallic bending. A coated cantilever shows a displacement in z-direction of 2.5 nm per 10 K, uncoated only one-fifth, 0.5 nm per 10 K.

The displacement in x-direction can become a crucial point where high position accuracy is needed. The value of 1 nm/10 K can lead to a shift of several tens of nanometre from the desired position at typical surface modification working conditions, which can decrease the applicability in e.g. high density data storage.

Therefore thermal equilibrium is necessary before modification experiments can be performed.

In experiments, bubble formation under the cantilever in the presence of water as cooling medium, can be rationalized by the photo-generation of holes in the n-type Si tip and the

_____

electrochemical oxidation of water to oxygen gas. Higher fluences led to water breakdown and cantilever devastation.

Substantial effort was exerted into the development of alignment strategies at the Viennese setup in order to identify the focus position on the tip at extremely high optical apertures. Three approaches have been discussed.

Nanostructuring experiments were undertaken to identify near-field parameters which lead to non-thermal morphological changes of metallic and polymeric substrates. SPM parameters were always chosen in a way that no modification of the substrate was observed without laser illumination.

There was clear evidence at 11 MHz irradiation with pulse number, $N \sim 10^7$ of a Si tip in contact mode, that heat accumulation in the tip induces melt structures with deep (several 10 nm) and wide (ca. 100 nm) cavities both in metal and polymer. This can be interpreted as melting by the contact of the hot tip. Tapping mode with 11 MHz leads to a completely different result. The contact time at typical SPM working conditions is ca. 100 ns and the pulse number can be appreciated to be of the order of $N \sim 1$ during a single contact event. This sums up to a total of $N \sim 3.5 \ 10^5$. Even though heat accumulation has to be assumed in the tip, the cavity depth is reduced to ca. 1 nm and the width to ca. 30 nm which compares with a tip diameter of ca. 20 nm on both material classes. A 1 kHz irradiation should not lead to heat accumulation in the tip. With this parameter $N \sim 10^3$, the polymer PC exhibits similar morphology like PPO with tapping mode with 11 MHz and $N \sim 3.5 \ 10^5$. There is however a nonlinear influence of the pulse number on the width and depth of the nanocavities on PC, where a linear increase with N would be expected, when simple evaporation would be assumed. Substantial incubation of the modification process is observed since it needed more than 3000 pulses to initiate morphology modification. The dependence of e.g. the depth, however, decreases rapidly with higher N. It has to be noted that no melt displacement is observed. Either material densification or evaporation could be responsible. In order to elucidate this surprising process further investigations are in progress.

It is remarkable that non-contact experiments at 82 MHz irradiation led to comparable non-melt structures during cantilever scans. The extent of spot overlap, determined by the variation of the scanning speed showed a linear correlation with N with a comparable change of depth (~0.5 nm) as observed with the 1 kHz contact experiment.

The experimental results suggest mainly thermally driven (heat transfer from the tip to the sample) modification mechanism. Although the influence of field enhancement can not be excluded completely its impact seems to be of minor importance. Based on the theoretical calculations the field enhancement is negligible for s-polarised laser illumination but the differences in the modification behaviour (depth) are not that pronounced and therefore also indicating that field enhancement is not the major ablation mechanism in these experiments. The modification based on laser ablation is only boosted by the field enhancement effect, as could be demonstrated by the polarisation dependency of surface modifications.

As demonstrated experimentally in Ch. 3.1 a change in polarisation also leads to a change in the tip temperature of several tens of degrees and therefore enough to explain the differences in depth.

The smaller modification threshold for PPO at similar glass transition temperature could be explained by infrared active optical phonon resonance, which would lead to increased heat flux between tip and substrate.[282, 283]

The polarisation dependent differences in the width of the surfaces structures might give an indication of optical near-field based surface structuring.

Whereas surface structuring of the polymer samples was possible for all modification parameters, the response of the gold sample changed significantly. In the contact and semicontact regime, where heat transfer through contact events could be realised and mechanical impact through thermal expansion was likely, surface features could be observed.

In the non-contact regime no surface modification on the gold substrate was evident.

Due to the different angles of incidence at the Weizmann and Viennese setup the field enhancement was expected to be two orders of magnitude higher at Weizmann than at the Viennese setup. Nevertheless no gold modification could be realised, indicating mechanical supported thermal mechanism instead of matter ablation through enhanced laser light.

For further investigations the setup at the University of Vienna was adapted recently, to better fulfil the demands of near-field microscopy.

By modification of the scanning head the angle of incidence has been increased to 8°, providing a field enhancement enlargement of at least one order of magnitude.

Furthermore a non-contact measuring mode based on the phase shift of an oscillating cantilever is under construction.

5 Supplementary Information

5.1 Appendix A: Matlab Toolbox

The following Matlab Toolbox is based on the MNPBEM Toolbox of Physical Department of the Karl Franzen University of Graz and was modified to fit the necessary boundary conditions for field enhancement studies at pointed probes.

Simulation of a metal-tip a distance d away from a substrate

Literature: Novotny & Hecht, Principles of Nanooptics

Dielectric constants and functions

```
epsm   = epsconst( 1.00 );          % background dielectric function
epsau  = epstable( 'gold.dat' );    % dielectric function of gold
epssi  = epstable( 'Si(111).dat' ); % dielectric function of silicon
% dielectric table, 1: background, 2: substrate, 3: tip
epstab = { epsm, epsau, epssi };
```

Simulation parameters

```
h = 300;    % total length of tip
r = 10;     % radius of hemispherical endcap
d = 2;      % distance between tip and metal plate in nm
a = 20;     % angle ( in degree ) of cone surface

% discretization of tip: 1st endcap values, 2nd number of points along
% tip circumference, 3rd number of points along height of cone
n = [ 20, 40, 65 ];

% angle of incident light in rad
alphai = 1.5 / 180 * pi;

% polarisation angle in rad
phi = 0 / 180 * pi;

% laser photon energy (nm)
enei =   800 ;
```

Generate silicon tip shaped as apex

```
[ psph, phull, ~ ] = triapex( r, h, 'd', d, 'n', n, 'angle', a );
```

Generate metal plate (e.g. for plotting)

```
polyin  = polygon( 30, 'size', [    1,   1 ] );
polyout = polygon( 30, 'size', [ 250, 250 ] );
plout   = triplatecut( polyout, polyin, 'z', 0, 'hdata', struct( 'hmax', 25 ) );
plin    = triplate(            polyin, 'z', 0, 'hdata', struct( 'hmax', 10 ) );
plate   = comparticle( epstab, { plout, plin }, [ 2, 1; 2, 1 ] );
```

Preallocate memory

```
emax    = zeros( length( alphai ), length( enei ) );
```

_____

```
results = cell( length( enei ), length( alphai ) );
```

Generate composite structure

```
c   = comparticle( epstab, { psph, phull, plout, plin }, [ 3, 1; 3, 1; 2, 1; 2, 1 ], [
1, 2 ] );
tip = comparticle( epstab, { psph, phull }, [ 3, 1; 3, 1 ], [ 1, 2 ] );
```

Start simulation

```
for ai = 1 : length( alphai )

  alpha = alphai( ai );

  %  light polarization and direction for incoming and reflected wave
  pol1 = [   sin( alpha ), 0,   cos( alpha ) ];
  dir1 = [   cos( alpha ), 0, - sin( alpha ) ];
  pol1 = cos( phi ) .* cross( cross( dir1, pol1 ), dir1 ) + sin( phi ) .* cross( dir1,
  pol1 );

  pol2 = [ - sin( alpha ), 0,   cos( alpha ) ];
  dir2 = [   cos( alpha ), 0,   sin( alpha ) ];
  pol2 = cos( phi ) .* cross( cross( dir2, pol2 ), dir2 ) + sin( phi ) .* cross( dir2,
  pol2 );

  %  plane wave excitation for incoming and reflected wave
  excin = planewaveret( pol1, dir1 );
  excre = planewaveret( pol2, dir2 );

  %  BEM simulation
  bem = bemret( c, [], green.options( 'cutoff', 4 ) );
  sca = zeros( length( enei ), 1 );

  %  wavenumber of light in medium
  eps1 = epsm(  enei ); k1 = 2 * pi ./ enei .* sqrt( eps1 );
  eps2 = epsau( enei ); k2 = 2 * pi ./ enei .* sqrt( eps2 );

  kz1 = sqrt( k1.^2 - ( k1 .* cos( alpha ) ).^2 );
  kz2 = sqrt( k2.^2 - ( k1 .* cos( alpha ) ).^2 );

  %  Fresnell coefficient for reflected TM-wave, see Eq. (2.49)
  rp = ( eps2 .* kz1 - eps1 .* kz2 ) ./ ( eps2 .* kz1 + eps1 .* kz2 );

  %  main loop over different excitation wavelengths
  for ien = 1 : length( enei )

    exci     = excin( c, enei( ien ) );
    excr     = excre( c, enei( ien ) );
    exci.a2  = exci.a2  + rp( ien ) * excr.a2;
    exci.a2p = exci.a2p + rp( ien ) * excr.a2p;

    %  surface charge
    sig = bem \ exci;
    sca( ien ) = excin.sca( sig );

    %  electromagnetic fields at surface of structure
    field = bem.field( sig, 2 );

    %  prepare plot results
    eint           = sum( transpose( field.e' ) .* field.e, 2 );%./ eint0;
    %  field intensity |E|^2
    emax( ai, ien ) = max( eint );
    %  maximum of |E|^2

    %  save resutlts in structure
    results{ ien, ai } = struct( 'eint', eint, 'ene', enei(ien), 'alpha', alpha, 'sca',
    sca( ien ), 'emax', max( eint ), 'sig', sig.sig1 );

   if ~mod( ien, 10 ); disp([ num2str( ien ), ' / ', num2str( length( enei ))]); end;

  end

  if ~mod( ai, 10 ); disp([ num2str( ai ), ' / ', num2str( length( alphai ))]); end;

end
```

Save results

```
t       = clock;
```

_____

```
actdate = [ num2str(t(1)), '-',  num2str(t(2)), '-', num2str( t(3)), '_',
num2str(t(4)), 'h',  num2str(t(5)),'m' ];
save( [ actdate,  '_solid_tip.mat' ], 'c', 'tip', 'enei', 'emax', 'n', 'results',
'alphai', 'h', 'r', 'd', 'a' );
```

Plot scattering cross section for different energies

```
if length( enei ) > 1
   figure; plot( enei, sca );
   title(  ' Scattering intensity ','FontSize',18,'fontweight','b' )
   xlabel( ' Wavelength of light (nm) ', 'FontSize',14,'fontweight','b' )
   ylabel( ' Scattering cross section (nm^2) ', 'FontSize',14,'fontweight','b' )
   save( [ 'normal_tip_sca_enei ', date ], 'sca', 'enei' )
end
```

Plot maximum of |E|^2 dependent on the excitation angle

```
if length( emax( :, 1 ) ) > 1
   figure;
   hold on;
   plot( alphai * 180 / pi, emax( :, 1 ), 'b-' );
   title(  ' Maximum of |E|^2 ','FontSize',18,'fontweight','b' )
   xlabel( ' Excitation angle (°) ', 'FontSize',14,'fontweight','b' )
   ylabel( ' |E|^2 ', 'FontSize',14,'fontweight','b' )
end
```

Plot maximum of |E|^2 dependent on the photon energy

```
if length( emax( 1, : ) ) > 1
   figure;
   hold on;
   plot( enei, emax( 1, : ), 'b-' );
   title(  ' Maximum of |E|^2 ','FontSize',18,'fontweight','b' )
   xlabel( ' Photon wavelength (nm) ', 'FontSize',14,'fontweight','b' )
   ylabel( ' |E|^2 ', 'FontSize',14,'fontweight','b' )
end
```

Plot field intensity on whole structure

```
   figure;
   plot( c, eint );
   title( ' Field intensity |E|^2 ','FontSize',18,'fontweight','b' )
   colorbar;
   lighting none
```

_____

Plot field intensity on tip

```
figure;
plot( tip, eint( 1 : tip.nfaces ), 'EdgeColor', 'b' );
title( [ ' Field intensity |E|^2, enei = ', num2str( enei(end) )
],'FontSize',18,'fontweight','b' )
colorbar;
lighting none
view( 0, 0 );
```


Field intensity |E|^2, enei = 800
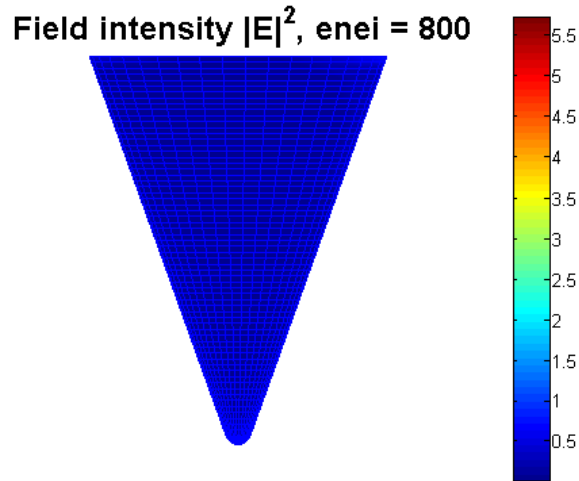
Plot field intensity on plate

```
figure;
plot( plate, eint( tip.nfaces + 1 : end ) );
title( ' Field intensity |E|^2 at plate ','FontSize',18,'fontweight','b' )
colorbar;
lighting none
```


Field intensity |E|^2 at plate
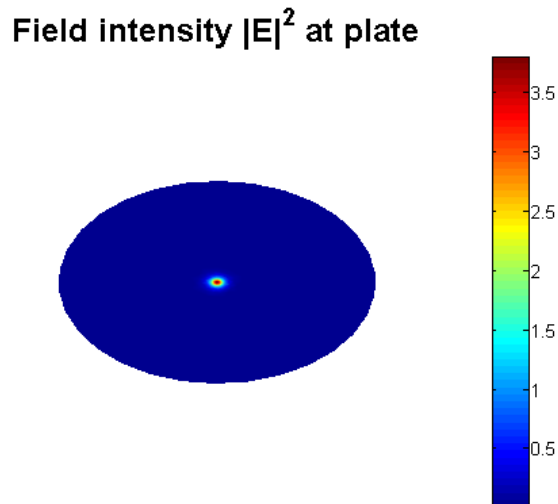
Plot field between tip and substrate

```
if length( enei ) == 1
  [ x, z ] = meshgrid( 50 * linspace( - 1, 1, 501 ), h/6 * linspace( -1, 1, 51 ) + h/6
  + 0.1 ); y = 0 * x;
  % place the points into the dielectric media
  pt = compoint( c, [ x( : ), y( : ), z( : ) ], 'medium',  1 );
```

_____

```
  % Green function between points and particle
  g = compgreen( pt, c, green.options( 'cutoff', 4, 'refine', 5 ) );
  % electric field at point positions
  field = g.field( sig ) + excin.field( pt, enei );

  figure;
  title( ' Real part of electric field E ','FontSize',18,'fontweight','b' )
  coneplot( pt.pos, real( field.e( :, :, 1 ) ), 'scale', 0.8 ); hold on;

  p1 = select( c, 'carfun', @( x, y, z ) ( z > 0 & z < h/3 ) );
  %p2 = triplate( polygon( 30, 'size', 2*max( p1.verts(:,1) ) ), 'z', 0 );
  p2 = tripolygon( polygon( 4, 'size', 2 * max( p1.verts(:,1) * [ -1, 1 ] ) ), [ -2, 0
  ] );
  plot( p1 ); plot( p2 );
  view( 0, 0 );
  camlight( 'left' ); axis off; axis equal;
end
```

Real part of electric field E
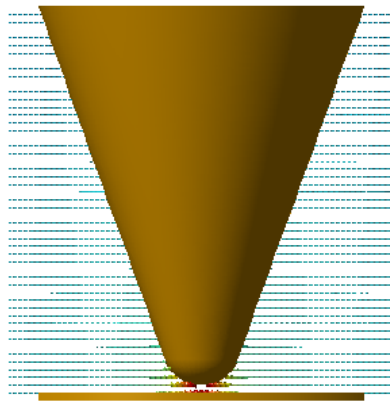
5.2 Appendix B: Floating Tip Principles

The whole description is based on the developments at the Weizmann Institute of Science and is already published elsewhere. This chapter will just summarise the major aspects for better understanding.

Although Atomic Force Microscopy is a well established tool in the surface science community real non-contact mode is still a sophisticated task. Typical approaches, where the tip is brought into contact with the surface and is then retracted are not very successful because with stiff cantilevers (~40 N/m) the contact event mostly leads to tip destruction, whereas soft cantilevers (~0.1 N/m) have to deal with sticking, due to capillary forces, electrostatic forces and so on, which leads to an overshooting when released from the surface. Beside the problem of accurate positioning, scanner drift due to heat, humidity etc. makes a distance control over time impossible without adequate feedback mechanism.

To overcome this problem the phase shift of the oscillating cantilever to its driving voltage is used as feedback signal. It was demonstrated that in close vicinity to the surface the phase shifts gradually up to 180°, which than could be regarded as contact. This was explained by a shift of the pivot of the cantilever motion from one end to the other.

The basic idea is shown in Fig. B.1, where the most important parameters are recorded. The black curve corresponds to the phase shift of the cantilever, the blue curve correlates with the bending of the cantilever, the red curve is the shear force signal and the pink curve is the scattered evanescent light intensity.

The scattered evanescent light was measured with a glass prism underneath the tip and was used to correct the tip to sample gap. This is possible because it is well known that the scattered light intensity decreases exponentially with distance according to the Fresnel evanescent wave equation.

The right side of Fig. B.1 is the zoomed area marked on the left side, where the corrected tip to sample gap (TSG) scale is already applied.
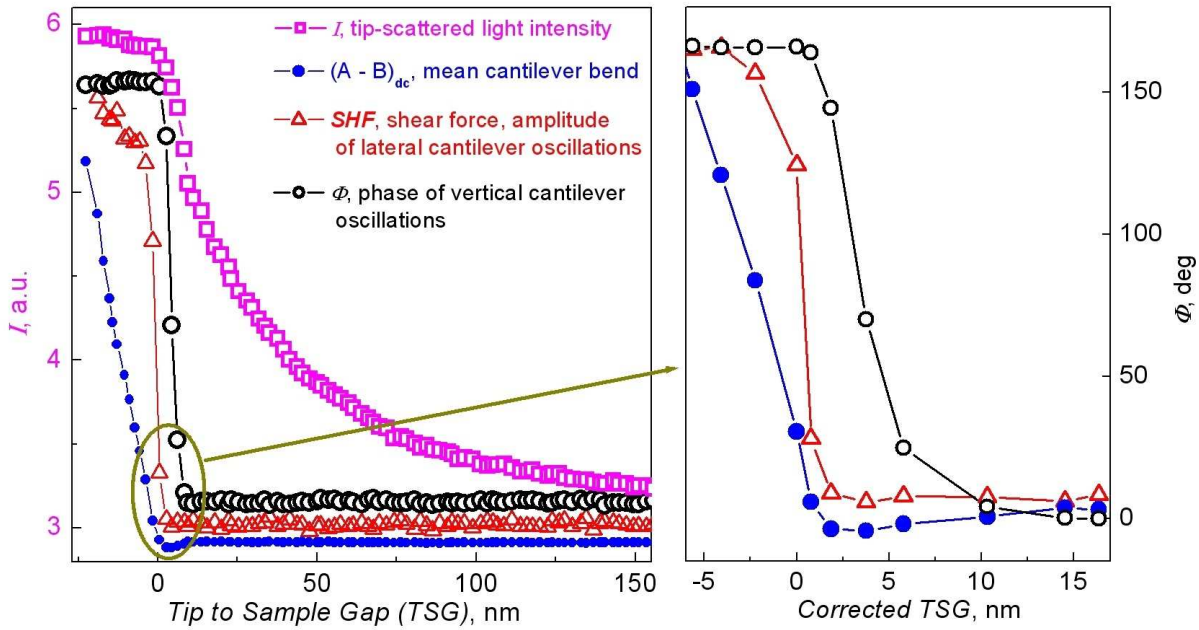
Fig. B.1: The measured parameters for tip to sample gap determination are shown. The steep dependency of the phase shift a few nanometres away from the surface, underlines its applicability as feedback signal for non-contact measurements. The corrected tip to sample gap (TSG) indicate the controllable TSG regime of 1-10 nm.

The sharp dependency of the phase shift on the distance between tip and substrate, underlines its applicability as feedback signal for non-contact measurements.

To use the phase shift as feedback signal a Lab View program was written to control all significant parameters. In Fig B.2 a screen shot of the used program is shown. The most important areas are marked with a red rectangle. The higher one includes the presets, which have to be defined before the approach starts e.g. starting frequency and amplitude, target phase and phase tolerance.

After the landing process the lower red rectangle becomes important because it informs about the quality of the tip to sample gap control. The narrower the phase histogram the more precise is the tip to sample control.
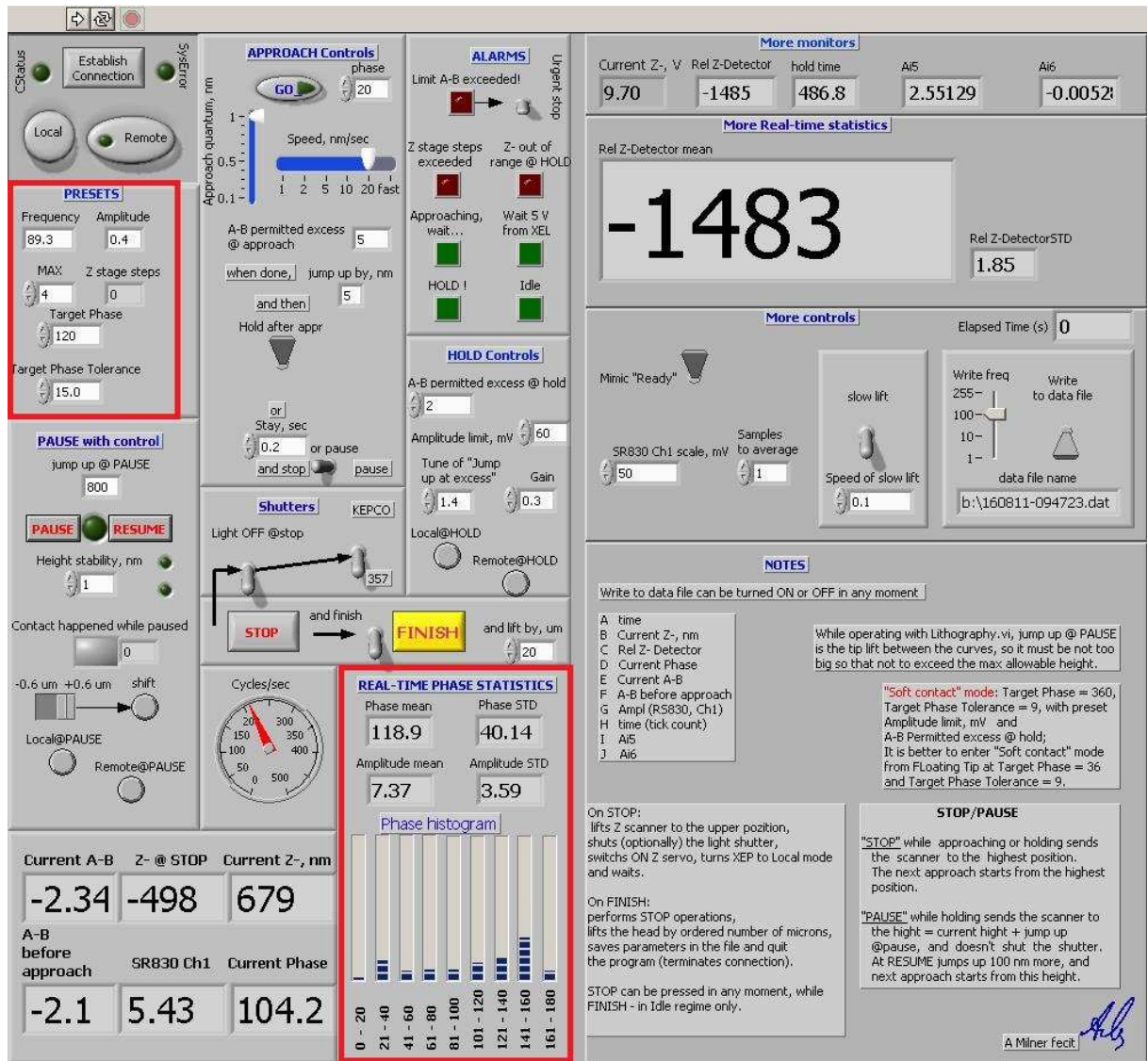
Fig. B.2: Lab View program for the control of the tip to sample gap at the Weizmann setup. The most important areas are marked with red rectangles.

It was proved experimentally in Ch. 3.2.3 that the position accuracy of the Floating Tip setup is better than 0.5 nm.

6 Literature

1.   Chong, T. C.; Hong, M. H.; Shi, L. P., Laser precision engineering: From microfabrication to nanoprocessing. *Laser and Photonics Reviews* **2010,** 4, (1), 123-143.
2.   Abbe, E., Beiträge zur Theorie des Mikroskops und der mikroskopischen Wahrnehmung. *Archiv für mikroskopische Anatomie* **1873,** 9, 413-468.
3.   Kawata S., S. V. M., *Tip enhancement*. Elsevier: Amsterdam, 2007.
4.   Sheats, J. R.; B.W., S., *Microlithography Science and Technology*. Marcel Dekker Inc.: New York, 1998.
5.   Ghislain, L. P.; Elings, V. B.; Crozier, K. B.; Manalis, S. R.; Minne, S. C.; Wilder, K.; Kino, G. S.; Quate, C. F., Near-field photolithography with a solid immersion lens. *Applied Physics Letters* **1999,** 74, (4), 501-503.
6.   Synge, E. H., A suggested model for extending microscopic resolution into the ultra-microscopic region. *Phil. Mag.* **1928,** 6, 356-362.
7.   Jackson, J. D., *Classical Electrodynamis*. John Wiley: New York, 1975.
8.   Hecht, B.; Bielefeldt, H.; Inouye, Y.; Pohl, D. W.; Novotny, L., Facts and artifacts in near-field optical microscopy. *Journal of Applied Physics* **1997,** 81, (6), 2492-2498.
9.   Kaupp, G., *Atomic Force Microscopy, Scanning Nearfield Optical Microscopy and Nanoscratching*. Springer Verlag: Heidelberg, 2006.
10.   Roth, R. M.; Panoiu, N. C.; Adams, M. M.; Osgood Jr, R. M.; Neacsu, C. C.; Raschke, M. B., Resonant-plasmon field enhancement from asymmetrically illuminated conical metallic-probe tips. *Optics Express* **2006,** 14, (7), 2921-2931.
11.   Bachelot, R.; H'Dhili, F.; Barchiesi, D.; Lerondel, G.; Fikri, R.; Royer, P.; Landraud, N.; Peretti, J.; Chaput, F.; Lampel, G.; Boilot, J. P.; Lahlil, K., Apertureless near-field optical microscopy: A study of the local tip field enhancement using photosensitive azobenzene-containing films. *Journal of Applied Physics* **2003,** 94, (3), 2060-2072.
12.   Esteban, R.; Vogelgesang, R.; Kern, K., Tip-substrate interaction in optical near-field microscopy. *Physical Review B - Condensed Matter and Materials Physics* **2007,** 75, (19).
13.   Hartschuh, A., Tip-enhanced near-field optical microscopy. *Angewandte Chemie - International Edition* **2008,** 47, (43), 8178-8191.
14.   Jersch, J.; Dickmann, K., Nanostructure fabrication using laser field enhancement in the near field of a scanning tunneling microscope tip. *Applied Physics Letters* **1996,** 68, (6), 868-870.
15.   Boneberg, J.; Münzer, H. J.; Tresp, M.; Ochmann, M.; Leiderer, P., The mechanism of nanostructuring upon nanosecond laser irradiation of a STM tip. *Applied Physics A: Materials Science and Processing* **1998,** 67, (4), 381-384.
16.   Mamin, H. J.; Rugar, D., Thermomechanical writing with an atomic force microscope tip. *Applied Physics Letters* **1992,** 61, (8), 1003-1005.
17.   Huang, S. M.; Hong, M. H.; Lu, Y. F.; Luká»³anchuk, B. S.; Song, W. D.; Chong, T. C., Pulsed-laser assisted nanopatterning of metallic layers combined with atomic force microscopy. *Journal of Applied Physics* **2002,** 91, (5), 3268-3274.
18.   Hwang, D.; Ryu, S. G.; Misra, N.; Jeon, H.; Grigoropoulos, C. P., Nanoscale laser processing and diagnostics. *Applied Physics A: Materials Science and Processing* **2009,** 96, (2), 289-306.
19.   Nolte, S.; Chichkov, B. N.; Welling, H.; Shani, Y.; Lieberman, K.; Terkel, H., Nanostructuring with spatially localized femtosecond laser pulses. *Optics Letters* **1999,** 24, (13), 914-916.

20.   Milner, A. A.; Zhang, K.; Karpovski, M.; Prior, Y., Apertureless near-field optics on commercial AFM: Tip to sample gap control. *Journal of Physics: Conference Series* **2008,** 100, (PART 5).
21.   Hohenester, U.; Krenn, J., Surface plasmon resonances of single and coupled metallic nanoparticles: A boundary integral method approach. *Physical Review B - Condensed Matter and Materials Physics* **2005,** 72, (19), 1-9.
22.   Wolf, E., *Progress in Optics*. Elsevier: Amsterdam, 2007.
23.   Synge, E. H., An application of piezo-electricity to microscopy. *Phil. Mag.* **1932,** 13, 297-300.
24.   Baez, V., Is resolving power independent of wavelength possible? An experiment with a sonic ´macroscope´. *Journal of the Optical Society of America* **1956,** 46, 901.
25.   McCutchen, C. W., Superresolution in microscopy and the Abbe resolution limit. *Journal of the Optical Society of America* **1967,** 57, (10), 1190-1192.
26.   Ash, E. A.; Nicholls, G., Super-resolution aperture scanning microscope. *Nature* **1972,** 237, (5357), 510-512.
27.   Pohl, D. W.; Denk, W.; Lanz, M., Optical stethoscopy: Image recording with resolution Î»/20. *Applied Physics Letters* **1984,** 44, (7), 651-653.
28.   Fischer, U. C.; Zingsheim, H. P., Submicroscopic contact imaging with visible light by energy transfer. *Applied Physics Letters* **1982,** 40, (3), 195-197.
29.   Lewis, A.; Isaacson, M.; Muray, A.; Harootunian, A., Scanning optical spectral microscopy with 500A spatial resolution. *Biophysical Journal* **1983,** 41, 405a.
30.   Harootunian, A.; Betzig, E.; Isaacson, M.; Lewis, A., Super-resolution fluorescence near-field scanning optical microscopy. *Applied Physics Letters* **1986,** 49, (11), 674-676.
31.   Fleischmann, M.; Hendra, P. J.; McQuillan, A. J., Raman spectra of pyridine adsorbed at a silver electrode. *Chemical Physics Letters* **1974,** 26, (2), 163-166.
32.   Jeanmaire, D. L.; Van Duyne, R. P., Surface Raman spectroelectrochemistry Part I. Heterocyclic, aromatic, and aliphatic amines adsorbed on the anodized silver electrode. *Journal of Electroanalytical Chemistry* **1977,** 84, (1), 1-20.
33.   Wessel, J., Surface enhanced optical microscopy. *Journal of the Optical Society of America B* **1985,** 2, 1538-1540.
34.   Betzig, E.; Trautman, J. K.; Harris, T. D.; Weiner, J. S.; Kostelak, R. L., Breaking the diffraction barrier: Optical microscopy on a nanometric scale. *Science* **1991,** 251, (5000), 1468-1470.
35.   Karrai, K.; Grober, R. D., Piezoelectric tip-sample distance control for near field optical microscopes. *Applied Physics Letters* **1995**, 1842.
36.   Trautman, J. K.; Macklin, J. J.; Brus, L. E.; Betzig, E., Near-field spectroscopy of single molecules at room temperature. *Nature* **1994,** 369, (6475), 40-42.
37.   Xie, X. S.; Trautman, J. K., Optical studies of single molecules at room temperature. In *Annual Review of Physical Chemistry*, 1998; Vol. 49, pp 441-480.
38.   Novotny, L.; Stranick, S. J., Near-field optical microscopy and spectroscopy with pointed probes. *Annual Review of Physical Chemistry* **2006,** 57, 303-331.
39.   Fischer, U. C.; Pohl, D. W., Observation of Single-Particle Plasmons by Near-Field Optical Microscopy. *Physical Review Letters* **1989,** 62, (4), 458-461.
40.   Inouye, Y.; Kawata, S., Near-field scanning optical microscope with a metallic probe tip. *Optics Letters* **1994,** 19, (3), 159-161.
41.   Kawata, S.; Inouye, Y., Scanning probe optical microscopy using a metallic probe tip. *Ultramicroscopy* **1995,** 57, (2-3), 313-317.
42.   Inouye, Y.; Kawata, S., Reflection-mode near-field optical microscope with a metallic probe tip for observing fine structures in semiconductor materials. *Optics Communications* **1997,** 134, (1-6), 31-35.

43.   Bachelot, R.; Gleyzes, P.; Boccara, A. C., Apertureless near field optical microscopy by local perturbation of a diffraction spot. *Ultramicroscopy* **1995,** 61, (1-4), 111-116.

44.   Gleyzes, P.; Boccara, A. C.; Bachelot, R., Near field optical microscopy using a metallic vibrating tip. *Ultramicroscopy* **1995,** 57, (2-3), 318-322.

45.   Bachelot, R.; Gleyzes, P.; Boccara, A. C., Reflection-mode scanning near-field optical microscopy using an apertureless metallic tip. *Applied Optics* **1997,** 36, (10), 2160-2170.

46.   Zenhausern, F.; O'Boyle, M. P.; Wickramasinghe, H. K., Apertureless near-field optical microscope. *Applied Physics Letters* **1994,** 65, (13), 1623-1625.

47.   Zenhausern, F.; Martin, Y.; Wickramasinghe, H. K., Scanning interferometric apertureless microscopy: Optical imaging at 10 angstrom resolution. *Science* **1995,** 269, (5227), 1083-1085.

48.   Martin, Y.; Zenhausern, F.; Wickramasinghe, H. K., Scattering spectroscopy of molecules at nanometer resolution. *Applied Physics Letters* **1996,** 68, (18), 2475-2477.

49.   Knoll, B.; Keilmann, F.; Kramer, A.; Guckenberger, R., Contrast of microwave near-field microscopy. *Applied Physics Letters* **1997,** 70, (20), 2667-2669.

50.   Knoll, B.; Keilmann, F., Scanning microscopy by mid-infrared near-field scattering. *Applied Physics A: Materials Science and Processing* **1998,** 66, (5), 477-481.

51.   Gorbunov, A. A.; Pompe, W., Thin film nanoprocessing by laser/STM combination. *Physica Status Solidi (A) Applied Research* **1994,** 145, (2), 333-338.

52.   Jersch, J.; Demming, F.; Hildenhagen, L. J.; Dickmann, K., Field enhancement of optical radiation in the nearfield of scanning probe microscope tips. *Applied Physics A: Materials Science and Processing* **1998,** 66, (1), 29-34.

53.   Dickmann, K.; Jersch, J.; Demming, F., Focusing of laser radiation in the near-field of a tip (FOLANT) for applications in nanostructuring. *Surface and Interface Analysis* **1997,** 25, (7-8), 500-504.

54.   Lu, Y. F.; Mai, Z. H.; Qiu, G.; Chim, W. K., Laser-induced nano-oxidation on hydrogen-passivated Ge (100) surfaces under a scanning tunneling microscope tip. *Applied Physics Letters* **1999,** 75, (16), 2359-2361.

55.   Lu, Y. F.; Hu, B.; Mai, Z. H.; Wang, W. J.; Chim, W. K.; Chong, T. C., Laser-scanning probe microscope based nanoprocessing of electronics materials. *Japanese Journal of Applied Physics, Part 1: Regular Papers and Short Notes and Review Papers* **2001,** 40, (6 B), 4395-4398.

56.   Jersch, J.; Demming, F.; Hildenhagen, J.; Dickmann, K., Nano-material processing with laser radiation in the near field of a scanning probe tip. *Optics and Laser Technology* **1998,** 29, (8), 433-437.

57.   Jersch, J.; Demming, F.; Dickmann, K., Nanostructuring with laser radiation in the near field of a tip from a scanning force microscope. *Applied Physics A: Materials Science and Processing* **1998,** 64, (1), 29-32.

58.   Huber, R.; Koch, M.; Feldmann, J., Laser-induced thermal expansion of a scanning tunneling microscope tip measured with an atomic force microscope cantilever. *Applied Physics Letters* **1998,** 73, (17), 2521-2523.

59.   Ukraintsev, V. A.; Yates Jr, J. T., Nanosecond laser induced single atom deposition with nanometer spatial resolution using a STM. *Journal of Applied Physics* **1996,** 80, (5), 2561-2571.

60.   Boneberg, J.; Münzer, H. J.; Tresp, M.; Ochmann, M.; Leiderer, P., The mechanism of nanostructuring upon nanosecond laser irradiation of a STM tip. *Applied Physics A: Materials Science and Processing* **1998,** 67, (4), 381-384.

61.   Boneberg, J.; Tresp, M.; Ochmann, M.; Münzer, H. J.; Leiderer, P., Time-resolved measurements of the response of a STM tip upon illumination with a nanosecond laser pulse. *Applied Physics A: Materials Science and Processing* **1998,** 66, (6), 615-619.

62.   Lyubinetsky, I.; DohnÃ¡lek, Z.; Ukraintsev, V. A.; Yates Jr, J. T., Transient tunneling current in laser-assisted scanning tunneling microscopy. *Journal of Applied Physics* **1997,** 82, (8), 4115-4117.

63.   Zayats, A.; Richards, D., *Nano-Optics and Near-Field Optical Microscopy*. Artech House: Boston/London, 2009.

64.   Ohtsu, M.; Kobayashi, K., *Optical Near Fields*. Springer Verlag: Berlin Heidelberg, 2004.

65.   Bethe, H. A., Theory of Diffraction by Small Holes. *Physical Review* **1944,** 66, (7-8), 163-182.

66.   Bouwkamp, C. J., On Bethe´s theory of diffraction by small holes. *Philips Res Rep.* **1950,** 5, 321-332.

67.   Wurtz, G.; Bachelot, R.; Royer, P., A reflection-mode apertureless scanning near-field optical microscope developed from a commercial scanning probe microscope. *Review of Scientific Instruments* **1998,** 69, (4), 1735-1743.

68.   Koglin, J.; Fischer, U. C.; Fuchs, H., Material contrast in scanning near-field optical microscopy at 1â€"10 nm resolution.*Physical Review B* **1997,** 55, (12), 7977-7984.

69.   Fillards, J. P., *Near Field Optics and Nanoscopy*. World Scientific: Singapore, 1996.

70.   Lieberman, K.; Lewis, A., Simultaneous scanning tunneling and optical near-field imaging with a micropipette. *Applied Physics Letters* **1993,** 62, (12), 1335-1337.

71.   Jackson, J. D., *Classical Electrodynamics*. John Wiley: New York, 1975.

72.   Kawata, S.; Ohtsu, M.; Irie, M., *Nano-Optics*. Springer Verlag: Berlin Heidelberg Newyourk, 2002.

73.   Hamann, H. F.; Gallagher, A.; Nesbitt, D. J., Enhanced sensitivity near-field scanning optical microscopy at high spatial resolution. *Applied Physics Letters* **1998,** 73, (11), 1469-1471.

74.   Haefliger, D.; Plitzko, J. M.; Hillenbrand, R., Contrast and scattering efficiency of scattering-type near-field optical probes. *Applied Physics Letters* **2004,** 85, (19), 4466-4468.

75.   Esteban, R.; Vogelgesang, R.; Kern, K., Simulation of optical near and far fields of dielectric apertureless scanning probes. *Nanotechnology* **2006,** 17, (2), 475-482.

76.   Krug Ii, J. T.; SaÌ nchez, E. J.; Xie, X. S., Design of near-field optical probes with optimal field enhancement by finite difference time domain electromagnetic simulation. *Journal of Chemical Physics* **2002,** 116, (24), 10895-10901.

77.   Knoll, B.; Keilmann, F., Mid-infrared scanning near-field optical microscope resolves 30 nm. *Journal of Microscopy* **1999,** 194, (2-3), 512-515.

78.   Hayazawa, N.; Inouye, Y.; Sekkat, Z.; Kawata, S., Near-field Raman imaging of organic molecules by an apertureless metallic probe scanning optical microscope. *Journal of Chemical Physics* **2002,** 117, (3), 1296-1301.

79.   Adam, P. M.; Benrezzak, S.; Bijeon, J. L.; Royer, P., Localized surface plasmons on nanometric gold particles observed with an apertureless scanning near-field optical microscope. *Journal of Applied Physics* **2000,** 88, (11), 6919-6921.

80.   Hillenbrand, R.; Keilmann, F., Complex optical constants on a subwavelength scale. *Physical Review Letters* **2000,** 85, (14), 3029-3032.

81.   Aigouy, L.; AndrÃ©ani, F. X.; Boccara, A. C.; Rivoal, J. C.; Porto, J. A.; Carminati, R.; Greffet, J. J.; MÃ©gy, R., Near-field optical spectroscopy using an incoherent light source. *Applied Physics Letters* **2000,** 76, (4), 397-399.

82.   Sasaki, Y.; Sasaki, H., Heterodyne detection for the extraction of the probe-scattering signal in scattering-type scanning near-field optical microscope. *Japanese Journal of Applied Physics, Part 2: Letters* **2000,** 39, (4 A), L321-L323.

83.   Akhremitchev, B. B.; Pollack, S.; Walker, G. C., Apertureless scanning near-field infrared microscopy of a rough polymeric surface. *Langmuir* **2001,** 17, (9), 2774-2781.

84.   Lahrech, A.; Bachelot, R.; Gleyzes, P.; Boccara, A. C., Infrared-reflection-mode near-field microscopy using an apertureless probe with a resolution of Î»/600. *Optics Letters* **1996,** 21, (17), 1315-1317.

85.   Kim, J.; Song, K. B., Recent progress of nano-technology with NSOM. *Micron* **2007,** 38, (4), 409-426.

86.   Hoffmann, P.; Dutoit, B.; SalatheÌ, R. P., Comparison of mechanically drawn and protection layer chemically etched optical fiber tips. *Ultramicroscopy* **1995,** 61, (1-4), 165-170.

87.   Zeisel, D.; Nettesheim, S.; Dutoit, B.; Zenobi, R., Pulsed laser-induced desorption and optical imaging on a nanometer scale with scanning near-field microscopy using chemically etched fiber tips. *Applied Physics Letters* **1996,** 68, (18), 2491-2492.

88.   Stöckle, R.; Fokas, C.; Deckert, V.; Zenobi, R.; Sick, B.; Hecht, B.; Wild, U. P., High-quality near-field optical probes by tube etching. *Applied Physics Letters* **1999,** 75, (2), 160-162.

89.   Valaskovic, G. A.; Holton, M.; Morrison, G. H., Parameter control, characterization, and optimization in the fabrication of optical fiber near-field probes. *Applied Optics* **1995,** 34, (7), 1215-1228.

90.   Hecht, B.; Sick, B.; Wild, U. P.; Deckert, V.; Zenobi, R.; Martin, O. J. F.; Pohl, D. W., Scanning near-field optical microscopy with aperture probes: Fundamentals and applications. *Journal of Chemical Physics* **2000,** 112, (18), 7761-7774.

91.   Fischer, U. C.; Koglin, J.; Fuchs, H., The tetrahedral tip as a probe for scanning near-field optical microscopy at 30 nm resolution. *Journal of Microscopy* **1994,** 176, (3), 231-237.

92.   Yatsui, T.; Kourogi, M.; Ohtsu, M., Highly efficient excitation of optical near-field on an apertured fiber probe with an asymmetric structure. *Applied Physics Letters* **1997,** 71, (13), 1756-1758.

93.   Yatsui, T.; Kourogi, M.; Ohtsu, M., Increasing throughput of a near-field optical fiber probe over 1000 times by the use of a triple-tapered structure. *Applied Physics Letters* **1998,** 73, (15), 2090-2092.

94.   Yatsui, T.; Itsumi, K.; Kourogi, M.; Ohtsu, M., Metallized pyramidal silicon probe with extremely high throughput and resolution capability for optical near-field technology. *Applied Physics Letters* **2002,** 80, (13), 2257-2259.

95.   Mononobe, S.; Saiki, T.; Suzuki, T.; Koshihara, S.; Ohtsu, M., Fabrication of a triple tapered probe for near-field optical spectroscopy in UV region based on selective etching of a multistep index fiber. *Optics Communications* **1998,** 146, (1-6), 45-48.

96.   Frey, H. G.; Keilmann, F.; Kriele, A.; Guckenberger, R., Enhancing the resolution of scanning near-field optical microscopy by a metal tip grown on an aperture probe. *Applied Physics Letters* **2002,** 81, (26), 5030-5032.

97.   Frey, H. G.; Witt, S.; Felderer, K.; Guckenberger, R., High-resolution imaging of single fluorescent molecules with the optical near-field of a metal tip. *Physical Review Letters* **2004,** 93, (20), 200801-1-200801-4.

98.   Naber, A.; Molenda, D.; Fischer, U. C.; Maas, H. J.; HÃ¶ppener, C.; Lu, N.; Fuchs, H., Enhanced light confinement in a near-field optical probe with a triangular aperture. *Physical Review Letters* **2002,** 89, (21), 2108011-2108014.

99.   Kneipp, K.; Kneipp, H.; Corio, P.; Brown, S. D. M.; Shafer, K.; Motz, J.; Perelman, L. T.; Hanlon, E. B.; Marucci, A.; Dresselhaus, G.; Dresselhaus, M. S., Surface-Enhanced and Normal Stokes and Anti-Stokes Raman Spectroscopy of Single-Walled Carbon Nanotubes. *Physical Review Letters* **2000,** 84, (15), 3470-3473.

100.   Kawata, S., *Near-Field Optics and Surface Plasmon Polaritons*. Springer Verlag: Heidelberg/Berlin/New York, 2001.

101.   Kreibig, U.; M., V., *Optical Properties of metal clusters*. Springer Verlag: Berlin, 1994.

_____

102.   Bohren, C. F.; Huffman, D. R., *Absorption and scattering of light by small particles* Wiley: New York, 1998.

103.   Raether, H., *Surface plasmons on smooth and rough surfaces and gratings*. Springer Verlag: Berlin, 1988.

104.   Mallan, Y. C., *Physics of lightning*. English University Press: London, 1963.

105.   Zeleny, J., Do lightning rods prevent lightning. *Science* **1932,** 79, 269-271.

106.   Novotny, L.; Bian, R. X.; Sunney Xie, X., Theory of Nanometric optical tweezers. *Physical Review Letters* **1997,** 79, (4), 645-648.

107.   Hafner, C., *The generalized multiple multipole technique for computional electromagnetics*. Artech House: Boston, 1990.

108.   Stutzman, W. L.; Thiele, G. A., *Antenna Theory and Design*. Wiley, 1998.

109.   Hertz, H., *Electric waves : being researches on the propagation of electric action with finite velocity through space*. Dover Publication: New York, 1962.

110.   McAlister, A. J.; Stern, E. A., Plasma resonance absorption in thin metal films. *Physical Review* **1963,** 132, (4), 1599-1602.

111.   Denk, W.; Pohl, D. W., Near-field optics: Microscopy with nanometre-size fields. *Journal of Vacuum Science and Technology B* **1991,** 9, (2), 510.

112.   Wang, Y.; Kempa, K.; Kimball, B.; Carlson, J. B.; Benham, G.; Li, W. Z.; Kempa, T.; Rybczynski, J.; Herczynski, A.; Ren, Z. F., Receiving and transmitting light-like radio waves: Antenna effect in arrays of aligned carbon nanotubes. *Applied Physics Letters* **2004,** 85, (13), 2607-2609.

113.   Grober, R. D.; Schoelkopf, R. J.; Prober, D. E. High efficiency near-field electromagnetic probe having a bowtie antenna structure. 5696372, 1997.

114.   Fumeaux, C.; Gritz, M. A.; Codreanu, I.; Schaich, W. L.; GonzÃ¡lez, F. J.; Boreman, G. D., Measurement of the resonant lengths of infrared dipole antennas. *Infrared Physics and Technology* **2000,** 41, (5), 271-281.

115.   Fumeaux, C.; Baumann, D.; Vahldieck, R., Advanced FVTD simulation of dielectric resonator antennas and feed structures. *Applied Computational Electromagnetics Society Journal* **2004,** 19, (3), 155-164.

116.   Gonzalez, F. J.; Boreman, G. D., Comparison of dipole, bowtie, spiral and log-periodic IR antennas. *Infrared Physics and Technology* **2005,** 46, (5), 418-428.

117.   Sundaramurthy, A.; Schuck, P. J.; Conley, N. R.; Fromm, D. P.; Kino, G. S.; Moerner, W. E., Toward nanometer-scale optical photolithography: Utilizing the near-field of bowtie optical nanoantennas. *Nano Letters* **2006,** 6, (3), 355-360.

118.   Markel, V. A.; George, T. F., *Optics of nanostructured Materials*. Wiley: New York, 2001.

119.   Martin, O. J. F.; Girard, C., Controlling and tuning strong optical field gradients at a local probe microscope tip apex. *Applied Physics Letters* **1997,** 70, (6), 705-707.

120.   Martin, Y. C.; Hamann, H. F.; Wickramasinghe, H. K., Strength of the electric field in apertureless near-field optical microscopy. *Journal of Applied Physics* **2001,** 89, (10), 5774-5778.

121.   Bohn, J. L.; Nesbitt, D. J.; Gallagher, A., Field enhancement in apertureless near-field scanning optical microscopy. *Journal of the Optical Society of America A: Optics and Image Science, and Vision* **2001,** 18, (12), 2998-3006.

122.   Knoll, B.; Keilmann, F., Enhanced dielectric contrast in scattering-type scanning near-field optical microscopy. *Optics Communications* **2000,** 182, (4), 321-328.

123.   Aravind, P. K.; Metiu, H., The effects of the interaction between resonances in the electromagnetic response of a sphere-plane structure; applications to surface enhanced spectroscopy. *Surface Science* **1983,** 124, (2-3), 506-528.

124.   Knoll, B.; Keilmann, F., Near-field probing of vibrational absorption for chemical microscopy. *Nature* **1999,** 399, (6732), 134-137.

125.   Hecht, B.; Novotny, L., *Principles of Nano-Optics*. Cambridge Univeristy Press: New York, 2006.

126.   Hillenbrand, R.; Knoll, B.; Keilmann, F., Pure optical contrast in scattering-type scanning near-field microscopy. *Journal of Microscopy* **2001,** 202, (1), 77-83.

127.   Hillenbrand, R.; Taubner, T.; Keilmann, F., Phonon-enhanced light-matter interaction at the nanometre scale. *Nature* **2002,** 418, (6894), 159-162.

128.   Chimmalgi, A.; Grigoropoulos, C. P.; Komvopoulos, K., Surface nanostructuring by nano-/femtosecond laser-assisted scanning force microscopy. *Journal of Applied Physics* **2005,** 97, (10), 1-12.

129.   Milner, A. A.; Zhang, K.; Garmider, V.; Prior, Y., Heating of an Atomic Force Microscope tip by femtosecond laser pulses. *Applied Physics A: Materials Science and Processing* **2010,** 99, (1), 1-8.

130.   Wang, Z. B.; Luk'Yanchuk, B. S.; Li, L.; Crouse, P. L.; Liu, Z.; Dearden, G.; Watkins, K. G., Optical near-field distribution in an asymmetrically illuminated tip-sample system for laser/STM nanopatterning. *Applied Physics A: Materials Science and Processing* **2007,** 89, (2), 363-368.

131.   Geshev, P. I.; Demming, F.; Jersch, J.; Dickmann, K., Calculation of the temperature distribution on laser-illuminated scanning probe tips. *Applied Physics B: Lasers and Optics* **2000,** 70, (1), 91-97.

132.   Jersch, J.; Demming, F.; Hildenhagen, J.; Dickmann, K., Nano-material processing with laser radiation in the near field of a scanning probe tip. *Optics and Laser Technology* **1997,** 29, (8), 433-437.

133.   Royer, P.; Barchiesi, D.; Lerondel, G.; Bachelot, R., Near-field optical patterning and structuring based on local-field enhancement at the extremity of a metal tip. *Philosophical Transactions of the Royal Society A: Mathematical, Physical and Engineering Sciences* **2004,** 362, (1817), 821-842.

134.   Wurtz, G.; Bachelot, R.; H'Dhili, F.; Triger, P. R. C.; Ecoffet, C.; Lougnot, D. J., Photopolymerization induced by optical field enhancement in the vicinity of a conducting tip under laser illumination. *Japanese Journal of Applied Physics, Part 2: Letters* **2000,** 39, (2 A), L98-L100.

135.   Aigouy, L.; Lahrech, A.; Grésillon, S.; Cory, H.; Boccara, A. C.; Rivoal, J. C., Polarization effects in apertureless scanning near-field optical microscopy: An experimental study. *Optics Letters* **1999,** 24, (4), 187-189.

136.   Yin, X.; Fang, N.; Zhang, X.; Martini, I. B.; Schwartz, B. J., Near-field two-photon nanolithography using an apertureless optical probe. *Applied Physics Letters* **2002,** 81, (19), 3663-3665.

137.   Natansohn, A.; Rochon, P., Photoinduced motions in azo-containing polymers. *Chemical Reviews* **2002,** 102, (11), 4139-4175.

138.   Davy, S.; Spajer, M., Near field optics: Snapshot of the field emitted by a nanosource using a photosensitive polymer. *Applied Physics Letters* **1996,** 69, (22), 3306-3308.

139.   Chimmalgi, A.; Choi, T. Y.; Grigoropoulos, C. P.; Komvopoulos, K., Femtosecond laser aperturless near-field nanomachining of metals assisted by scanning probe microscopy. *Applied Physics Letters* **2003,** 82, (8), 1146-1148.

140.   Hong, M.; Lim, C. S.; Zhou, Y.; Tan, L. S.; Shi, L.; Chong, T. C., Surface Nano-fabrication by Laser Precision Engineering. *APLS The Review of Laser Engineering* **2008,** 36.

141.   Yin, X.; Fang, N.; Zhang, X.; Martini, I. B.; Schwartz, B. J. In *Near-Field Multiphoton Nanolithography Using an Apertureless Optical Probe*, Proceedings of SPIE - The International Society for Optical Engineering, 2003; 2003; pp 96-103.

142.   Milner, A. A.; Zhang, K.; Prior, Y., Floating tip nanolithography. *Nano Letters* **2008,** 8, (7), 2017-2022.

143.   Guo, S. X.; Ben-Yakar, A., Femtosecond laser nanoablation of glass in the near-field of single wall carbon nanotube bundles. *Journal of Physics D: Applied Physics* **2008,** 41, (18).

144.   Wang, S., Antenna properties and operation of metal-barrier-metal devices in the infrared and visible regions. *Applied Physics Letters* **1976,** 28, (6), 303-305.

145.   Wang, S., Erratum: Antenna properties and operation of metal-barrier-metal devices in the infrared and visible regions((Applied Physics Letter) (1976) 28 8 (518)). *Applied Physics Letters* **1976,** 29, (8), 518.

146.   Völcker, M.; Krieger, W.; Walther, H., Laser-frequency mixing in a scanning force microscope and its application to detect local conductivity. *Journal of Vacuum Science and Technology B* **1994,** 12, (3), 2129-2132.

147.   Kim, Z. H.; Liu, B.; Leone, S. R., Nanometer-scale optical imaging of epitaxially grown GaN and InN islands using apertureless near-field microscopy. *Journal of Physical Chemistry B* **2005,** 109, (17), 8503-8508.

148.   Ocelic, N.; Hillenbrand, R., Subwavelength-scale tailoring of surface phonon polaritons by focused ion-beam implantation. *Nature Materials* **2004,** 3, (9), 606-609.

149.   Brehm, M.; Taubner, T.; Hillenbrand, R.; Keilmann, F., Infrared spectroscopic mapping of single nanoparticles and viruses at nanoscale resolution. *Nano Letters* **2006,** 6, (7), 1307-1310.

150.   Huber, A.; Ocelic, N.; Taubner, T.; Hillenbrand, R., Nanoscale resolved infrared probing of crystal structure and of plasmon-phonon coupling. *Nano Letters* **2006,** 6, (4), 774-778.

151.   Huber, A. J.; Kazantsev, D.; Keilmann, F.; Wittborn, J.; Hillenbrand, R., Simultaneous IR material recognition and conductivity mapping by nanoscale near-field microscopy. *Advanced Materials* **2007,** 19, (17), 2209-2212.

152.   Hillenbrand, R.; Keilmann, F., Material-specific mapping of metal/semiconductor/dielectric nanosystems at 10 nm resolution by backscattering near-field optical microscopy. *Applied Physics Letters* **2002,** 80, (1), 25-27.

153.   Cvitkovic, A.; Ocelic, N.; Hillenbrand, R., Analytical model for quantitative prediction of material contrasts in scattering-type near-field optical microscopy. *Optics Express* **2007,** 15, (14), 8550-8565.

154.   Raschke, M. B.; Lienau, C., Apertureless near-field optical microscopy: Tip-sample coupling in elastic light scattering. *Applied Physics Letters* **2003,** 83, (24), 5089-5091.

155.   Renger, J.; Grafström, S.; Eng, L. M.; Hillenbrand, R., Erratum: Resonant light scattering by near-field-induced phonon polaritons (Physical Review B (2005) 71 (075410)). *Physical Review B - Condensed Matter and Materials Physics* **2005,** 71, (11), 1.

156.   Renger, J.; Grafström, S.; Eng, L. M.; Hillenbrand, R., Resonant light scattering by near-field-induced phonon polaritons. *Physical Review B - Condensed Matter and Materials Physics* **2005,** 71, (7), 1-7.

157.   Ocelic, N.; Huber, A.; Hillenbrand, R., Pseudoheterodyne detection for background-free near-field spectroscopy. *Applied Physics Letters* **2006,** 89, (10).

158.   Taubner, T.; Hillenbrand, R.; Keilmann, F., Performance of visible and mid-infrared scattering-type near-field optical microscopes. *Journal of Microscopy* **2003,** 210, (3), 311-314.

159.   Knoll, B.; Keilmann, F., Infrared conductivity mapping for nanoelectronics. *Applied Physics Letters* **2000,** 77, (24), 3980-3982.

160.   Taubner, T.; Keilmann, F.; Hillenbrand, R., Nanomechanical resonance tuning and phase effects in optical near-field interaction. *Nano Letters* **2004,** 4, (9), 1669-1672.

161.   Hillenbrand, R.; Keilmann, F.; Hanarp, P.; Sutherland, D. S.; Aizpurua, J., Coherent imaging of nanoscale plasmon patterns with a carbon nanotube optical probe. *Applied Physics Letters* **2003,** 83, (2), 368-370.

162.   Samson, J. S.; Wollny, G.; Bründermann, E.; Bergner, A.; Hecker, A.; Schwaab, G.; Dirk Wieck, A.; Havenith, M., Setup of a scanning near field infrared microscope (SNIM): Imaging of sub-surface nano-structures in gallium-doped silicon. *Physical Chemistry Chemical Physics* **2006,** 8, (6), 753-758.

163.   Nie, S.; Emory, S. R., Probing single molecules and single nanoparticles by surface-enhanced Raman scattering. *Science* **1997,** 275, (5303), 1102-1106.

164.   Pettinger, B.; Ren, B.; Picardi, G.; Schuster, R.; Ertl, G., Nanoscale probing of adsorbed species by tip-enhanced Raman spectroscopy. *Physical Review Letters* **2004,** 92, (9), 096101-1.

165.   Pettinger, B.; Ren, B.; Picardi, G.; Schuster, R.; Ertl, G., Tip-enhanced Raman spectroscopy (TERS) of malachite green isothiocyanate at Au(111): Bleaching behavior under the influence of high electromagnetic fields. *Journal of Raman Spectroscopy* **2005,** 36, (6-7), 541-550.

166.   Ren, B.; Picardi, G.; Pettinger, B., Preparation of gold tips suitable for tip-enhanced Raman spectroscopy and light emission by electrochemical etching. *Review of Scientific Instruments* **2004,** 75, (4), 837-841.

167.   Kawata, S.; V.M., S., *Tip enhancement*. Elsevier: Amsterdam, 2007.

168.   Stöckle, R.; Setz, P.; Deckert, V.; Lippert, T.; Wokaun, A.; Zenobi, R., Nanoscale atmospheric pressure laser ablation-mass spectrometry. *Analytical Chemistry* **2001,** 73, (7), 1399-1402.

169.   Nieman, L. T.; Krampert, G. M.; Martinez, R. E., An apertureless near-field scanning optical microscope and its application to surface-enhanced Raman spectroscopy and multiphoton fluorescence imaging. *Review of Scientific Instruments* **2001,** 72, (3), 1691-1699.

170.   Stokes, D. L.; Chi, Z.; Vo-Dinh, T., Surface-Enhanced-Raman-Scattering-Inducing Nanoprobe for Spectrochemical Analysis. *Applied Spectroscopy* **2004,** 58, (3), 292-298.

171.   Hartschuh, A.; Anderson, N.; Novotny, L., Near-field Raman spectroscopy using a sharp metal tip. *Journal of Microscopy* **2003,** 210, (3), 234-240.

172.   Hayazawa, N.; Inouye, Y.; Sekkat, Z.; Kawata, S., Metallized tip amplification of near-field Raman scattering. *Optics Communications* **2000,** 183, (1), 333-336.

173.   Patanè, S.; Gucciardi, P. G.; Labardi, M.; Allegrini, M., Apertureless near-field optical microscopy. *Rivista del Nuovo Cimento* **2004,** 27, (1).

174.   Hartschuh, A.; Sánchez, E. J.; Xie, X. S.; Novotny, L., High-resolution near-field Raman microscopy of single-walled carbon nanotubes. *Physical Review Letters* **2003,** 90, (9), 095503/1-095503/4.

175.   Bulgarevich, D. S.; Futamata, M., Apertureless tip-enhanced Raman microscopy with confocal epi-illumination/collection optics. *Applied Spectroscopy* **2004,** 58, (7), 757-761.

176.   Mills, D. L., Theory of STM-induced enhancement of dynamic dipole moments on crystal surfaces. *Physical Review B - Condensed Matter and Materials Physics* **2002,** 65, (12), 1254191-12541911.

177.   Demming, A. L.; Festy, F.; Richards, D., Plasmon resonances on metal tips: Understanding tip-enhanced Raman scattering. *Journal of Chemical Physics* **2005,** 122, (18), 1-7.

178.   Mehtani, D.; Lee, N.; Hartschuh, R. D.; Kisliuk, A.; Foster, M. D.; Sokolov, A. P.; Maguire, J. F., Nano-Raman spectroscopy with side-illumination optics. *Journal of Raman Spectroscopy* **2005,** 36, (11), 1068-1075.

179.   Stöckle, R. M.; Suh, Y. D.; Deckert, V.; Zenobi, R., Nanoscale chemical analysis by tip-enhanced Raman spectroscopy. *Chemical Physics Letters* **2000,** 318, (1-3), 131-136.

180.   Cancado, L. G.; Hartschuh, A.; Novotny, L., Tip-enhanced Raman spectroscopy of carbon nanotubes. *Journal of Raman Spectroscopy* **2009,** 40, (10), 1420-1426.

181.   Anderson, N.; Hartschuh, A.; Cronin, S.; Novotny, L., Nanoscale vibrational analysis of single-walled carbon nanotubes. *Journal of the American Chemical Society* **2005,** 127, (8), 2533-2537.

182.   Bouhelier, A.; Beversluis, M.; Hartschuh, A.; Novotny, L., Near-field second-harmonic generation induced by local field enhancement. *Physical Review Letters* **2003,** 90, (1), 013903/1-013903/4.

183.   Saito, Y.; Hayazawa, N.; Kataura, H.; Murakami, T.; Tsukagoshi, K.; Inouye, Y.; Kawata, S., Polarization measurements in tip-enhanced Raman spectroscopy applied to single-walled carbon nanotubes. *Chemical Physics Letters* **2005,** 410, (1-3), 136-141.

184.   Watanabe, H.; Ishida, Y.; Hayazawa, N.; Inouye, Y.; Kawata, S., Tip-enhanced near-field Raman analysis of tip-pressurized adenine molecule. *Physical Review B - Condensed Matter and Materials Physics* **2004,** 69, (15), 155418-1-155418-11.

185.   Hayazawa, N.; Ichimura, T.; Hashimoto, M.; Inouye, Y.; Kawata, S., Amplification of coherent anti-Stokes Raman scattering by a metallic nanostructure for a high resolution vibration microscopy. *Journal of Applied Physics* **2004,** 95, (5), 2676-2681.

186.   Ichimura, T.; Hayazawa, N.; Hashimoto, M.; Inouye, Y.; Kawata, S., Application of tip-enhanced microscopy for nonlinear Raman spectroscopy. *Applied Physics Letters* **2004,** 84, (10), 1768-1770.

187.   Tian, Z. Q.; Ren, B.; Wu, D. Y., Surface-enhanced Raman scattering: From noble to transition metals and from rough surfaces to ordered nanostructures. *Journal of Physical Chemistry B* **2002,** 106, (37), 9463-9483.

188.   Hell, S. W., Far-field optical nanoscopy. *Science* **2007,** 316, (5828), 1153-1158.

189.   Lewis, A.; Lieberman, K., Near-field optical imaging with a non-evanescently excited high-brightness light source of sub-wavelength dimensions. *Nature* **1991,** 354, (6350), 214-216.

190.   Trabesinger, W.; Kramer, A.; Kreiter, M.; Hecht, B.; Wild, U. P., Single-molecule near-field optical energy transfer microscopy. *Applied Physics Letters* **2002,** 81, (11), 2118-2120.

191.   Hu, D.; Micic, M.; Klymyshyn, N.; Suh, Y. D.; Lu, H. P., Correlated topographic and spectroscopic imaging beyond diffraction limit by atomic force microscopy metallic tip-enhanced near-field fluorescence lifetime microscopy. *Review of Scientific Instruments* **2003,** 74, (7), 3347-3355.

192.   Anger, P.; Bharadwaj, P.; Novotny, L., Enhancement and quenching of single-molecule fluorescence. *Physical Review Letters* **2006,** 96, (11), 1-4.

193.   Azoulay, J.; DÃ©barre, A.; Richard, A.; TchÃ©nio, P., Quenching and enhancement of single-molecule fluorescence under metallic and dielectric tips. *Europhysics Letters* **2000,** 51, (4), 374-380.

194.   Chance, R. R.; Prock, A.; Silbey, R., Lifetime of an emitting molecule near a partially reflecting surface. *The Journal of Chemical Physics* **1974,** 60, (7), 2749-2758.

195.   Chance, R. R.; Prock, A.; Silbey, R., Comments on the classical theory of energy transfer. II. Extension to higher multipoles and anisotropic media. *The Journal of Chemical Physics* **1976,** 65, (7), 2527-2531.

196.   Chance, R. R.; Prock, A.; Silbey, R., Erratum: Comments on the classical theory of energy transfer. II. Extension to higher multipoles and anisotropic media (The Journal of Chemical Physics (1976) 65 (2527)). *The Journal of Chemical Physics* **1976,** 66, (4), 1765.

197.   Kawata, Y.; Xu, C.; Denk, W., Feasibility of molecular-resolution fluorescence near-field microscopy using multi-photon absorption and field enhancement near a sharp tip. *Journal of Applied Physics* **1999,** 85, (3), 1294-1301.

198.   Gerton, J. M.; Wade, L. A.; Lessard, G. A.; Ma, Z.; Quake, S. R., Tip-Enhanced Fluorescence Microscopy at 10 Nanometer Resolution. *Physical Review Letters* **2004,** 93, (18), 180801.

199.   Novotny, L., Near-field optical characterization of nanocomposite materials. *Journal of the American Ceramic Society* **2002,** 85, (5), 1057-1060.

200.   Sanchez, E. J.; Novotny, L.; Xie, X. S., Near-Field Fluorescence Microscopy Based on Two-Photon Excitation with Metal Tips. *Physical Review Letters* **1999,** 82, (20), 4014-4017.

201.   Hayazawa, N.; Furusawa, K.; Taguchi, A.; Kawata, S., One-photon and two-photon excited fluorescence microscopies based on polarization-control: Applications to tip-enhanced microscopy. *Journal of Applied Physics* **2009,** 106, (11).

202.   Hayazawa, N.; Furusawa, K.; Taguchi, A.; Kawata, S.; Abe, H., Tip-enhanced two-photon excited fluorescence microscopy with a silicon tip. *Applied Physics Letters* **2009,** 94, (19).

203.   Nowak, D. B.; Lawrence, A. J.; SÃ¡nchez, E. J., Apertureless near-field/far-field CW two-photon microscope for biological and material imaging and spectroscopic applications. *Applied Optics* 49, (35), 6766-6771.

204.   Hartschuh, A.; Beversluis, M. R.; Bouhelier, A.; Novotny, L., Tip-enhanced optical spectroscopy. *Philosophical Transactions of the Royal Society A: Mathematical, Physical and Engineering Sciences* **2004,** 362, (1817), 807-819.

205.   Frey, H. G.; Paskarbeit, J.; Anselmetti, D., Tip-enhanced single molecule fluorescence near-field microscopy in aqueous environment. *Applied Physics Letters* **2009,** 94, (24).

206.   Zayats, A. V.; Sandoghdar, V., Apertureless scanning near-field second-harmonic microscopy. *Optics Communications* **2000,** 178, (1), 245-249.

207.   Zayats, A. V.; Sandoghdar, V., Apertureless near-field optical microscopy via local second-harmonic generation. *Journal of Microscopy* **2001,** 202, (1), 94-99.

208.   Franken, P. A.; Hill, A. E.; Peters, C. W.; Weinreich, G., Generation of optical harmonics. *Physical Review Letters* **1961,** 7, (4), 118-119.

209.   Armstrong, J. A.; Bloembergen, N.; Ducuing, J.; Pershan, P. S., Interactions between light waves in a nonlinear dielectric. *Physical Review* **1962,** 127, (6), 1918-1939.

210.   Shen, Y. R., *The Principles of Nonlinear Optics*. Wiley: New York, 1984.

211.   Neacsu, C. C. Tip-enhanced near-field optical microscopy: from symmetry selectivity to single molecule sensitivity. Humboldt-Universität, Berlin, 2008.

212.   Petukhov, A. V.; Brudny, V. L.; Luis MochÃ¡n, W.; Maytorena, J. A.; Mendoza, B. S.; Rasing, T., Energy conservation and the manley-rowe relations in surface nonlinear-optical spectroscopy. *Physical Review Letters* **1998,** 81, (3), 566-569.

213.   Dadap, J. I.; Shan, J.; Eisenthal, K. B.; Heinz, T. F., Erratum: Second-harmonic Rayleigh scattering from a sphere of centrosymmetric material (Phys. Rev. Lett. (1999) 83 (004045)). *Physical Review Letters* **2003,** 91, (14).

214.   Dadap, J. I.; Shan, J.; Eisenthal, K. B.; Heinz, T. F., Second-Harmonic Rayleigh Scattering from a Sphere of Centrosymmetric Material. *Physical Review Letters* **1999,** 83, (20), 4045-4048.

215.   Yang, N.; Angerer, W. E.; Yodh, A. G., Angle-resolved second-harmonic light scattering from colloidal particles. *Physical Review Letters* **2001,** 87, (10), 103902/1-103902/1.

216.   Roke, S.; Bonn, M.; Petukhov, A. V., Nonlinear optical scattering: The concept of effective susceptibility. *Physical Review B - Condensed Matter and Materials Physics* **2004,** 70, (11), 115106-1-115106-10.

217.   Neacsu, C. C.; Reider, G. A.; Raschke, M. B., Second-harmonic generation from nanoscopic metal tips: Symmetry selection rules for single asymmetric nanostructures. *Physical Review B - Condensed Matter and Materials Physics* **2005,** 71, (20).

218.   Labardi, M.; Allegrini, M.; Zavelani-Rossi, M.; Polli, D.; Cerullo, G.; De Silvestri, S.; Svelto, O., Highly efficient second-harmonic nanosource for near-field optics and microscopy. *Optics Letters* **2004,** 29, (1), 62-64.

219.   Zayats, A. V.; Smolyaninov, I. I., Near-field second-harmonic generation. *Philosophical Transactions of the Royal Society A: Mathematical, Physical and Engineering Sciences* **2004,** 362, (1817), 843-860.

220.   Neacsu, C. C.; Van Aken, B. B.; Fiebig, M.; Raschke, M. B., Second-harmonic near-field imaging of ferroelectric domain structure of YMnO3. *Physical Review B - Condensed Matter and Materials Physics* **2009,** 79, (10).

221.   Maiman, T. H., Stimulated optical radiation in Ruby. *Nature* **1960,** 187, (4736), 493-494.

222.   Sansone, G.; Kelkensberg, F.; Pérez-Torres, J. F.; Morales, F.; Kling, M. F.; Siu, W.; Ghafur, O.; Johnsson, P.; Swoboda, M.; Benedetti, E.; Ferrari, F.; Lépine, F.; Sanz-Vicario, J. L.; Zherebtsov, S.; Znakovskaya, I.; Lhuillier, A.; Ivanov, M. Y.; Nisoli, M.; Martín, F.; Vrakking, M. J. J., Electron localization following attosecond molecular photoionization. *Nature* **2010,** 465, (7299), 763-766.

223.   Kautek, W.; Krüger, J.; Lenzner, M.; Sartania, S.; Spielmann, C.; Krausz, F., Laser ablation of dielectrics with pulse durations between 20 fs and 3 ps. *Applied Physics Letters* **1996,** 69, (21), 3146-3148.

224.   Lenzner, M.; Krüger, J.; Sartania, S.; Cheng, Z.; Spielmann, C.; Mourou, G.; Kautek, W.; Krausz, F., Femtosecond optical breakdown in dielectrics. *Physical Review Letters* **1998,** 80, (18), 4076-4079.

225.   Lenzner, M.; Krüger, J.; Kautek, W.; Krausz, F., Precision laser ablation of dielectrics in the 10-fs regime. *Applied Physics A: Materials Science and Processing* **1999,** 68, (3), 369-371.

226.   Kowalevicz, A. M.; Sharma, V.; Ippen, E. P.; Fujimoto, J. G.; Minoshima, K., Three-dimensional photonic devices fabricated in glass by use of a femtosecond laser oscillator. *Optics Letters* **2005,** 30, (9), 1060-1062.

227.   Osellame, R.; Chiodo, N.; Maselli, V.; Yin, A.; Zavelani-Rossi, M.; Cerullo, G.; Laporta, P.; Aiello, L.; De Nicola, S.; Ferraro, P.; Finizio, A.; Pierattini, G., Optical properties of waveguides written by a 26 MHz stretched cavity Ti:sapphire femtosecond oscillator. *Optics Express* **2005,** 13, (2), 612-620.

228.   Cho, S. H.; Bouma, B. E.; Ippen, E. P.; Fujimoto, J. G., Low-repetition-rate high-peak-power Kerr-lens mode-locked Ti:Al2O3 laser with a multiple-pass cavity. *Optics Letters* **1999,** 24, (2-6), 417-419.

229.   Apolonski, A.; Poppe, A.; Tempea, G.; Spielmann, C.; Udem, T.; Holzwarth, R.; Hänsch, T. W.; Krausz, F., Controlling the phase evolution of few-cycle light pulses. *Physical Review Letters* **2000,** 85, (4), 740-743.

230.   Fernandez, A.; Fuji, T.; Poppe, A.; Fürbach, A.; Krausz, F.; Apolonski, A., Chirped-pulse oscillators: A route to high-power femtosecond pulses without external amplification. *Optics Letters* **2004,** 29, (12), 1366-1368.

231.   Forster, M. Physico-chemical modification and ablation of solid materials by ultrashort laser pulses. University of Vienna, Vienna, 2010.

232.   Keldysh, L. V., Ionization in Field of a Strong Electromagnetic Wave. *Soviet Physics JETP* **1965,** 20, (5), 1307-1314.

233.   August, S.; Strickland, D.; Meyerhofer, D. D.; Chin, S. L.; Eberly, J. H., Erratum: Tunneling ionization of noble gases in a high-intensity laser field (Physical Review Letters (1991) 66, 9, (1247)). *Physical Review Letters* **1991,** 66, (9), 1247.

234.   Augst, S.; Strickland, D.; Meyerhofer, D. D.; Chin, S. L.; Eberly, J. H., Tunneling ionization of noble gases in a high-intensity laser field. *Physical Review Letters* **1989,** 63, (20), 2212-2215.

235.   Stoian, R.; Ashkenasi, D.; Rosenfeld, A.; Wittmann, M.; Kelly, R.; Campbell, E. E. B., The dynamics of ion expulsion in ultrashort pulse laser sputtering of Al2O3. *The dynamics of ion expulsion in ultrashort pulse laser sputtering* **2000,** 166-167, 682-690.

236. Dermota, T. E.; Zhong, Q.; Castleman Jr, A. W., Ultrafast dynamics in cluster systems. *Chemical Reviews* **2004,** 104, (4), 1861-1886.

237. Corkum, P. B.; Brunel, F.; Sherman, N. K.; Srinivasan-Rao, T., Thermal response of metals to ultrashort-pulse laser excitation. *Physical Review Letters* **1988,** 61, (25), 2886-2889.

238. Miotello, A.; Kelly, R., Critical assessment of thermal models for laser sputtering at high fluences. *Applied Physics Letters* **1995,** 67, 3535.

239. Binnig, G.; Quate, C. F.; Gerber, C., Atomic force microscope. *Physical Review Letters* **1986,** 56, (9), 930-933.

240. Mironov, V. L., *Fundamentals of Scanning Probe MIcroscopy*. The Russian Academy of Science: Nizhniy Novgorod, 2004.

241. Morita, S.; Wiesendanger, R.; Meyer, E., *Noncontact Atomic Force Microscopy*. Springer: Berlin/Heidelberg/New York, 2002.

242. Prokhorov, V. V., *Semicontact mode*. NT-MDT.

243. Garcia, R.; San Paulo, A., Dynamics of a vibrating tip near or in intermittent contact with a surface. *Physical Review B - Condensed Matter and Materials Physics* **2000,** 61, (20), R13381-R13384.

244. Cleveland, J. P.; Anczykowski, B.; Schmid, A. E.; Elings, V. B., Energy dissipation in tapping-mode atomic force microscopy. *Applied Physics Letters* **1998,** 72, (20), 2613-2615.

245. Zhong, Q.; Inniss, D.; Kjoller, K.; Elings, V. B., Fractured polymer/silica fiber surface studied by tapping mode atomic force microscopy. *Surface Science* **1993,** 290, (1-2), L688-L692.

246. Albrecht, T. R.; Grütter, P.; Horne, D.; Rugar, D., Frequency modulation detection using high-Q cantilevers for enhanced force microscope sensitivity. *Journal of Applied Physics* **1991,** 69, (2), 668-673.

247. Giessibl, F. J., A direct method to calculate tip-sample forces from frequency shifts in frequency-modulation atomic force microscopy. *Applied Physics Letters* **2001,** 78, (1), 123-125.

248. Giessibl, F. J. In *Atomic Force Microscopy on Its Way to Adolescence*, Scanning Tunneling Microscopy/Spectroscopy and Related Techniques, Eindhoven, 2003; American Institute of Physics: Eindhoven, 2003; pp 60-67.

249. Milner, A. A.; Zhang, K.; Prior, Y. In *Tip-to-sample distance control in apertureless near-field optical microscopy*, Conference on Lasers and Electro-Optics, 2007, CLEO 2007, 2007; 2007.

250. Porto, J. A.; Johansson, P.; Apell, S. P.; López-Ríos, T., Resonance shift effects in apertureless scanning near-field optical microscopy. *Physical Review B - Condensed Matter and Materials Physics* **2003,** 67, (8), 854091-854099.

251. Krug, J. T.; Sanchez, E. J.; Xie, X. S., Design of near-field optical probes with optimal field enhancement by finite difference time domain electromagnetic simulation. *Journal of Chemical Physics* **2002,** 116, (24), 10895-10901.

252. Sajanlal, P. R.; Subramaniam, C.; Sasanpour, P.; Rashidian, B.; Pradeep, T., Electric field enhancement and concomitant Raman spectral effects at the edges of a nanometre-thin gold mesotriangle. *Journal of Materials Chemistry* **2010,** 20, (11), 2108-2113.

253. Lu, Y. F.; Mai, Z. H.; Chim, W. K., Electromagnetic calculations of the near field of a tip under polarized laser irradiation. *Japanese Journal of Applied Physics, Part 1: Regular Papers and Short Notes and Review Papers* **1999,** 38, (10), 5910-5915.

254. Martin, O. J. F.; Girard, C.; Dereux, A., Generalized field propagator for electromagnetic scattering and light confinement. *Physical Review Letters* **1995,** 74, (4), 526-529.

255. Bailo, E.; Deckert, V., Tip-enhanced Raman scattering. *Chemical Society Reviews* **2008,** 37, (5), 921-930.

256.   Martin, O. J. F.; Paulus, M., Influence of metal roughness on the near-field generated by an aperture/apertureless probe. *Journal of Microscopy* **2002,** 205, (2), 147-152.

257.   Downes, A.; Salter, D.; Elfick, A., Finite element simulations of tip-enhanced Raman and fluorescence spectroscopy. *Journal of Physical Chemistry B* **2006,** 110, (13), 6692-6698.

258.   Geshev, P. I.; Fischer, U.; Fuchs, H., Calculation of tip enhanced Raman scattering caused by nanoparticle plasmons acting on a molecule placed near a metallic film. *Physical Review B - Condensed Matter and Materials Physics* **2010,** 81, (12).

259.   Demming, F.; Jersch, J.; Dickmann, K.; Geshev, P. I., Calculation of the field enhancement on laser-illuminated scanning probe tips by the boundary element method. *Applied Physics B: Lasers and Optics* **1998,** 66, (5), 593-598.

260.   Hohenester, U.; Trügler, A., MNPBEM - A Matlab toolbox for the simulation of plasmonic nanoparticles. *Computer Physics Communications* **2012,** 183, (2), 370-381.

261.   Trügler, A. Optical properties of metallic nanoparticles. Karl-Fanzens-Univsity, Graz, 2011.

262.   García de Abajo, F. J.; Howie, A., Retarded field calculation of electron energy loss in inhomogeneous dielectrics. *Physical Review B - Condensed Matter and Materials Physics* **2002,** 65, (11), 1154181-11541817.

263.   García De Abajo, F. J., Optical excitations in electron microscopy. *Reviews of Modern Physics* **2010,** 82, (1), 209-275.

264.   Zhang, W.; Xudong, C.; Martin, O. J. F., Local field enhancement of an infinite conical metal tip illuminated by a focused beam. *Journal of Raman Spectroscopy* **2009,** 40, 1338-1342.

265.   Sun, W. X.; Shen, Z. X., Optimizing the near field around silver tips. *Journal of the Optical Society of America* **2003,** 20, (12), 2254-2259.

266.   Chen, X.; Wang, X., Near-field thermal transport in a nanotip under laser irradiation. *Nanotechnology* **2011,** 22, (7).

267.   Balkanski, M.; Wallis, R. F.; Haro, E., Anharmonic effects in light scattering due to optical phonons in silicon. *Physical Review B* **1983,** 28, (4), 1928-1934.

268.   Datskos, P. G.; Lavrik, N. V.; Rajic, S., Performance of uncooled microcantilever thermal detectors. *Review of Scientific Instruments* **2004,** 75, (4), 1134-1148.

269.   Barnes, J. R.; Stephenson, R. J.; Woodburn, C. N.; O'Shea, S. J.; Welland, M. E.; Rayment, T.; Gimzewski, J. K.; Gerber, C., Erratum: A femtojoule calorimeter using micromechanical sensors (Rev. Sci. Instrum. 65, 3793 (1994)). *Review of Scientific Instruments* **1995,** 66, (4), 3083.

270.   Barnes, J. R.; Stephenson, R. J.; Woodburn, C. N.; O'Shea, S. J.; Welland, M. E.; Rayment, T.; Gimzewski, J. K.; Gerber, C., A femtojoule calorimeter using micromechanical sensors. *Review of Scientific Instruments* **1994,** 65, (12), 3793-3798.

271.   Zhang, K., A method for reducing laser heating on atomic force microscope tips. *EPJ Applied Physics* **2011,** 53, (1).

272.   Vurpillot, F.; Gault, B.; Vella, A.; Bouet, M.; Deconihout, B., Estimation of the cooling times for a metallic tip under laser illumination. *Applied Physics Letters* **2006,** 88, (9).

273.   Kirsanov, A.; Kiselev, A.; Stepanov, A.; Polushkin, N., Femtosecond laser-induced nanofabrication in the near-field of atomic force microscope tip. *Journal of Applied Physics* **2003,** 94, (10), 6822-6826.

274.   Houard, J.; Vella, A.; Vurpillot, F.; Deconihout, B., Three-dimensional thermal response of a metal subwavelength tip under femtosecond laser illumination. *Physical Review B - Condensed Matter and Materials Physics* **2011,** 84, (3).

275.   McCarthy, B.; Zhao, Y.; Grover, R.; Sarid, D., Enhanced Raman scattering for temperature measurement of a laser-heated atomic force microscope tip. *Applied Physics Letters* **2005,** 86, (11), 1-3.

276.   Schaffer, C.; Nishimura, N.; Glezer, E.; Kim, A.; Mazur, E., Dynamics of femtosecond laser-induced breakdown in water from femtoseconds to microseconds. *Opt. Express* **2002,** 10, (3), 196-203.

277.   Lefévre, S.; Volz, S.; Chapuis, P. O., Nanoscale heat transfer at contact between a hot tip and a substrate. *International Journal of Heat and Mass Transfer* **2006,** 49, (1-2), 251-258.

278.   Thomson, R. E., Development of highly conductive cantilevers for atomic force microscopy point contact measurements. *Journal of Vacuum Science and Technology B* **1995,** 12, (3), 1123-1125.

279.   M.Rosoff, *Nano-surface chemistry*. Marcel Dekker Inc.: New York, 2002.

280.   Sleytr, U. B.; SÃ¡ra, M.; Pum, D.; Schuster, B., Characterization and use of crystalline bacterial cell surface layers. *Progress in Surface Science* **2001,** 68, (7-8), 231-278.

281.   Steinbüchel, A.; Fahenstock, S. R., *Biopolymers*. Wiley-VCH: Weinheim, 2003.

282.   Mulet, J. P.; Joulain, K.; Carminati, R.; Greffet, J. J., Nanoscale radiative heat transfer between a small particle and a plane surface. *Applied Physics Letters* **2001,** 78, (19), 2931-2933.

283.   Chapuis, P. O.; Greffet, J. J.; Joulain, K.; Volz, S., Heat transfer between a nano-tip and a surface. *Nanotechnology* **2006,** 17, (12), 2978-2981.

List of Figures

List of Figures
_____

List of Tables

Curriculum Vitae

Personal Details

Name:	Christoph Huber
Date of Birth:	24 July 1982
Nationality:	Austria

Education

07/2007-present	PhD at the Department of Physical Chemistry, University of Vienna, Austria Title of the thesis: "*Apertureless scanning near-field optical microscopy and manipulation of nanostructures at electrified interfaces*"
10/2001-07/2007	Diploma study at the University of Vienna, finished with excellent success Title of the thesis: "*Modification and Characterisation of Carbon Nanotubes*"
06/2000	BG/BRG St. Martin, Villach, Austria

Employment record

02/2012-present	Scientific collaborator at the Department of Nanobiotechnology, University of Natural Resources and Life Science
11/2007-01/2012	Praedoc at the Department of Physical Chemistry, University of Vienna
05/2005-02/2001	Project staff, Fronius Int. GmbH, *Development and characterisation of air separation membranes*. (Project confidential)
07-09/2004+05	Environmental scientist, Water board of the Ossiacher lake, *Investigation of the algae problem.*
07-2003	Quality management, Austrian Chemical Industry (ÖCW), *Analysis of the quality of various chemicals like hydrogen peroxide etc*.
07-08/2002	Fundraising, Red Cross, Germany
08-12/2001	Clean room worker, Infineon Technologies Austria, *Production of microelectronics*

Stay abroad

05-08/2011	Scientific collaboration with the Weizmann Institute of Science, Rehovot, Israel in the Nonlinear Optic Group of Prof. Yehiam Prior